MICROSTRUCTURAL INVESTIGATIONS OF RARE-EARTH TRANSITION-METAL-BASED MAGNETOCALORIC MATERIALS FOR NEAR-ROOM-TEMPERATURE

BENJAMIN PODMILJŠAK

Doctoral Dissertation
Jožef Stefan International Postgraduate School
Ljubljana, Slovenia, September 2010

Evaluation Board:

doc. dr. Goran Dražič, Chairman, Institut Jožef Stefan, Ljubljana
prof. dr. Miran Čeh, Member, Institut Jožef Stefan, Ljubljana
prof. dr. Janez Dolinšek, Member, University of Ljubljana, Ljubljana

Benjamin Podmiljšak

Microstructural investigations of rare-earth transition-metal-based magnetocaloric materials for near-room-temperature applications

Doctoral Dissertation

Raziskave mikrostruktur magnetokaloričnih materialov na osnovi redkih zemelj in elementov prehoda za uporabo pri sobni temperaturi

Doktorska disertacija

Supervisor: Prof. Dr. Spomenka Kobe

Co-Supervisor: Assist. Prof. Dr. Paul McGuiness

Ljubljana, Slovenia, September 2010

MEDNARODNA PODIPLOMSKA ŠOLA JOŽEFA STEFANA
JOŽEF STEFAN INTERNATIONAL POSTGRADUATE SCHOOL

For my father.

Index

Abstract

Magnetocaloric materials are promising materials for magnetic refrigerators which would substitute present compressor refrigerators. They work on the principle of the magnetocaloric effect (MCE), where the magnetocaloric material increases its temperature when exposed to an external magnetic field. These new type of refrigerators are energetically more efficient and environmentally friendly.

One of the promising materials, discovered in 1997, is the $Gd_5Si_2Ge_2$ alloy with a giant magnetocaloric effect ($-\Delta S_m$), because it has a simultaneous structural and magnetic transition. This giant MCE has a disadvantage that it has very high hysteresis losses when cycled through a changing magnetic field. To reduce this, a small amount of germanium was substituted in small amounts with iron. With this an increase in the net refrigeration capacity (NRC) was achieved. The lower hysteresis losses were explained with the suppression of the structural transformation.

The goal in this thesis was to investigate different preparation techniques of $Gd_5Si_2Ge_2$, such as arc melting, mechanical alloying and melt spinning to improve the properties of these alloys. Also we wanted to investigate more thoroughly the effect of iron on $Gd_5Si_2Ge_2$. For this we have investigated the magnetic properties as well as the macro-, micro- and nanostructural changes for a wide range of iron substitutions. The affect of iron was researched on three sets of samples. In the first one we substituted germanium with iron by the following formula $Gd_5Si_2Ge_{2-x}Fe_x$, where x=0, 0.06, 0.125, 0.25, 0.5, 0.75 and 1. The second we substituted silicon with iron by the formula $Gd_5Si_{2-x}Ge_2Fe_x$, where x=0, 0.06, 0.125, 0.25, 0.5, 0.75 and 1. In the third set of samples we substituted silicon and germanium equally with iron by the formula $Gd_5Si_{2-x/2}Ge_{2-x/2}Fe_x$, where x=0, 0.06, 0.125, 0.25, 0.5, 0.75. The samples were prepared with an arc-melter and homogenized in an inert atmosphere. They were analyzed with an optical microscope, field-emission-gun scanning electron microscope (FEG SEM) and a transmission electron microscope (TEM). The structural changes were analyzed with an X-ray diffractometer at room temperature and at cryogenic temperatures. The magnetic measurements were made with a cryogenic vibrating-sample magnetometer (VSM) and a physical properties measurement system (PPMS), with a vibrating-sample magnetometer attachment. Adiabatic temperature changes where measured with a modified magnetocaloric measurement setup.

The preparation of $Gd_5Si_2Ge_2$ presented many problems when trying to prepare them with mechanical alloying or melt spinning. Only arc melting produced the desired phase effectively.

The substitutions in all three sets of samples presented us with some unusual macrostructures and a consistent change in the microstructures of the samples. Iron reduces the silicon and germanium concentration in the main matrix phase, by forming a grain boundary phase. Because of the reduction of Si and Ge, the main matrix phase is converted to the $Gd_5(Si,Ge)_3$ phase.

Low temperature XRD confirmed the structural transformation in the SI and GESI sample. In the GE sample only a partial transformation is observed suggesting that iron can suppress the structural transformation only in the GE samples.

We also observed that the addition of iron has a pronoun effect on the Curie temperature of the $Gd_5Si_2Ge_2$ phase. When substituting Si the T_C is reduced and when substituting Ge T_C increases. If we substitute both the transition temperature does almost not change. In all substitutions $-\Delta S_m$ is reduced. The difference is that it is reduced faster with GE substitutions then with GESI and SI substitutions. Also the hysteresis losses are reduced faster in the GE samples than in the other two. This has to do with the change in the Si/Ge ratio in the main phase and the reduction of the main phase on account of the new 5:3 phase. We also observe a broadening of the lowered $-\Delta S_m$ peaks. This results in a increase of the net refrigeration capacity in the GESI samples compared to the unsubstituted $Gd_5Si_2Ge_2$ sample. Adiabatic temperature change measurements confirmed the reduction of the MCE in these alloys with added iron. The reduction is comparable to the $-\Delta S_m$ results with a broadening of the peak.

TEM investigations confirmed the formation of twins in the $Gd_5Si_2Ge_2$ alloy. The results also suggest that additions of Fe produce complex changes to the structure of the Gd5Ge2Si2 material, like amorphous regions, dislocations and planar faults, as well as crystallographically related grains.

We have achieved an increase of the refrigeration capacity by carefully substituting some of the elements with iron. Also with iron we can tailor the transition temperature of the magnetocaloric material. With these findings this material is a promising candidate as a working material in a magnetic refrigerator.

Povzetek

Magnetokalorični materiali so obetavni materiali za magnetne hladilnike, ki bi lahko zamenjali dosedanje kompresorske hladilnike. Delujejo na principu magnetokaloričnega efekta (MCE), kjer se magnetokaloričnemu materialu dvigne temperatura, če ga izpostavimo zunanjemu magnetnemu polju. Ta nova vrsta hladilnikov je energijsko bolj učinkovita in okolju bolj sprejemljiva.

Eden od obetavnih magnetokaloričnih materialov, odkrit 1997, je zlitina $Gd_5Si_2Ge_2$ s tako imenovanim velikanskim magnetokaloričnim efektom ($-\Delta S_m$), zaradi njene istočasne strukturne in magnetne transformacije. Ta velikanski MCE ima tudi negativno lastnost, to so velikanske histerezne izgube, če material ciklično izpostavljamo zunanjemu magnetnemu polju. Da bi te izgube zmanjšali, so majhno količino germanija zamenjali z železom. S tem so dosegli povečanje skupne hladilne kapacitete (NRC). Nižje histerezne izgube so razložili z zaviranjem strukturne transformacije.

Cilj teze je bilo raziskovanje različnih načinov priprave zlitine $Gd_5Si_2Ge_2$, kot so obločno taljenje, mletje in indukcijsko taljenje z hitrim ohlajanjem. Želeli smo tudi bolj natančno raziskovati efekt železa na $Gd_5Si_2Ge_2$. Zato smo raziskovali magnetne lastnosti, kot tudi makro, mikro ter nano strukturne spremembe za široko območje zamenjav z železom. Vpliv železa smo raziskovali na treh sistemih. V prvem sistemu smo zamenjali germanij z železom po formuli $Gd_5Si_2Ge_{2-x}Fe_x$, kjer je x=0, 0.06, 0.125, 0.25, 0.5, 0.75 in 1. V drugem sistemu smo zamenjali silicij z železom po formuli $Gd_5Si_{2-x}Ge_2Fe_x$, kjer je x=0, 0.06, 0.125, 0.25, 0.5, 0.75 in 1. V tretjem sistemu smo zamenjali silicij in germanij enakomerno z železom po formuli $Gd_5Si_{2-x/2}Ge_{2-x/2}Fe_x$, kjer je x=0, 0.06, 0.125, 0.25, 0.5, 0.75 in 1. Vzorci so bili pripravljeni z obločnim taljenjem in nato homogenizirali v inertni atmosferi. Nato so bili analizirani na optičnem mikroskopu, na vrstičnem elektronskem mikroskopu s poljsko emisijo (FEG SEM) ter presevnem elektronskem mikroskopu (TEM). Strukturne spremembe so bile analizirane z praškovnim rentgenskim difraktometrom, pri sobni temperaturi in pri temperaturi pod sobno. Magnetne lastnosti so bile izvedene na magnetometru z nihajočim vzorcem z nizko temperaturno enoto (VSM), ter z sistemom za merjenje fizikalnih lastnosti (PPMS) z dodatkom magnetometra z nihajočim vzorcem. Adiabatne temperaturne spremembe so bile izmerjene z modificiranim magnetokaloričnim merilnim sistemom.

Priprava $Gd_5Si_2Ge_2$ z mletjem ali s taljenjem z hitrim ohlajanjem se je izkazalo kot zelo neprimerno. Obločno taljenje se je izkazalo kot najučinkovitejša metoda za izdelavo želene faze.

Zamenjava v vseh treh sistemih je pokazala zelo nenavadne makro strukture in skladno spremembo v mikrostrukturi vzorca. Železo zmanjšuje koncentracijo silicija in germanija v glavni fazi, s tem da ustvari novo fazo med zrni. Zaradi zmanjšanja koncentracije Si in Ge se glavna matrična faze spremeni v $Gd_5(Si,Ge)_3$ fazo.

Nizko temperaturna praškovna difrakcija je potrdila strukturne spremembe v vzorcih SI in GESI. V vzorcih GE smo opazili delno strukturno spremembo. Železo lahko zavira strukturno spremembo samo, če ga zamenjamo namesto germanija.

Opazili smo tudi, da ima železo zelo velik vpliv na Curiejevo temperaturo $Gd_5Si_2Ge_2$ faze. Če zamenjamo Si se temperatura T_C znižuje in če zamenjamo Ge se T_C zvišuje. Če pa zamenjamo oba hkrati se temperatura magnetnega prehoda skoraj ne spremeni. V vseh zamenjavah se znižuje $-\Delta S_m$. Razlika je v tem, da $-\Delta S_m$ hitreje pada pri zamenjavah Ge kot pri drugih dveh sistemih. To je zaradi spremembe v Si/Ge razmerju v glavni fazi in zmanjšanjem deleža le te na račun nove 5:3 faze. Opazili smo tudi širitev vrhov pri znižanju $-\Delta S_m$ vrednosti. Ta razširitev privede do zvišanje skupne hladilne kapacitete v vzorcih GESI glede na vzorec brez železa.

Meritev adiabatnih temperaturnih sprememb je potrdila znižanje magnetokaloričnega efekta z dodajanjem železa. Sprememba z referenčnim vzorcem je primerljiva s $-\Delta S_m$ spremembami, kje pride tudi do razširitve vrhov.

TEM raziskave so potrdile nastanek dvojčkov v $Gd_5Si_2Ge_2$ zlitini. Rezultati tudi pokažejo, da dodatek železa privede do kompleksnih sprememb v strukturi materiala, kot so amorfne regije, dislokacije in planarne defekte, kot tudi kristalografsko sorodna zrna.

Dosegli smo zvišanje skupne hladilne kapacitete s skrbno zamenjavo elementov v $Gd_5Si_2Ge_2$ zlitini z železom. Prav tako lahko izdelamo zlitino z določeno Curiejevo temperaturo. S temi najdbami lahko ta material postane primeren kandidat za delovni material v magnetnem hladilniku.

Abbreviations

ADC = analogue digital convert
AM = arc melting
AFM = anti ferromagnetic, anti ferromagnet
AMR = active magnetic regenerator
BSE = back-scattered electrons
CMCE = colossal magnetocaloric effect
COP = coefficient of performance
DC = direct current
EDS = energy dispersive spectroscopy
EDXS = energy dispersive X-ray spectroscopy
EELS = Electron Energy Loss Spectroscopy
et al. = and co-workers
FFT = fast Fourier transformation
FM = ferromagnetic, ferromagnet
FOMT = first order magnetic transition
FWHM = full width at half-maximum
GB = grain boundary
GMCE = giant magnetocaloric effect
HRTEM = high-resolution transmission electron microscopy
HM = Halbach magnet
HT = heat treatment
JSI = Jožef Stefan Institute
L.B. = layered bed
M = monoclinic
MA = mechanical alloying
MC = magnetocaloric
MCE = magnetocaloric effect
MR = magnetic refrigeration
MS = melt spinning
NDR = nuclear demagnetization refrigeration
NRC = net refrigerant capacity
$O(I)$ = orthorhombic (I) Gd_5Si_4-type structure
$O(II)$ = orthorhombic (II) Sm_5Ge_4-type structure
PEM = permanent magnet
PM = paramagnetic, paramagnet
PPMS = physical property measurement system
SAED = selected-area electron diffraction
SCM = superconducting magnet
SEI = secondary-electron image
SEM = scanning electron microscopy/microscope
SOMT = second order magnetic transition
STEM = scanning transmission electron microscopy/microscope
SQUID = superconducting quantum interference device
RC = refrigerant capacity
VSM = vibrating-sample magnetometer
TEM = transmission electron microscopy/microscope
TB-LMTO = tight binding linear muffin tin orbital method
XRD = X-ray diffraction

1 The magnetocaloric effect

1.1 Introduction

The magnetocaloric effect (MCE) is a magneto-thermodynamic phenomenon and is defined as the heating or cooling of a magnetic material due to the application of a magnetic field.

Similarities can be drawn with the processes in a gas in response to a changing pressure. When isothermally compressing a gas, the positional disorder and, therefore, the corresponding component of the entropy are suppressed. The same thing happens when isothermally magnetizing a paramagnetic solid near absolute zero or a ferromagnetic material near its spontaneous magnetic ordering temperature—the Curie temperature, T_C. They reduce the disorder of the spin system, thus substantially lowering the magnetic part of the total entropy. In the reverse process, which is similar to the expansion of a gas at constant temperature, isothermal demagnetizing restores the zero-field magnetic entropy of the system. Figure 1 shows the relationship between the two methods.

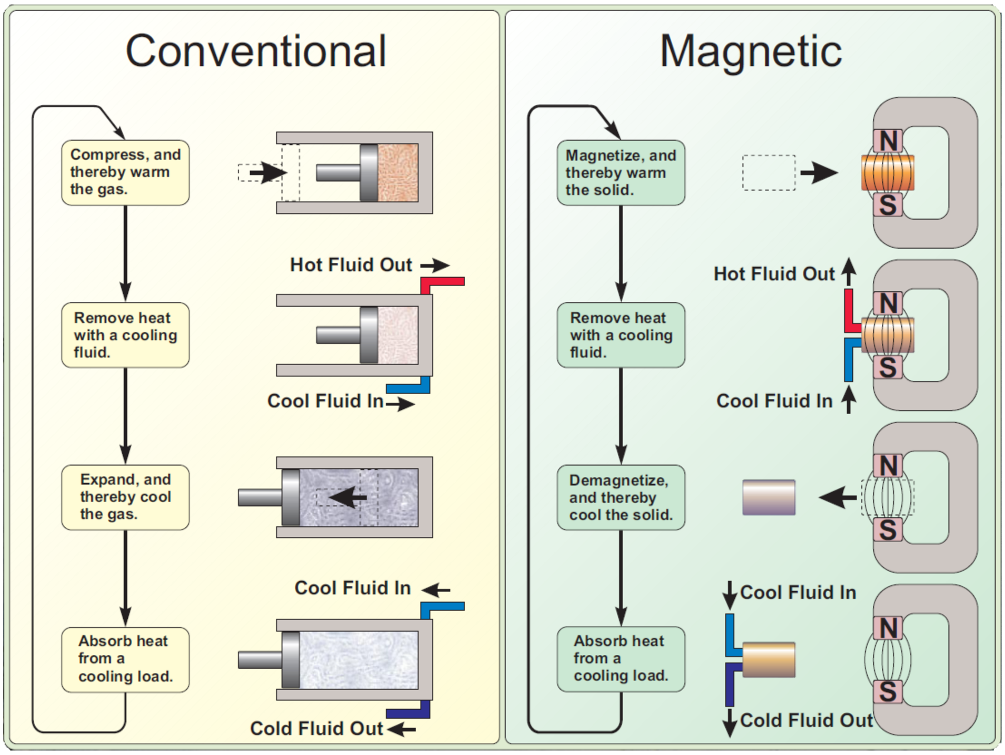

Figure 1: Comparison of a vapor compressor and a magnetic refrigerator [1]

The magnetocaloric effect was first discovery by Warburg in 1881, where he observed this effect in iron. [2] However, it was 45 years later that this effect was explained independently by Debye [3] and Giauque [4], for which they got the Nobel prize. They also proposed the practical use of such an effect – cooling via adiabatic magnetization. In the early 1930s Giauque and MacDougall [5] demonstrated the process for the first time, reaching a temperature of 0.25 K. Since then most of the research has focused on finding materials with high MCE in cryostatic regions. Commonly, paramagnetic salts are used to reach low temperatures of 100 mK. Although for this they have to be pre-cooled with liquid 4He (1.2 K) or 3He (0.3 K). One variant of adiabatic demagnetization that continues to find many research applications is nuclear demagnetization refrigeration (NDR). NDR follows the same principle described above, but in this case the cooling power arises from the magnetic dipoles of the nuclei of the refrigerant atoms. Thus achieving temperatures of μK, but it has to be pre-cooled to 100 mK.

Although magnetocalorics are commonly used in the low-temperature region there has been in the last century no use for them in the room temperature region, because other cooling mechanisms were more efficient. Pure Gd was the only known material that had a high magnetocaloric effect at room temperature. In 1976 Brown [6] showed a continuously operating device working near room temperature, filled with Gd plates, that achieved a maximum temperature span of 47 K in an alternating 70 kOe field produced by a superconducting magnet. But no practical applications were realized. Not until 1997, when two breakthroughs occurred. First, the unveiling of a proof-of-principle magnetic refrigerator demonstrating that magnetic refrigeration is a viable and competitive cooling technology in the near-room-temperature region with potential energy savings of up to 30%. [7] Second the discovery of the giant MCE (GMCE) in $Gd_5Si_2Ge_2$. [8] These two breakthroughs boosted the research in the field of magnetic refrigeration at room temperature increasing the number of publications exponentially (Figure 2). An important increase of interest was produced also with the new fluorine-gas regulation and the Kyoto regulation on reducing the CO_2 concentration in the atmosphere. The fear of global warming in the last decade has also increased the research on saving energy. With 15% of the total worldwide energy consumption involving the use of refrigeration (air conditioning, refrigeration, freezing, chilling, etc.) any improvement could have an enormous effect on the energy consumption. With a technology that has no ozone-depleting gases, reduces the CO_2 output and uses less energy, funding for research was easier to get. This makes this field in magnetic research so interesting. For a number of excellent reviews on this subject see references [9 – 15].

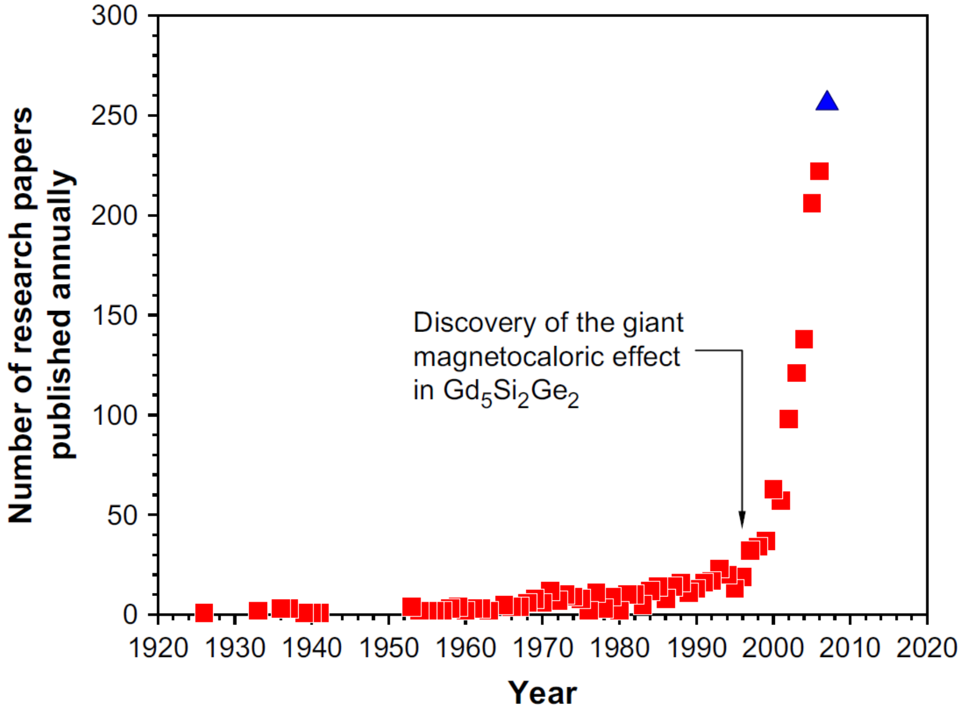

Figure 2: The number of research papers published annually over the past 80 years containing the word ‘‘magnetocaloric’’ in the title, abstract, or among the keywords. The values for 2007 (triangle) are based on the number of papers abstracted during the first three-fourths of the year. Taken from Ref. [14].

1.2 Theory

All magnetic materials intrinsically show a MCE. The intensity of each depends on the properties of the material. To explain the theory behind the magnetocaloric effect thermodynamics is used.

The important characteristics of a magnetic material are its total entropy and the entropy of its magnetic subsystem S_M, called the magnetic entropy. By varying the thermodynamic parameters like the magnetic field, temperature or pressure the entropy can be changed. This influences the MCE because they are closely related to each other.

The total entropy of a magnetic material can in general, at constant pressure, be presented as [16]

$$S(H,T) = S_M(H,T) + S_L(H,T) + S_E(H,T), \qquad (1)$$

where S_M is the magnetic entropy, S_L is the lattice and S_E is the electron contribution to the total magnetic entropy. In general, all three contributions depend on the temperature and the magnetic field and cannot be clearly separated. In a first approximation we can believe that the lattice and electronics parts of the entropy depend only on the temperature, and all the contributions depending on the magnetic field (from any changes of magnetic subsystem) are presented in the total value of the entropy in Equation (1) by $S_M(H,T)$.

The heat capacity C at constant parameter x is defined as

$$C_X = \left(\frac{\delta Q}{dT}\right)_X , \qquad (2)$$

where δQ is the heat quantity changing the system temperature with respect to dT. Using the Second law of thermodynamics

$$dS = \frac{\delta Q}{T} \qquad (3)$$

and the heat capacity can be written as

$$C_X = T\left(\frac{\partial S}{\partial T}\right)_X . \qquad (4)$$

Using the Equations 1 and 4, we can present the total heat capacity of a magnetic material as

$$C_H = C'_H + C_L + C_E, \qquad (5)$$

where C'_H, C_L and C_E are the magnetic, lattice and electron contributions, respectively. The index H means that the heat capacity is calculated at constant magnetic field.

Let us change the total entropy $S(H,T)$ of a magnetic material by changing the magnetic field and temperature under isobaric conditions. If we include the heat capacity (Equation 4) in Equation 1 and taking into account the suggestion about the independence of S_L and S_E on a magnetic field, we can write the total differential of $S(H,T)$ as

$$dS(H,M) = \frac{C_L(T)}{T}dT + \frac{C_E(T)}{T}dT + \frac{C'_H(H,T)}{T}dT + \left(\frac{\partial S_M(H,T)}{\partial H}\right)_T dH. \qquad (6)$$

The last two terms represent the total differential of the magnetic entropy:

$$dS_M(H,T) = \frac{C'_H(H,T)}{T}dT + \left(\frac{\partial S_M(H,T)}{\partial H}\right)_T dH, \qquad (7)$$

using the Maxwell equation

$$\left(\frac{\partial S}{\partial H}\right)_{T,p} = \left(\frac{\partial M}{\partial T}\right)_{H,p} , \qquad (8)$$

Equation (5) can also be written as

$$dS_M(H,T) = \frac{C'_H(H,T)}{T}dT + \left(\frac{\partial S_M(H,T)}{\partial T}\right)_H dH, \qquad (9)$$

dS_M is made up out of two parts, one related to the change of temperature (field constant part) and the other due to the change of the magnetic field (isothermal field).

We can calculate the finite change of the total magnetic entropy for a temperature change (ΔT) from T_1 to T_2 and a magnetic field change (ΔH) from H_1 to H_2 as

$$\begin{aligned}\Delta S_{M tot}(H,T) &= S_M(H+\Delta H, T+\Delta T) - S_M(H,T) \\ &= \int_T^{T+\Delta T}\left(\frac{C'_H(H,T)}{T}\right)dT + \int_H^{H+\Delta H}\left(\frac{\partial M(H,T+\Delta T)}{\partial T}\right)dH\end{aligned} \qquad (10)$$

The first integral represents the finite isofield change of the magnetic entropy ΔS_{MH}. The second integral in Equation (9) (the isothermal part ΔS_{MT}), for a field change $\Delta H = H_2 - H_1$, can be calculated from the

Maxwell relation (8) on the basis of magnetization data and can be defined as

$$\begin{aligned}\Delta S_{MT}(H,T) &= S_M(H_2,T)-S_M(H_1,T)=\int_{H_1}^{H_2}\left(\frac{\partial S_M(H,T)}{\partial H}\right)_T dH \\ &=\int_{H_1}^{H_2}\left(\frac{\partial M(H,T)}{\partial T}\right)_H dH = S(H_2,T)-S(H_1,T) \\ &=\Delta S(H,T).\end{aligned} \tag{11}$$

It can be seen that ΔS_{MT} is equal to the change of the total entropy ΔS. This is valid if S_L and S_E are not field dependent. Figure 3 shows how ΔS_{MT} and ΔS_{MH} contribute to the total magnetic entropy ΔS for a ferromagnetic material under isobaric-adiabatic magnetization process from H_1 to H_2. The total entropy change in this process is equal to zero.

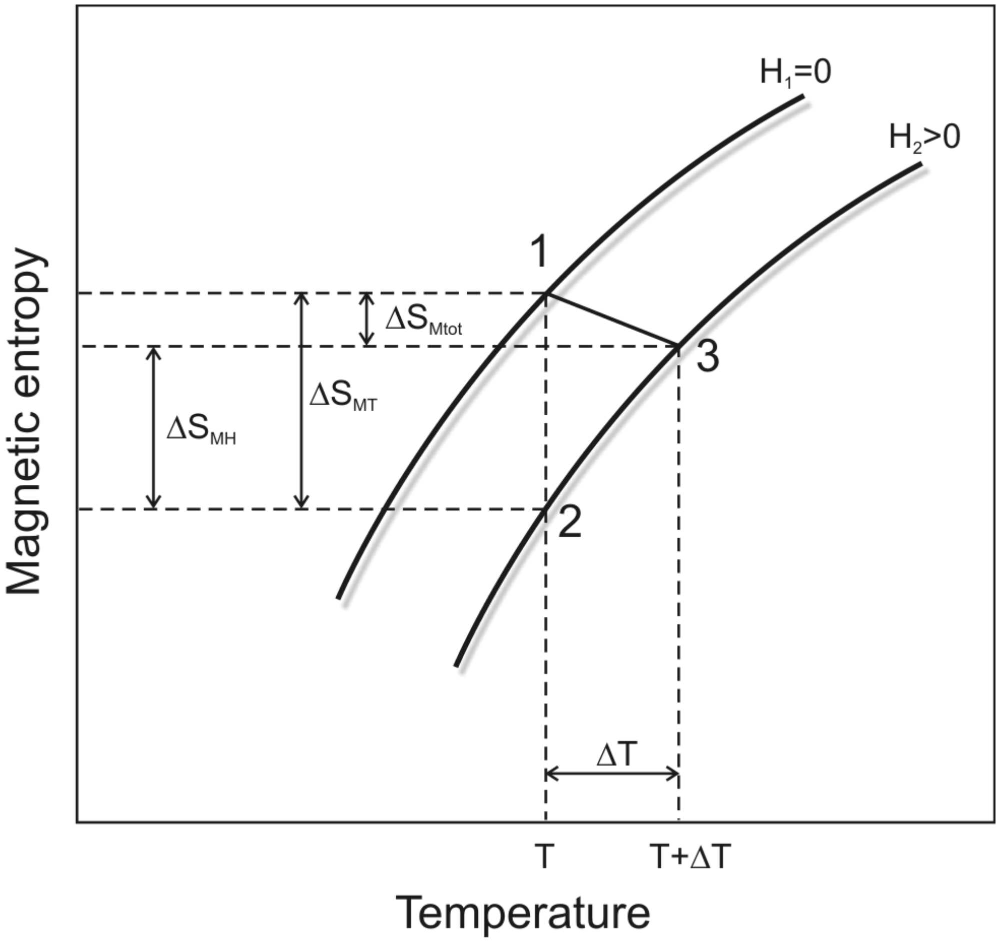

Figure 3: Temperature dependence of the magnetic entropy S_M at two different fields H_1 and H_2 in a ferromagnetic material

The process can be divided into two steps. First the isothermal change of magnetization, represented as the process from 1→2, corresponding to the entropy change ΔS_{MT}, and second the isofield temperature change, represented as the process from 2→3, corresponding to the entropy change ΔS_{MH}. Both steps influence ΔT. ΔS_{MH} determines the distance between 2→3 and ΔS_{MT} the displacement of the initial $\Delta S_M(T)$ curve. To reach the maximum MCE value one should provide such conditions at which $\Delta S_{M\ tot}$ should be equal to zero ($\Delta S_{MT} = \Delta S_{MH}$). Under such a “magnetic adiabatic” condition the MCE can be calculated using Equation (9)

$$
\begin{aligned}
dT(T,H) &= -\frac{T}{C'_H(T,H)}\left(\frac{\partial S_M(T,H)}{\partial H}\right)_T dH \\
&= -\frac{T}{C'_H(T,H)}\left(\frac{\partial M(T,H)}{\partial T}\right)_H dH,
\end{aligned}
\tag{12}
$$

The same conclusions can be made for the processes taking place in antiferromagnets, when $S(H_2,T)$ lies above $S(H_2,T)$ for $H_2 > H_1$.

In the literature is conventional to use the value of isothermal magnetic entropy changes ΔS_{MT} referring to it without the symbol T. The same marking, ΔS_M or dS_M, will be used from now on.

For an infinitesimal change of magnetic entropy dS_M can be written as

$$dS_M = \frac{C_H}{T} dT . \tag{13}$$

After integrating Equation (13) and taking into account the third law of thermodynamics, which assumes that the entropy is zero at $T = 0$, the magnetic entropy change $\Delta S_M(T)$ can be calculated from the data of the heat capacity temperature dependences $C_H(T)$:

$$\Delta S_M(T) = \int_0^T \frac{\left[C_H(H_2,T) - C_H(H_1,T)\right]}{T} dT . \tag{14}$$

The equation shows that we can expect large changes the $S_M(T)$ when the magnetic field strongly affects the heat capacity and when T is very low (providing that ΔC_H stays the same). The maximum and minimum for $\Delta S_M(T)$ can be calculated from Equation (14). Pecharsky *et al.* [17] showed that the maximum in $\Delta S_M(T)$ is observed for

$$C_H(H_1,T) = C_H(H_2,T) \text{ and } \frac{\partial C_H(H_2,T)}{\partial T} < \frac{\partial C_H(H_1,T)}{\partial T} \tag{15}$$

And the minimum in $\Delta S_M(T)$ is observed for

$$C_H(H_1,T) = C_H(H_2,T) \text{ and } \frac{\partial C_H(H_2,T)}{\partial T} > \frac{\partial C_H(H_1,T)}{\partial T} \tag{16}$$

When adiabaticaly changing the magnetic field from H_1 to H_2 in a reversible process, there is with the finite change of the magnetic entropy also a finite change of the sample temperature from T_1 to T_2. This change in temperature (ΔT_{ad}) is called the magnetocaloric effect. This change can be visualized as the isentropic difference between the corresponding $S(T)_H$ functions as shown in Figure 4 by the horizontal arrow. The vertical arrow shows the isothermal difference between the corresponding $S(T)_H$ functions by which the MCE can also be expressed. According to the diagram, the MCE ΔT_{ad} at a given temperature can be determined by the adiabatic condition $S(T,H_1) = S(T + \Delta T_{ad}, H_2)$.

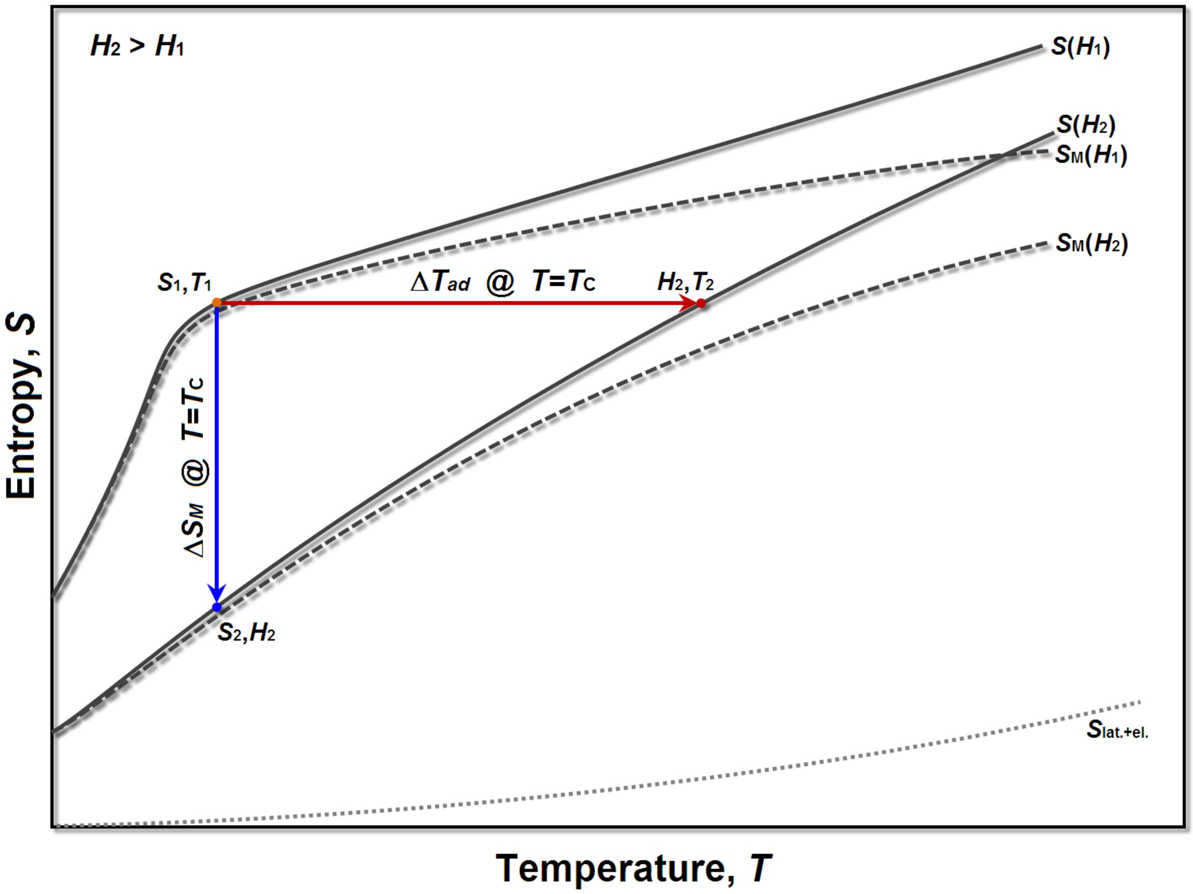

Figure 4: Temperature dependence of the total entropy $S(T)$ of a simple ferromagnet in two different magnetic fields. The dotted line shows the electronic and lattice contribution to the entropy. The dashed lines show the magnetic contribution. The two arrows represent the two quantitative characteristics of the magnetocaloric effect. The horizontal arrow represents the ΔT_{ad} and the vertical arrow represents the ΔS_{M}. Taken from Ref. [8].

If we integrate Equation (12) and assume that the heat capacity does not depend on the magnetic field, we can simplify the equation for the magnetocaloric effect ΔT_{ad}:

$$\Delta T_{ad}(T,\Delta H) = T\left\{\exp\left[-\frac{\Delta S_M(T,\Delta H)}{C_H(T)}\right]-1\right\}. \qquad (17)$$

A further simplification can be made assuming that $\Delta S_{\mathrm{M}}/C_{\mathrm{H}}$ is small (Equation (18)). It was noted that this can only be true in regions very far from the transition temperature and /or in very weak fields. [18]

$$\Delta T = -\frac{T\Delta S_M}{C_H}, \qquad (18)$$

ΔT_{ad} and ΔS_{M} represent the two quantitative characteristics of the magnetocaloric effect. The above equations (11 and 12) can give us some information about their behavior in solids. It can be seen that materials whose entropy is strongly influenced by a magnetic field and whose magnetization varies rapidly with temperature, are expected to exhibit an enhanced MCE. ΔS_{M} peaks when $|(\partial M/\partial T)_H|$ is the greatest, i.e., around the T_{C} in a ferromagnet or near absolute zero temperature in a paramagnet. The MCE of a simple ferromagnet is gradually lowered both below and above T_{C}, as Figure 5 clearly shows. High ΔT_{ad} values can be reached in simple ferromagnets and paramagnets with high absolute values of negative ΔS_{M}, and low contributions to the total heat capacity from the lattice and conduction electron subsystems, because they act as an additional heat load, reducing the MCE. The latter condition can be reached in the low-temperature region, where C_{L} and C_{E} approach zero. The counterbalance can be seen from Equation (17) where the value of ΔT_{ad} is directly proportional to the temperature. ΔT_{ad} is positive for negative ΔS_{M}

and changes the sign at $\Delta S_M = 0$. If $\Delta S_M(T)$ has a maximum in absolute value, ΔT_{ad} should also have one.

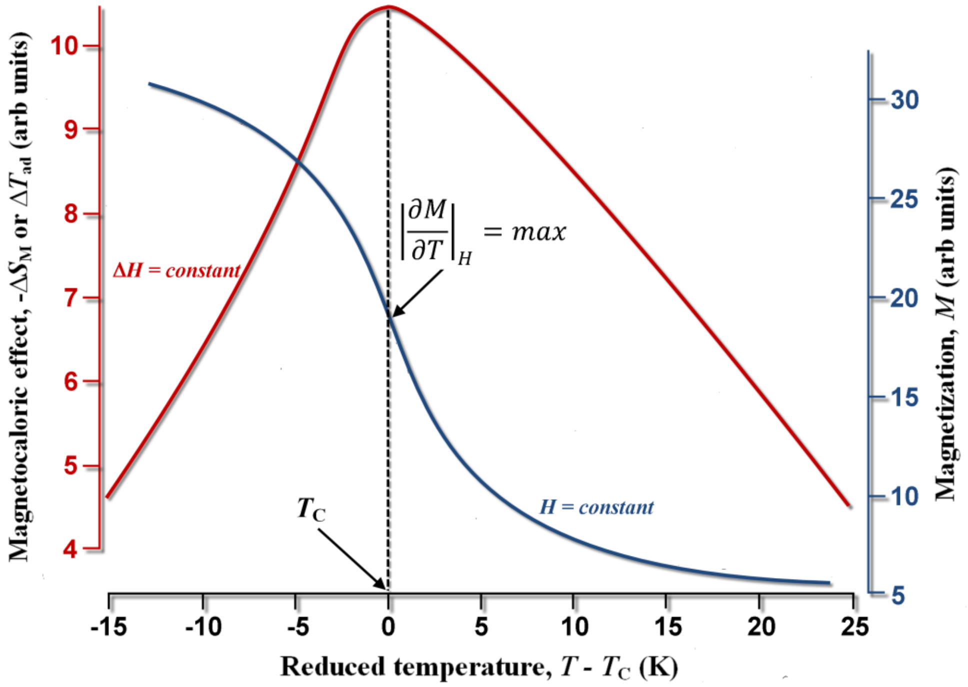

Figure 5: Temperature dependence of the magnetocaloric effect for a fixed magnetic field change ΔH (red curve) and temperature dependence of the magnetization for constant magnetic field H (blue curve). Both near its Curie temperature, T_C.

The equations above describing the MCE can be applied for materials with a second order magnetic transition (SOMT), a transition where the magnetization continuously changes with the change of temperature. If the material has a first order magnetic transformation (FOMT), where the material has a non-continuous change in magnetization due to simultaneous processes occurring, then one has to use the above equations carefully, because they can produce unreal MCE values. This problem will be discussed in the next chapter. The equations take into account the contributions corresponding to various processes occurring under magnetization, including contributions from paraprocesses and magneto-crystalline anisotropy. Other processes that can influence the MCE are: the contribution from magnetoelastic energy change, the contribution related to the destruction of the magnetic metastable states and the contribution from nonreversible processes. Different kinds of metastable processes, which could arise during a first-order phase transition, especially simultaneous magnetic and crystal structure transformation processes, have a huge effect on the MCE.

1.3 MCE during a first-order transition

The previous section assumed that the magnetic phase transition is a phase transition of the second-order type. For this transition it is known that the first derivatives of the thermodynamic potential are continuous functions and the second derivatives undergo a discontinuous change. The first derivative of the temperature of the thermodynamic potential is the entropy, which is a continuous function for this type of transition. Because of the continuity there are no jumps in entropy and there is no latent heat in the second-order phase transition. There are no differences between the initial and the new phase. Both phases have the same physical properties, which become different only far away from the transition. The second derivative, which in this case is heat capacity, should occur at the point of the second transition a finite discontinuous change.

If the first-order derivatives of the thermodynamic potential change discontinuously, then the material undergoes a first-order transition. The heat capacity in the point of the first-order transition should be infinite. Figure 6 shows a schematic S-T diagram of a magnetic system undergoing a first-order transition where the magnetic field has a small effect on the heat capacity above and below the first-order phase transition. The transition temperature is effected by the magnetic field, from $T_{pt}(H_1)$ to $T_{pt}(H_2)$. The enthalpy of the transition at $T_{pt}(H_1)$ and $T_{pt}(H_1)$ is ΔE_{H_1} and ΔE_{H_2}, respectively. This results in a total entropy change of the value $\Delta E(H)/T_{pt}(H)$. A theoretical analysis of the behaviour of the MCE in first-order phase-transition materials was first made by Pecharsky *et al.* [18] The total entropy of the system can be represented as:

$$S(T,H)=\int_0^{T_{pt}(H)}\frac{C_H^l(T,H)}{T}dT+\int_{T_{pt}(H)}^{T}\frac{C_H^h(T,H)}{T}dT+\frac{\Delta E(H)}{T_{pt}(H)}, \tag{19}$$

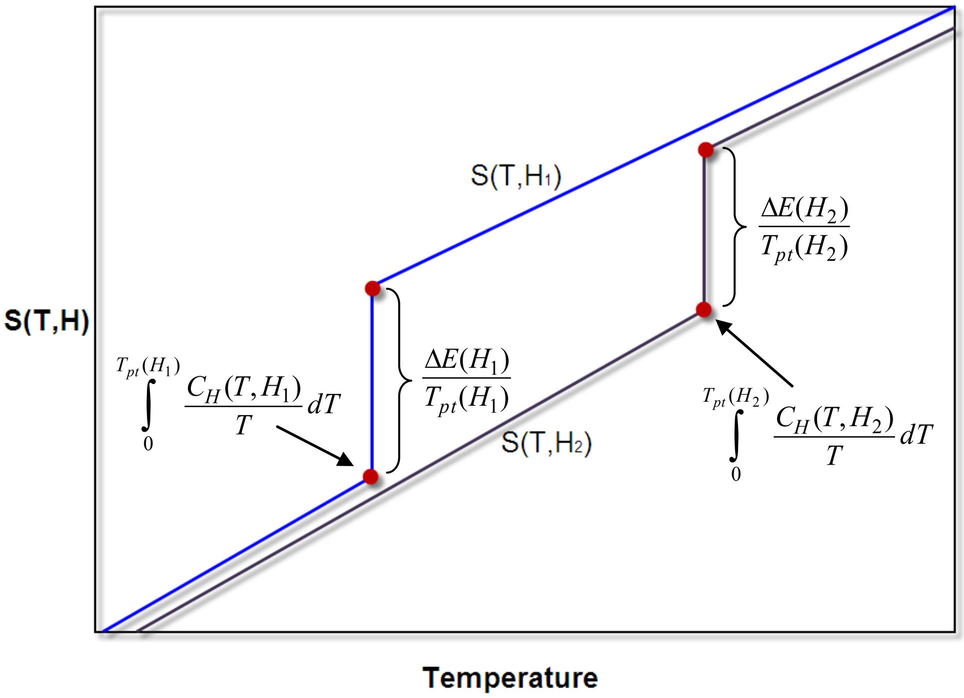

Figure 6: A schematic *T-S* diagram of a magnetic system in the vicinity of the first-order phase transition in two magnetic fields, H_1 and H_2. The corresponding values of the total entropies are marked on the plot.

$C^l_H(H,T)$ and $C^h_H(H,T)$ are the heat capacities of the phases stable above and below $T_{pt}(H)$, respectively. When the constant magnetic field heat capacity of both the low- and high-temperature phases is essentially the same, $C^l_H(H,T) \approx C^h_H(H,T)$, we can write the magnetic entropy change, for a defined field change, in different temperature ranges as follows:

$T<T_{pt}(H_1)$
$$\Delta S_M(T,\Delta H)=\Delta S(T,\Delta H)\cong\int_0^T\frac{(C_H(T,H_2)-C_H(T,H_1))}{T}dT \tag{20}$$

$T_{pt}(H_1)<T<T_{pt}(H_2)$
$$\Delta S_M(T,\Delta H)=\Delta S(T,\Delta H)\cong\int_0^T\frac{(C_H(T,H_2)-C_H(T,H_1))}{T}dT-\frac{\Delta E(H_1)}{T_{pt}(H_1)} \tag{21}$$

$T_{pt}(H_2)<T$
$$\Delta S_M(T,\Delta H)=\Delta S(T,\Delta H)\cong\int_0^T\frac{(C_H(T,H_2)-C_H(T,H_1))}{T}dT \\ -\left(\frac{\Delta E(H_1)}{T_{pt}(H_1)}-\frac{\Delta E(H_2)}{T_{pt}(H_2)}\right) \tag{22}$$

Because ΔE_{H_1} and ΔE_{H_2} are theoretically temperature-independent constants, the Equations (15) and (16) provide a good approximation also for the first-order phase transition. Because the magnetic field has little effect on the heat capacity below $T_{pt}(H_1)$ and above $T_{pt}(H_2)$, we can use the approximation $C_H(H_1,T) \approx C_H(H_2,T)$, at any temperature except $T_{pt}(H_1)$ and $T_{pt}(H_2)$. This simplifies Equation (21) to

$$\Delta S_M(T,\Delta H) \cong -\frac{\Delta E(H_1)}{T_{pt}(H_1)} \cong -\frac{\Delta E(H_2)}{T_{pt}(H_2)} \tag{23}$$

resulting in a large and constant magnetic entropy change, between $T_{\mathrm{pt}}(H_1)$ and $T_{\mathrm{pt}}(H_2)$. From previous equations it is clear that the high entropy for the first-order phase transition, between both temperatures, is defined by the value of enthalpy of the phase transformation.

As for the magnetic entropy change one can expect the highest magnetocaloric effect, the adiabatic temperature change, to occur in the same temperature range between $T_{\mathrm{pt}}(H_1)$ and $T_{\mathrm{pt}}(H_2)$. The difference is that ΔT_{ad} is critically dependent on the temperature. The temperature span between $T_{\mathrm{pt}}(H_1)$ and $T_{\mathrm{pt}}(H_2)$ can be separated into two regions, which are separated by the temperature T_{m}. This temperature is defined as the temperature where the total entropy at H_1 has the same value as the total entropy at H_2 at the beginning of the first-order transformation, which occurs at the temperature $T_{\mathrm{pt}}(H_2)$. This is visualized in Figure 7.

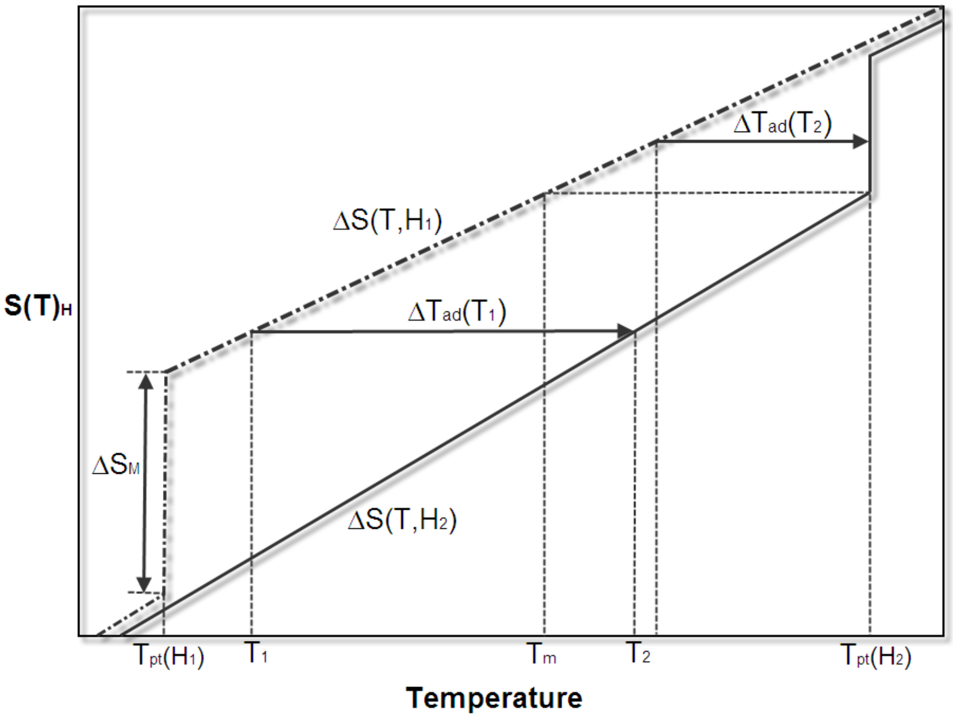

Figure 7: A shematic S-T diagram of a magnetic material in two magnetic fields H_1 and H_2 near the first-order transition. T_{m} is the temperature where the total entropy of the material in the magnetic field H_1 equals to the total entropy of the material in the magnetic field H_2 at the start of the first-order phase transition at $T_{\mathrm{pt}}\ (H_2)$.

In the first region where the temperature T_1 is between $T_{\mathrm{pt}}(H_1)$ and T_{m}, the material does not reach $T_{\mathrm{pt}}(H_2)$ when the magnetic field is changed from H_1 to H_2 regardless of how large is the ΔT_{ad}. In the second region when the initial temperature is situated between T_{m} and $T_{\mathrm{pt}}(H_2)$, the temperature increases up to $T_{\mathrm{pt}}(H_2)$ before reaching the magnetic field H_2 because of the MCE and cannot exceed this temperature, because of the infinite value of the heat capacity of the material during the first-order transition. Considering that the heat capacity is only effected by the magnetic field between $T_{\mathrm{pt}}(H_1)$ and $T_{\mathrm{pt}}(H_2)$, the ΔT_{ad} can be expressed with the Equations (18) and (23):

$$\Delta T_{ad}(T,\Delta H) = -\frac{T}{C_H(H,T)}\Delta S_M(T,\Delta H) \cong -\frac{T}{C_H(H,T)}\frac{\Delta E(H_1)}{T_{pt}(H_1)} \tag{24}$$

The MCE temperature dependence is only determined by the behavior of $T/C_H(H,T)$, because $\Delta E(H_1)/T_{pt}(H_1)$ is constant. When the temperature exceeds T_{m} , i.e., when $T_m < T \leq T_{\mathrm{pt}}(H_2)$, the value of $\Delta T_{\mathrm{ad}}(T,\Delta H)$ becomes dependent only on the difference between T and $T_{\mathrm{pt}}(H_2)$ (arrow $\Delta T_{\mathrm{ad}}(T_2)$ in Figure 7) and can be written:

$$\Delta T(T,\Delta H)=T_{pt}(H_2)-T\,, \tag{25}$$

This means that the MCE begins to decrease above T_m, because as the magnetic system approaches the phase-transition temperature practically no further temperature change occurs in response to the changing magnetic field as long as the two different phases coexist. If the magnetic field change or its effect on the magnetic phase transition is small, then T_m becomes $T_{pt}(H_1)$ and Equation (25) becomes:

$$\Delta T(T,\Delta H)\cong T_{pt}(H_2)-T_{pt}(H_1)\,. \tag{26}$$

The MCE is then the difference between the temperatures of the first-order transformation in the fields H_1 and H_2. This provides an easy estimate of the maximum adiabatic temperature change without thermodynamic or magnetic measurements as long as both $T_{pt}(H_1)$ and $T_{pt}(H_2)$ are known. Also, if the magnetic field strongly influences the magnetic ordering temperature, a larger giant adiabatic temperature change in small magnetic fields is expected.

To evaluate the first-order magnetic phase transition we use the Clausius-Clapeyron equation:

$$\frac{dH}{dT}=-\frac{\Delta S_M}{\Delta M} \tag{27}$$

where ΔS_M and ΔM are the differences in the magnetic part of the entropy and the magnetic moment between the magnetic states at the temperature of the transition. With this equation it is possible to calculate the entropy change at the transition from the magnetization data. From Equations (18) and (27) we can obtain the equation for the MCE during the first-order transition:

$$\Delta T=\frac{T}{C_H}\left(\frac{\partial H}{\partial T}\right)\Delta M \tag{28}$$

Because of the jumps and the high speed of the jumps in the magnetization, for the first-order magnetic transition, ΔS_M and ΔM are much higher than in second-order magnetic transitions for the same value of magnetization. First–order magnetic transitions are usually order-order transitions. They are usually accompanied by the structural transition, which also enforces the magnetization change, making it sharper.

1.4 MCE in the vicinity of magnetic phase transitions

To explain the magnetic field and temperature dependence of ΔT in the vicinity of the magnetic phase transition Tishin *et al.* [19] proposed a thermodynamic model.

Consider a reversible closed thermodynamic cycle *WXYZ* in the (S, T) coordinates as shown in Figure 8. Starting from point W and adiabatically magnetize with a field change of $\Delta H = H_2 - H_1$, it follows the path *WX*. The temperature is changed by $\Delta T = T_X - T_W$ because of the magnetocaloric effect. When it reaches X, it is connected to a hot sink, which has a lower T than T_X. Because of the energy that has been given to the hot sink it follows path *XY*, where the total entropy is reduced from S_X to S_Y and its temperature from T_X to T_Y, Then the material is disconnected from the hot sink and adiabatically demagnetized which leads to a decreases in its temperature from T_Y to T_Z because of the inverse magnetocaloric effect (path $Y \rightarrow Z$). To close the cycle the material is connected to a cold sink ($T_{cold} > T_Z$) from which it absorbs a finite amount of energy, thus increasing its entropy from $S_W - S_Z$ and its temperature from T_Z to T_W. For infinitesimal *XY* and *ZW* paths we can write:

$$\begin{aligned} dS_{WX} &= 0, \\ dS_{XY} &= -C(H_2,T_X)dT_X/T_X, \\ dS_{YZ} &= 0, \\ dS_{ZW} &= -C(H_1,T_Z)dT_Z/T_Z, \end{aligned} \tag{29}$$

where $C(H_2,T_X)$ and $C(H_1,T_Z)$, and T_X and T_Z are the heat capacities and the temperatures of a material at X and Z, respectively. Because of the closed thermodynamic cycle, we can write

$$\Delta S = dS_{WX}+dS_{XY}+dS_{YZ}+dS_{ZW}=0. \tag{30}$$

Combining Equation (29) and (30) yields:

$$\frac{C(H_2,T_X)}{T_X}dT_X=\frac{C(H_1,T_Z)}{T_Z}dT_Z. \tag{31}$$

Considering that:

$$\Delta T(\Delta H,T_W)=T_X-T_W\cong T_Y-T_Z\cong T_X-T_Z, \tag{32}$$

and introducing $T_2 = T_X \cong T_Y$, $T_1 = T_W \cong T_Z$ and $T_2 = T_1 + \Delta T(\Delta H, T_1)$ Equation (31) can be written as:

$$\Delta T(\Delta H,T_1)=-T_1\left[\Delta C(H,T)-\frac{\partial \Delta T(\Delta H,T_1)}{\partial T}\frac{C(H_2,T_2)}{C(H_1,T_1)}\right] \tag{33}$$

where

$$\Delta C(T,H)=\frac{C(H_1,T_1)-C(H_2,T_2)}{C(H_1,T_1)}. \tag{34}$$

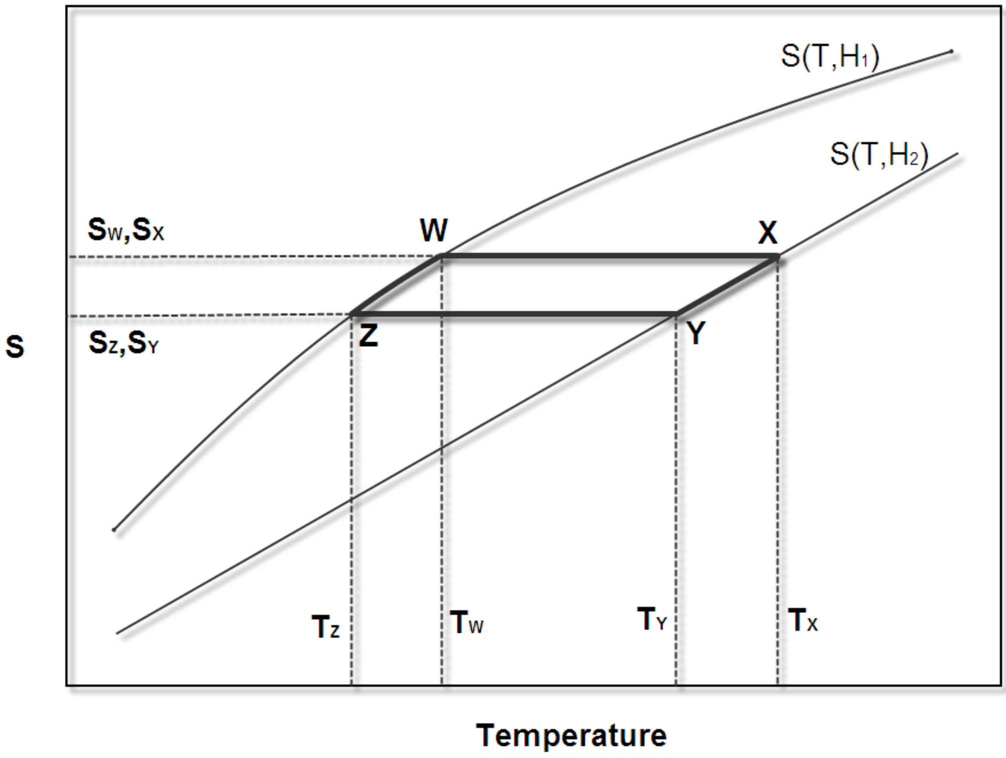

Figure 8: *S-T* diagram with an ideal reversible thermodynamic cycle *WXYZ*, represented as thick lines, with corresponding entropy and temperature denotations.

At the position where MCE has a maximum (or minimum) the condition $\partial\Delta T/\partial T=0$ is fulfilled and Equation (33) is reduced to

$$\Delta T(\Delta H,T_1)_{peak}=-T_1\Delta C(T,H) \tag{35}$$

for the peak MCE. It can be seen that ΔC defines the sign before the MCE value. Tishin experimental showed that $\Delta C(H,T)<0$ for ferromagnets in various magnetic fields at temperatures below and just above the zero magnetic field heat-capacity peak. It changes the sign and becomes negative at higher temperatures. This was observed in numerous experiments. Figure 9 shows the results for GdPd. It could be concluded that the maximum magnetocaloric effect should occur above the zero magnetic field heat-capacity peak.

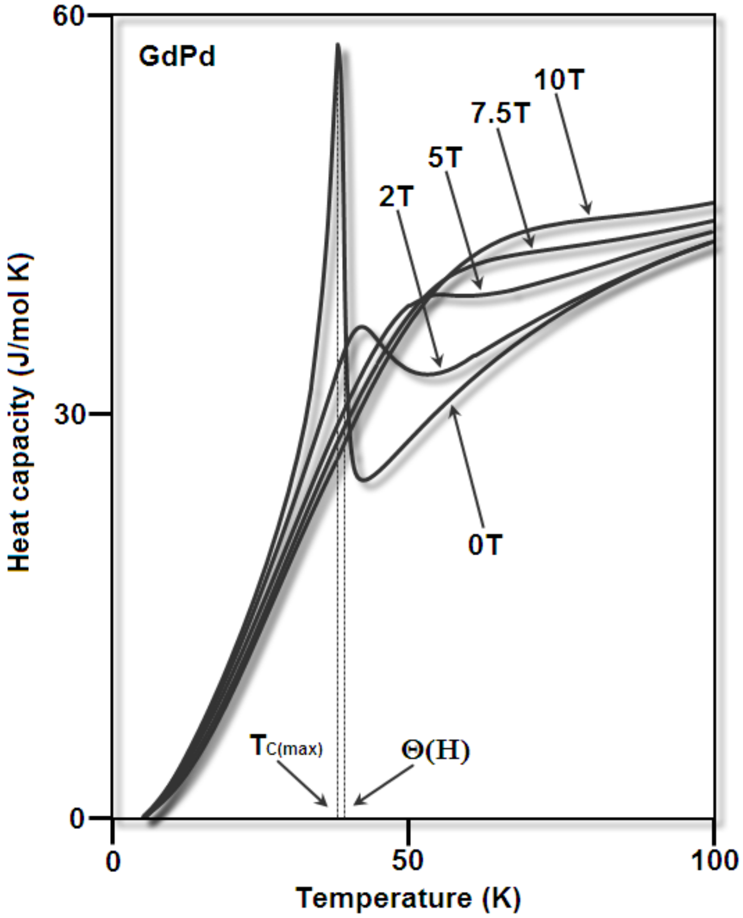

Figure 9: Heat capacity measurements for polycrystalline GdPd at different magnetic fields. $T_{C\,(max)}$ corresponds to the heat-capacity maximum in zero magnetic field. Θ(H) is the temperature where $C(H_1,T)$ and $C(H_2,T)$ are equal. [19]

For small magnetic fields and/or for relatively high temperatures (room temperatures), $\Delta T(H,T_1)_{peak}/T_1$ is small and can be neglected. This simplifies Equation (35) at temperature $T_M(H)$, where the peak MCE occurs, to:

$$C(H_1,T_M) \cong C(H_2,T_2). \tag{36}$$

We can see that the heat capacity is independent of the magnetic field at the MCE peak temperature. The temperature where $C(H_1,T)$ and $C(H_2,T)$ are equal is noted as Θ(H) and should be close to the MCE peak.

The previous statement of neglecting $\Delta T(H,T_1)_{peak}/T_1$ is not true for a magnetic material near its ordering temperature and Equation (35) has to be written:

$$C(H_1,T_M)\frac{T_2}{T_M} = C(H_2,T_2). \tag{37}$$

For a ferromagnet T_2 is always larger then T_M (positive MCE) making T_2/T_M larger than 1. From this it can be seen that the MCE maximum is higher than Θ(H), but because the zero magnetic-field heat capacity in ferromagnets changes sharply right after its peak (Figure 9), we can neglect the difference between them.

One can conclude that the maximum MCE is higher than the zero magnetic-field heat-capacity peak. The maximum MCE with decreasing field approaches the temperature Θ(H) where the heat capacity becomes independent of the magnetic field. Also, both temperatures approach the Curie temperature when $H \to 0$. This was also experimentally proven in [19], where T_M for GdPd decreases from 38.7 K for a field change of 10 T to 38.1 K for a field change of 2 T (Figure 10), which gets close to the T_C of the material of 38.0 K. At the same time Θ(H) decreases from 38.5 K to 38.0 K for the same field changes (Figure 9). Also the MCE is lowered below and above the $\Theta(H)$ temperature which can be concluded from Equation (33), and a typical caret-like shape is expected which is observed in all material with a single ferromagnetic ordering, as can be seen in Figure 10. It can be seen from Figure 9 that the maximum MCE is indeed at higher temperatures then the heat-capacity peak.

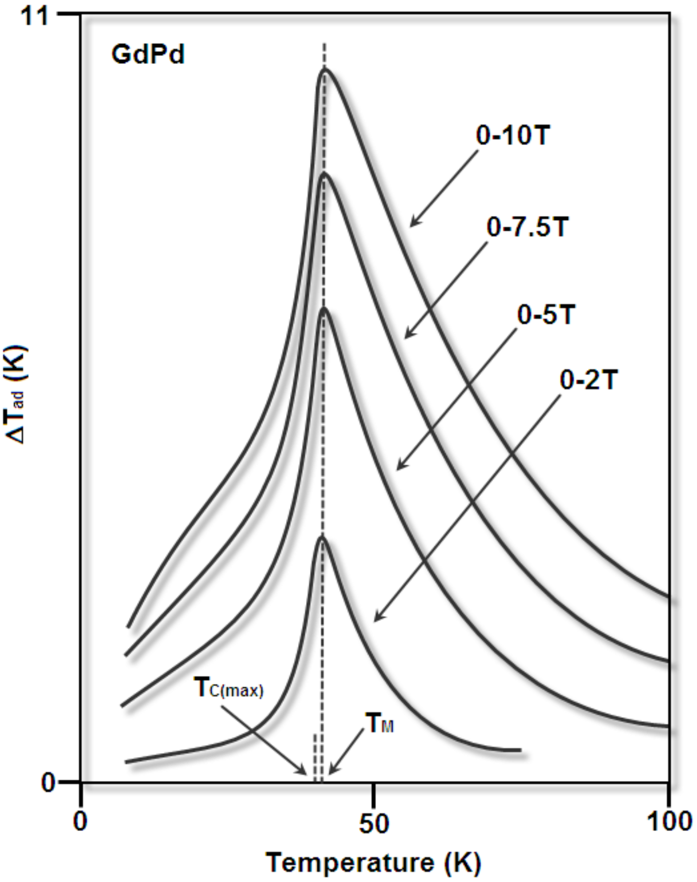

Figure 10: The magnetocaloric effect of a polycrystalline GdPd from 3.5 to 100 K for a magnetic-field change from 0 to 2, from 0 to 5, from 0 to 7.5 and from 0 to 10 Tesla. [19]

1.5 Magnetocaloric materials

1.5.1 MCE materials for cryogenic temperatures

Magnetocaloric materials are commonly used for adiabatic demagnetization to achieve cryogenic temperatures. This was first demonstrated by Giauque and MacDougall in 1927, where they achieved temperatures under 1 K using the paramagnetic salt $Gd_2(SO_4)_3 \cdot 8H_2O$ [5]. Later, the MCE at low temperatures was studied in other PM salts, such as ferric ammonium alum [20], chromic potassium alum [21] and cerous magnesium nitrate [22]. However, paramagnetic salts were not practical as cooling materials, because of their low thermal conductivity. Paramagnetic intermetallic compounds are more suitable and $PrNi_5$ is one of the most studied examples reaching as low as 27 μK [23]. PM garnets also have excellent thermal conductivity, low lattice heat capacity and low ordering temperature. Good examples are ytterbium iron ($Y_3Fe_5O_{12}$), gadolinium iron ($Gd_3Fe_5O_{12}$) and gadolinium gallium ($Gd_3Ga_5O_{12}$) garnets in the 10–30 K range. [24, 25]. Large ΔS_M has been observed in magnetic nanocomposites on the iron gadolinium gallium garnets, $Gd_3Ga_{5-x}Fe_xO_{12}$, for $x \leq 2.5$ [26]. Numazawa and Sato observed a twice as large entropy change when substituting Dy with Gd in $(Dy_xGd_{1-x})_3Ga_5O_{12}$ garnet single crystals with $x = 0.25$. [27]

Other intermetallic compounds for low temperature MCE are $REAl_2$, where RE = Er, Ho, Dy, $Dy_{0.5}Ho_{0.5}$ [28] and Dy_xEr_{1-x} ($0 \leq x \leq 1$) [29, 30], GdPd [31] and $RENi_2$, where RE = Gd [32], Dy and Ho [33]. The MCE gets lower with higher temperatures, because of the rise of the lattice heat capacity. The MCE values lie in the range of 1–2 K/T.

1.5.2 MCE materials for room temperatures

1.5.2.1 Gd

Gadolinium is the oldest known MC for room-temperature applications and often serves as a standard to compare the magnetocaloric effect in new materials. With a Curie temperature T_C of 294 K and a ΔS_M of −5 Jkg/K and ΔT_{ad} of 5.7 K (both for a 2 kOe field change) [34], Gd is a good MC material and is still the best MC for magnetic refrigeration. These results, however, are only possible with Gd of high purity. Commercial Gd generally has about two times lower MCE than high-purity samples [12]. The high price of Gd is its major drawback. For example, the price for 300 g of Gd lumps with 99.9 % purity (approximately the mass needed for a magnetic refrigerator) is around 1000 € [35]. New materials being researched have better MCE then Gd, but they still have major drawbacks in the preparation, toxicity, magnetic and temperature hysteresis and other critical issues. Until they are resolved Gd is still the best MC material on the market.

1.5.2.2 $Gd_5(Si_xGe_{1-x})_4$ alloys and related R_5T_4 materials

$Gd_5(Si_xGe_{1-x})_4$ alloys are some of the more extensively researched MC materials. After the discovery of the useful properties of $Gd_5Si_2Ge_2$ [8], the whole range of stoichiometries was investigated for their structural and magnetic properties [36 − 43]. These materials are interesting not only by their MCE, but also because of the unusual features observed in these compounds, such as colossal magnetostriction and giant magnetoresistance [44]. When the temperature, pressure or the applied magnetic field is changed, these alloys undergo a simultaneous change of crystallographic symmetry and magnetic order, the so-called FOMT. This type of transformation, termed magnetic-martensitic, is extremely rare. For alloys with $0.24 \leq x \leq 0.5$, a transformation from the paramagnetic monoclinic $Gd_5(Si_2Ge_2)$-type structure to the ferromagnetic orthorhombic Gd_5Si_4-type structure occurs. For alloys with $0 \leq x \leq 0.2$, a transformation from antiferromagnetic Sm_5Ge_4-type structure to ferromagnetic orthorhombic Gd_5Si_4-type structure occurs, but only at low temperatures.

These two groups of alloys exhibit a GMCE. The first group, alloys with $0.24 \leq x \leq 0.5$, is more interesting due to its higher transition temperatures. The transition temperature ranges from 140 K for $x = 0.24$ to 276 K for $x = 0.5$ [10]. The maximum magnetic entropy change was found in $x = 0.25$ with a value of -68.5 J/kgK for $\Delta H = 50$ kOe at 143 K [39] and the maximum ΔT_{ad} was found in $x = 0.43$ with a value of 19 K for $\Delta H = 50$ kOe at 235 K [45]. The alloys $Gd_5(Si_{1-x}Ge_x)_4$ with $x \geq 0.5$ exhibits a SOMT. Because of that the maximum magnetic entropy change is substantially lower than in the FOMT, because there is no structural transformation, but also no hysteresis losses which reduces the overall cooling capacity.

Composite materials were produced with a spark plasma sintering technique. $Gd_x(Gd_5Si_2Ge_2)_{1-x}$ with $x = 0.3$, 0.5, and 0.7 produced a changed in the ΔT_{ad} peak. Increasing x from 0.3 to 0.7 shifted the ΔT_{ad} peak temperature from 286 to 293 K and the peak value of ΔT_{ad} slowly increased from 1.6 to 2.0 K at a magnetic field change of 1.5 T. [46]

Partially substituting Gd by other rare-earths always lowers the T_C compared to the starting alloy, while the change in ΔS_M can vary. Spichkin *et al.* [47] showed that in $(Gd_{1-y}R_y)_5Si_4$, both Pr and Tb lowers the Curie temperature. The T_C of Gd_5Si_4 was lowered from 346 K to 292 K for Pr and $y = 1.0$, and to 280 K for Tb and $y = 2.5$. Pr also lowers the MCE (ΔS_M by ~25% for a field change of 50 kOe), while Tb may enhance ΔS_M slightly. The as-cast $(Gd_{0.74}Tb_{0.26})_5(Si_{0.43}Ge_{0.57})_4$ still displayed a large magnetic entropy change up to -18.89 Jkg/K [48].

Exposing the material to high pressure (9.2 kbar) increased the Curie temperature of $Gd_5Ge_2Si_2$ up to 305 K, but did not affect the saturation magnetization and markedly decreased its magnetocaloric effect. [49]

Other R_5T_4 systems were also studied. The second most studied after $Gd_5(Si_xGe_{1-x})_4$ is the $Tb_5(Si_xGe_{1-x})_4$ system. It shows the same crystallographic sequence of phases at room temperature as $Gd_5(Si_xGe_{1-x})_4$ with a first-order character for $Tb_5Si_2Ge_2$. This alloy also has the highest ΔS_M of -15 J/kgK for ΔH=50 kOe, but with a T_C at only 100 K [50]. Morellon *et al.* [51] studied the effects of pressure on $Tb_5Ge_2Si_2$. With a pressure of 8.6 kbar, the high-temperature second-order ferromagnetic transition was found to be coupled with the low-temperature first-order structural phase change into a single first-order magnetic-crystallographic transformation, transforming the material from an ordinary material into a GMCE material. The same crystallographic sequence of phases at room temperature is also observed in the $Dy_5(Si_xGe_{1-x})_4$ alloy system, with the monoclinic phases occurring for $x = 0.67$–0.78. $Dy_5Si_3Ge_1$ showed the highest ΔS_M of -33 J/kgK for ΔH=50 kOe at 75 K. This value is still 22 % lower than the related Gd alloy with the same ordering temperature ($Gd_5Si_{0,33}Ge_{3,67}$). [52, 53] Other elements did reduce the ΔS_m significantly. For $Nd_5(Si_{1-x}Ge_x)_4$ alloys T_C and ΔS_m(max) are substantially lower than for the Gd-based alloys [54].

These results depend strongly on the proper heat treatment and the purity of the starting elements [55]. Available rare-earth metals have a significant content of interstitial impurities, primarily H, C, N and O. This content varies between 2 and 5 atomic %. XRD studies of the effect of using low purity Gd showed that these alloys consist of multiple phases, including $Gd_5Si_2Ge_2$-type, Gd_5Si_3-type, and GdGe-type, making it difficult to prepare a single-phase material [56]. Oxygen has a large influence on $Gd_5(Si_xGe_{1-x})_4$. Oxygen favors the decomposition of the monoclinic phase into the $GdSi_yGe_{1-y}$ (1:1) and the $Gd_5Si_zGe_{3-z}$ (5:3) phases, in the process destroying the GMCE by suppressing the structural transition [57].

One of the major problems of these alloys are their large hysteresis losses. However, by adding different elements one can reduce these losses almost to zero at the cost of ΔS_M(max).

1.5.2.3 Mn-based compounds

Numerous different metallic manganese compounds have interesting MCE behaviors with quite large MCE values, even the term colossal magnetocaloric effect (CMCE) has been introduced for some alloys having values far greater than predicted by the theoretic magnetic limit.

1.5.2.3.1 $Mn(As_{1-x}Sb_x)$ alloys

The base material MnAs undergoes a coupled structural/magnetic FOMT at 318 K. The ferromagnetic hexagonal NiAs-type structure transforms to the paramagnetic orthorhombic MnP-type structure upon heating or demagnetizing. The MCE values are large enough to consider these compounds in the GMCE class of magnetic refrigerants: ΔS_M = -30 J/kgK and ΔT_{ad} = 13 K for a 0 to 50 kOe field change at T_C [58]. The downside is that it has very large thermal hysteresis at the transition. This can be overcome by substituting arsenic with antimony. [59, 60] This results in a reduction of ΔS_M and ΔT_{ad}, because Sb stabilizes the NiAs-type structure when $x \geq 0.1$, and the FOMT changes to a SOMT. Adding Sb also lowers the T_C. The $MnAs_{1-x}Sb_x$ system behaves differently from most families of magnetic refrigerant materials in that ΔS_M decreases with decreasing T_C. The high vapor pressure of As, whose boiling point is 876 K, makes it difficult to economically prepare large quantities (tons) of MnAs. Also, As is a governmentally regulated poison, which means special handling facilities would be required for preparing $MnAs_{1-x}Sb_x$ materials, and special environmental regulations would have to be met to place such cooling devices into domestic applications.

An interesting effect was found by Gama *et al.* [61]. Hydrostatic pressure, up to 2.23 kbar, enhanced the isothermal entropy changes in MnAs, reaching values up to -267 Jkg/K. These values are far greater than predicted by the magnetic limit, which is calculated by assuming magnetic field independence of the lattice and electronic entropy contributions. They called it the colossal magnetocaloric effect (CMCE). Others claimed also to have found the CMCE in similar compositions [62, 63, 64], which turned out to be an error in calculating the ΔS_M using the Maxwell relation from the magnetization data. The Maxwell relation showed to be incorrect for calculating the ΔS_M near the first-order transition. Using the Clausius-Clapeyron equation avoided the overestimated values and gave more realistic results for the MnAs system. [65, 66, 67].

1.5.2.3.2 $MnFe(P_{1-x}As_x)$ alloys

$MnFeP_{0.45}As_{0.55}$ [68] showed interesting MCE properties, namely ΔS_M = -18 J/kgK for a 0 to 50 kOe field change, and an ordering temperature of 307 K. Substituting 10 at.% of Fe for Mn ($Mn_{1+y}Fe_{1-y}(P_{0.5}As_{0.5})$) does not change T_C, but increases ΔS_M by ~40% for a field change of 0 to 50 kOe [69]. On the other hand, the substitution of Ge for As, i.e. $MnFe(P_{0.5}As_{0.5-x}Ge_x)$, has just the opposite effects - a large increase of T_C from 282 K for $x = 0$ to 570 K for $x = 0.5$, and a reduction of the MCE [70]. But further studies of the $MnFe(P_{1-x}Ge_x)$ ($0.1 \leq x \leq 0.5$) showed comparable results with the As system. This eliminated the problem of As toxicity [71]. Further studies showed that the lattice parameters *a* and *c*, and their ratio *c*/*a* have a great effect on the T_C. Compounds with larger a parameter and smaller *c*/*a* ratio have higher T_C [72, 73].

Pressure experiments were done by Yabuta *et al.* [74] and Brueck *et al.* [75]. Applying pressure slightly increased the T_C for MnFe(P,As), but reduced it for the MnFe(P,Ge) system. Pressure also increased the temperature and the magnetic hysteresis.

The preparation of the P-containing alloys is similar to that for $MnAs_{1-x}Sb_x$ alloys and the problems are the same. P presents some special handling problems.

1.5.2.3.3 Ni–Mn–X (X = Ga, In, Sn, Sb) Heusler alloys

These compounds have a high Curie temperature, over 350 K, with a usually negative ΔS_M (SOMT). At lower temperatures they undergo a first-order magnetic phase transition corresponding to a reversible structural transition from the high-temperature cubic austenite phase to the low-temperature tetragonal martensite phase. The transition causes a distortion of the crystal lattice structure, leading to hardening of the magnetic saturation process. Consequently, the magnetization of the martensitic phase is lower than that of the austenitic one, which leads to an inverse MCE and a positive ΔS_M. Such a magnetization change is very sharp, which provides high ΔS_M values.

In 2001 Hu *et al.* [76] reported MCE in Ni-Mn-Ga Heusler alloys (ratio 2:1:1). Their results suggested that a negative MCE is associated with a first-order martensitic transition. The MCE is quite large at low magnetic fields and decreases as the magnetic change becomes larger. Zhou *et al.* [77] reported a large ΔS_M for an alloy of the composition $Ni_{55.2}Mn_{18.6}Ga_{26.2}$. They obtained a value of -20.4 J/kgK for $\Delta H = 50$ kOe at $T_C = 317$ K. Yu *et al.* substituted Ni with Co in this type of alloy, resulting in a higher T_C and a lower ΔS_M [78]. Stadler *et al.* researched the substituted Heusler alloy $Ni_2Mn_{1-x}Cu_xGa$, which shows a very high maximum magnetic entropy change of $\Delta S_M = -64$ Jkg/K at 308 K for a magnetic field change $\Delta H = 5$ T [79].

A large inverse MCE was found in $Ni_{0.50}Mn_{0.50-x}Sn_x$ ($0.13 \leq x \leq 0.15$) alloys in 2005 [80]. Krenke *et al.* reported a large positive ΔS_M of 19 J/kgK near 300 K for a magnetic field change of 5 T in $Ni_{50}Mn_{37}Sn_{13}$. Han *et al.* investigated magnetic entropy changes in $Ni_{50-x}Mn_{39+x}Sn_{11}$ alloys (x = 5, 6, and 7). Under an applied magnetic field of 10 kOe, they found high magnetic entropy changes of 6.8, 10.1, and 10.4 J kg/K for x = 5, 6, and 7, respectively [81].

Oikawa *et al.* was the first to report on the magnetic and martensitic transition behaviours of $Ni_2Mn_{1+x}In_{1-x}$ Heusler alloys [82]. Sharma *et al* found in $Ni_{50}Mn_{34}In_{16}$ a ΔS_M value of 19 J/kgK around 240 K for the martensitic transition, while near room temperature, this alloy showed a conventional MCE. The ΔS_M at 300 K was −7.5 J/kgK. Sharma et al. noted that the Curie temperature of the ferromagnetic martensite phase of NiMnIn lies in the same temperature region as the martensitic transition, thus increasing the overall MCE and explaining the high ΔS_M [83].The transition temperature can be easily tuned by changing the composition [82] or substituting Co for Ni [84]. Moya et al. directly measured the adiabatic temperature change in the $Ni_{50}Mn_{34}In_{16}$ alloy and showed the possibility of both cooling and heating in a giant inverse magnetocaloric compound. It has been shown that the irreversibility of the first-order structural transition gives rise to measured temperature changes which are lower than those calculated using equilibrium thermodynamics [85].

Krenke et al. introduced small amounts of Fe and Co in place of Ni. Adding 3 at. % of Fe increased the ΔS_M while increasing the thermal hysteresis. Co had the opposite effect [86]. Xuan et al. studied the effect of annealing $Ni_{44.1}Mn_{44.2}Sn_{11.7}$ ribbons. By changing the annealing temperature of the ribbons, they could control the transition temperature and the ΔS_M [87]. T. Yasuda et al. showed that applying pressure increased the martensitic transition temperature linearly, while the T_C did not change with increasing pressure [88].

Amongst the ferromagnetic Heusler alloys showing a martensitic transition, those systems in which the T_C of the martensite phase lies in the same temperature region or below that of the martensitic transition temperature are likely to show a large inverse magnetocaloric effect.

1.5.2.4 La($Fe_{13-x}M_x$)-based compounds

The $LaFe_{13}$ phase does not exist; in fact, no intermetallic compounds form in the La-Fe binary system, and La and Fe form immiscible liquids at the Fe-rich side between 8 and 20 at% La above 1460 °C [89]. Consequently, other elements must be added to La–Fe alloys in order to form the intermetallic La($Fe_{13-x}M_x$) phases. It has been shown that with the addition of at least 10 % Si or Al the cubic $NaZn_{13}$ structure can be stabilized. [90]

In 2001, Hu *et al.* [91] were the first to find the GMCE in La($Fe_{13-x}Si_x$) alloys. They reported that La($Fe_{11.4}Si_{1.6}$), which orders at 208 K, had a ΔS_M value of −19.4 J/kgK for a magnetic field change of 0 to

50 kOe. They also found that when x was increased (i.e., more of the Fe was replaced by Si), the magnetic ordering temperature increased and the MCE was substantially reduced. The Curie temperature increased monotonically from 180 K at $x = 1.3$ to 250 K at $x = 2.6$ and ΔS_M dropped rather rapidly with increasing x, from −30 J/kgK at $x = 1.3$ [92] to −13 J/kgK at $x = 1.8$ [93]. For $x > 1.8$, ΔS_M was small and appeared to level off at −3.7 J/kgK [94] (all at $\Delta H = 5$ kOe).

It should be pointed out that all the $La(Fe_{13-x}Si_x)$ samples prepared to date are two-phase alloys containing up to 5% α-Fe. This is not surprising, considering that La and Fe form immiscible liquids. Even long-term anneals, up to 30 days, do not eliminate the second phase α-Fe. This can be overcome by melt spinning the alloy. Gutfleisch *et al.* [95] reduced the annealing time to 2 hours by melt spinning the material, presumably because the elements could be more homogeneously distributed this way. A very large magnetic entropy change of $\Delta S_M = -31$ J /kg K was obtained at 201 K under 5 T in $LaFe_{11.8}Si_{1.2}$ melt-spun ribbons, which is much higher than for the bulk sample [96]. Also, thermal- and/or field-hysteresis is can be practically overcome by melt spinning.

Pressure has a positive effect on the ΔS_M especially at low magnetic fields, but the T_C of the sample rapidly decreases. [97] Substituting Fe with Co led to an increase in the T_C up to 274 K for the composition $LaFe_{11.2}Co_{0.7}Si_{1.1}$, which still showed a large ΔS_M [98]. Melt spinning the sample increased the T_C even further [99].

Many researchers have investigated substituting La with other elements. Partially substituting La for Pr in $La(Fe_{0.88}Si_{0.12})_{13}$ enhances the MCE [100] and reduces the hysteresis losses [101]. The same group investigated Nd substitutions. In $La_{1-z}Nd_z(Fe_{0.88}Si_{0.12})_{13}$ with z = 0.2, for a magnetic field change from 0 to 5 T, the isothermal magnetic entropy change and the relative cooling power increased to −27 $Jkg^{-1}K^{-1}$ and 518 J/kg, respectively [102].

The addition of interstitial hydrogen has a large effect on the magnetic properties of these alloys. In contrast to other interstitial atoms, interstitial hydrogen not only increases the critical temperature but also leads to an increase in magnetic moment [103 − 108]. The lattice expansion due to the addition of three hydrogen atoms per formula unit is about 4.5 %. The critical temperature can be increased up to 450 K and the field-induced phase transition remains first order for all hydrogen concentrations. Heat capacity measurements also confirmed large adiabatic temperature changes.

The material cost for this alloy makes it a very attractive candidate for magnetic refrigeration, but the difficulties of preparing the alloy are still a major problem.

Table 1: Advantages and disadvantages of various near room temperature magnetic refrigerant materials. Gd is taken as a reference material. [15]

Property	Gd	Gd_5T_4	$RMnO_3$	LaFeSi	MnAs	FeMnPAs	Ni_2MnGa
Raw material costs	0	–	++	++	++	++	+
Preparation	0	–	– –	–	– –	– –	– –
Vapor pressure	0	0	0	0	– –	– – –	0
>1 kg production	0	0	?	0	?	?	?
MCE, ΔS_M	0	++	–	+	+	+	+
MCE, ΔT_{ad}	0	+	–	–	–	0	–
Refrigeration capacity	0	+	?	+	?	+	?
Hysteresis	0	– –	0	–	–	–	– –
Environmental concerns	0	0	0	0	– –	–	0
Corrosion	0	++	?	–	?	?	0

We can see from Table 1 that there is no universal material that would fulfill all criteria's for the perfect magnetocaloric material. With the Gd_5T_4 and the Heusler alloys having high hysteresis losses, the MnAs and FeMnPAs alloys having problems with the high vapor pressure and the environmental concerns and all have preparation problems. Many questions are yet to be answered that are here presented with a question mark. The overall picture suggests that the best material is still the pure Gd metal, but research is in progress and properties will improve and new materials will fill this table.

1.6 Measuring the MCE

Both $\Delta S_M(T)_{\Delta H}$ and $\Delta T_{ad}(T)_{\Delta H}$ depend on temperature and ΔH and are usually studied and reported as functions of temperature for a given ΔH, or as functions of ΔH for a given temperature. The behavior of both characteristics of the magnetocaloric effect, i.e. $\Delta S_M(T)_{\Delta H}$ and $\Delta T_{ad}(T)_{\Delta H}$, is material dependent, cannot be easily predicted from first principles, and therefore, must be experimentally measured. Only $\Delta T_{ad}(T)_{\Delta H}$ can be measured directly (direct techniques) or calculated (indirect techniques) from the measured magnetization or heat capacity, both as a function of temperature and magnetic field, while $\Delta S_M(T)_{\Delta H}$ can be calculated from the measured magnetization data. The direct and indirect techniques have certain advantages and disadvantages.

Special care should be taken in both techniques when a FOMT occurs. The kinetics of the first-order transformation may be slow and the rapid magnetic field change required to fulfill adiabatic conditions may not be slow enough to allow the transformation to go to completion.

1.6.1 Direct methods

The direct techniques provide only one measure of the magnetocaloric effect, the adiabatic temperature change. They involve the measurement of the initial temperature (T_0) and final temperature (T_F), when the external magnetic field is changed from an initial (H_0) to a final value (H_0). ΔT_{ad} is then determined as the difference

$$\Delta T_{ad}(T_0, H_F - H_0) = T_F - T_0. \qquad (38)$$

Measurements can be performed ether in contact or non-contact mode, depending on whether the temperature sensor is physically in contact with the sample or not. During the direct measurement a rapid change of magnetization is required. This can be achieved either by changing the magnetic field on a static sample [109] or by moving the sample in and out of a static magnetic field [110]. The field application to or removal from the sample is usually achieved using pulsed or ramped magnetic fields changing with a rate of about 10 kOe/s. Pulsed magnetic fields up to 100 T can be used for measuring the MCE, electromagnets achieve only fields up to 2 T. Permanent or superconducting magnets are used when the sample is moved in and out of the magnetic field, which limits the magnetic field range to 0.1 to 2.0 T, and 0 to 10 T, respectively.

Direct measurements have an accuracy of about 5-10%, depending on the errors in thermometry, errors in field setting, the quality of thermal isolation of the sample (this becomes a critical source of error when the MCE is large and thus disrupts the adiabatic conditions), and the quality of the compensation circuitry to eliminate the effect of the changing magnetic field on the temperature sensor.

Most of the direct measurements were carried out on self-made devices, making the comparability of these results not a straight forward task. That is why data of the most important magnetocaloric material exist from the equipment of the Moscow State University [111 − 116]. They use a liquid nitrogen cooled pulse magnet in combination with a He flow cryostat. The variation of sample temperature during the sweeping of the field is monitored with a thermocouple. Sweeping to the maximum field takes approximately 3 s [117]. For now only one commercial magnetocaloric effect measuring setup can be acquired from the Russian company AMTC [118].

It is also critical how to interpret the direct measurements data. Adiabatic temperature change measured by a direct method in $La(Fe_{13-x}Si_x)$ [92] and $Gd_5Si_2Ge_2$ [42] showed 30%–50% smaller values as compared to that calculated from isothermal magnetic entropy change and specific-heat data. Gschneidner *et al.* [119] proposed that in the case of first-order magnetic transitions the kinetics of the simultaneously occurring structural transformation can be not fast enough to follow a sweep rate of the applied magnetic field.

Khovaylo *et al.* [120] showed that there are many parameters to take into account and that the results are not strait forward. They measured the ΔT_{ad} in $Ni_{2.19}Mn_{0.81}Ga$ Heusler alloy, because of its small volume change at the transition and high lattice coherence, which would make the kinetic of thermoelastic martensitic transformations fast and would follow the sweep rate of applied magnetic field. They measured a temperature change of around 1 K, which is a huge difference compared to the calculated value of 10 K. This was not because of the slow kinetics of the material, but because of other factors which are intrinsic to first-order magnetic phase transitions. One factor is that the magneto-structural transition temperature lies between the virtual Curie temperature of the high temperature austenitic phase (T_C^A) and the low temperature martensitic phase (T_C^M). Because the magnetic field has a weak influence on the magnetic order parameter far below (above) T_C^M (T_C^A) temperature, the experimentally measured adiabatic temperature change in $Ni_{2.19}Mn_{0.81}Ga$ is much smaller than that calculated. Another factor is that material is structurally and magnetically inhomogeneous in the transition region. Because of that the partially paramagnetic phase will not contribute to ΔT_{ad} and will act as a parasitic loading. To really understand the kinetics of first-order magnetic phase transitions, it is instructive to compare magnetization curves measured, at the same temperatures and on the same samples, under near equilibrium (steady magnetic field) and non-equilibrium (impulse magnetic field) conditions. Figure 11 shows the direct temperature measurement of $Ni_{2.19}Mn_{0.81}Ga$.

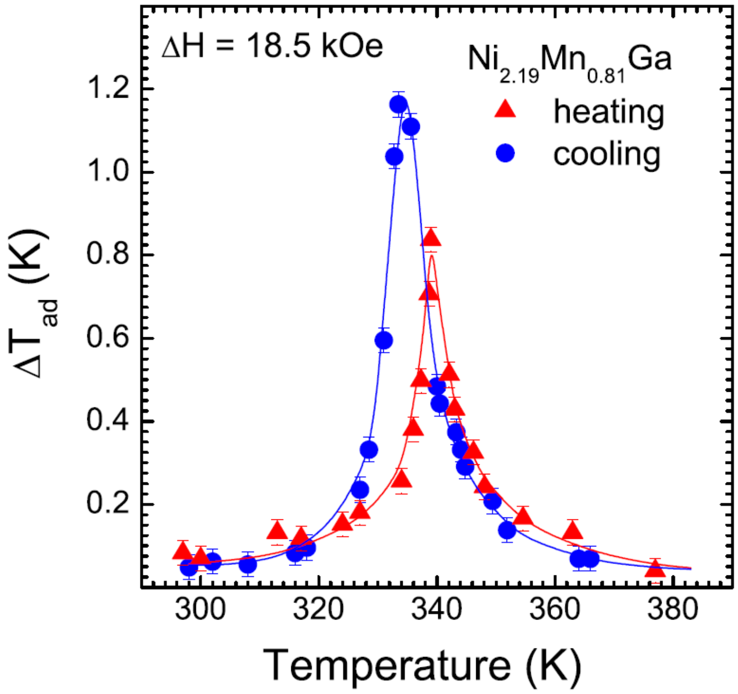

Figure 11: Temperature dependencies of the adiabatic temperature change ΔT_{ad} in $Ni_{2.19}Mn_{0.81}Ga$ measured upon heating and cooling. The magnetic field was applied at a sweep rate of 20 kOe/s. The hysteresis in the peak value of ΔT_{ad} is due to the first-order character of the magneto-structural phase transition. The difference in the peak values of ΔT_{ad} measured upon heating and cooling is caused by the release of latent heat of the transformation during exothermic process (austenite → martensite transformation).

1.6.2 Indirect methods

1.6.2.1 Isothermal magnetization measurements

The magnetic entropy change ΔS_{M} can be calculated from the experimental data on magnetization isotherms using the Equation (11):

$$\Delta S_M = \int_{H_1}^{H_2} \left(\frac{\partial M}{\partial T} \right)_H dH. \tag{39}$$

The equation can be numerically integrated by a set of magnetic isotherms taken at different temperatures. McMichael *et al.* [121] proposed a simple formula for the numerical calculation of ΔS_{M}:

$$|\Delta S_M| = \sum_i \frac{1}{T_{i+1} - T_i} (M_i - M_{i+1}) \Delta H_i. \tag{40}$$

Theoretically, Equation (33) can be used only for second-order magnetic phase transitions, because at the first-order transition the derivative $\partial M/\partial T$ becomes infinitive. A true first-order magnetic phase transition can be described with the Clapeyron-Clausius Equation (27). Because an ideal first-order magnetic transition does not take place in real life one can use Equation (33) instead, but this has still to be used with caution, because one can overestimate ΔS_{M}. In some reported papers in the past years there have been highly speculative ΔS_{M} values [61-64], which turned out to be because of the incorrect use of Equation (32) [122].

Errors in the ΔS_{M} depend on the measuring errors in temperature, magnetic moment, and magnetic field. Because numerical integration is involved, and because the exact differentials (dM, dT, and dH) are substituted, respectively, by the measured ΔM, ΔT, and ΔH, the typical accuracy of ΔS_{M} from magnetization measurements without the proper error analysis was reported to be about ±7.5% error in the values of ΔS_M if magnetization data are measured with 0.5% accuracy [123]. When the errors are analyzed comprehensively, it was shown that the errors in the ΔS_M calculated from magnetization data can be as high as 20 to 30% [124].

1.6.2.2 Adiabatic magnetization measurements

Another method for measuring the MCE (ΔT_{ad}) is based on the comparison of the magnetization field dependences measurements under isothermal and adiabatic conditions [125]. It is well known that the temperature of ferro- and paramagnets increases during the adiabatic magnetization. As a result, the adiabatic magnetization curve of the samples with initial temperature T_0 will intersect the isothermal curves obtained at still higher temperatures $T_1, T_2, ..., T_n$. A demonstration of these intersections is presented in Figure 12 for a paramagnetic single crystal $Gd_3Ga_5O_{12}$. The crossing points of the adiabatic curve with the set of isothermal curves determine the fields, in which a studied sample has corresponding temperatures. So, it is possible to construct (from point to point) full field dependence of the sample temperature during its adiabatic magnetization.

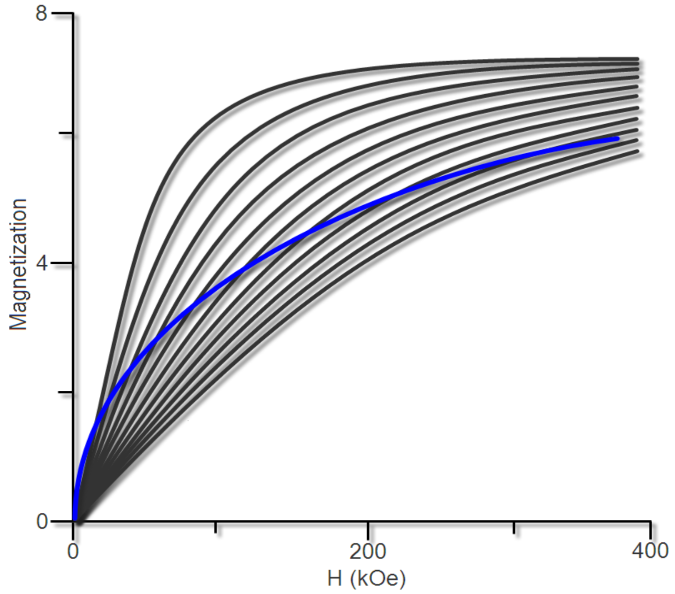

Figure 12: The blue line represents the adiabatic magnetization curve measured in $Gd_3Ga_5O_{12}$ single crystal with a field raising rate of 50 MOe/s. The thin lines represent the isothermal magnetization curves starting from 5 K with a 5 K step. A value of $\Delta T = 46$ K was obtained for $\Delta H = 400$ kOe at 4.2 K.

To achieve adiabatic measuring conditions we use pulsed magnetic fields with a field rising rate of about 10^4 kOe/s or higher. Smaller rates lead to a practically isothermal process.

1.6.2.3 Heat capacity measurement

Heat-capacity measurements give the most complete characterization of the MCE. By measuring the heat capacity as a function of temperature at a constant field we can calculate the entropy of a solid as:

$$S(T,H) = \int_0^T \frac{C(T,H)}{T} dT + S_0, \tag{41}$$

where S_0 is the entropy at $T = 0$ K, which, in a condensed system, is usually assumed to be zero. The following equation was proposed by Pecharsky and Gschneidner [124] for the total entropy calculation from heat capacity data:

$$S(T,H) = 0.5\left\{C(T_1,H) + \sum_{i=1}^{n-1}\left[\left(\frac{C(T_i,H)}{T_i} + \frac{C(T_{i+1},H)}{T_{i+1}}\right)(T_{i-1} - T_i)\right]\right\} \tag{42}$$

where n is the number of measured heat-capacity data points between T_1 and T, $C(T_1, H)$ accounts for the missing heat-capacity data between the lowest temperature of the experiment T_1 and $T = 0$ K assuming that the heat capacity at $T = 0$ K is zero. These approximations lead to a small error which is the same for any $S(T, H)$ at different magnetic fields. From the calculated total entropy temperature dependence in an initial magnetic field (H_I) and in a final magnetic field (H_F), the isothermal magnetic entropy change $\Delta S_M(H, T)$ can be determined at any temperature T as:

$$\Delta S_M(T,H) = \Delta S(T,H) = S(T,H_F) - S(T,H_I) \qquad (43)$$

Pecharsky and Gschneidner showed that the unknown but constant factor has no effect on the $\Delta S_M(T, H)$ when calculated from the heat capacity, because they cancel each other out when calculating the entropy change.

The adiabatic temperature change can be calculated as the isentropic difference between the $S(T, H_I)$ and $S(T, H_F)$ functions:

$$\Delta T_{ad}(T,H) = T(S,H_F) - T(S,H_I) \qquad (44)$$

where $T(S,H_F)$ and $T(S,H_I)$ are the temperatures in the field H_2 and H_1 at constant total entropy S. Figure 3 shows how $\Delta S_M(T, H)$ and $\Delta T_{ad}(T, H)$ are determined from $S(T, H)$ curves.

Using the model presented by Pecharsky and Gschneidner the error occurring in the ΔT_{ad} calculated from heat capacity measurements depends on the influence of the magnetic field on the heat capacity. If this influence is small the error can be considerable. In a ferromagnet the error in ΔT_{ad} increases above T_C because the heat capacity is decreasing. This can be seen in Figure 13.

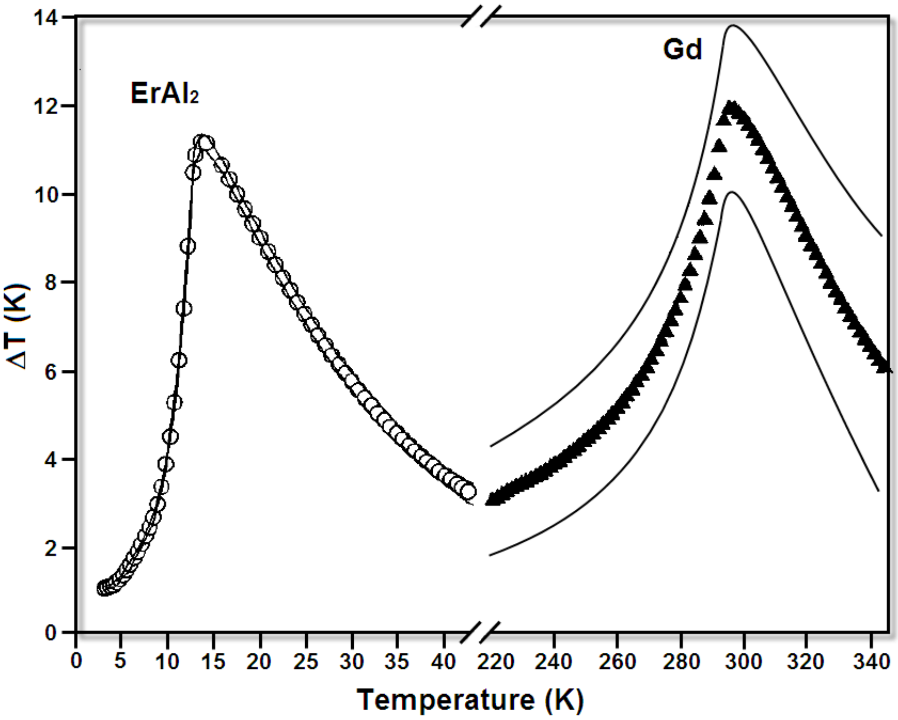

Figure 13: ΔT values for two different materials determined on the basis of the heat-capacity measurements for a field difference of 50 kOe. The solid lines represent the margins of the error in the ΔT calculations according to calculations by Pecharsky and Gschneidner [124].

1.7 Refrigerant capacity

When comparing the ΔS_M values the problem is that ΔT_{ad} is not taken into consideration. A better parameter for comparing magnetocaloric materials is the refrigerant capacity (RC), which is defined as

$$q = \int_{T_1}^{T_2} \Delta S_M(T)dT, \qquad (45)$$

where T_1 and T_2 are the temperatures of the hot and cold sinks, respectively, and $\Delta S_M(T)$ is the refrigerant's magnetic entropy change as a function of temperature. The refrigerant capacity, therefore, is a measure of how much heat can be transferred between the cold and hot sinks in one ideal refrigeration cycle. [13] To get the total refrigerant capacity we need to take into account the hysteresis losses that occur during the

FOMT. These losses have to be subtracted from the RC to compare the values with materials that have a SOMT, where those losses do not occur.

1.8 Magnetic refrigeration

Magnetic refrigeration (MR) is, compared to the vapor-cycle technology, a environmental friendly cooling technology, because it does not use ozone-depleting chemicals or greenhouse gases. Also the energy loss during a refrigeration cycle is quite lower. While the vapor-cycle technology operates way below the maximum theoretical (Carnot) efficiency (40%) it has been shown that the cooling efficiency of magnetic refrigerators is as high as 60 % because it has no compressor, which is the most ineffective part of the refrigerator.

The magnetic refrigerator should contain a magnetic working body, a magnetization system, hot and cold heat exchangers and a heat-transfer fluid with a system providing its flow. It works on the principle that the working material (refrigerant) absorbs heat at the low-temperature load (cold heat exchanger) and discharges heat at the high-temperature sink (hot heat exchanger). With a cycling repetition the load is cooled. A comparison between both systems can be seen in Figure 14.

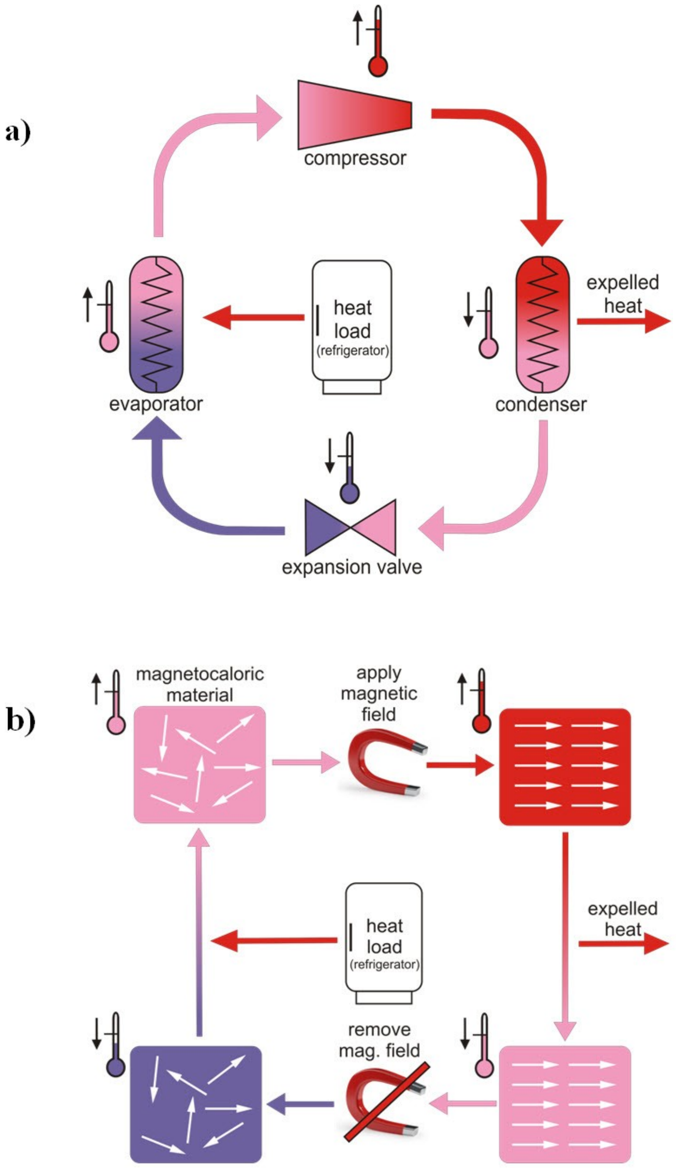

Figure 14: Schematic representation of both refrigeration cycles: the conventional vapor-cycle (a) and the magnetic refrigeration cycle (b).

The true beginning of near room temperature cooling has its origin in the seminal paper by Brown (1976). He showed that a continuously operating device working near room temperature could achieve much larger temperature spans than the maximum observed magnetocaloric effect. Brown's near room temperature reciprocating magnetic refrigerator used one mole of 1 mm thick Gd plates separated by a wire screen (Curie temperature, T_C = 294 K) and an 80% water–20% ethyl alcohol solution as a regenerator in an alternating 70 kOe field produced by a superconducting magnet. A maximum temperature span of 47 K was attained after 50 cycles (T_{hot} = 319 K [46 ºC] and T_{cold} = 272 K [-1 ºC] where T_{hot} is the hot end temperature and T_{cold} is the cold end temperature).

Following the early work of Brown, the concept of using an active magnetic regenerator (AMR) in the cooling device to facilitate heat transfer was introduced by Steyert (1978) who was evaluating the Stirling cycle for magnetic refrigerators and heat engines. This AMR cycle, which is a Brayton-like cycle, showed that it is possible to get much larger temperature lifts than just the adiabatic temperature rise of the magnetic refrigerant by using the magnetic material simultaneously as a regenerator and as the active magnetic component.

Over 20 years later Zimm et al. in 1998 realized the first reciprocating magnetic refrigeration that very much resembles the design proposed by Brown. With the collaboration of Ames Laboratory and Astronautics the group achieved extremely good performances on this machine. They used a 5 T superconducting magnet and 3 kg of Gd spheres and achieved a cooling power of 600 W at an operating frequency of 0.17 Hz and realized a temperature span of 10 K.

After the proof-of-principle MR numerous prototypes have been developed with different designs and working material to improve the still low maximum cooling power and the low COP (coefficient of performance) values. A brief summary of the operational near-room-temperature refrigerators that have been reported in the literature is presented in Table 2.

Table 2: Room temperature magnetic refrigerators

Institute/Company	**Year**	**Type**	**Max. cooling power (W)**(1)	**Max ΔT (K)**(2)	**Magnetic field (T)**	**Solid refrigerant**	**Ref.**
Ames Laboratory/Astronautics	1997	Reciprocating	600	10	5 (SCM)	Gd spheres	[126]
Mater. Science Institute Barcelona	2000	Rotary	?	5	0.95 (PEM)	Gd foil	[127]
Chubu Electric/Toshiba	2000	Reciprocating	100	21	4 (SCM)	Gd spheres	[128]
University of Victoria	2001	Reciprocating	2	14	2 (SCM)	Gd & $Gd_{1-x}Tb_x$	[129]
Astronautics	2001	Rotary	95	25	1.5 (PEM)	Gd spheres	[130]
Chubu Electric/Toshiba	2003	Rotary	60	10	0.76 (PEM)	$Gd_{1-x}Dy_x$ L.B.	[131]
Lab. d'Electrotechnique Grenoble	2003	Reciprocating	8.8	4	0.8 (PEM)	Gd foil	[132]
Astronautics	2004	Rotary	95	25	1.5 (PEM)	Gd / GdEr / $La(Fe_{0.88}Si_{0.12})_{13}H_{1.0}$	[133]
University of Victoria	2006	Reciprocating	15	50	2 (SCM)	Gd, $Gd_{0.74}Tb_{0.26}$ and $Gd_{0.85}Er_{0.15}$	[134]
Astronautics	2007	Rotating magnet	220	11	1.4 (HM)	Gd plates	[135]
Tokyo Inst. Tech.	2007	Rotary	540	7.5	1.1 (PEM)	Gd spheres	[136]

(1) maximum cooling power at zero temperature difference (ΔT=0),
(2) maximum temperature span at zero cooling capacity (W=0),
L.B. = layered bed
PEM = permanent magnet;
SCM = superconducting magnet
HM = Halbach magnet

In the latest magnetic refrigerator reported by Okamura et al. [136], form the Tokyo Institute of Technology, a permanent magnet rotates inside a four segmented magnetocaloric ring which is surrounded by an iron yoke (Fig. 15). The magnetic field in the AMR ducts when the poles of the inner permanent magnet are next to the duct is 11 kOe. The authors tested four different Gd-based alloys as the magnetic refrigerant, each weighing 4 kg. They realized a cooling power of 540 W, and a COP of 1.8 when the hot end of the AMR duct was 21 ºC with a 0.2 K temperature span in the water flow.

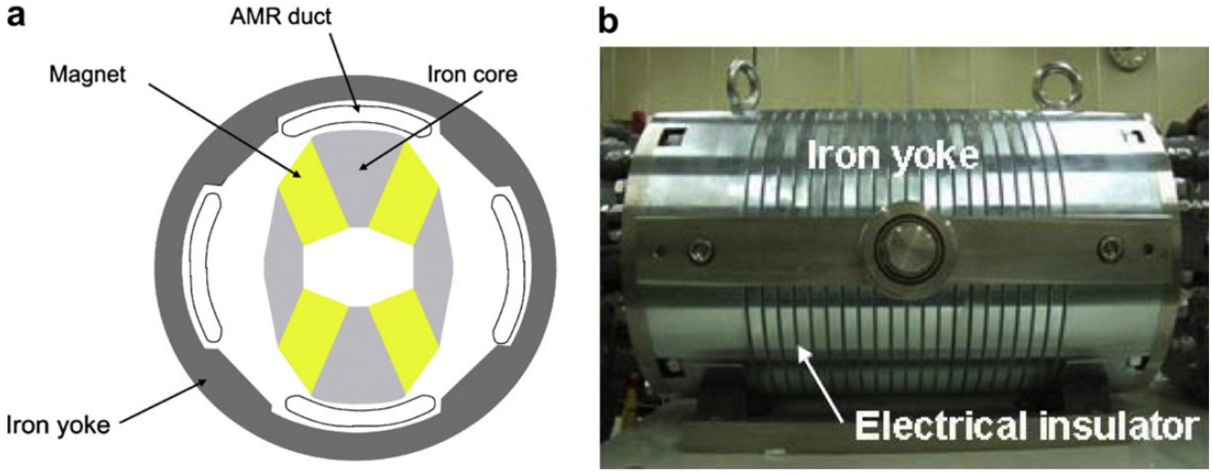

Figure 15: Magnetic refrigerator by Okamura et al.. Figure 15a shows the schematics of the MR with the four ‘‘AMR ducts’’, Figure 15b shows a photograph of the device.

The number MR being designed and tested is exponentially growing. Since the start in 1997 there have been almost 30 new devices been designed in 2007. With this growth it has been predicted that the MR will be comersionalized already in 2015[15].

2 $Gd_5Si_2Ge_2$

2.1 The $Gd_5(Si,Ge)_4$ system and the giant MCE

The $Gd_5(Si,Ge)_4$ system is one of the most researched magnetocaloric systems. This is because of the large magnetic entropy change and other magnetic and structural phenomena, such as colossal magnetostriction and giant magnetoresistance. The binary compounds Gd_5Si_4 and Gd_5Ge_4 were first discovered by Smith et al. [137] and Holtzberg et al. [138]. It was reported that both intermetallides crystallize in the Sm_5Ge_4-type [139] orthorhombic structure. Holtzberg et al. also reported the extended solubility of Si in Gd_5Ge_4 ($0.0 \leq x \leq 0.3$) and Ge in Gd_5Si_4 ($0.5 \leq x \leq 1.0$). They also acknowledged the existence of the ternary intermediate phase with unidentified crystal structure extending between $0.3 < x < 0.5$. The magnetic measurements showed that Gd_5Si_4 orders ferromagnetically at $T_C = 335$ K and that Gd_5Ge_4 orders antiferromagnetically at $T_N \cong 125$ K and ferromagnetically at $T_C \cong 20$ K [138, 39].

The discovery of the giant magnetocaloric effect in $Gd_5(Si_xGe_{1-x})_4$ alloys [8] renewed the interest in this series of intermetallic compounds. $Gd_5Si_2Ge_2$ has a FOMT closest to room temperature compared to other alloys in this system. The magnetic entropy change is larger than that of Gd, with a value of -18.5 J/kgK for a field change of 5 T. [8] The adiabatic temperature rise for $Gd_5Si_2Ge_2$ was measured to be 16.5 K [140] when the magnetic field was ramped up to a rate of 20 kOe min^{-1} up to a 5 Tesla field. The value agreed quite well with the ΔT_{ad} value of 16.8 K calculated from heat capacity measurements made on the same sample. The ΔT_{ad} peak is higher (>30 %) and also narrower than that of Gd. To explain this phenomenon many papers were produced afterwards.

Pecharsky et al. [39, 36, 45] produced the first phase diagram of the $Gd_5(Si_xGe_{1-x})_4$ system, where they also identify the unknown ternary intermediate phase. It turns out that this phase has a monoclinic structure. They also showed that the binary compounds Gd_5Si_4 and Gd_5Ge_4 crystallize in a different structure and that the transitions in the Ge-rich and the monoclinic regions were first order and reversible. The MCE increases in the Ge-rich region form $x = 0$ to $x = 0.2$ and decreases in the monoclinic region from $x = 0.24$ to $x = 0.5$. In the composition range from 0.5 to 1.0 the PM-FM transition was second order, which reduced the MCE substantially. Morellon et al. [141] later on showed in $Gd_5(Si_{1.8}Ge_{2.2})$ that a ferromagnetic (low temperature) to paramagnetic (high temperature) magnetic phase transition occurs simultaneously with an orthorhombic (low temperature) to monoclinic (room temperature) crystallographic phase transformation, according to x-ray powder diffraction, which explained the giant MCE.

2.2 The phase diagram

The first phase diagram from 1997 was improved by Pecharsky et al. in 2002 [142].The zero magnetic field phase diagram of the pseudobinary system Gd_5Si_4–Gd_5Ge_4 as a function of Si- concentration is based on as-cast (i.e. non-heat treated) alloys and is presented in Figure 16.

The phase diagram is composed of three extended solid solutions. The first is the Si-rich $Gd_5(Si_xGe_{1-x})_4$, when $0.575 \leq x \leq 1$. The compounds from this region crystallize in the Gd_5Si_4-type ortorhombic (space group *Pnma*) crystal structure (*O*(*I*)), and they undergo a second-order paramagnetic to ferromagnetic phase transformation on cooling with no structural changes during this transformation. The ordering temperature slowly decreases with the increase of Ge in the alloy. The second solid solution is the intermediate $Gd_5Si_2Ge_2$-type monoclinic (space group $P112_1/a$) region, when $0.4 \leq x \leq 0.503$, and it is also known as the M-type polymorph. All alloys from this region change their magnetic state during a first-order paramagnetic to ferromagnetic phase transformation coupled with the crystallographic phase change from the monoclinic $Gd_5Si_2Ge_2$-type structure to the orthorhombic Gd_5Si_4-type structure, on cooling from room temperature. The ordering temperatures decrease much more rapidly compared to the alloys from the *O*(*I*) phase region when the Si:Ge ratio is reduced below $x = 0.575$. The third single-phase region is the Ge-rich $Gd_5(Si_xGe_{1-x})_4$, Sm_5Ge_4-type solid solution (*O*(*II*)), when $0 < x \leq 0.3$. When the compounds from this region are cooled, they exhibit two successive phase transformations: (a) a second-order paramagnetic to antiferromagnetic (AFM) transitions at nearly constant temperature (i.e. 120 – 130 K), regardless of the alloy composition and (b) the coupled magnetic (antiferromagnetic to ferromagnetic) and crystallographic (Sm_5Ge_4- to Gd_5Si_4-type) first-order phase transformations at lower temperatures [44]. The structural transformation in the Ge-rich region from *O*(*II*) to *O*(*I*) on cooling does not change the symmetry, but drastically varies the cell parameters and atomic positions, which will be discussed in the next chapter. The transition temperatures marked red exhibit, because of the coupled magnetic–crystallographic phase change, a giant MCE, while the transition temperatures marked green exhibit only a normal MCE. These structural-magnetic phase transitions can be induced not only by changing the temperature, but also by changing the magnetic field [38, 39, 142], or pressure [142,143,144].

It has been show by V.K. Pecharsky et al. [145] that the monoclinic paramagnetic phase transforms to the orthorhombic Gd5Si4-type structure when heated to 690 K. Unlike the low-temperature magnetic–crystallographic transition, the high-temperature crystallographic-only transformation is only triggered by temperature. This process is irreversible below 730 K and the orthorhombic structure can be retained after cooling to room temperature. Because of that, the proper heat treatment is necessary to produce a purely monoclinic phase. The monoclinic structure is restored by heat treatment at temperatures exceeding 1200 K, i.e. the orthorhombic to monoclinic transformation occurs at high temperature. They concluded that the monoclinic phase is in fact a high-temperature phase, metastable at room temperature. The monoclinic to orthorhombic transformation is thermoelastic, which means that the fraction of the formed orthorhombic-phase remains constant as long as the temperature remains constant. [146]

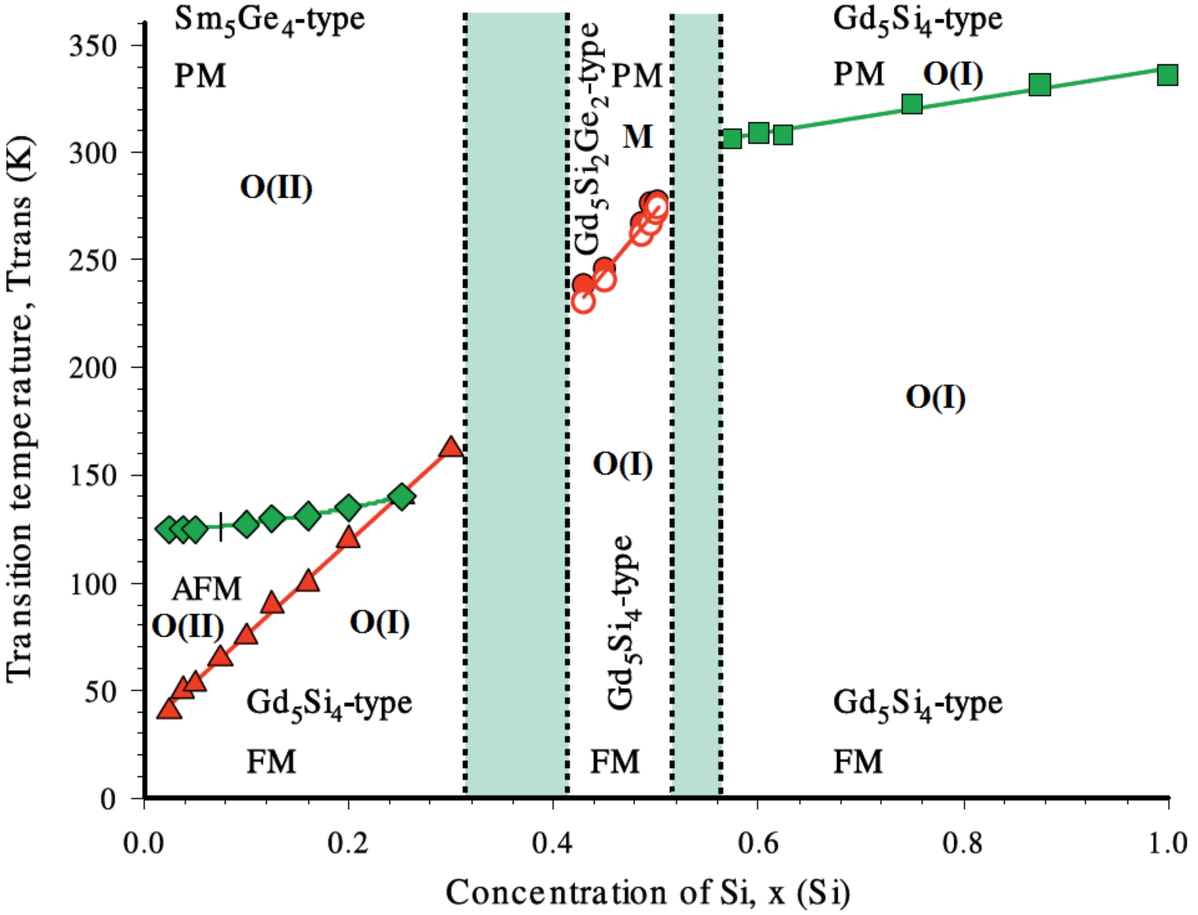

Figure 16: The magnetic phase diagram of the Gd_5Ge_4-Gd_5Si_4 pseudo-binary system at zero field. The green and red lines separate the different magnetic phases, while the vertical dotted lines separate the single phase and the gray two phase regions. The solid marks indicate as-cast samples and the open marks heat treated ones. PM-paramagnetic, FM-ferromagnetic, AFM-antiferromagnetic, M-monoclinic structure, *O*(*I*)-Gd_5Si_4-type structure, *O*(*II*)-Sm_5Ge_4-type structure.

2.3 Crystal structure

The crystal structures of the $Gd_5(Si_xGe_{1-x})_4$ phases consist of 36 atoms per unit cell distributed among six to nine independent crystallographic sites. [147, 36, 37, 38] The Gd atoms are located in the corners of cubes and trigonal prisms, and inside the cubes (blue atoms). These Gd atoms form two-dimensional (3^2434) nets that are infinite in two dimensions (*a* and *c*). Two adjacent Gd (3^2434) nets create a slab composed of distorted cubes and trigonal prisms sharing common faces. These slabs are common for all structures and Figure 17a shows a projection of one of these slabs along the *b* axis. The Si and Ge atoms are divided into two groups of atoms. One groupe of the Si and Ge atoms, called *T* atoms (green atoms), occupy the trigonal prisms in these slabs, which share a common rectangular face to create *T* - *T* dimers. The rest of the Si and Ge atoms, called *T*’atoms (red atoms), are located on the slab surface and are responsible for the bonding between the slabs. The Gd atom at the center of each cube is surrounded by an octahedral arrangement of 4 *T* and 2 *T*’ atoms. Figure 17b, c and d shows the projection of all three possible structures along the **c** axis. The only difference between all three structures is the covalent-like bond between the *T*’ atoms. If the two-dimensional slabs are not connected with one another, the crystal structure is the orthorhombic Gd_5Si_4-type (*O*(*I*)). When all slabs are connected with each other the crystal structure is the orthorhombic Sm_5Ge_4-type (*O*(*II*)). If every second slab is connected, then the room-temperature crystal structure of the alloy is monoclinically distorted and is composed of alternating strongly and weakly interacting slabs. The drastic changes in inter-slab bonding, crystal structures, and properties occur because one of the thermodynamic parameters (chemical composition) affects the interactions between the slabs, while the interactions inside the slabs remain essentially the same. At low temperatures all the *T*’- *T*’ bonds are connected, independently of the composition. With the increment of temperature the composition defines how many *T*’- *T*’ bonds break. In the Si-rich compounds no bond is broken, while in the Ge-rich compounds all the bonds break, because of the increase in distance between all *T*’ atoms, when heated up. For the composition $Gd_5Si_2Ge_2$ the *T* atoms have 60 % of Ge and 40 % of Si atoms, while the *T*’ atoms have 40 % of Ge and 60 % of Si atoms. At a temperature of 243 K the *T* - *T* distance in the slabs is ca. 2.56 Å and the *T*’- *T*’ distance between the slabs is 2.629(3) Å (all slabs are connected). When we increase the temperature to room temperature the shear movement of the slabs increases the distance of every second *T*’- *T*’ bond by 32.7% to 3.488(3) Å and thus breaking them. Within a pair of adjacent slabs maintaining the *T*’- *T*’ connection, interatomic distances change less than 3% during the orthorhombic-monoclinic transformation. The distance between the *T* - *T* atoms remain the same. The crystallographic data for $Gd_5Si_2Ge_2$ is in Table 3. This shear movement is illustrated by the two arrows in Figure 17b. If we lower the temperature again to 243 K the slabs move back to the starting position and the *T*’- *T*’ atoms bond again, making this process reversible.

Table 3: Crystallographic data for Gd5Si2Ge2.

Temperature	**163 K**	**243 K**	**292 K**
Space group	***Pnma***	***Pnma***	***P*112$_1$/*a***
a,Å	7.5137(11)	7.5132(11)	7.5891(17)
b,Å	14.792(2)	14.797(2)	14.827(3)
c,Å	7.7858(11)	7.7942(11)	7.7862(17)
γ, deg	90	90	93.262(4)
V,Å^3	865.3(2)	866.5(2)	874.7(3)

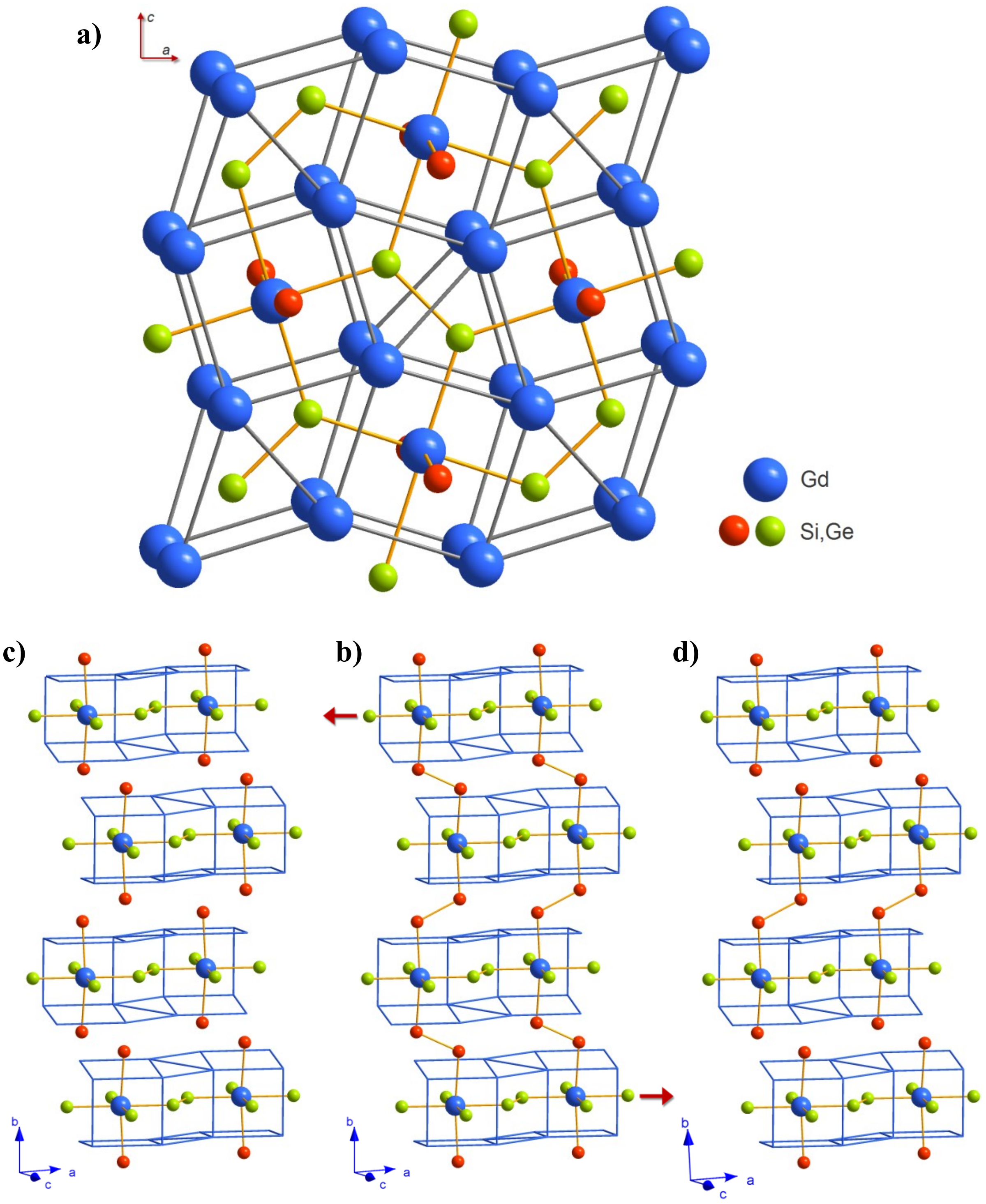

Figure 17: Crystallographic structures of $Gd_5(Si_xGe_{1-x})_4$ alloys. (a) shows a projection along the *b* axis. This basic building slab (3^2434 net) is common for all structures. The centers and the corners of all cubes and the corners of all trigonal prisms traced in (a) are occupied by Gd atoms, represented as blue atoms. Si and Ge atoms which are located inside the slab are shown in green (a). The red atoms represent exterior Si and/or Ge atoms (depending on the composition) responsible for bonding between the slabs. (b)-(d) shows a projection along the c axis with the bonding arrangement between *T*'- *T*' atoms for all three structures. (b) shows the orthorhombic Sm_5Ge_4-type structure, (c) the orthorhombic Gd_5Si_4-type structure and (d) the monoclinic $Gd_5Si_2Ge_2$-type structure.

As the magneto-structural transition in $Gd_5Si_2Ge_2$ occurs, the crystals show macroscopic twinning [37], which was first indicated by significant residual electron densities (ca. 7.9 $e^- / Å^3$) in the fully refined, initial monoclinic-phase model. No such residual electron densities were seen in the orthorhombic-phase model. These electron density residues reveal an additional (3^2434) net next to the Gd (3^2434) net already present in the refined orthorhombic-phase model. It was found that nonmerohedral twinning is responsible for this. Twinning can be classified as merohedral or nonmerohedral. In the case of nonmerohedral twinning only some subsets of the diffraction reflections from different domains overlap, whereas for a merohedrally twinned crystal the diffraction patterns from different domains overlap exactly in three dimensions. These findings also improve in the statistical fit of observed and calculated structure factors. This phenomenon is also coupled to the crystallographic changes: twinning vanishes when the crystal is cooled below ca. 260 K as the orthorhombic phase forms, and it reappears on heating to room temperature as the monoclinic phase forms. It is suggested that twinning is an intrinsic feature of the monoclinic phase. Figure 18 illustrates a model of the possible twin mechanism during the phase transition.

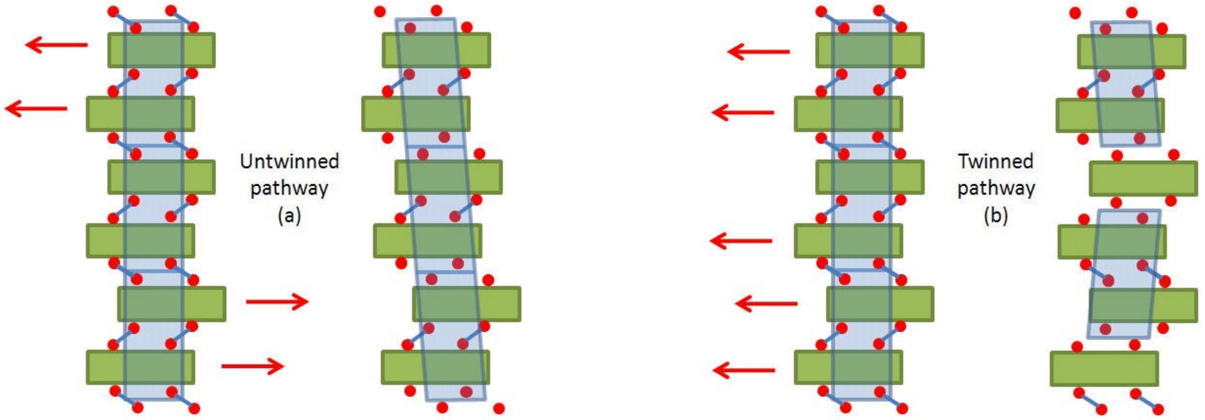

Figure 18: Two possible pathways for the orthorhombic-monoclinic structural transformation by the shear movement along *a* axis. The first and the third Figure are the orthorhombic structure and the second and the fourth Figure are the monoclinic structure models.

For no twinning in the β-phase adjacent pairs of slabs shift in the opposite directions along **a** axis (see the arrows in Figure 18(a)). On the other hand, if two neighboring inter-slab Si(Ge)-Si(Ge) bonds are broken, then two different orientations of equivalent monoclinic unit cells are generated, which are related to each other by a mirror operation in the *a c* plane (perpendicular to the *b* axis; see Figure 18(b)), and nonmerohedral twinning occurs.

2.4 Interplay of structure, magnetism, and thermodynamics

The large shear displacements of atomic layers in $Gd_5(Si_xGe_{1-x})_4$ coupled with the change of crystallographic symmetry and magnetic order, characterizes these transformations as magnetic-martensitic, which are extremely rare.

As stated earlier the Curie temperatures of the $Gd_5(Si_xGe_{1-x})_4$ alloys are largely dependent on *x*. For PM *O*(*I*)-type compounds (T_C > 300 K) the T_C's are higher than that of the elemental Gd (T_C = 294 K), indicating the enhancement of exchange interactions despite a 55:45 (atomic) dilution of Gd with nominally nonmagnetic Si and Ge. The gradual reduction of the Curie temperature from 336 to 300 K is consistent with a gradual increase of the phase volume and elongation of the inter-atomic distances with increasing Ge content. In the *M*-type polymorph crystal structure the T_C of these alloys becomes strongly dependent on the composition, even though the phase volume keeps rising with decreasing *x* at practically the same rate as in the *O*(*I*) phase region. Thermodynamically, this PM–FM transition becomes a first-order transformation because it overlaps with a structural change between the *M*- and *O*(*I*)-types of crystal structures. At lower *x* the PM $Gd_5(Si_xGe_{1-x})_4$ alloys adopt the *O*(*II*)-type structure which on cooling goes through a second order PM-AFM phase change and a coupled magnetic–crystallographic phase change.

Regardless of *x*, the ground state of the $Gd_5(Si_xGe_{1-x})_4$ system is *O*(*I*)-FM phase, i.e., it appears to be structurally and magnetically homogeneous over the whole range of concentrations, unlike the PM state, which has three structurally distinct phase regions. But experiments showed [148 - 151] that the *O*(*I*)-FM state may not, however, be completely magnetically homogeneous since the easy magnetization direction changes from parallel to the *a*-axis for $x = 0.425$ and $x = 0.5$ to the *b*-axis when $x = 0$. Furthermore, as follows from temperature-dependent, low magnetic field measurements of $Gd_5Si_2Ge_2$ single crystals [152], the easy magnetization direction in the ferromagnetically ordered state is temperature-dependent.

The magnetic properties in $Gd_5Si_2Ge_2$ are defined by the bonding and crystallography, which have been indicated by the first principle calculations. [153 - 155] Thus, breaking and reforming of the interslab T'-T' dimers, which accompanies the $O(I)$-M structural transition, and the related 0.9 Å elongation and contraction, respectively, of the interslab T'-T' bonds affects both the location of the Fermi level and the effective magnetic exchange coupling, J_0. Comparing the FM-ordered $O(I)$-$Gd_5Si_2Ge_2$ with the hypothetical FM M-$Gd_5Si_2Ge_2$, the former is characterized by larger magnetic moments of the individual Gd atoms (the difference arises from the varying contribution from the 5d electrons of Gd), a larger J_0, and a lower total energy (at 0 K) than the latter, thus explaining the stability of the $O(I)$-type structure in the ferromagnetically ordered state.

Paudyal et al. [156] described the temperature of the magnetostructural transition, T_C, and its first-order nature in $Gd_5Si_2Ge_2$ using the tight binding linear muffin tin orbital (TB-LMTO) method. Figure 19 shows the T_C calculated from first principles (thick solid line) and the experimental values (solid circles). We can see that the agreement between the theory and experiment is nearly quantitative. Why there is a big jump in magnetic moment can be easily described from Figure 19. In the lower right part the predicted FM ordering temperatures of the $O(I)$- and M-type $Gd_5Si_2Ge_2$ phases can be seen, with values of $T_C{}^{O(I)} = 301$ K and $T_C{}^{M} = 209$ K, respectively. Both should order ferromagnetically via a second-order transformation typical for magnetic order-disorder transitions. However, when we cool down from higher temperatures we can see that the free energy of the PM M-$Gd_5Si_2Ge_2$ is lower compared to the PM and FM $O(I)$-$Gd_5Si_2Ge_2$ (upper right part of Figure 19). At T_C the free energies become equal and we get a huge jump in the magnetic moment because we are already below the T_C of the $O(I)$-$Gd_5Si_2Ge_2$ phase, hence already in the FM state.

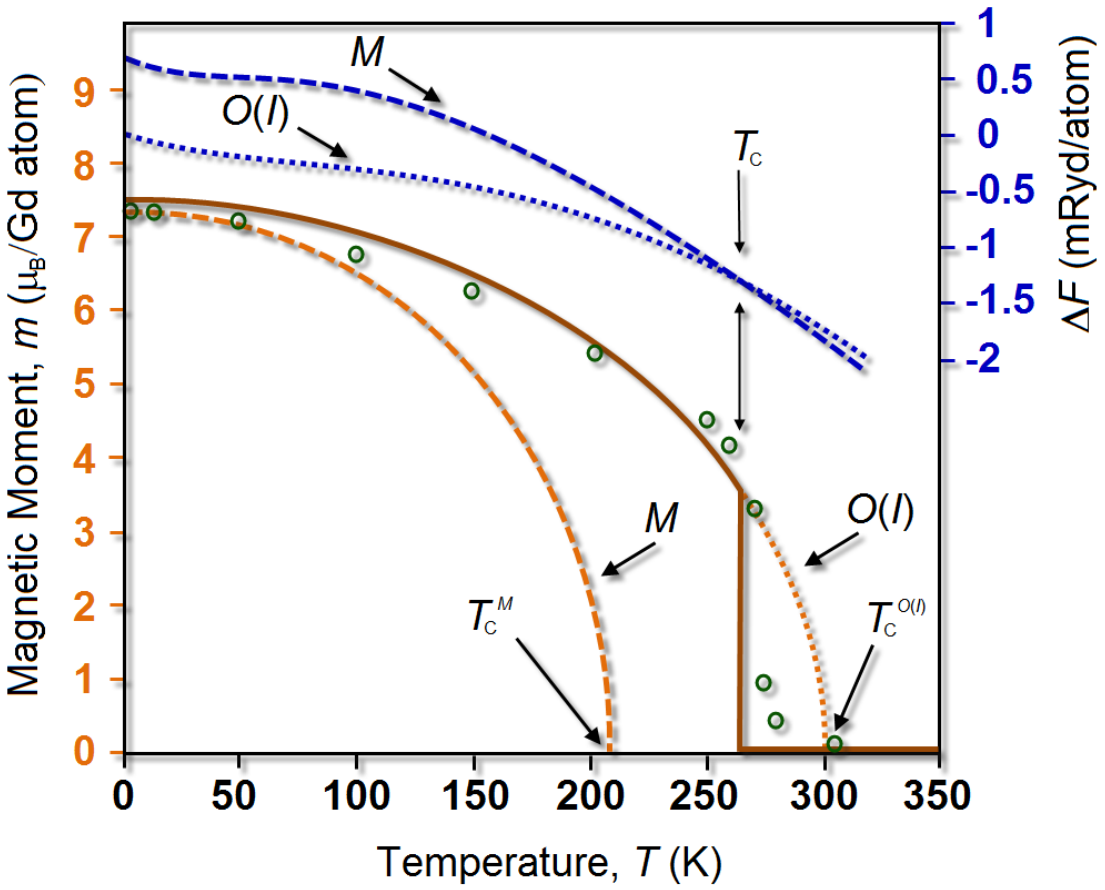

Figure 19: Spontaneous magnetization (orange) and Helmholtz free energy (blue) as a function of temperature of M-$Gd_5Si_2Ge_2$ (dashed lines) and $O(I)$-$Gd_5Si_2Ge_2$ (dotted lines) calculated from first principles. At T_C the FM-ordered $O(I)$-$Gd_5Si_2Ge_2$ transforms into M-$Gd_5Si_2Ge_2$. At that point the M-$Gd_5Si_2Ge_2$ is already PM, resulting in the discontinuous change in magnetization. The thick solid line represents the calculated model and the solid circles represent the experimental data.

A typical magnetic-field dependence of the magnetization for a magnetic-field-induced transition is represented in Figure 20 for $Gd_5Si_{1.5}Ge_{2.5}$ [157]. At low temperatures the sample response as a normal ferromagnet and at high temperatures as a paramagnet. From the temperatures 212 to 238 K we observe a two-step magnetization increase and also a hysteresis of about 10 kOe between increasing and decreasing magnetic fields. The first step is due to domain-wall displacement and rotation of the magnetization of the domains in the fraction of the sample which is ferromagnetic at each temperature. The second step is due to a magnetic-field-induced PM/FM transformation of the fraction which is paramagnetic at a given temperature with a simultaneous magnetization of the formed ferromagnetic phase. This is visualized for the data at 220 K. The second step like magnetization increase starts at a critical magnetic field H_{CR1} and then reaches saturation at H_{CR2}. During the magnetic-field reduction from its maximum to zero, the magnetization begins to decrease sharply at H_{CR3} and returns almost to its original behavior at H_{CR4}. This results in a remanence-free hysteresis. The approximate locations of the four critical fields at 220 K are determined from the maximum curvature of the corresponding magnetization isotherm and are shown by vertical arrows. A possible behavior of the magnetization at 212 and 220 K without the field-induced PM/FM transformation is shown by the green lines in Figure 20.

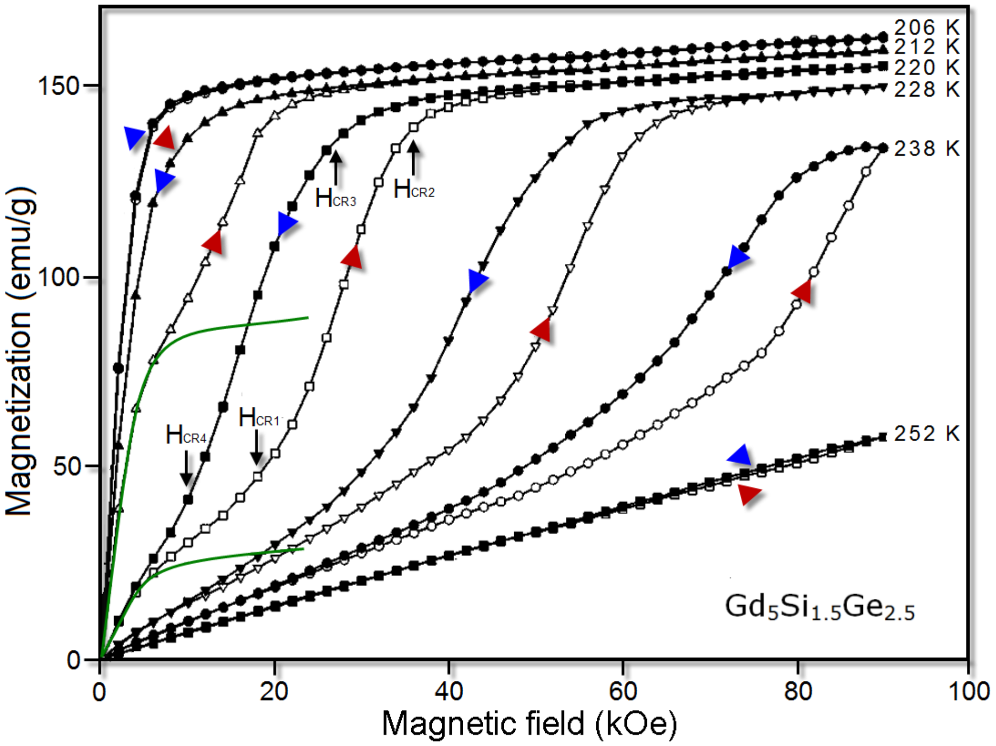

Figure 20: Magnetic-field dependence of the magnetization of $Gd_5Si_{1.5}Ge_{2.5}$ at various temperatures. The arrows on the isotherms represent the direction of the field change. The extrapolated behavior of the magnetization at 212 and 220 K without the field-induced PM/FM transformation is shown by the green lines. Locations of critical magnetic fields are shown for an isotherm at 220 K.

From Figure 20 we can see that the start and the end of the magnetic-martensitic transitions depends strongly on the direction of change (i.e., increasing or decreasing) of either or both the temperature and magnetic field. This is true for all $Gd_5(Si_xGe_{1-x})_4$ alloys with a magnetic-martensitic transition.

Figure 21 represents the critical magnetic fields for $Gd_5Si_2Ge_2$. [44] The orange area is the region where the paramagnetic/monoclinic phase transforms into the ferromagnetic/orthorhombic phase during magnetic field increase and/or temperature reduction. The blue area is the region where the ferromagnetic/orthorhombic phase transforms into the paramagnetic/monoclinic phase during magnetic field reduction and/or temperature increase. We see that the four critical fields (border lines of the orange and blue area) increase nearly linearly. The system is, between the start an end of the magnetic-martensitic transitions (between H_{CR1} - H_{CR2} and H_{CR3} - H_{CR4}), magnetically and structurally inhomogeneous i.e., it consists of the two phases, ferromagnetic/orthorhombic and paramagnetic/monoclinic. The hysteresis that appears at the increase and decrease of temperature and/or magnetic field is clear evidence that the field-induced structural transition is of first order.

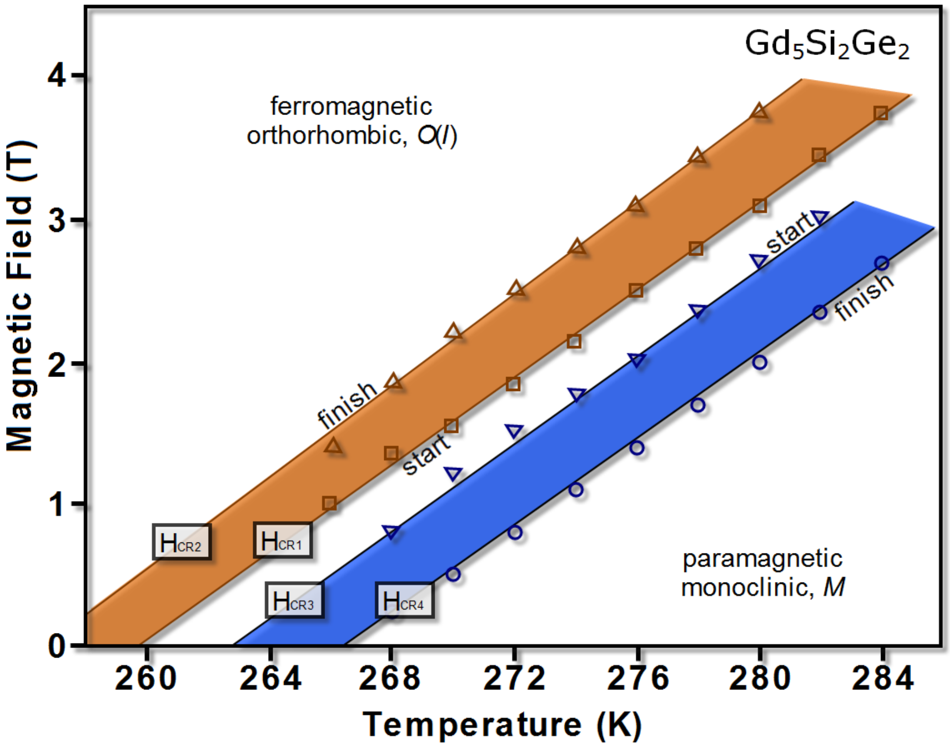

Figure 21: $Gd_5Si_2Ge_2$ phase diagram. The figure shows the different starting and finishing areas where the magnetic-martensitic transition happens, depending on whether we increase/decrease the temperature or if we increase/decrease the magnetic field.

2.5 Microstructure

The microstructures of $Gd_5(Si_xGe_{1-x})_4$ alloys were first examined by Szade et al. [158] who studied the surface structure of single crystals. They reported that the surface of the single crystalline plates show a regular system of lines and an increase of gadolinium and oxygen was observed in these linear features. Meyers et al. [159] used EDS to analyze the linear features and also found an increase in Gd and O along with a decrease in Si. They concluded that the linear features were a separate phase forming in a manner indicative of a Widmanstätten structure and hypothesized that they were possibly rods of $Gd_5(Si,Ge)_3$. Gama et al. found that these features disappear after heat treatment. [160] The Widmanstätten structure forms by a solid-state precipitation reaction from a supersaturated solid solution and usually results in the precipitate phase having a characteristic shape such as plates or needles. A Widmanstätten type precipitate generally forms along a specific set of $\{h\,k\,l\}$ planes or directions in the matrix. For a plate shaped precipitate these planes are called the habit planes and for the needle shaped ones these directions are called the habit directions of the matrix. Ugurlu et al. [161] found that the average width of the plates is on the order of 250 nm with plate dimensions running to hundreds of microns. EDS and selected-area electron diffraction (SAED) studies using the TEM indicate that the second phase in $Gd_5Si_2Ge_2$ alloys is hexagonal with composition and lattice parameters that match extremely well to a compound of the type $Gd_5Si_1Ge_2$. Meyers et al. also observed a phase consisting of about 35 at.% Si, 15 at.% Ge and 50 at.% Gd as determined using EDS and identified it as $Gd_1(Si,Ge)_1$, with a leaflike structure.

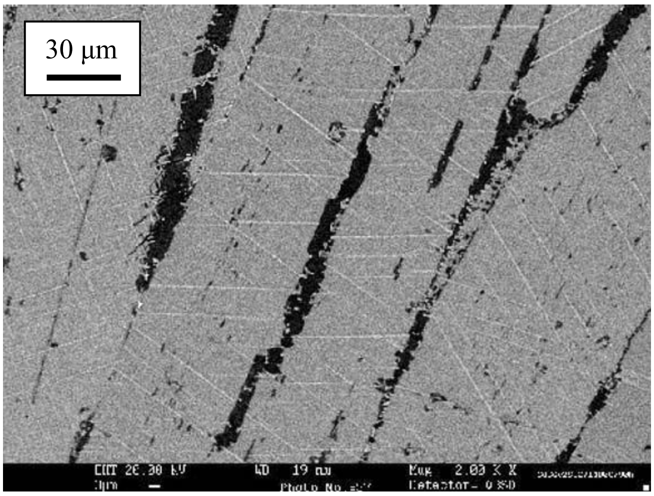

Figure 22: Microstructure of the $Gd_5Ge_2Si_2$ as-cast sample with the typical Widmanstätten structure (very thin and long straight white lines), which have a strict angular relationship with the grains of the majority phase where they occur.

Moore et al. [162] used scanning Hall probe imaging to examine these features when changing the field. They showed that these platelets act as seeds for the nucleation and growth of FM clusters in the PM matrix. Even if they are paramagnetic and have no net magnetic moment, they create a range of critical fields that define the onset of the PM to FM transition. This also produces an effective range of local hysteresis widths, suggesting that the hysteresis can be only controlled locally. But these features do not control the reverse FM to PM transition. Here other morphological features, such as cracks and edges, control the transition.

The purity of the starting materials also has a major effect on the microstructure of the alloy. Fu et al. [163] demonstrated that $Gd_5Si_{1.9}Ge_{2.1}$ prepared with high purity Gd is $Gd_5Si_2Ge_2$-type single-phase; whereas $Gd_5Si_{1.9}Ge_{2.1}$ with prepared low purity Gd consist of $Gd_5Si_2Ge_2$-type, Gd5Si3-type, and GdGe-type. They also observed a $GdSi_{2-x}$-type phase, but could not prove it with XRD.

2.6 Substitutions

One of the major problems of these alloys is their large hysteresis losses. Provenzano et al. [164] first showed that by adding a small amount of iron to the alloy a reduction of hysteresis losses (over 90%) in $Gd_5Ge_2Si_2$, forming $Gd_5Ge_{1.9}Si_2Fe_{0.1}$, can be achieved (Figure 23). Also, the peak magnetic entropy change shifted from 275 K to 305 K, broadening its width but reducing its value. Due to the reduction in hysteresis losses, a greater net capacity of 355 J/kg was obtained for the iron-containing alloy. The iron suppressed the formation of the monoclinic phase, making the transition second order, which reduced the hysteresis losses. The T_C shift for the iron-added alloy was reported already in 1997, by Pecharsky [165], but no hysteresis losses measurements were done. They observed that small amounts of impurities like some common 3d-elements (Fe, Co, Ni, Cu) as well as some common p-elements (C, Al) increase T_C, but have a negative effect on the magnetocaloric properties of the $Gd_5Ge_2Si_2$ parent, because of the suppression of the first order transformation. Only a small substitution of Si+Ge with Ga increased the T_C while keeping the first order transition.

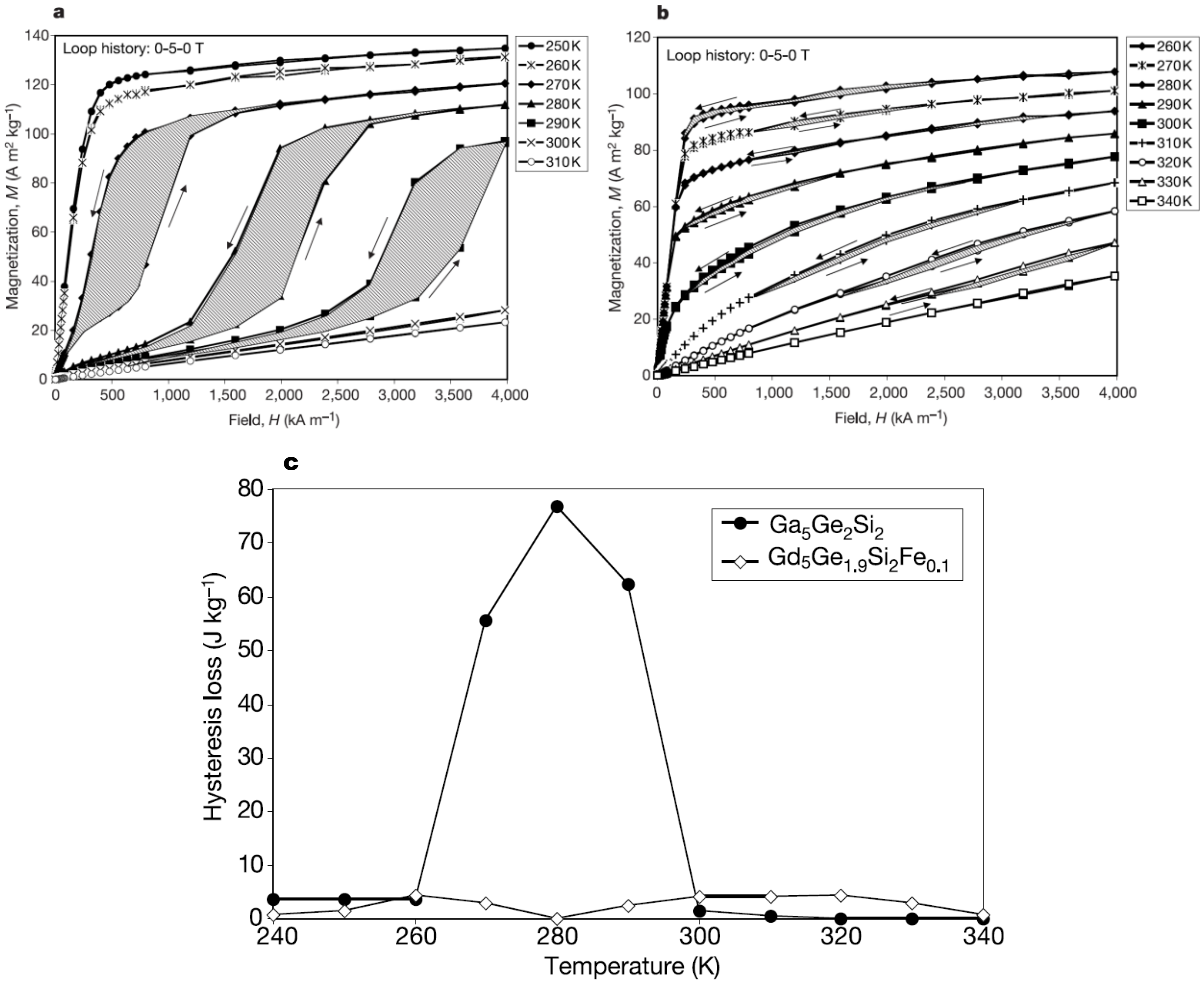

Figure 23: Magnetization versus field curves for the $Gd_5Ge_2Si_2$ compound between 250 K and 310 K (a) and for the $Gd_5Ge_{1.9}Si_2Fe_{0.1}$ alloy between 260 K and 340 K (b). The hysteresis losses are represented as hatched areas. By computing the hatched area inside each magnetization (*M*) versus field (*H*) the hysteretic losses were determined. (c) shows the comparison of hysteresis losses of the $Gd_5Ge_2Si_2$ (filled circles) and $Gd_5Ge_{1.9}Si_2Fe_{0.1}$ (open diamonds) alloys plotted as a function of temperature.

After the 2004 Provenzano report, many researchers published studies substituting with different elements. Shull et al. [166], for example, reported similar reductions in hysteresis losses with other elements (Co, Cu, Ga, Mn and Al), although no change was observed when substituting Bi or Sn. Y.H. Zhuang et al. [167] added Pb and found that the first-order structural/magnetic transition was preserved, which increased the T_C and the ΔS_M. T. Zhang et al. [168] investigated the thermal hysteresis and phase composition of $Gd_5Ge_2Si_2$ and $Gd_5Ge_{1.9}Si_2T_{0.1}$ (where T stands for Mn, Fe, Co or Ni) series of alloys. With the addition of Fe and Co, the alloys have a monoclinic $Gd_5Ge_2Si_2$-type and an orthorhombic Gd_5Si_4-type diphase structure. With Mn and Ni addition, only the orthorhombic Gd_5Si_4-type structure is observed. In all these cases the thermal hysteresis of $Gd_5Ge_2Si_2$ was significantly reduced. Also, Ga was observed to be homogenously distributed throughout the matrix and suppressed the structural transformation [169].

Zhang et al. melt spun $Gd_5Ge_{1.8}Si_{1.8}Sn_{0.4}$ and observed a reduction in the magnetic and thermal hysteresis [170]. The morphology and composition of the phases in a $Gd_5Ge_2Si_2$ alloy depend strongly on the solidification rate.

3 Experimental techniques

3.1 Sample synthesis

3.1.1 Chemical composition

We produced alloys with different substitutions of iron. All the samples were prepared from high-purity starting elements of gadolinium (99.99 wt.%), silicon (99.995 wt.%), germanium (99.999 wt.%) and iron (99.99 wt.%). We have to note that the purity of gadolinium refers to the weight percentage against other rare earths. This excludes interstitial impurities, primarily H, C, N and O, for which the content has not been additionally analyzed. All elements where purchased from the company PI-KEM, England, only Gadolinium was produced by the company LTS (Chemical) Inc., New York. The materials are bulk pieces with the size of a few millimeters. The compositions of the alloys are collected in Table 4, together with their respective sample codes; SI for silicon substitution, GE for germanium substitution and GESI for substituting equal amount of silicon and germanium. The number behind the letter represents the stohiometric amount of iron substitution. In the further text only the sample codes will be used to present a sample.

At the beginning we used different techniques to find out which of these is the most suitable for producing these alloys out of pure elements. Standard techniques like arc-melting and mechanical alloying where used as also more advanced methods like melt spinning.

Table 4: Composition of produced alloys

Silicon substitution (SI)

Alloy	**Sample code**	at.% Gd	at.% Si	at.% Ge	at.% Fe
$Gd_5Si_2Ge_2$	SI0	55.6	22.2	22.2	/
$Gd_5Si_{1.94}Ge_2Fe_{0.06}$	SI0.06	55.6	21.5	22.2	0.7
$Gd_5Si_{1.875}Ge_2Fe_{0.125}$	SI0.125	55.6	20.8	22.2	1.4
$Gd_5Si_{1.75}Ge_2Fe_{0.25}$	SI0.25	55.6	19.4	22.2	2.8
$Gd_5Si_{1.5}Ge_2Fe_{0.5}$	SI0.5	55.6	16.6	22.2	5.6
$Gd_5Si_{1.25}Ge_2Fe_{0.75}$	SI0.75	55.6	13.8	22.2	8.4
$Gd_5Si_1Ge_2Fe_1$	SI1	55.6	11.1	22.2	11.1

Germanium substitution (GE)

Alloy	**Sample code**	at.% Gd	at.% Si	at.% Ge	at.% Fe
$Gd_5Si_2Ge_2$	GE0	55.6	22.2	22.2	/
$Gd_5Si_2Ge_{1.94}Fe_{0.06}$	GE0.06	55.6	22.2	21.5	0.7
$Gd_5Si_2Ge_{1.875}Fe_{0.125}$	GE0.125	55.6	22.2	20.8	1.4
$Gd_5Si_2Ge_{1.75}Fe_{0.25}$	GE0.25	55.6	22.2	19.4	2.8
$Gd_5Si_2Ge_{1.5}Fe_{0.5}$	GE0.5	55.6	22.2	16.6	5.6
$Gd_5Si_2Ge_{1.25}Fe_{0.75}$	GE0.75	55.6	22.2	13.8	8.4
$Gd_5Si_2Ge_1Fe_1$	GE1	55.6	22.2	11.1	11.1

Germanium+Silicon substitution (GESI)

Alloy	Sample code	at.% Gd	at.% Si	at.% Ge	at.% Fe
$Gd_5Si_2Ge_2$	GESI0	55.6	22.2	22.2	/
$Gd_5Si_{1.97}Ge_{1.97}Fe_{0.06}$	GESI0.06	55.6	21.9	21.9	0.7
$Gd_5Si_{1.938}Ge_{1.938}Fe_{0.125}$	GESI0.125	55.6	21.5	21.5	1.4
$Gd_5Si_{1.875}Ge_{1.875}Fe_{0.25}$	GESI0.25	55.6	20.8	20.8	2.8
$Gd_5Si_{1.75}Ge_{1.75}Fe_{0.5}$	GESI0.5	55.6	19.4	19.4	5.6
$Gd_5Si_{1.625}Ge_{1.625}Fe_{0.75}$	GESI0.75	55.6	18.0	18.0	8.4
$Gd_5Si_{1.5}Ge_{1.5}Fe_1$	GESI1	55.6	16.6	16.6	11.1

3.1.2 Arc melting

This simple and effective method is mostly used for producing this kind of alloys. The process consists in melting pure elements of the alloy in a desired stohiometry by discharging an electric arc due to the application of a large tension between two electrodes. We used a commercially available Arc Melter from the company Edmund Bühler GmbH, Germany. The model MAM-1 with Arc Melting Generator H180T (Figure 24) has a high vacuum chamber with a volume of approximate 1.1 liter which enables it to be used to produce samples of small quantities up to 15 g in an extremely pure inert argon atmosphere. Argon acts also as the ionizing gas. The water cooled cathode, which is made out of tungsten to bear high temperatures without melting, is designed as a sharp rod and is integrated in the support frame of the chamber by means of a metal bellow so as to be movable and electrically isolated against the chamber. The bottom water-cooled copper base plate acts as the anode with incorporated crucible shapes. The pressure working range of the chamber is from 0 up to 1300 mbar. The melting current can be adjustable from 3-100 %, i.e. from 3-180 A. For the electric arc to from over the loading material at least one of the elements must be metallic (conductive). Depending on the loading material we can reach temperatures up to 4000 °C. [171]

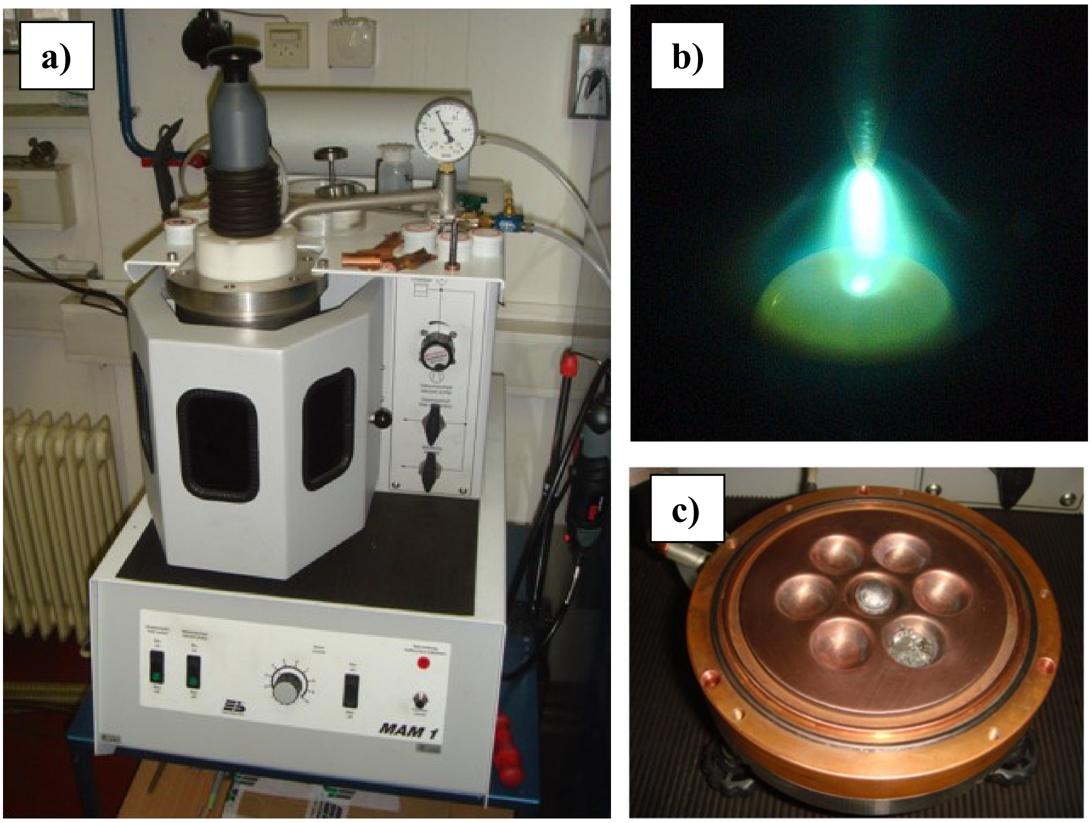

Figure 24: a) arc melter, b) electric arc, c) copper base plate

The carefully weighed elements are placed into the machined depressions of the chamber, which is then purged three times with argon and filled the last time up to 700 mbar. With the isolated knob handle at the upper end of the electrode we move the electrode tip in the vicinity of our sample (3 mm). With the activation of the current switch the arc is formed between the electrode and the sample. First we melt a piece of titanium to reduce the oxygen that has been left in the chamber after purging. Then we move the arc to our sample. After a few seconds the elements mix and the tension can be broken off. This process has to be repeated four times, with the sample being turned over each time in order to ensure the alloys homogeneity. After that the samples are weighed to ensure that no mass loss occurred during melting, because the process can be very fast, which can produce splats around the chamber thus reducing the initial mass.

It is easy to obtain many samples with this method. One drawback is that the cooling of the sample is not homogeneous after the melting, because the cooling at the bottom of the sample is faster than at the top. This gives very special facets on the surface (top) that differ from that on the bottom.

We produced samples with a mass of approximately 4g. Because the cooling rate has a pronoun effect on the sample we started our investigations by producing samples with different masses, from 1 to 5 grams, to investigate the effect of cooling (mass) on the sample structure.

3.1.3 Mechanical alloying

Mechanical alloying (MA) is a solid-state powder-processing technique involving repeated cold welding, fracturing, and re-welding of powder particles in a high-energy ball mill. The actual process of MA starts with mixing of the powders in the right proportion and loading the powder mix into the mill along with the grinding medium (generally steel balls). This mix is then milled for the desired length of time until a steady state is reached when the composition of every powder particle is the same as the proportion of the elements in the starting powder mix. The milled powder is then consolidated into a bulk shape and heat treated to obtain the desired microstructure and properties. For this we used a planetary mill. The planetary ball mill owes its name to the planet-like movement of its vials. These are arranged on a rotating support disk and a special drive mechanism causes them to rotate around their own axes. The centrifugal force produced by the vials rotating around their own axes and that produced by the rotating support disk both act on the vial contents, consisting of material to be ground and the grinding balls. [172]

For our investigation we used a Pulverisette 5 from the company Fritsch. The vial is filled with the starting elements of the desired stohiometry and with grinding balls occupying 1/3 of the volume of the vial. The material is then milled for 40 hours and taken out of the vial.

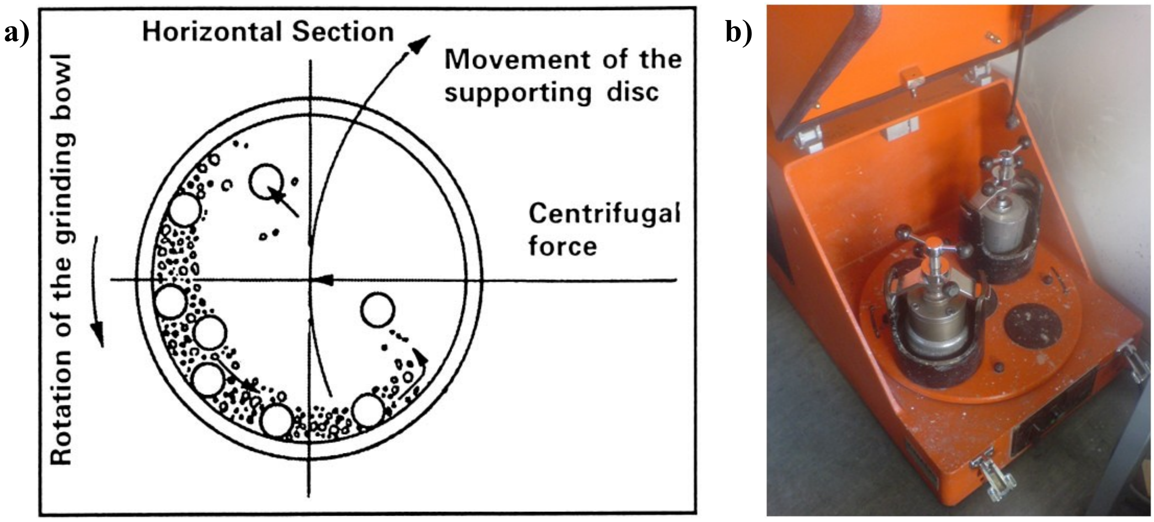

Figure 25: a) Schematic description of the ball movement inside the ball mill, b) Pulverisette 5 ball mill.

3.1.4 Melt spinning

Melt spinning (MS) is a technique used for rapid cooling of liquids. A jet of molten metal is propelled against the moving surface of a cold, rotating copper cylinder. The fast cooling causes rapid solidification. A solid film of metallic glass is spun off as a continuous ribbon at a speed that can exceed a kilometer per minute. This technique is used to develop materials that require extremely high cooling rates in order to form, such as metallic glasses. The cooling rates achievable by melt-spinning are on the order of 10^4–10^7 Kelvin per second (K/s).

We used a melt spinner from the company Edmund Bühler GmbH, Germany, version SC, complete with built-in high-vacuum pumping system and RF generator HIT 6. In this type of melt spinner the sample is in a crucible which is induction heated up to the melting point of the alloy. For the induction to work the material or the crucible in the coil must be conductive. Temperatures up to 2000 °C can be achieved depending on the material that we are heating and the type of crucible. The temperature is monitored with a pyrometer from 900 °C upwards. The melt is then pushed with overpressure onto the copper wheel from which the solidified ribbons are collected in a long tube. The process happens in an inert atmosphere, which can be Ar, N_2 or He. The crucible can be made out of glass, born-nitride or graphite. Glass is the cheapest for temperatures up to 1300 °C. For higher temperatures graphite is used. The problem with graphite is that it can contaminate the sample. This can be prevented if we use boron-nitride crucibles, but they are expensive. There are many factors that influence the properties of the produced ribbons: the shape of the crucible nozzle, the distance of the nozzle from the wheel, the pressure with which the molt is propelled onto the wheel, the shape of the wheel and the atmosphere in the chamber. The most critical parameter is the wheel speed. This can be varied from 10 to 80 Hz. The faster the wheel, the faster the molt is cooled. With this we can control the crystallinity of the alloy, from nano-crystalline to amorphous alloys. The starting material has to be in a bulk form. That is why the alloy is previously arc-melted with the same procedure as previously described.

For our experiment two buttons with the total weight of approximately 8 g are put into a graphite crucible and mounted into the induction heater. The chamber is evacuated to a pressure of $1\text{x}10^{-5}$ mbar and refilled up to 800 mbar. The wheel speed is set to 20 Hz. The heating power is slowly increased up to the temperature 1850 °C. At that point pressure from a storage vessel, which was previously filled with 1 bar, is released into the crucible pushing the molt onto the copper wheel. The process takes less than a second. Everything is shut down and we wait for it to cool down.

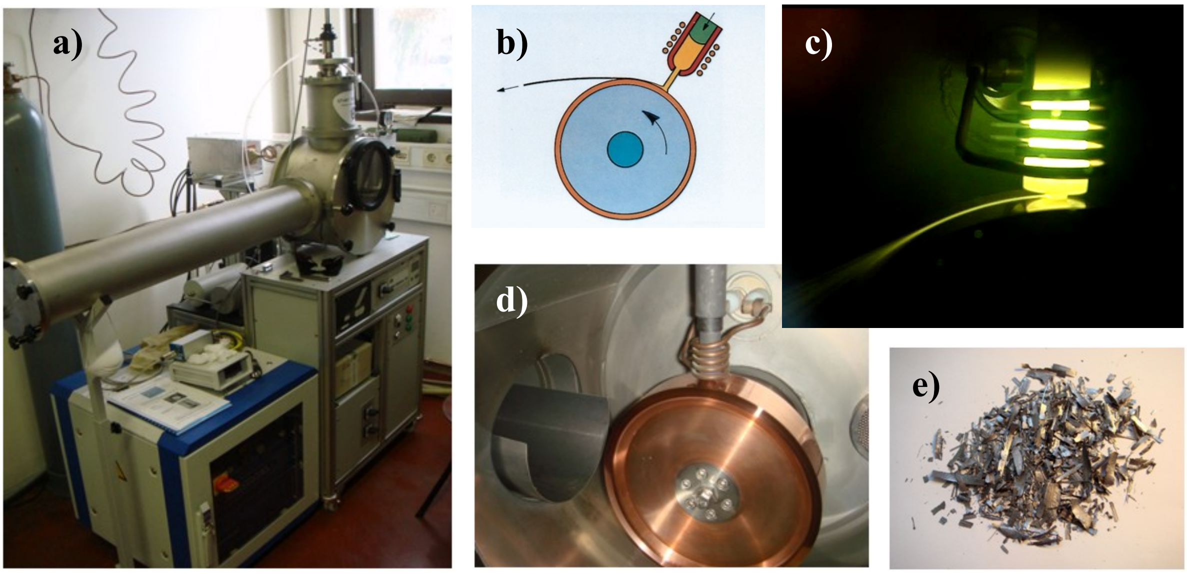

Figure 26: a) melt spinner, b) schematic draw of the spin, c) live melt spin, d) copper wheel with the crucible on top of it and the induction coil, e) melt spun flackes.

3.1.5 Heat treatment

To reduce the amount of secondary phase we heat treated (HT) the sample after one of the previous synthesis methods. The samples were sealed in a quartz tube under argon atmosphere. The pressure in the tube is kept 50 % lower than that of the surrounding atmosphere to ensure that the pressure increase because of the heat treatment would not damage the quartz tube. For the heat treatment a tube furnace from the company Carbolite is used. It used resistance heaters around an Al_2O_3 tube. The heating speed is 20 °C per minute up to 1300 °C where it is kept for 4 hours. The parameters are taken from Pecharsky's paper from 2003 [55]. After that the furnace is turned off and we wait for it to cool down. Then we break the tube and remove the sample.

3.2 Sample characterization

3.2.1 X-ray diffraction

X-ray Diffraction (Powder XRD) is perhaps the most widely used technique for characterizing materials. Because the wavelength of x-rays is comparable to the size of atoms, they are ideally suited for probing the structural arrangement of atoms and molecules in a wide range of materials. X-rays are produced generally by x-ray tubes. X-rays are generated when a focused electron beam accelerated across a high voltage field bombards a stationary or rotating solid target. The high energy electrons eject inner shell electrons in atoms through the ionization process. When a free electron fills the shell, an x-ray photon with energy characteristic of the target material is emitted. Common targets used in x-ray tubes include Cu and Mo, which emit 8 keV and 14 keV x-rays with corresponding wavelengths of 1.541 Å and 0.709 Å, respectively.

X-rays primarily interact with electrons in atoms. When x-ray photons collide with electrons, some photons from the incident beam will be deflected away from the direction where they originally travel, much like billiard balls bouncing off one another. If the wavelength of these scattered x-rays did not change (meaning that x-ray photons did not lose any energy), the process is called elastic scattering (Thompson Scattering) in that only *momentum* has been transferred in the scattering process. These are the x-rays that we measure in diffraction experiments, as the scattered x-rays carry information about the electron distribution in materials.

If the atoms are arranged in a periodic fashion, as in crystals, the diffracted waves will consist of sharp interference maxima (peaks) with the same symmetry as in the distribution of atoms. Measuring the diffraction pattern therefore allows us to deduce the distribution of atoms in a material. For the diffraction to occur Bragg's Law must be fulfilled. In crystalline solids the X-rays are scattered from lattice planes separated by the interplanar distance d. Where the scattered waves interfere constructively; they remain in phase since the path length of each wave is equal to an integer multiple of the wavelength. The path difference between two waves undergoing constructive interference is given by $2d\sin\theta$, where θ is the scattering angle. This leads to Bragg's law which describes the condition for constructive interference from successive crystallographic planes (h,k,l) of the crystalline lattice:

$$n\lambda = 2d\sin\vartheta\,, \tag{46}$$

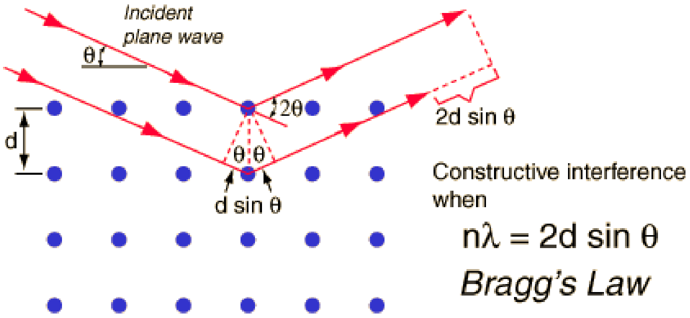

Figure 27: Interference of X-rays, scattered on crystal planes.

where n is an integer determined by the order given, and λ is the wavelength. A diffraction pattern is obtained by measuring the intensity of scattered waves as a function of scattering angle. Very strong intensities known as Bragg peaks are obtained in the diffraction pattern when scattered waves satisfy the Bragg condition. Powder diffraction data can be collected using either transmission or reflection geometry, as shown below. Because the particles in the powder sample are randomly oriented, these two methods will yield the same data.

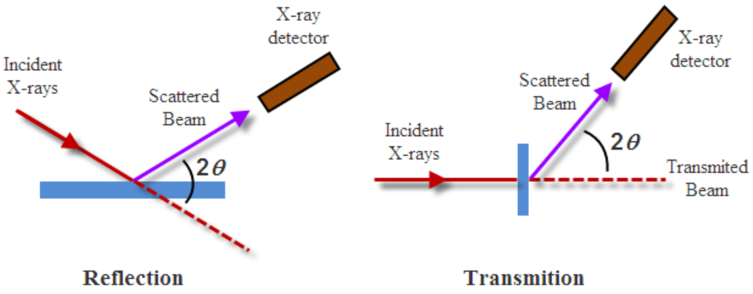

Figure 28: Different diffractometer systems.

For our investigations we used a Bruker AXS, D4 Endeavor spectrometer with Cu-Kα radiation in the range from 15 to 60 degrees and a Panalytical X'Pert PRO diffractometer with Co-Kα radiation in the range from 20 to 80 degrees. Both systems use the refection geometry data collection. The samples were crushed in a mortar and the powder was sieved with a 40 µm sieve to get a average diffraction pattern from all planes.

For the low temperature X-ray Diffraction we used a Transmission/Debye-Scherrer STOE diffractometer with Mo-Kα radiation in the range from 5 to 40 degrees. The sample was powderized and diluted with amorphous glass at a ratio of 1 to 10 and sealed in a capillary. Glass was added because Gd absorbs most of the radiation. The sample was cooled with a “cold finger” which blows under cooled nitrogen onto the sample. With this we could achieve temperatures down to 100 K.

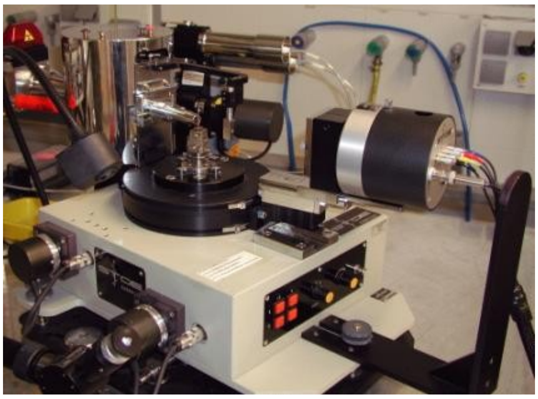

Figure 29: STOE diffractometer.

3.2.2 Scanning Electron Microscopy (SEM)

The SEM is a high-powered indirect microscope that produces an image by bombarding a sample with a beam of high-energy electrons. The electrons emitted from the sample are then scanned to form a magnified image which allows the examination of the structure, relief, and morphology of materials between 20× and 1 000 000× magnification. The types of signals produced by an SEM include secondary electrons (SE), back scattered electrons (BSE), characteristic x-rays, light (cathodoluminescence), specimen current and transmitted electrons. In the most common or standard detection mode, secondary electron imaging or SEI, the SEM can produce very high-resolution images of a sample surface, revealing details about less than 1 to 5 nm in size. Generation of secondary electrons depends strongly on the topography. Due to their low energy of ~5 eV, only the secondary electrons that are created near to the surface (10 nm) can leave the sample and be collected. Any change in topography of the sample that is larger than this sampling depth will change the collection efficiency. Collection of these electrons is made by a collector in combination with a secondary electron detector. The collector is a mesh with a +100V potential applied to it which is placed in front of the detector, attracting the negatively charged secondary electrons. The electrons then pass through the grid-holes into the detector to be counted. For each point on the studied area the microscope counts the number of secondary electrons reaching the detector and displays it as a pixel on a picture or display. The pixel intensity is determined by the number of the counted electrons. This process can be repeated in a scanning mode, e.g. 30 times per second, thus obtaining a

Scanning/Secondary Electron Microscope (SEM) picture of the investigated area. Back-scattered electrons (BSE) are beam electrons that are reflected from the sample by inelastic scattering. BSE are often used in analytical SEM along with the energy-dispersive X-ray spectrometer (EDS). Because the intensity of the BSE signal is strongly related to the atomic number (Z) of the specimen, BSE images can provide information about the distribution of different elements in the sample. Characteristic X-rays are emitted when the electron beam interacts with an inner shell electron from the sample, causing a higher-energy electron to fill the shell and release energy. These characteristic X-rays are used to identify the composition and measure the abundance of elements in the sample.

For our investigations we used a Jeol JSM 5800 with a SE-BSE detector, Oxford instruments ISIS 300 and an EDXS detector. For this instrument the sample was fixed in a metallographic specimen with Technovit resin and polished to achieve a flat surface which is needed to get phase contrast. After that the sample in the resin is fixed on a SEM holder and sputtered with graphite to achieve conductivity. The sample was then placed in the vacuum column and evacuated. The high voltage was set to 20 kV and the aperture of the column to 100 μm. After the sample was moved from the initial position to the central position, we check the spot size of the beam and the working distance. When we achieved a vacuum better 5×10^{-4} mbar we switched on the high-voltage and start working. For EDXS analysis we set the working distance to 10 mm to achieve the best results. For observation of non-polished samples, like powder and melt spun ribbons, the sample was placed on conductive sticky tape impregnated with graphite powder and placed on the sample holder

Figure 30: Jeol JSM 5800 scanning electron microscope.

3.2.3 Transmission electron microscopy (TEM)

Transmission electron microscopy uses the same technique as the SEM, only here we use an electron-transparent sample which is bombarded with an electron beam and the intensity of the transmitted electrons which is determined by scattering phenomena (electron absorption phenomena) in the interior of the sample is recorded. A magnified image is formed using a set of lenses. This image is projected onto a fluorescent screen or a CCD camera. The TEM allows for a resolution of 0.2 nm with which atomic arrangements in crystalline structures can be imaged in large detail. As in the SEM, the image contrast is obtained by interaction of the electron beam with the sample. Several contrast effects play a role. In the resulting TEM image denser areas and areas containing heavier elements appear darker due to scattering of the electrons in the sample. In addition, scattering from crystal planes introduces diffraction contrast. This contrast depends on the orientation of a crystalline area in the sample with respect to the electron beam. As a result, in a TEM image of a sample consisting of randomly oriented crystals each crystal will have its own grey-level. In this way one can distinguish between different materials, as well as image individual crystals and crystal defects. The electron diffraction can provide crystallographic information from thin films, bulk materials as well as from nanometer sized particles. The combination of Scanning TEM (STEM), a mode in which this narrow beam scans a selected area of the specimen, with chemical analysis techniques such as Electron

Energy Loss Spectroscopy (EELS) and Energy Dispersive X-Ray analysis (EDX) allows for mapping of the lateral distribution of elements with high spatial resolution. The STEM is more flexible then TEM, because you can control L, which changes the collection angle of the detector. In this way we can control which electrons contribute to the image. They can enhance the contrast, but show poorer resolution. To get a reasonable intensity in a scanning image we have to use a larger beam.

To prepare an electron-transparent sample the sample is first cut into a few millimeter slice. Then a disk with a diameter of 3mm is cut out of this slice with a ultra sonic cuter. This 3 mm disk is than polished from both sides to a thickness of 120 µm with a disk grinder. Then the sample is mounted on a dimple grinder, where a copper disk is grinding the sample to a thickness of 20 µm. With such a sample we used an argon ion-mill (RES 010, Bal-Tec AG, Balzers, Liechtenstein) and etch it with 6 keV Ar^+ ions at an incidence angle of 10° until perforation of the disk in central area.

TEM analysis (selected-area electron diffraction and bright-field imaging) was made with a Jeol JEM-2010 F (Jeol Ltd., Tokyo, Japan) at 200 kV accelerating voltage. This microscope is a field emission gun microscope with a STEM unit, bright field-dark filed detector, a Gatan PEELS 677 and a Gatan off-axis TC camera.

Figure 31: Jeol JEM-2010 F transmission electron microscope.

3.2.4 Vibrating sample magnetometer (VSM)

The vibrating sample magnetometer is the most common used for measuring magnetic materials. This experimental technique was invented in 1956 by Simon Foner, a scientist of the MIT. It has a flexible design and combines high sensitivity with easy of sample mounting and exchange. Samples may be interchange rapidly even at any operating temperature. Measurements of magnetic moments as small as $5x10^{-5}$ emu are possible. Maximum applied fields of 2-3 Tesla or 9 Tesla are reached using conventional laboratory electromagnets and superconducting solenoids, respectively. Vibrating sample magnetometers normally operate over a temperature range of 2.0 to 1050 K. Powders, bulk and thin films can be measured and studied.

If a sample of any material is placed in a uniform magnetic field, created between the poles of a electromagnet, a dipole moment will be induced. If the sample vibrates with sinusoidal motion a sinusoidal electrical signal can be induced in suitable placed pick-up coils. The signal has the same frequency of vibration and its amplitude will be proportional to the magnetic moment, amplitude, and relative position with respect to the pick-up coils system.

The sample is fixed to a small sample holder located at the end of a sample rod mounted in a electromechanical transducer. The transducer is driven by a power amplifier which itself is driven by an oscillator at a frequency of 90 Hertz and the sample vibrates along the Z axis perpendicular to the magnetizing field. The latter induced a signal in the pick-up coil system that is fed to a differential amplifier. The output of the differential amplifier is subsequently fed into a tuned amplifier and an internal lock-in amplifier that receives a reference signal supplied by the oscillator. The output of this lock-in amplifier, or the output of the magnetometer itself, is a DC signal proportional to the magnetic moment of the sample being studied. The electromechanical transducer can move along X, Y and Z directions in order to find the saddle point (which calibration of the vibrating sample magnetometer is done by measuring the signal of a pure Ni standard of known the saturation magnetic moment placed in the saddle point).

Using a vibrating sample magnetometer one can measure the DC magnetic moment as a function of temperature, magnetic field, angle and time. So, it allows performing susceptibility and magnetization studies. Some of the most common measurements done are: hysteresis loops, susceptibility or saturation magnetization as a function of temperature (thermo-magnetic analysis), magnetization curves as a function as a function of angle (anisotropy), and magnetization as a function of time.

We use a VSM model 7303, with a cryostat attached, from the company Lake Shore Cryotronics, Inc. With it we can achieve field from -1.4 to 1.4 Tesla and reach temperatures down to 7 K. The cryostat operates with a closed liquid helium circuit. The samples are mounted on a plastic sample holder and positioned in the VSM. We did thermo magnetic measurements to determine the magnetic transition temperature and hysteresis loops at different temperatures to calculate the magnetic entropy change.

3.2.5 Physical property measurement system (PPMS)

The PPMS is an open architecture, variable temperature-field system that is optimized to perform a variety of automated measurements. Sample environment controls include fields up to ± 16 Tesla and temperature range of 1.9 - 400 K. The PPMS has integrated applications for heat capacity, magnetometry, electro-transport and thermal transport. To achieve these high fields the PPMS uses a superconducting magnet. A superconducting magnet is a solenoid made of superconducting wire. This solenoid must be kept at liquid helium temperature in a liquid-helium dewar. The uniform magnetic field is produced along the axial cylindrical bore of the coil. Currently, superconducting solenoids that produce magnetic fields in the range 5-18 Tesla are commercially available. To operate a superconducting magnet requires an appropriate programmable bipolar power supply. To control the temperature, a vacuum pump draws helium into the annular region where heaters warm the gas to the correct temperature. This design reduces thermal gradients and increases system flexibility by making the sample chamber a controllable environment. For example, the sealed sample chamber may hold a high vacuum without the need for additional inserts. This is significant for the design of the Heat Capacity.

Figure 32: Physical property measurement system. Left is the liquid helium tank with the superconducting magnet and right is the controller. [173]

3.2.5.1 VSM unit

The PPMS uses a model P525 vibrating sample magnetometer (VSM) measurement system, which is a fully automated DC magnetometer. The VSM detection coil is inserted into the PPMS sample chamber by using the standard PPMS sample interface design. Unlike other vibrating sample magnetometers that use a short-throw resonant voice-coil design, the PPMS VSM linear motor is designed to operate at 40 Hz, with rapid slewing possible over about 6.5 cm of travel. The large range of motion enables the PPMS VSM system to perform rapid, completely automated centering operations. The system is able to resolve magnetization changes of less than 10^{-6} emu at a data rate of 1 Hz. The sample holder can be a brass half tube with a diameter of 3.6 mm, or fused quartz paddle with a diameter of 4 mm. The sample mass should be less than 1 gram. The VSM can use the same environments then the PPMS.

For our measurements we used a brass half tube on which we glued our sample. We conducted the same experiments then in the VSM, but with higher fields.

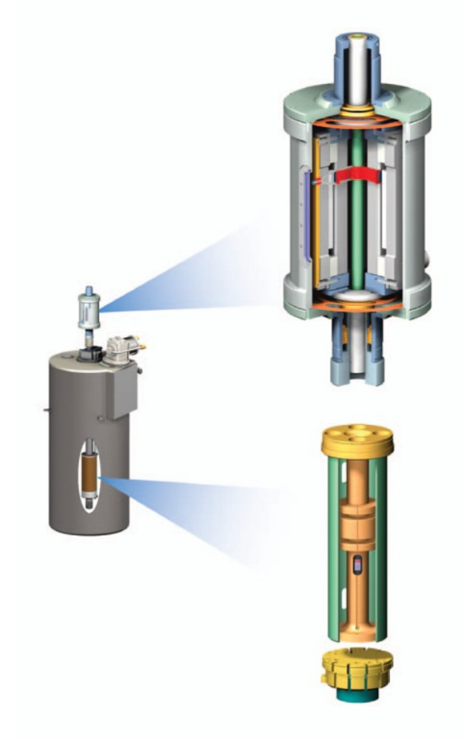

Figure 33: Vibrating sample magnetometer for the PPMS. The upper part shows the long-throw linear motor sample drive and the lower part the “sample puck” mounted detection coilset.

3.2.6 Direct adiabatic temperature measuring unit

Direct measurements of the adiabatic temperature change ΔT_{ad} were performed in a modified Magnetocaloric Measuring Setup (MMS) which is produced by Advanced Magnetic Technologies and Consulting, Ltd. (AMTC). The modification where performed by the Leibniz Institute for Solid State and Materials Research Dresden by the supervision of Dr. Konstantin Skokov. The modifications improved the accuracy of the measurements and faster data acquirement. A schematic of the setup can be seen in Figure 34. The magnetic field was produced by the permanent magnet magnetic field source on the basis of a Halbach cylinder structure. The maximum field in a bore centre was $\mu_0 H = 1.93$ T. Magnetic field change rate was 2 T/s what allow to prevent heat losses from the specimen during the measurement. The temperature of the sample was monitored with accuracy better than ± 0.02 K by a Copper-Constantan thermocouple which was in direct contact with the sample. For the best thermal contact between a reference junction of thermocouple and the specimen the junction was squeezed between two pieces of the sample. Also small amount of silver thermoconductive paste was added on junction of the thermocouple for improving thermal contact. Specimen was fixed on nylon threads for ensuring adiabatic conditions. For the same reason all measurements were performed in high vacuum. Also adiabatic screen was used in order to decrease the radiative heat exchange between the sample and sample holder. An image of the sample holder can be seen in Figure 35. The external magnetic field was measured by a Hall probe. After pre-amplification, both signals, from thermocouple and Hall probe were collected using analogue digital convertor (ADS). ADS time resolution was 1000 points/s and allowed to observe the adiabatic temperature change carefully and unequivocally. During the measurements, the target temperature was approached without overheating/overcooling.

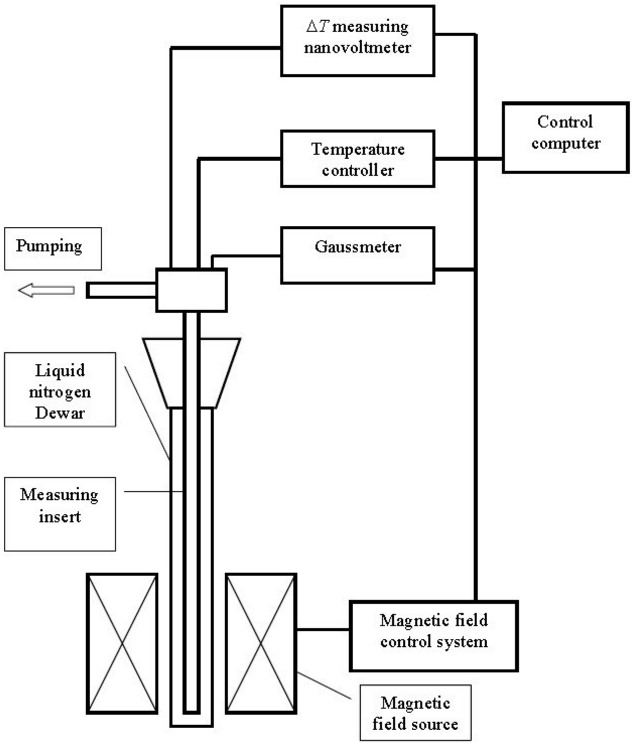

Figure 34: Schematic diagram of the MMS. [174]

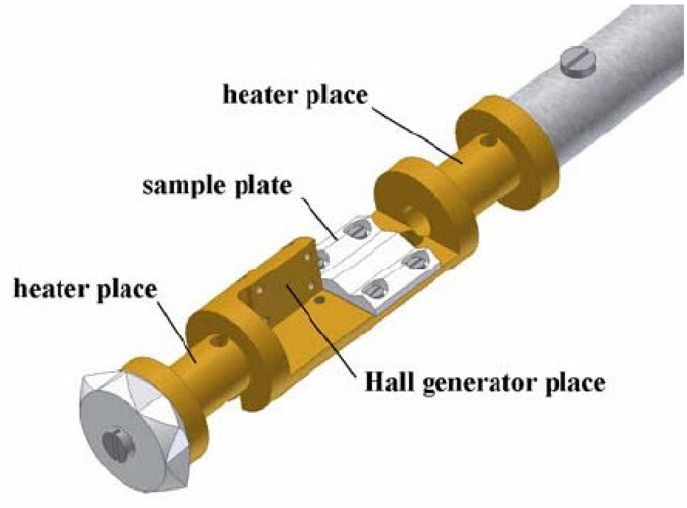

Figure 35: Schematic picture of the sample holder (temperature sensor, Hall generator, thermocouple and heaters are not shown).

4 Results and discussion

4.1 $Gd_5Si_2Ge_2$

4.1.1 Arc-melting

In this section the effect of different cooling rates of the arc melted buttons after the arc is turned off and the effect of heat treatment, are presented. We compared different masses of buttons, with the same composition, which cooled down differently, from the 1g button which cooled down the fastest to the 5 g button which cooled down the slowest. The synthesized buttons were first examined using scanning electron microscopy to reveal the effect of the cooling rate on both the macrostructure (Figure 36) and the microstructure (Figure 37).

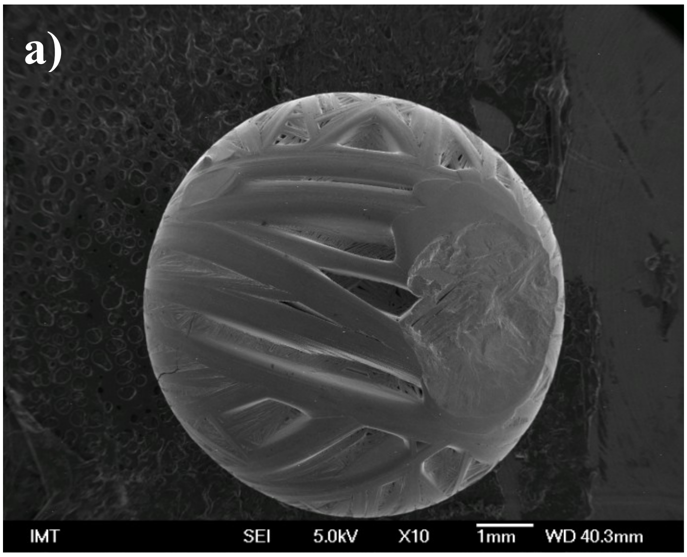

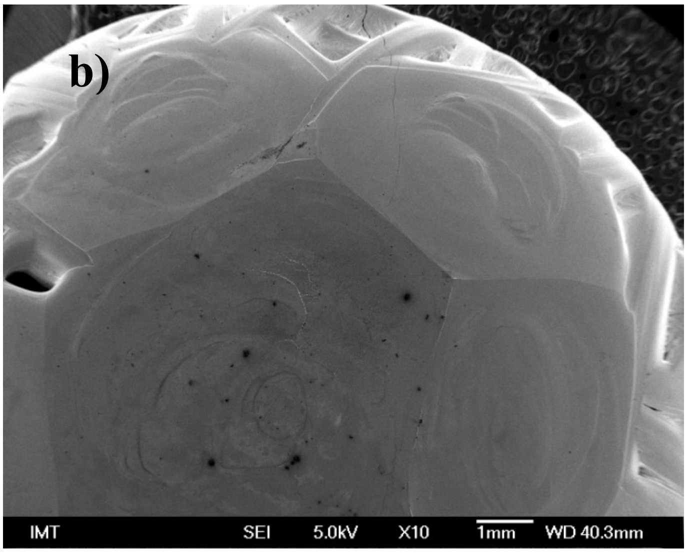

Figure 36: Macrostructure of the $Gd_5Ge_2Si_2$ alloy button in the as-cast state: (a) 1 g of charge material and (b) 5 g of charge material.

It is obvious from Figure 36 that the cooling rate, which is higher in the case of the 1 g sample, has a profound effect on the macrostructure, with the formation of a “sinew” effect on the upper surface of the button (Figure 36 a). This feature is all but absent in the 5 g sample (Figure 36 b). The 5 g sample has a smoother surface consisting of fairly regular pentagons and hexagons (reminiscent of the Fullerene structure) that is typical for the crystallization of semi-conducting elements, such as silicon and germanium (often referred to as half metals) when moderate cooling rates are present. The metals, on the other hand, tend to form a curvaceous crystallization front because of the small difference in the melting entropy. This is not the case with silicon and germanium, both of which have large melting entropies, leading to the formation of facets during the process of crystallization. The comparison of the microstructure of the sample with the highest cooling rate (Figure 37 a) and the sample with the lowest cooling rate (Figure 37 b) reveals that in both cases the as-cast state provides us with at least three phases, with the dendritic phase being the dominant one.

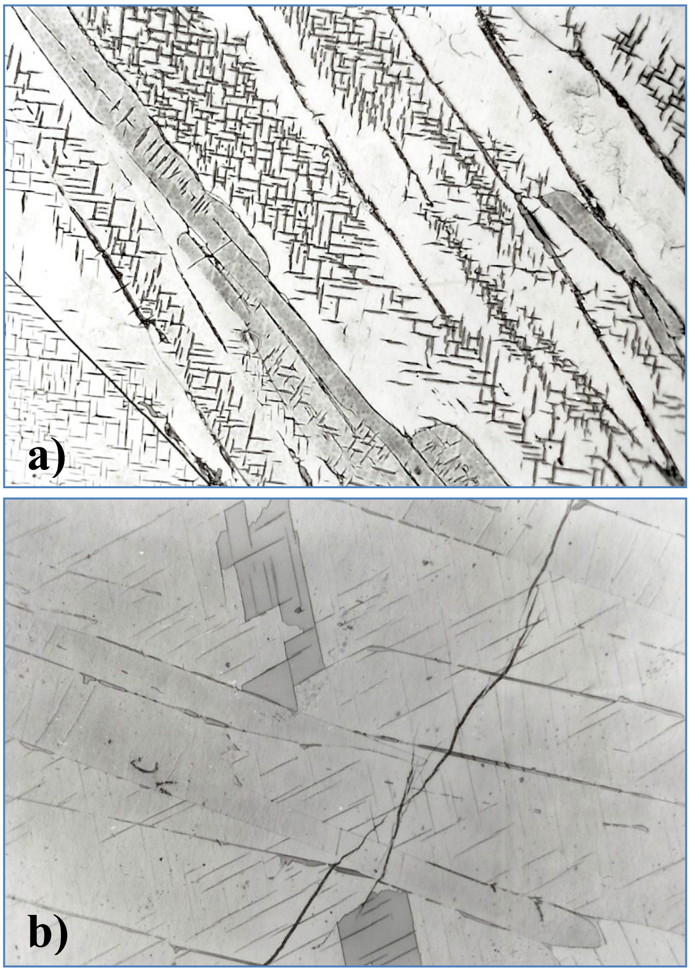

Figure 37: Optical micrographs of the microstructure of the $Gd_5Ge_2Si_2$ alloy in as-cast state: (a) 1 g of charge material and (b) 5 g of charge material.

This phase also contains small needle like precipitates that lie within the dendrites at an angle of 90º and cca. 75º to each other. The precipitates form in a manner indicative of a Widmanstätten structure, as seen in previous reports. The interdendritic space is filled with a third phase, which is rich in Gd and Si. The dendritic phase exhibits different shade effects because of the differences in the orientation of individual dendrites towards the sample surface, so that they produce the so-called orientation contrast.

The number of phases revealed by the optical microscope is also confirmed by the SEM and EDS (Figure 38), which shows that the dendritic phase has 22.9 at.% Si, 21.0 at.% Ge and 56.1 at.% Gd, the interdendritic phase has 31.6 at.% Si,17.5 at.% Ge and 50.9 at.% Gd and the precipitated phase has composition of 17.3 at.% Si, 21.9 at.% Ge and 60.8 at.% Gd. This indicates that the precipitates are the 5:3 phase that was also found by Meyers et al. [159]. These features disappear after the heat treatment. The x-ray spectra of the as-cast 1 g and 5 g samples are the same. Although there may be significant microstructural differences between the two samples the crystal structure of the main phase is the same for both samples. The x-ray diffraction pattern of the as-cast 5 g button is shown in Figure 39a together with the calculated spectrum for the Gd_5Si_4 structure. This Gd_5Si_4-based solid solution allows Ge to substitute for Si in the range $0.5 \leq x \leq 1.0$. On the other hand, the Gd_5Ge_4 solid solution extends from $0 \leq x \leq 0.2$. If we compare the two spectra, the experimentally obtained spectrum and the calculated spectrum, it is clear that they represent a good fit, albeit with a slight shift to higher angles, which is increasingly obvious to the right-hand side of the graph. This shift is due to the substitution of approximately 50% of the Si atoms by Ge atoms, and is in line with the observations of Pecharsky and Gschneidner [36]. However, after heat treating the material at 1300°C for one hour a change in crystal structure is observed (Figure 38b). Here we observe the monoclinically distorted derivative of the orthorhombic Sm_5Ge_4-type phase, which we refer to in the figure as the $Gd_5Ge_2Si_2$ structure. It is believed that the heat treatment for 1 hour at 1300°C results in some phase purification and homogenization of the arc-melted buttons, leading to a partial ordering of the crystal structure via a redistribution of Si and Ge atoms among the various crystallographic sites. The annealing causes an enrichment of Ge for the sites responsible for the interslab bonding, thereby resulting in a considerable enhancement of the giant magnetocaloric effect.

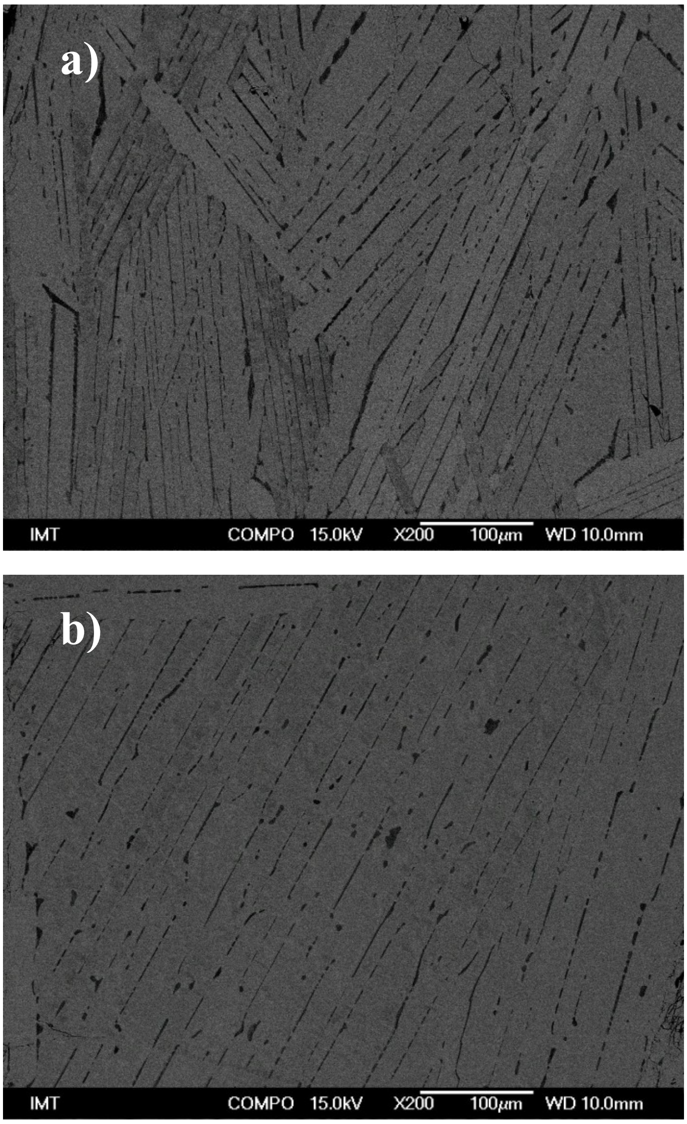

Figure 38: SEM micrographs of the microstructure of the $Gd_5Ge_2Si_2$ alloy in as synthesized state: (a) 1 g of charge material and (b) 5 g of charge material.

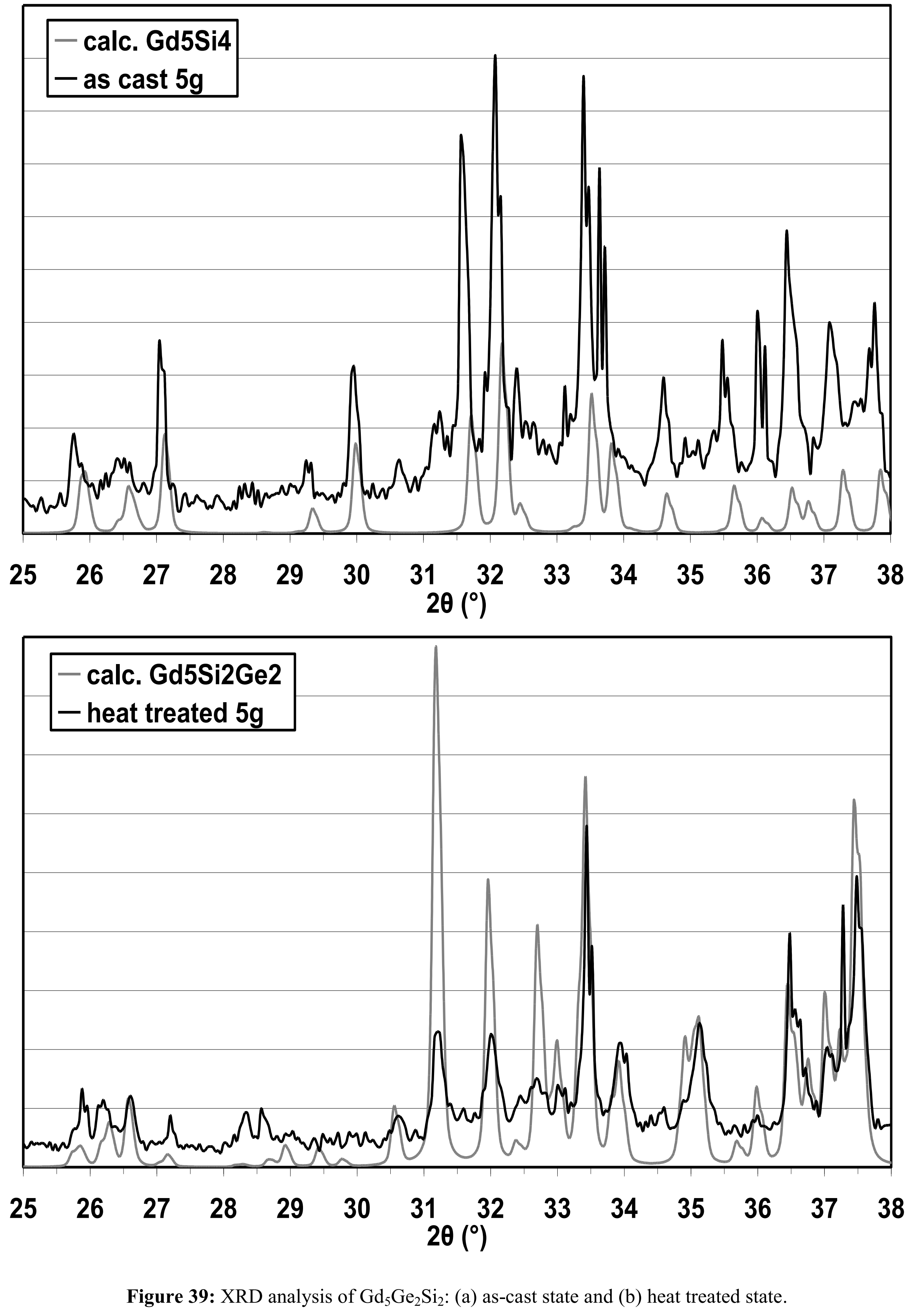

Figure 39: XRD analysis of $Gd_5Ge_2Si_2$: (a) as-cast state and (b) heat treated state.

From Figure 40 we can see that after the heat treatment at 1300 ºC we get a largely single-phase alloy with the composition very close to $Gd_5Ge_2Si_2$.

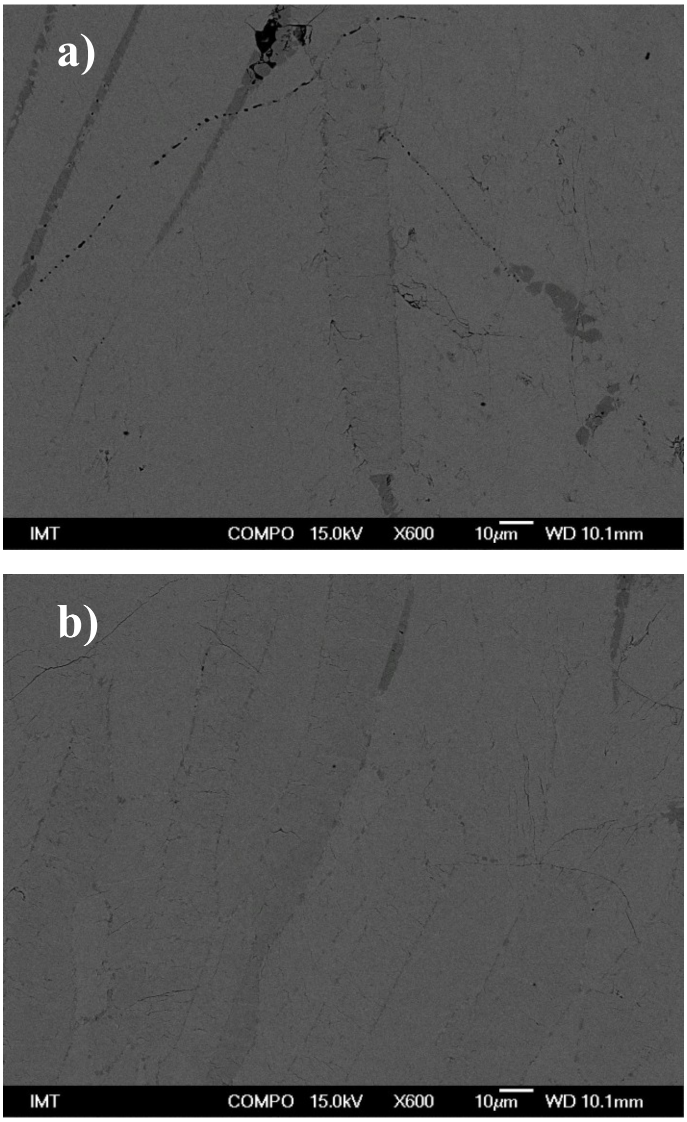

Figure 40: SEM micrograph of the microstructure of the $Gd_5Ge_2Si_2$ alloy in heat treated state: (a) 1 g of charge material and (b) 5 g of charge material.

The variations in the mass of the initial charge of material effectively influenced the cooling rate, causing marked effects on the surface of the buttons, producing a sinew appearance at fast cooling rates, which disappears as the mass of buttons increases towards 5 g. The crystal structures of the main phases in the buttons were found to be largely independent of mass, and therefore of cooling, rate, and a heat treatment at 1300°C for one hour was sufficient to produce the single-phase crystal structure.

4.1.2 Mechanical alloying

The direct method of mechanical alloying $Gd_5Si_2Ge_2$ from pure elements has proven to be very time consuming and uneconomical, because of the ductile nature of gadolinium. In our system we have one ductile component and two brittle components, germanium and silicon. For alloying to occur we have to have at least one ductile component, but the milling time also plays an important factor.

In the initial stage of milling, the ductile gadolinium particles get flattened by the ball-particle-ball collision, while the brittle intermetallic particles get fragmented. These fragmented brittle particles tend to become occluded by the ductile constituents and trapped in the ductile particles. The brittle constituent is closely spaced along the interlamellar spacings. With further milling, the ductile powder particles get work hardened, the lamellae get convoluted, and refined. But this method is very time consuming and even after 100 h of milling we did not achieve chemical homogeneity. Particles were still of different sizes, with flat gadolinium particles and fine-milled silicon and germanium. For alloying to occur between these three elements longer times would be necessary, which resulted into abandoning this method, because of the time factor.

For mechanical alloying to be feasible we would have to start milling already with the alloy and not with the pure elements. But this is not mechanical alloying anymore, because we have only one component. With this method we produce amorphous powder which after heat treatment would be more homogeneous than the starting alloy. This is also the method used when milling gadolinium based alloys.

4.1.3 Melt spinning

Melt spinning $Gd_5Si_2Ge_2$ has proven to be a very difficult task. The first problem was that one cannot start with pure elements, but already with arc-melted buttons. This introduces the same technical problems that occur when arc-melting, like stoichiometry problems. Because we have to start with the alloy, we have to produce higher temperatures for melting than with pure elements. The regular used crucibles for melt spinning proved to be not suitable. These are made out of boron-nitride and are usually very suitable if we do not want to contaminate our sample, but they are not suitable for melting $Gd_5Si_2Ge_2$, because the induction heater heats only the sample and not the non-conductive boron-nitride holder. This does not provide enough heat to melt the sample, even at full power of the melt spinner. Even at longer heating times we could not extract the melt out of the crucible on to the spinning copper wheel. To overcome this problem, we used graphite crucibles which are also conductive and heat up in an induction heater, thus helping to achieve the desired temperature for melting the alloy. In our case this temperature was over 1800 °C. The melt could be easily ejected and melt spun. We produced nice ribbons with sizes up to 5 cm which are shown in Figure 41.

Figure 41: Melt spun ribbons from a graphite crucible.

The melt spun ribbons have a metallic look and are very stable in the air. But in the XRD spectrum no $Gd_5Si_2Ge_2$ could be found. The only spectrum that fitted was $Gd_3Si_2C_2$. This led to the conclusion that the graphite from the crucible reacted with the alloy and transformed it. A closer look at the crucible also showed that graphite has been "etched" away where the melt was (Figure 42a). After the melt spinning some of the melt always stays on the crucible and is very hard to grind off (Figure 42b). But leaving it in the air for a few days turns it into powder, as seen in Figure 42c. A later analysis showed that it oxidizes into Gd_2O_3. But the ribbons with the same composition stay intact. This can be explained with a thin amorphous layer that forms on the ribbons surface, thus preventing oxidation.

To produce $Gd_5Si_2Ge_2$ melt spun ribbons, we had to make a crucible that incorporates the non reactivity of boron-nitride and the conductivity of graphite. We produced a crucible that had an inner shell of boron-nitride and an outer shell of graphite. The two materials have different expansion coefficients. This can produce problems about how to combine the two materials so that they do not interact on each other. The design of such a crucible is shown in Figure 43. After melt spinning in such a crucible the XRD did not show any $Gd_3Si_2C_2$, but it also did not show the desired $Gd_5Si_2Ge_2$. The XRD showed a mixture of the 1:1 phase, the 5:3 phase, some 5:4 phase and some other phases that we could not identify. The main reason for using melt spinning as a production technique is the ability to produce an amorphous phase because of the fast cooling of the melt. We also did not succeed to produce an amorphous phase, not even at the highest wheel speed of the melt spinner of 80 Hz. Because of this the technique has no advantages against arc melting, which is still the most suitable technique for producing this kind of alloy.

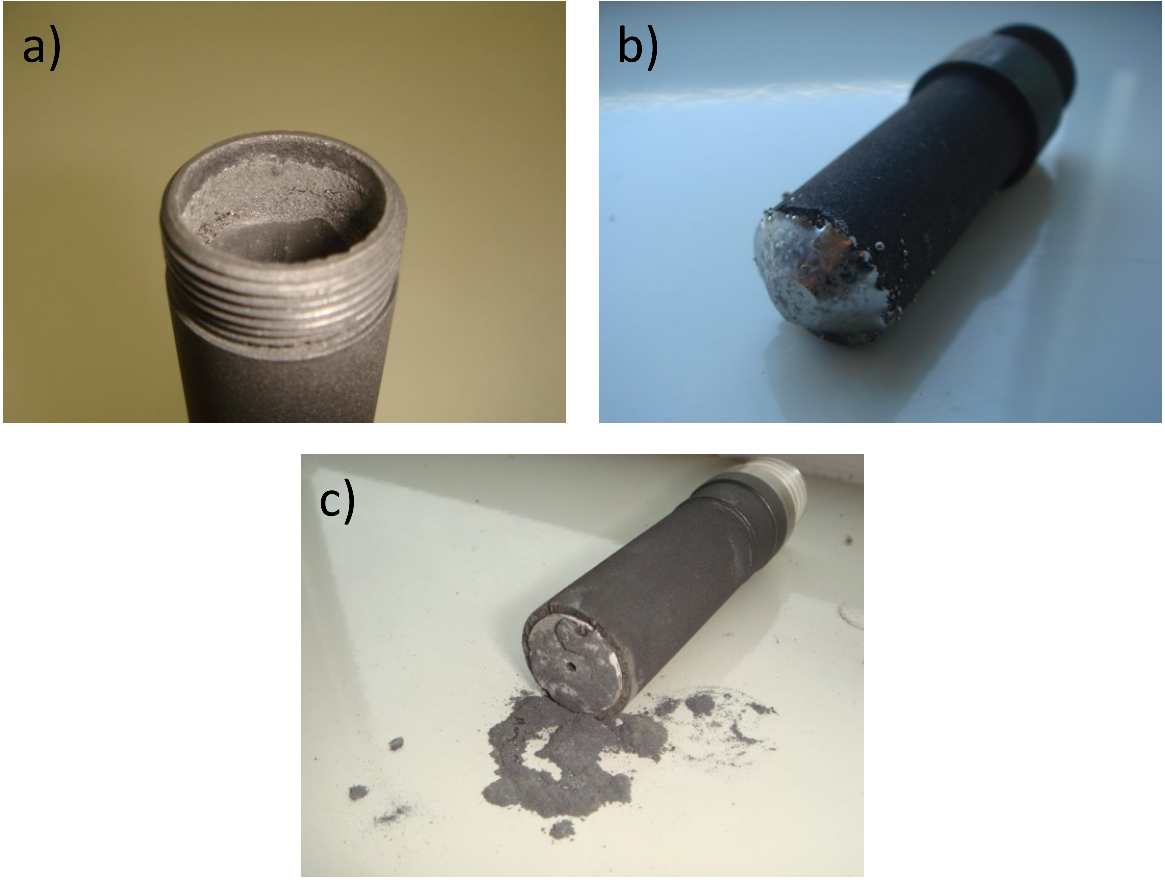

Figure 42: Graphite crucible. a) shows how the melt etched the graphite out of the crucible. b) shows how some of the melt stays on the crucible after melt spinning on the bottom of it. c) shows powder of oxidized Gd which forms out of the melt from the crucible after a few days.

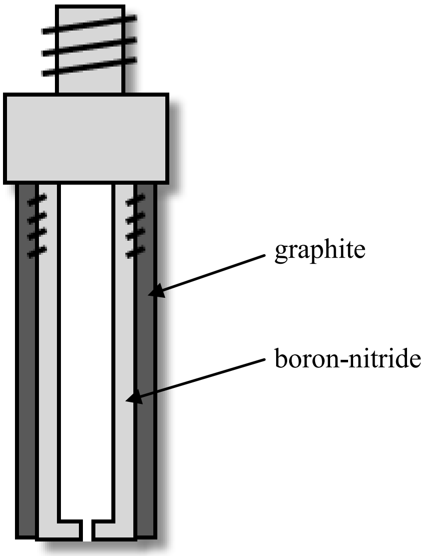

Figure 43: Homemade boron-nitride-graphite crucible.

4.2 Substitutions with iron

Because mechanical alloying and melt spinning proved to be unsuitable for producing Gd-based alloys, we continued our research with arc melting. With this technique we could produce many different compositions in a short time, making it easier to research the influence of iron.

4.2.1 Macrostructure

The electron microscopy secondary-electron images (SEI) in Figure 44 show the macrostructures of three of the arc-melted buttons of the SI series of alloys. The same macrostructures were found also in the SI and GESI series of alloys and are not presented here. The SI0 sample exhibits regular pentagons and hexagons reminiscent of a buckyball. The SI0.5 sample's surface shows a sinew effect, rather like columnar grains running at angles to each other on the upper surface of the sample. The SI1 sample has a smooth upper surface, much more characteristic of an intermetallic arc-melted button.

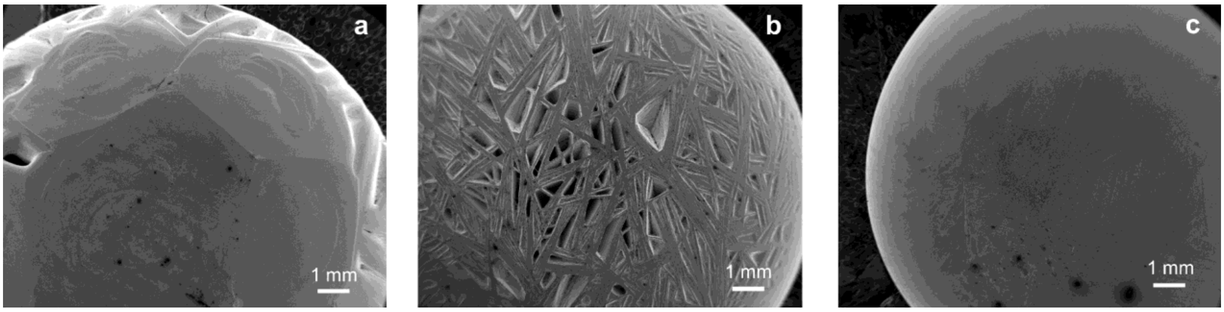

Figure 44: SEI taken of arc-melted buttons with SI0 (a), SI0.5 (b) and SI1 (c) composition.

The unusual macrostructural features observed for the samples with no iron and very small amounts of iron are very striking; however, during our microstructural investigations on the sample's surface, which must be a consequence of the dissolved iron, where as the buckyballs point to a surface-energy effect, with the flat surfaces representing the growth of particular atomic planes. The smooth surface of the SI1 sample implies that minimizing the surface area during the molten phase is still the main factor in determining the final shape of the solid button.

It is clear from Figure 44 that in the case of alloy SI0, where no iron is present, the surface of the button has regular pentagons and hexagons; this is typical for the solidification of so-called semi metals such as silicon and germanium and intermetallic phases with low crystallographic symmetry. Both, silicon and germanium have melting entropies of the order of ~3.6 k_B/atom, which gives approximately 30.0 J/Kmol, whilst most metals including gadolinium and iron have melting entropies of around 1 k_B/atom, i.e., ΔS_{Fe} = 8.48 J/Kmol and ΔS_{Gd} = 5.51 J/Kmol. This means that the high melting entropies for both silicon and germanium will increase the tendency for the established intermetallic phases to form facets during the process of solidification. Since the phases in the examined alloys have predominantly monoclinic (lower symmetry) and orthorhombic structure at room temperature, they will also solidify forming a faceted solidification front in the absence of iron. As the concentration of iron in the alloy SI0.5 increases (Figure 44b) the pentagon- and hexagon-shaped facets in Figure 44c break up because of the reduction of the high melting entropies due to the presence of iron and the fact that iron substitutes for silicon in the $Gd_5Si_2Ge_2$ according to the formula $Gd_5Fe_xSi_{2-x}Ge_2$. Iron, like most metals, has a low melting entropy and will solidify forming an uneven solidification front (on the atomic scale) thus hindering the formation of regular facets (e.g., pentagons and hexagons) during solidification when added to an alloy containing silicon and germanium. The sinew like feature can be explained by the existence of two phases with different temperature expansion coefficients. This means that when cooling in the copper mold one phase contracts more than the other one, thus sucking the phase into the button, producing this extraordinary feature. Finally, as the iron concentration was almost doubled (alloy SI1 with 11.1 at. % Fe) the facets or sinew effects completely disappeared as the surface of the button adopts a smooth finish, typical for the solidification of metallic materials. The effect of the high cooling rate has to be accounted for, since when it is high, as in our case, it hinders the formation of large facets by a reduction of the diffusivities, thus adding to the effect that iron has on the process of faceting.

4.2.2 Microstructure

The first set of images in Figure 45 shows optical micrographs taken of the samples SI0, SI0.125, SI0.25, SI0.5, SI0.75 and SI1. It is clear from the six images that all the samples are composed of multi-phase structures. The microstructure of the SI0 sample, where there is no iron added, consists of the $Gd_5(Si,Ge)_4$ matrix phase, A, and a grain-boundary phase, GB1. A new matrix phase, the B phase, appears with the smallest addition of iron, i.e., the SI0.125 sample, together with the grain-boundary phase GB2. The GB1 phase was neither observed here nor in any of the subsequent samples. The composition of the matrix phase B suggests that it is a $Gd_5(Si,Ge)_3$-type phase. With increasing amounts of added iron, the amount of matrix phase A is seen to decrease until it disappears completely in sample SI0.75. On the other hand, matrix phase B is increasing on the account of the decrease of matrix phase A. Approximately half of the matrix phase A is replaced by matrix phase B in the SI0.5 sample. In the sample SI0.75 we see another grain boundary phase appearing, which we marked GB3. With the composition of 33.1 at.% Gd, 5.5 at.% Si 59.9 at.% Fe and 1.5 at.% Ge it suggests the composition Gd_1Fe_2 with a small substitution of Si and Ge for Fe. This phase appears also the sample SI1, with phase B and GB2.

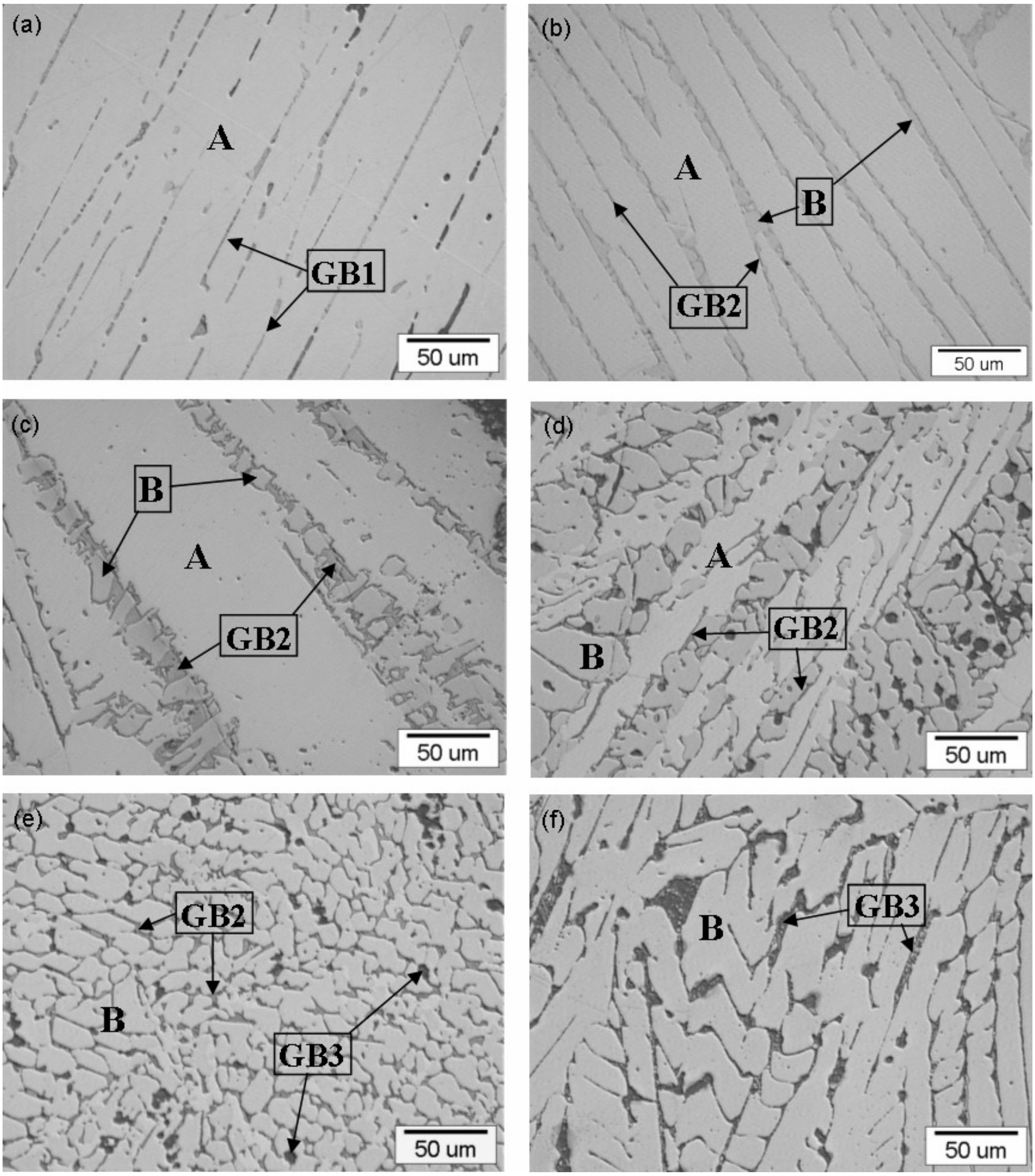

Figure 45: Optical images of the etched microstructures of arc-melted SI0 (a), SI0.125 (b), SI0.25 (c), SI0.5 (d), SI0.75 (e) and SI1 (f) samples.

The compositions of the matrix phases A and B with respect to the amount of added iron can be seen in Table 5. The compositions strongly suggest that matrix phase A is a Gd_5Si_4-type phase, while matrix phase B is better described by the composition Gd_5Si_3. The ratio of Si versus Ge in both main phases is in favor of germanium and this ratio increases with more iron added. This is expected because of the substitution of silicon with iron, increasing the germanium content. No iron could be found in the main 5:4 matrix phase as in the new 5:3 phase. Even at the highest concentration no iron was found, suggesting that iron does not affect the main 5:4 phase directly, because it does not dissolve into the main phase.

Table 5: Elemental compositions in at.% of the two main phases present in the samples evaluated using EDS. Analyzing errors to be considered are Gd ±0.2, Si ±0.1, Fe ±0.2 and Ge ±0.3.

SI	Phase A				Phase B			
	Gd	**Si**	**Fe**	**Ge**	**Gd**	**Si**	**Fe**	**Ge**
SI0	55.8	22.7	–	21.5	–			
SI0.125	55.2	20.7	–	24.1	61.5	16.1	–	22.4
SI0.25	56.2	20.0	–	23.8	62.8	16.2	–	21.0
SI0.5	56.2	17.6	–	26.2	63.2	13.8	–	23.0
SI0.75	–				61.8	11.1	–	27.1

The compositions of the grain-boundary phases of the SI set of samples were analyzed for all six samples. They are collected in Table 6. Three different grain-boundary phases were identified. The grain-boundary phase found in sample SI0, marked as GB1, is richer in Si than the matrix phase; however, it is only present in this sample, which is the sample with no iron in the initial composition. This phase is the $Gd_1(Si,Ge)_1$ phase. The grain-boundary phase GB2 appears in all the samples with any amount of iron present in the alloy. The composition of this GB2 phase does not vary with increasing amounts of added Fe, and the ratio for Gd:(Si,Ge):Fe is approximately 1:1:1. There is also a higher amount of silicon compared to germanium in the GB2. The grain-boundary phase GB3 starts forming in the structure of the samples as a grain-boundary phase when X becomes larger than 0.5, i.e., in samples SI0.75 and SI1. The composition of the GB3 phase indicated much lower levels of Si than for GB2, with Fe being the largest single element. All the iron can be found in the GB phases and non in the matrix phases. It indirectly affects the composition of the main phase by changing the SI/Ge ratio in the main phase.

Table 6: Elemental compositions in at.% of the grain-boundary phases present in the samples evaluated using EDS. Analyzing errors to be considered are Gd ±0.2, Si ±0.1, Fe ±0.2 and Ge ±0.3.

SI	GB1 phase				GB2 phase				GB3 phase			
	Gd	**Si**	**Fe**	**Ge**	**Gd**	**Si**	**Fe**	**Ge**	**Gd**	**Si**	**Fe**	**Ge**
SI0	51.5	31.7	–	17.0	–				–			
SI0.125	–				34.8	27.4	33.3	4.5	–			
SI0.25	–				35.5	28.0	30.8	5.6	–			
SI0.5	–				35.5	26.9	31.7	5.9	–			
SI0.75	–				35.3	26.3	31.4	7.0	33.1	5.5	59.9	1.5

The second set of images in Figure 46 show secondary electron images taken of the samples GE0.06, GE0.125, GE0.25, GE0.5 and GE0.75. The images are comparable to the SI set of samples with a multi-phase structure. The addition of iron results in the appearance of the new matrix phase D with the grain boundary GB4. The main phase C is slowly disappearing with more iron until in sample GE0.75 there is no $Gd_5(Si,Ge)_4$ matrix phase left and the predominant phase becomes phase D with the $Gd_5(Si,Ge)_3$ composition. The amount of the GB4, which appears as a black area in the microstructure, is slowly increasing with the amount of iron. Also, a new grain boundary (white area) is appearing in sample GE0.75, which is marked as GB5.

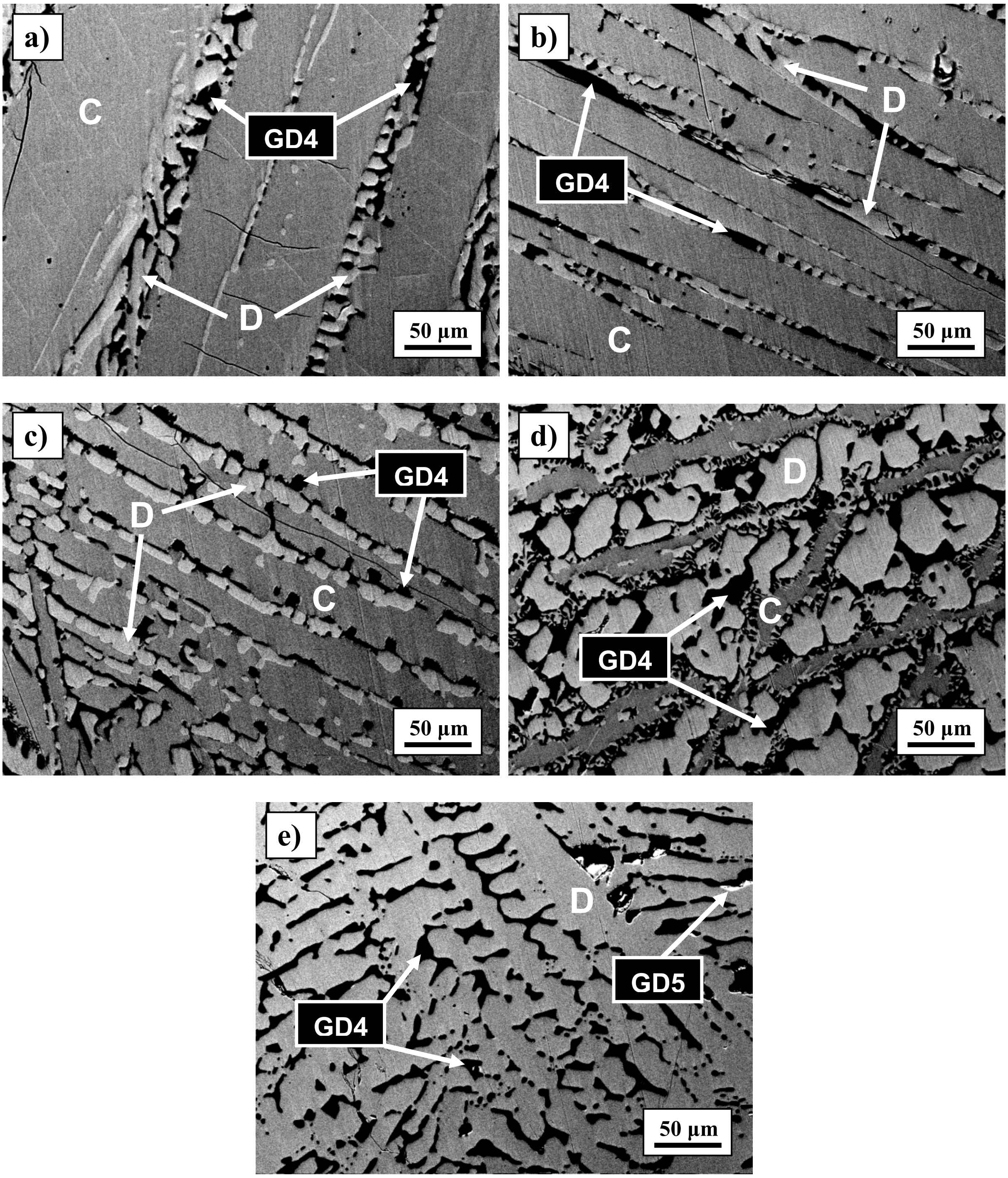

Figure 46: SE SEM images for the GE set of samples; GE0.06 (a), GE0.125 (b), GE0.25 (c), GE0.5 (d) and GE0.75 (e).

Table 7 presents the compositions of the matrix phases C and D with respect to the amount of added iron. The matrix phase C has a different composition to the matrix phase A in the SI samples. The main phase in the GE0.06 sample, i.e., phase C, has the composition $Gd_{60.6}Si_{19.1}Ge_{20.3}$, the same as that observed by Provenzano et al. [164] Also the newly formed matrix phase D has in the sample GE0.06 a Gd-rich composition, $Gd_{66.3}Si_{12.8}Ge_{21.9}$. This suggests that the main phase is a $Gd_3(Si,Ge)_2$-type phase, while matrix phase D is better described by the composition $Gd_2(Si,Ge)$. The amount of iron was too low to be detected with the EDXS in any of the matrix phases. The compositions of both matrix phases are constant, independent of the amount of added iron. Only at very high iron concentrations does the Gd:(Si,Ge) ratio change. While the Si/Ge ratio in the phase C is equal, the ratio in the phase D, is in favor of germanium.

Table 7: Elemental compositions in at.% of the two main phases present in the samples evaluated using EDS. Analyzing errors to be considered are Gd ±0.2, Si ±0.1 and Ge ±0.3.

GE	Phase C				Phase D			
	Gd	**Si**	**Fe**	**Ge**	**Gd**	**Si**	**Fe**	**Ge**
GE0.06	60.6	19.1	–	20.3	66.1	11.7	–	22.2
GE0.125	60.0	19.4	–	20.6	66.0	12.0	–	22.0
GE0.25	60.9	19.9	–	20.2	66.0	13.0	–	21.0
GE0.5	59.1	21.2	–	19.7	65.2	14.8	–	21.0
GE0.75	–				64.7	15.9	–	20.4

A summary of the compositions of the observed grain-boundary phases in the GE samples is given in Table 8. The composition of the GB4 changes with added iron. If we exclude the sample GE0.125 which does not fit into the continuous change in composition, then the gadolinium and iron content slowly decreases while the silicon and germanium content slowly increases. This in contrast to the GB2 of the SI set of samples, where the ratio is constant. All the iron can be found only in this phase. A second grain boundary appears in the sample GE 0.75, which we marked as GB5. This grain boundary has a germanium-rich $Gd_5(Si,Ge)_4$-type composition with no iron. This so-called starting composition can be found only in this sample with a high content of iron.

Table 8: Elemental compositions in at.% of the grain-boundary phases present in the samples evaluated using EDS. Analyzing errors to be considered are Gd ±0.2, Si ±0.1, Fe ±0.2 and Ge ±0.3.

GE	GB4 phase				GB5 phase			
	Gd	**Si**	**Fe**	**Ge**	**Gd**	**Si**	**Fe**	**Ge**
GE0.06	51.0	21.8	9.8	17.4	–			
GE0.125	36.8	30.7	20.9	11.7	–			
GE0.25	44.9	23.0	16.6	15.5	–			
GE0.5	44.1	23.1	17.7	15.1	–			
GE0.75	33.1	24.9	31.7	10.3	54.4	20.1	–	25.5

The last set of images in Figure 47 shows secondary electron images taken of the samples GESI0.06, GESI 0.125, GESI 0.25, GESI 0.5 and GESI 0.75. Compared to the previous sets we can see a difference in the sample with the least amount of iron. The GESI0.06 sample is composed of the main matrix phase E, a dark grain boundary phase GB7 with a different composition than in previous samples and an additional phase that precipitates in the main phase. It is not the usual $Gd_5(Si,Ge)_3$ phase that we have seen before, because the 5:3 phase starts to appear only at the phase boundary and never inside of it. We marked the new phase as the GB6. After that we see the regular appearance of the new matrix phase F and the usual dark phase which we marked as GB8. Phase F slowly increases in size, at the expense of the main phase E. Again, the main phase E disappears after enough iron is added (GESI0.75), leaving only phase F and phase GB8. The GB8 is, in comparison to the other GB phases, more isolated in the 0.75 samples. No new grain boundary phase is appearing like in the other two samples with the mark 0.75.

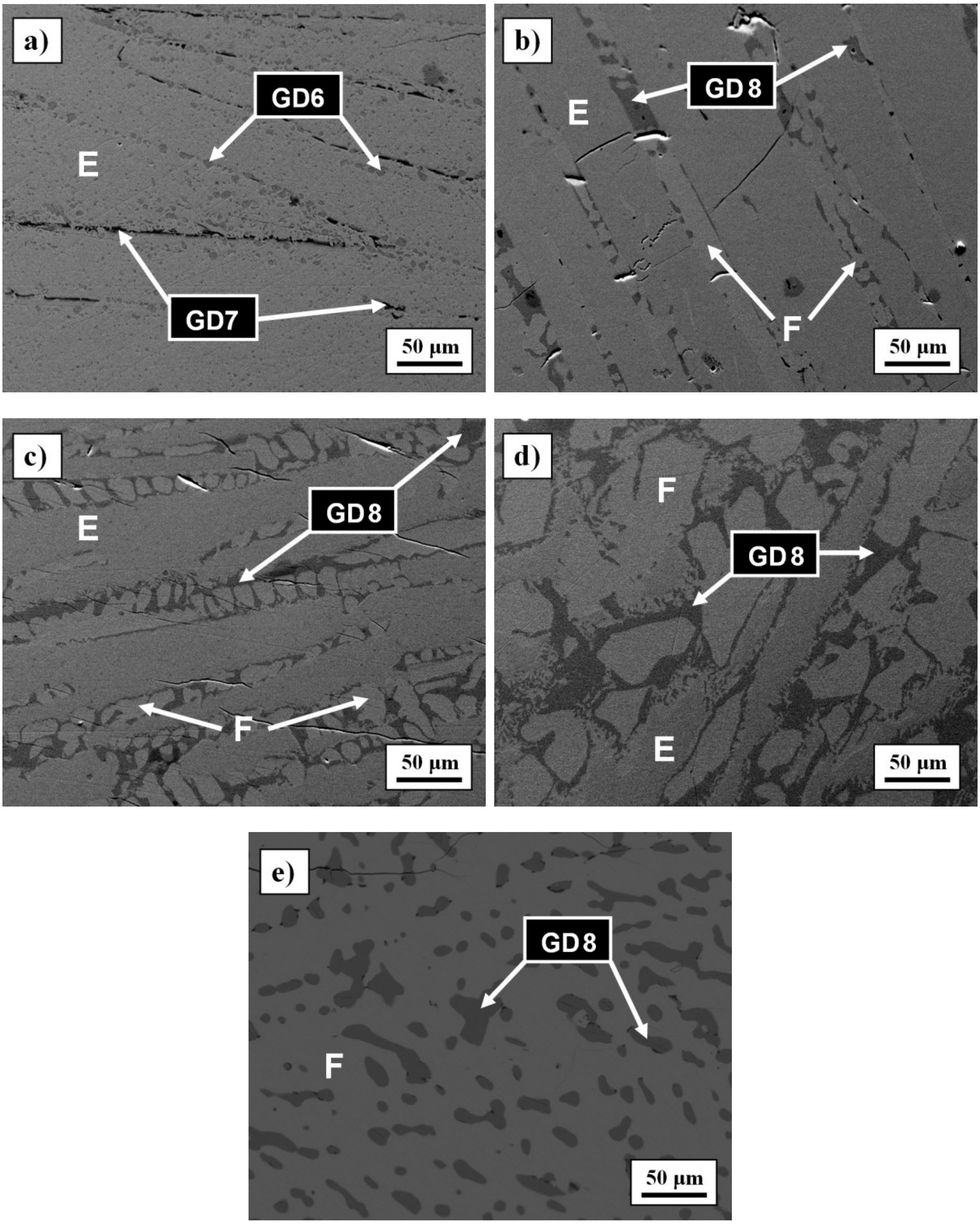

Figure 47: SE SEM images for the GESI set of samples; GESI0.06 (a), GESI0.125 (b), GESI0.25 (c), GESI0.5 (d) and GESI0.75 (e).

Table 9 presents the compositions of the matrix phases E and F with respect to the amount of added iron. The EDXS shows that with the addition of iron, the main matrix phase has a deficit of silicon and a surplus of germanium. But with the increase of iron this ratio stays the same. The same constant ratio between Gd, Si and Ge can also be observed in the newly formed matrix phase F, where the composition has again a ratio of 5:3, with the double amount of germanium against silicon. This tells us that changing the amount of iron does not change the composition of the two main phases. The major change in the composition appears after the first addition of iron where the silicon and germanium ratio changes from 22.2 % and 22 % to 19 % and 25 %, respectfully. Again, no iron could be detected in the two main phases as in the other two sets of samples.

Table 9: Elemental compositions in at.% of the two main phases present in the samples evaluated using EDS. Analyzing errors to be considered are Gd ±0.2, Si ±0.1, Fe ±0.2 and Ge ±0.3.

GESI	Phase E				Phase F			
	Gd	**Si**	**Fe**	**Ge**	**Gd**	**Si**	**Fe**	**Ge**
GESI0.06	55.3	19	–	25.2	–			
GESI0.125	55.1	19.3	–	25.2	61.7	12,7	–	25,1
GESI0.25	56.7	19.4	–	23.3	62.3	12,9	–	24,3
GESI0.5	56.4	19.3	–	23.3	62.7	13	–	23,6
GESI0.75	–				62.9	12.8	–	23.4

Table 10 shows a summary of the grain boundary phases found in the GESI set of samples. In the GESI0.06 we find that the light gray phase is of a similar composition to the matrix phase, but with a higher silicon concentration, making the image brighter. Also the composition of the dark grain boundary is different than the following ones, suggesting that this is not the same phase that appears with enough iron substituted. This phase disappears in the sample GESI0.125 where the composition is similar to what we have seen before. Because we are, with the substitution, not changing the Si/Ge ratio in the main phase as in the previous set of samples and the substitution of Si and Ge is very small in GESI0.06 it could be that the substitution was too small to affect the alloy. After the amount of iron is increased we see that the concentration of GB8 is similar to the GB4 in the GE samples with a concentration of 43 % Gd, 25 % Si, 16 % Fe and 16 % Ge.

Table 10: Elemental compositions in at.% of the grain-boundary phases present in the samples evaluated using EDS. Analyzing errors to be considered are Gd ±0.2, Si ±0.1, Fe ±0.2 and Ge ±0.3.

GESI	GB6 phase				GB7 phase				GB8 phase			
	Gd	**Si**	**Fe**	**Ge**	**Gd**	**Si**	**Fe**	**Ge**	**Gd**	**Si**	**Fe**	**Ge**
GESI0.06	51.5	30.4	–	18.1	24.6	37.6	4,8	33,0	–			
GESI0.125	–				–				43.0	25.2	15.6	16.2
GESI0.25	–				–				43.5	23.6	15.0	17.9
GESI0.5	–				–				43.7	23.5	18.3	14.5
GESI0.75	–				–				35.0	25.5	34.6	4.9

We see that substituting iron with one of the two elements has a similar effect on the microstructure. In all three samples first the 1:1 phases disappears, after this phase is used up the 5:4 phase is converting into the 5:3 phase till there is no 5:4 left anymore. This happens because iron is taking mostly Si and Ge, and some Gd, out of the main phase and forming a new one. Because we are substituting different elements this effects the ratio of the Si/Ge in the main phase and presumably also the properties of the alloy. We see two different GBs forming. The first one has a Gd:(Si,Ge):Fe ratio of 1:1:1 and can be found in the SI samples. The other one has a composition approximately 43 % Gd, 25 % Si, 16 % Fe and 16 % Ge and can be found in the GE and GESI samples. It is interesting that this phase is transformed into the 1:1:1 phase in the 0.75 samples in the GE and GESI samples.

4.2.3 Room temperature XRD

The XRD diffractograms of the Si-substituted samples can be seen in Figure 48. The peaks in the pattern that belong to the SI0 sample confirm that the main phase seen in the microstructure (Figure 45a) is the $Gd_5Si_2Ge_2$ monoclinic phase. Also the secondary phase is observed, which was visible in the microstructure of the sample. The three additional observed peaks at 47.1, 48.0 and 49.0° belong to the Gd_1Ge_1 orthorhombic phase with the space group 63. Although the peak positions should be at 47.1, 47.2 and 48.7 this can be explained by the fact that there is not only Gd and Ge in the phase but also some Si substituting Ge, which changes the cell parameters of the unit cell and shifts the diffraction peaks to higher values. The amount of this phase is very small and should not significantly affect the overall magnetocaloric effect. The vast majority of the peaks agree with the calculated pattern for the $Gd_5Si_2Ge_2$

compound. The positions of the calculated $Gd_5Si_2Ge_2$ peaks are identified by circles and the Gd_1Ge_1 peaks with triangles. After the first addition of iron (SI0.06) the spectrum looks similar to the sample without iron with a peak reduction of the Gd_1Ge_1 phase. This is because iron is forming with Si and Ge out of the Gd_1Ge_1 phase a new phase which was visible on the microscope as a dark phase, but is not visible in the SI0.06 XRD specter. This reduces the Si,Ge amount in the 1:1 phase converting it into the 5:4 phase. New peaks can be observed after the sample SI0.125. These peaks belong to the newly formed $Gd_5(Si,Ge)_3$ matrix phase. The peaks that belonged to the 1:1 phase have now totally disappeared, suggesting that all 1:1 phase have been transformed to the 5:4 phase. This transformation can be now observed in the 5:4 phase where additional iron reduces this phase into the 5:3 phase. This transformation continuous up to SI0.75 where all of the 5:4 phase is transformed into the 5:3 phase. The dark phase that was visible on the microscope already with the smallest addition of iron as the GB2 can be seen not until SI0.125 and that the peaks steadily increase with more iron substituted. The structure of the dark phase could not be defined with any of the known XRD spectra. The EDS suggested that the formula is $Gd_1(Si,Ge)_1Fe_1$, but no data could be found for such a stoichiometry, suggesting that it is a new structure not yet been identified. A reduction of the peaks of the dark phase can be observed in the SI0.75 sample, suggesting that the phase would disappear with more iron. The GB3 phase that was identified with the EDS was not observed in the SI0.75 specter. This could be because of the small amount of the phase in the sample. Some shifts in the peaks, while maintaining the same structure, can also be seen, and these shifts result from the changes in the ratio between Si and Ge in the main phase. The pattern of the SI0.75 sample indicates that the matrix phase B is the only matrix phase still present in the sample with the additional peaks of the dark phase.

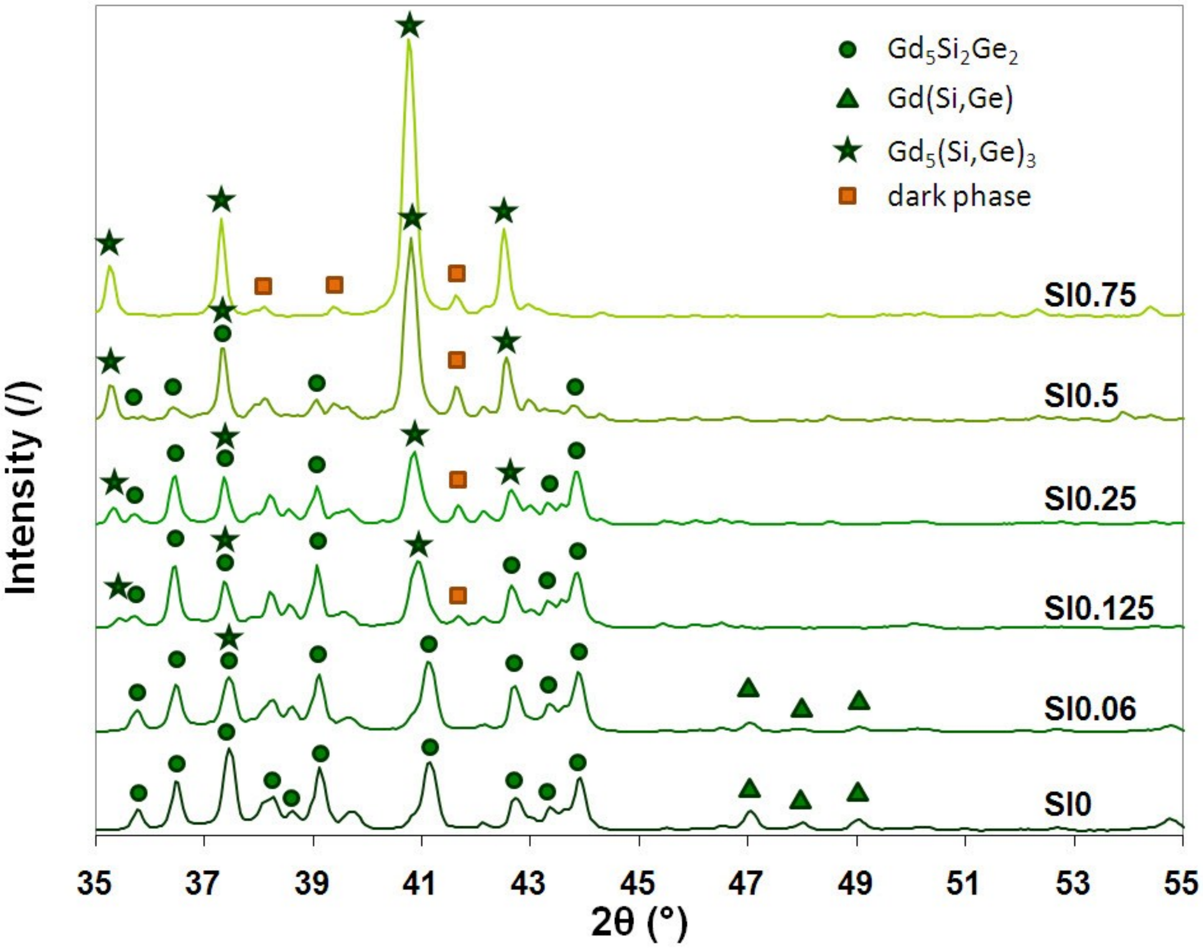

Figure 48: XRD diffractograms for the SI set of samples measured with cobalt radiation.

The XRD diffractograms of the set of GE samples are shown in Figure 49. The graph looks similar to the one of the SI samples. We can see that the 1:1 phase that is observed in the 0 sample already disappears after the smallest substitution of iron and is not visible in the sample GE0.06. The same transformation from the 5:4 phase to the 5:3 phase is visible with more iron addition. Because the peaks of the 5:4 and the 5:3 phase overlap we can see a clear appearance of the 5:3 phase not until GE0.25. The 5:4 phase totally disappears in the sample GE0.75 as in the SI sample. The dark phase is visible already in the sample GE0.06 and in the following samples. The difference here is that the dark phase disappears in the GE0.75 sample and is substituted with a new dark phase, which is marked as dark phase II. This phase could also not be identified with the known database. This supports our suggestion that enough iron causes the dark phase to disappear, which we have seen already in the SI samples. The new peaks appear at 40.3, 46.2 and 48.4. The peaks suggest that the unknown dark phase has a simple structure, but this could be misleading because of the weak spectrum.

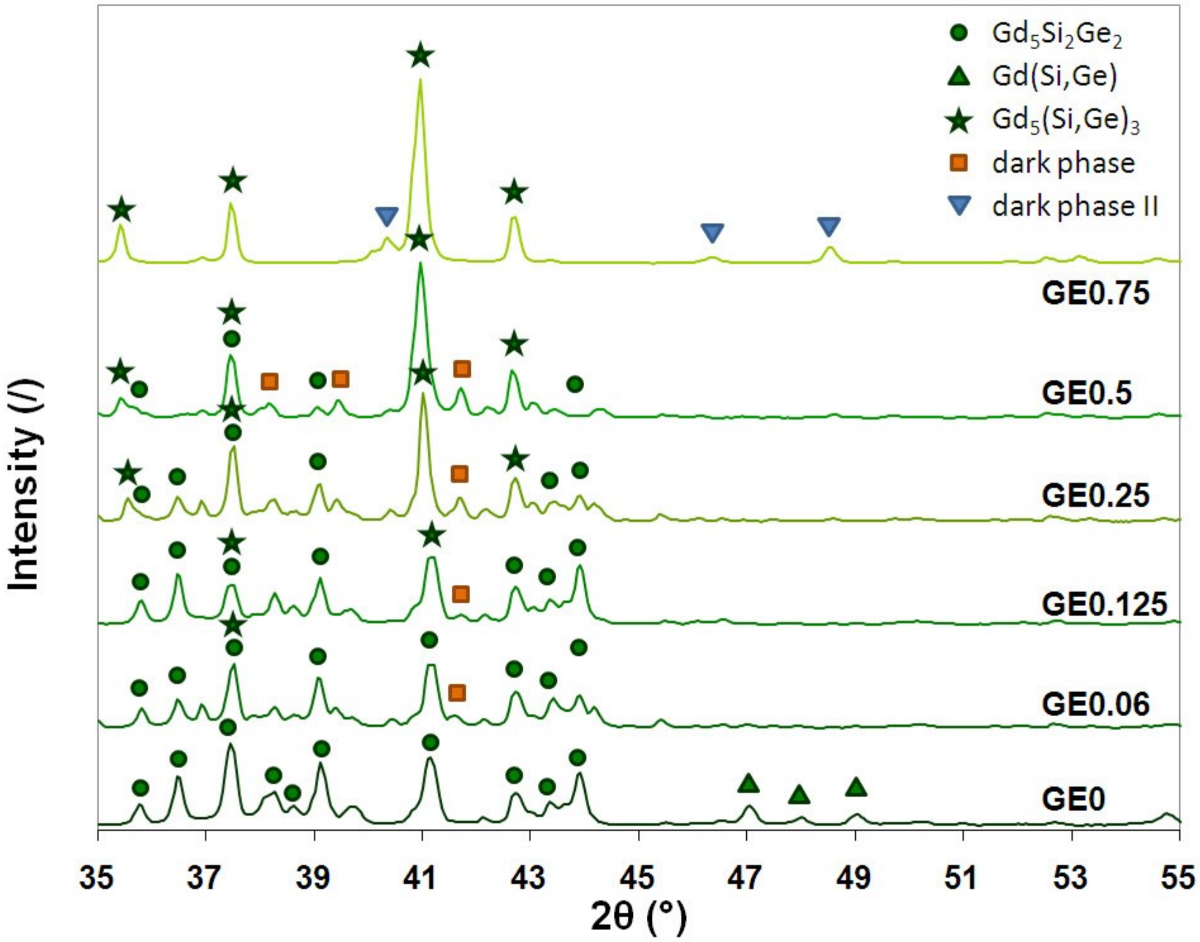

Figure 49: XRD diffractograms for the GE set of samples measured with cobalt radiation.

The last XRD figure shows the XRD diffractograms of the GESI samples. Again similarities can be drawn. The 1:1 phase converts to the 5:4 phase and after that the 5:4 phase converts to the 5:3 phase leaving only the 5:3 phase in the GESI0.75 sample. The 1:1 sample disappears after GESI0.125. The dark phase is observed already at GESI0.125, while the 5:3 phase is observed after GESI0.25. This suggests that the amount of iron was not enough to convert the 1:1 phase into the 5:4 phase. Again the same change of the dark phase into the dark phase II in sample GESI0.75 is observed.

The change of the XRD diffractograms look quite similar for all three set of samples. In all three set of samples the iron changes the 1:1 phase into the 5:4 phase and with more iron the 5:4 phase into the 5:3 phase because of the reduction of Si and Ge out of the main phase into the grain boundary phase. These findings confirm the results from the SEM and EDS. The most interesting things are the two grain boundary phases. All low iron concentration samples have the initial dark grain boundary phase and it changes to a second dark boundary phase with a different structure, but the structure could not be identified for either one. The change of structures in all sets of samples are the same, the difference is only when they appear, i.e. the amount of iron that changes the structure. If we would increase the amount of iron in the SI samples we would see the same change of the dark phase, because we could already see the reduction of the dark phase in the SI0.75 sample.

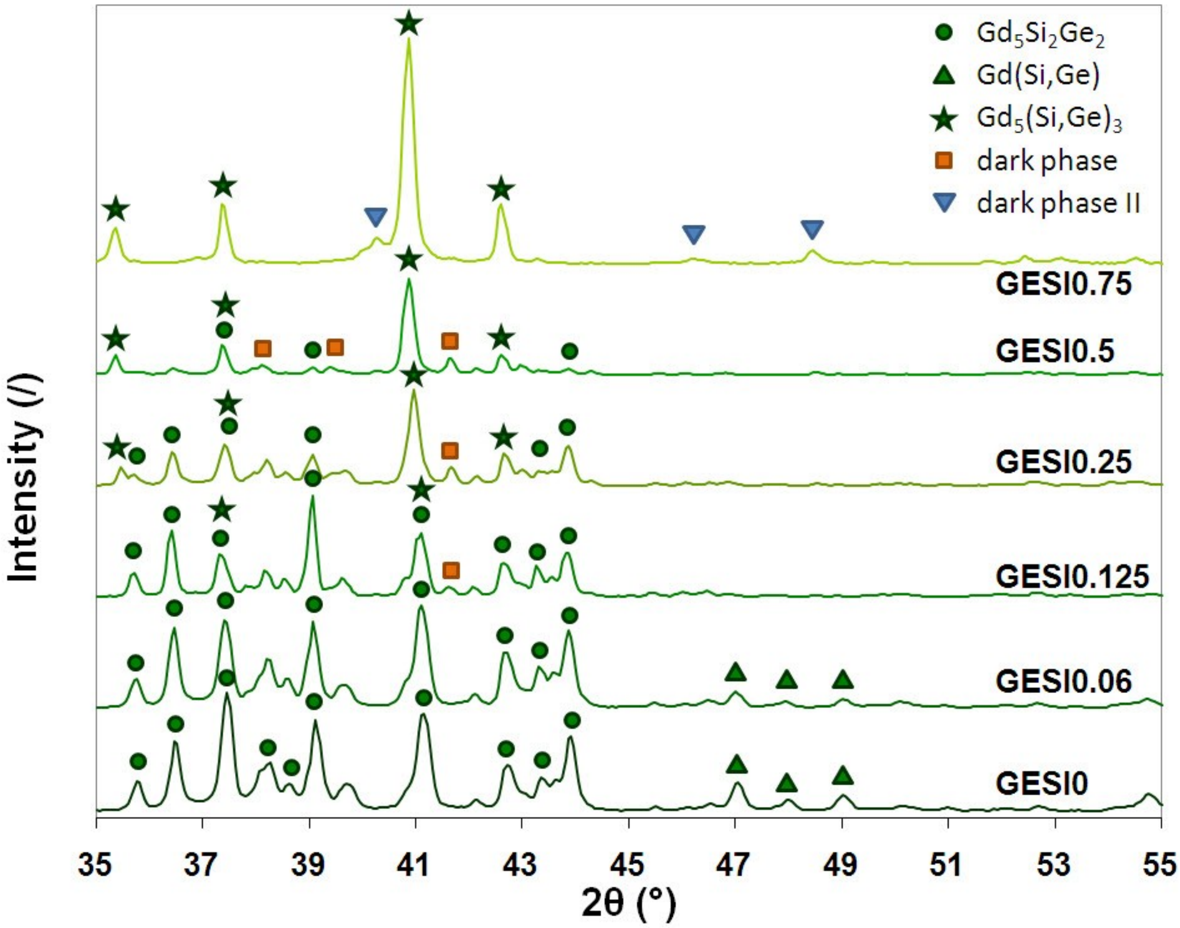

Figure 50: XRD diffractograms for the GESI set of samples measured with cobalt radiation.

4.2.4 Low temperature XRD

We were interested to know whether the addition of iron prevents the structural transformation of the orthorhombic to the monoclinic phase while changing the temperature through the magnetic transition temperature, which is the main reason for the high hysteresis losses that occur because of the structural transformation.

Figure 51 shows the results that we obtained by measuring the same sample at different temperatures. It shows that at low temperatures we have the orthorhombic $Gd_5Si_2Ge_2$ structure. As we increase the temperature we can see a change in the structure. The orthorhombic structure changes into the monoclinic between the temperature 250 K and 260 K. This can be clearly seen by the disappearance of the orthorhombic peaks at the angles 13.4, 13.7, 14.5, 15.4, 17.2 and 17.6. The phase is still visible at the temperature 260 K but is absent at 270 K. The monoclinic structure can be first observed at the temperature 250 K. Here peaks are formed at the angles 14.2, 14.9 an 17,0. It is clear that the transition is not sharp and that it takes place between a temperature interval of a few ten degrees. Both phases are present between 250 and 260 K. We see that iron did not prevent the formation of the monoclinic phase, thus preventing the first-order transformation.

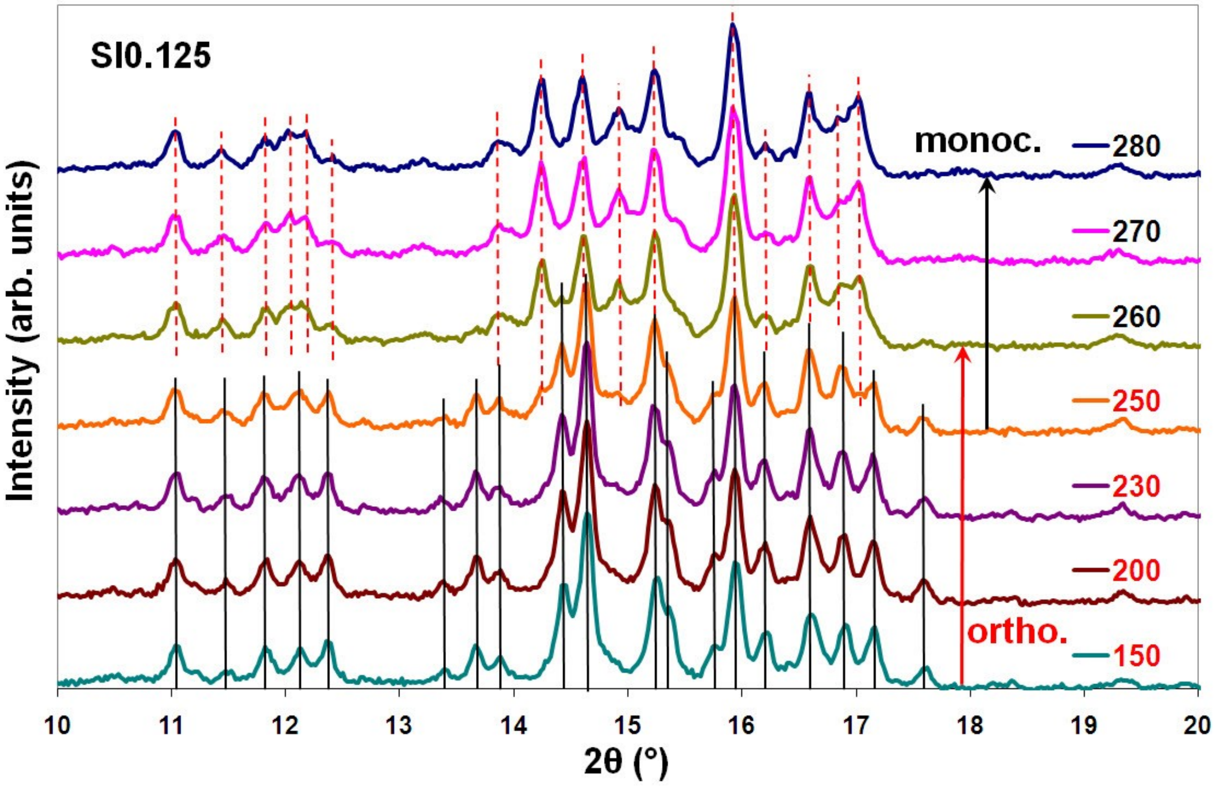

Figure 51: XRD diffractograms for the sample SI0.125 measured at different temperatures with molybdenum radiation. The two arrows show where which structures are present. The black arrow represents the orthorhombic structure and the red represents the monoclinic structure.

Figure 52 shows the results for the sample GE0.06 measured from 100 K up to 330 K. The difference compared to the SI0.125 sample is obvious. While increasing the temperature the formation of the monoclinic phase starts much later than in the SI sample. Up to 280 K no monoclinic phase is observed. At 310 K we see the monoclinic phase appearing and at 330 K both phases are still present. This suggests that not all of the orthorhombic phase has been transformed to the monoclinic phase at this temperature. The transformation starts between 280 and 310 K and up to 330 K it is not finished. One can see that the peaks of the orthorhombic phase slowly decrease and that at higher temperatures we could find only the monoclinic phase. We could not measure at higher temperatures because the limit of the apparatus was at 330 K.

Sample GESI0.06 shows a transition temperature from the orthorhombic to the monoclinic structure similar to the SI0.125 sample. Figure 53 shows the XRD spectra of the GESI0.06 sample. The orthorhombic phase can be observed up to the temperature 280 K, but only very weak peaks can be associated to the orthorhombic structure. There are still visible peaks at 12.3°, 14.6° and 15.3°. At 14.6° a clear splitting of the peak is visible at temperatures 260 K and 280 K, belonging to the orthorhombic and monoclinic phase. The monoclinic phase starts to appear at 260 K with peaks at 14.2, 14.6, 14.8 and 17.0 degrees as in the previous samples. After 280 K no orthorhombic structure can be observed and only the monoclinic structure is present.

Between the samples we can see small shifts of the spectra against each other. This is expected because of the small differences in the Gd, Si and Ge ratio of the sample which minimally changes the unit cell parameters. It could not be shown that the addition of iron has an effect on the structural change other than the temperature where it happens. The large difference in the Gd ratio between the SI Ge and GESI could have a large effect on the structural transformation temperature. In all samples the structural transformation is present and we cannot see any suppression of the transition, which was suggested the reason for the lower hysteresis losses in the sample in Provenzano's paper [164]. Only in the GE sample could there be a possible suppression of the structural transformation, but because we cannot measure at higher temperatures, we are not sure if both phases are still present. But we are sure that in all samples the first order transition is still present suggesting that the hysteresis losses should still be high.

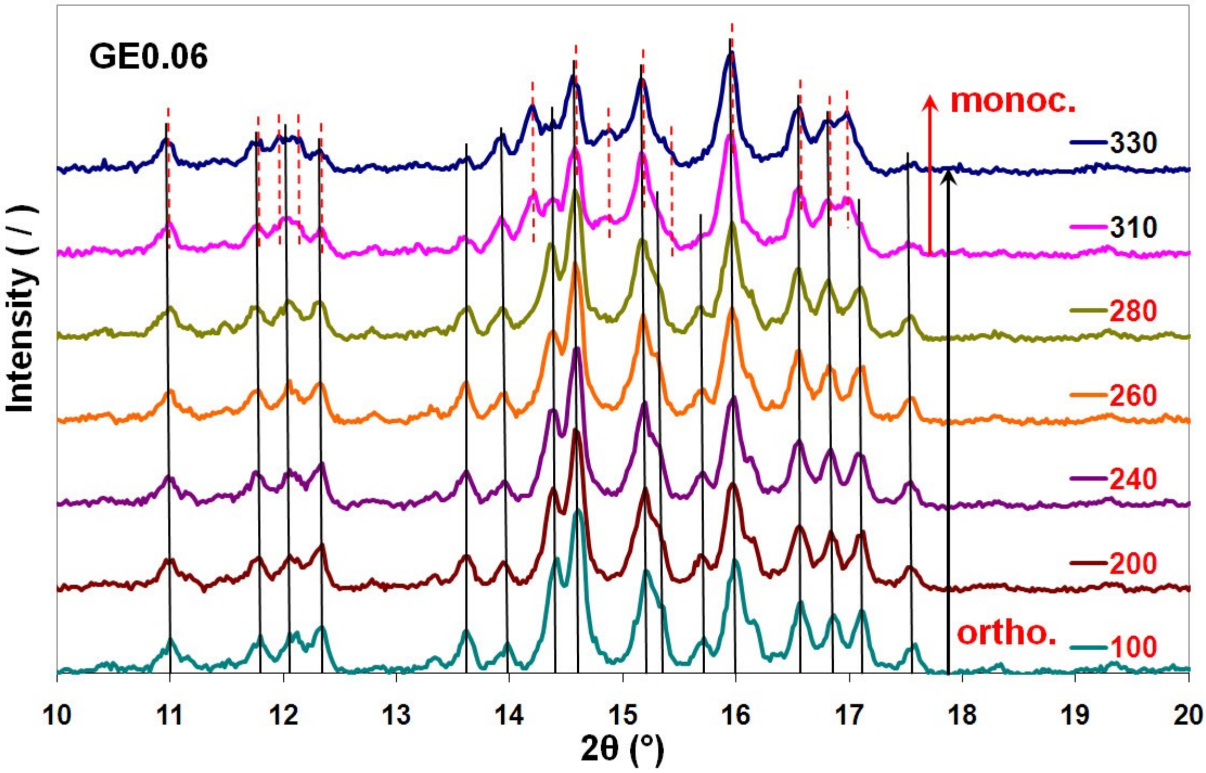

Figure 52: XRD diffractograms for the sample GE0.06 measured at different temperatures with molybdenum radiation. The two arrows show where which structure is present. The black arrow represents the orthorhombic structure and the red represents the monoclinic structure.

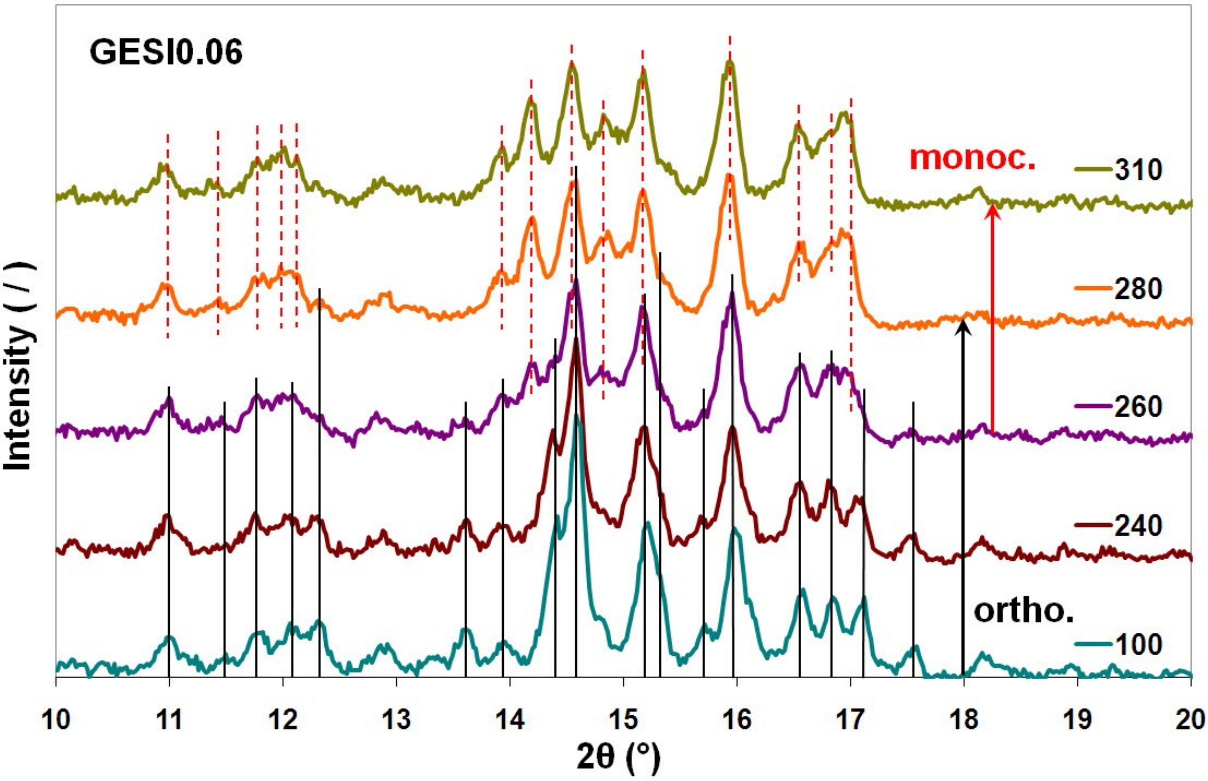

Figure 53: XRD diffractograms for the sample GESI0.06 measured at different temperatures with molybdenum radiation. The two arrows show where which structure is present. The black arrow represents the orthorhombic structure and the red represents the monoclinic structure.

4.2.5 Magnetic properties

4.2.5.1 Thermomagnetic properties

The largest effect of the iron substitution can be seen in the magnetic properties of the material. For all samples the thermomagnetic curves have been measured. All the curves were measured while heating up the sample with a heating speed of 1 degree per minute. The external magnetic field that the samples were exposed to was 100 Oe. The results were normalized by dividing with the mass of the sample.

The first figure represents the thermomagnetic curves for the SI set of samples. SI0 is the reference curve which is the same in all three set of samples with the notation SI0, GE0 and GESI0. We see that the reference curve has two magnetic transitions, one at 272 K and a second one at 306 K. The first magnetic transition is the combined structural/magnetic transition which marks the first order transformation: the orthorhombic/ferromagnetic to monoclinic/paramagnetic at 272 K. This is in agreement with the low temperature XRD, where the structural transformation occurs between 270 K and 280 K. After that we have a second transition at 307 K. This transformation is a normal second-order ferromagnetic to paramagnetic phase of the orthorhombic phase that has not been transformed into the monoclinic phase. This suggests that we do not have only the monoclinic phase at room temperature but a combination of both, the monoclinic and orthorhombic $Gd_5Si_2Ge_2$ phase. After the smallest substitution of iron we see that the first order transformation shifts to lower temperatures, while the second order transition shifts to higher temperatures. An additional magnetic transition is observed at 111 K. This additional magnetic transition belongs to the newly formed $Gd_5(Si,Ge)_3$ phase. This magnetic transition is a second order antiferromagnetic to paramagnetic transition. The observed reduction of magnetization after the first magnetic transition compared to the reference sample is due to the reduction of the starting 5:4 phase which is converted into the 5:3 which after 120 K shows no magnetic moment anymore. Similar curves can be observed for all the subsequent SI samples. The transition temperature of the first order transition shifts to lower temperatures with more added iron, except for the sample SI0.75, where no first or second order magnetic transition of the 5:4 phase is observed. This is in agreement with the SEM and XRD measurements where no 5:4 phase can be found. The transition temperature of the newly formed 5:3 phase stays almost the same, except for the SI0.75 sample where the temperature is reduced to 100 K. This reduction is because of the change in the Si/Ge ratio, where the Ge concentration is increased from 22 at.% to 26 at.% and Si is reduced from 16 at.% to 11 at.%. The reduction of the magnetization when we cross the T_C of the 5:3 phase increases with the increase of substituted iron. More iron is added the more 5:3 phase is in the system and the higher is the reduction in magnetization at the transition point. For all the curves the magnetization reduces almost to zero after the second order magnetic transition around 310 K, except for the SI0.75 sample. This magnetization belongs to a magnetic phase with a magnetic transition temperature higher than our measurements. This could belong to the unidentified iron rich dark phase that was found in the system, or free iron that has a Curie temperature of 1043 K, which we did not check. But because no Fe peaks were found in the XRD data, we suspect it is one of the unidentified phases. Because this magnetization is only visible in the sample SI0.75 and the GD3 phase occurs after SI0.75 we can say that the magnetization is from the Gd_1Fe_2 phase which has a Curie temperature above 350 K. The reduction of the first order magnetic phase transition temperature we explain with the change in the Si/Ge ratio of the matrix phase. Because we reduce the amount of silicon in the sample by substituting it with iron and iron is additional removing more silicon than germanium out of the matrix phase we get a SI/Ge ratio which moves the transition temperature down, as can be seen in the magnetic phase diagram of the Gd_5Ge_4-Gd_5Si_4 pseudo-binary system at zero field in Figure 16.

If we observe Figure 55 we see a quite different picture. Here the first noticeable difference is that with the addition of iron, the main magnetic transition occurs for all additions around 310 K. For GE0.06 at 304 K, for GE0.25 at 306 K, for GE0.5 at 311 K and for GE0.75 we can see that there is still a small change in magnetization at 325 K. Because the XRD and SEM show no 5:4 phase anymore this could belong to the GB phase. This is shown in the inset of Figure 55. The temperatures are in the area where the second order magnetic transition occurred for the SI set of samples, but because the structural transition still takes place as show by the low temperature XRD, the transition temperature of the magneto/structural first order transition of the 5:4 phase should occur. There can be no first-order magnetic phase transition observed. We can say that these temperatures belong to the second-order magnetic transition, because the composition fits the magnetic phase diagram. The FOMT could occur at the same temperature as the SOMT and is covered by it. This is the most reasonable explanation, because the low temperature XRD confirmed both monoclinic and orthorhombic phase after the phase transition. Also, the transition temperature for the 5:3 phase changes differently with more iron compared to the SI samples. With the smallest addition of iron we get a transition temperature of 65 K. This temperature increases to 95 K for the sample GE0.25, 112K for GE0.5 and 151 K for GE0.75. This is an opposite effect than in the SI samples. If we look at the change in the composition we see that also the Si/Ge ratio is going in the opposite direction. Si increases from 11.7 at.% for GE0.06 up to 15.9 at.% for GE0.75. At the same time Ge decreases from 22.2 at.% to 20.4 at.% changing the SI/Ge ratio from 0.53 to 0.78. The magnetizations in the samples change for two reasons; one is the magnetic transition and the other is the amount of the different phases in the alloy. As the percentage of iron increases, the amount of the 5:3 phase increases and the amount of the 5:4 phase decreases, as can be seen by the difference in the fall of magnetization at the transition points. The magnetizations for all samples reduce to zero after 340 K which indicates that only paramagnetic phases are present. There is no 1:2 phase present in the sample GE0.75 as in the SI sample. That is why we have a peak in magnetization at around 140 K. Because we have only one magnetic phase in the system, the antiferromagnetic 5:3 phase, for which this curve shape is typical. All other samples that have two magnetic phases the magnetization is increasing below the Neel temperature of the 5:3 phase because of the 5:4 magnetization.

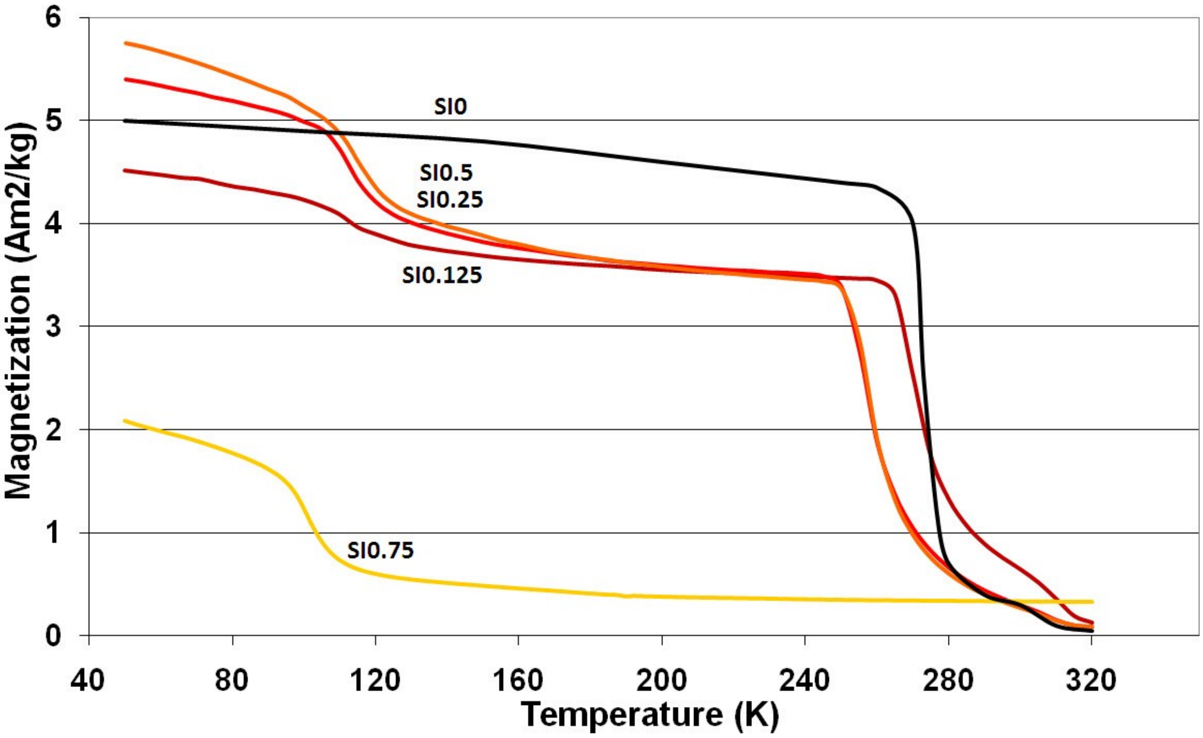

Figure 54: Thermomagnetic properties of the samples SI0.125, SI0.25, SI0.5 and SI0.75. The curve SI0 stands as a reference curve. The measurements were taken when heating up the sample.

The last thermomagnetic curves in Figure 56 belong to the GESI set of samples. The thermomagnetic curves look like a combination of the SI and GE curves. The 5:3 magnetic phase transitions are similar to the GE curves and the two 5:4 magnetic phase transitions are similar to the SI curves. The 5:4 magnetic transition temperatures do not change significantly compared to the GESI0 sample. The temperatures for the FOMT are 268 K for GESI0.06, 274 K for GESI0.125 and 276 K for GESI0.25. Compared to GE0.5 there is also no FOMT in GESI0.5 only a SOMT. The SOMT temperatures are almost the same for all samples. There is only a slight increase with more iron, from 299 K for GESI0.06 to 303K for GESI0.5. This is expected, because with the equal substitution of iron we do not change the SI/Ge ratio in the sample which defines the T_C. The 5:3 transitions look similar to the GE samples. Apart from the sample GESI0.06 we see an increase in the Neel temperature with more iron added into the sample. The temperature shifts from 63 K for GESI0.125 to 158 K for GESI0.75. The temperatures are almost the same as for the GE set of samples, but the EDS looks quite different. In the 5:3 phase of the GE samples the Si content increases while the Ge is almost the same. For the GESI samples the Ge content decreases while the Si content stays the same. The GESI0.06 sample does not show a 5:3 magnetic transition as the phase is also not present in the SEM images. The magnetization changes as in the GE samples. With more added iron the magnetization increases in the 5:3 samples while it decreases in the 5:4 samples. No magnetization can be seen after 320 K. The same magnetization peak is observed at around 150 K in GESI0.75 as in the GE0.75 sample. All the transition temperatures are presented in Table 11.

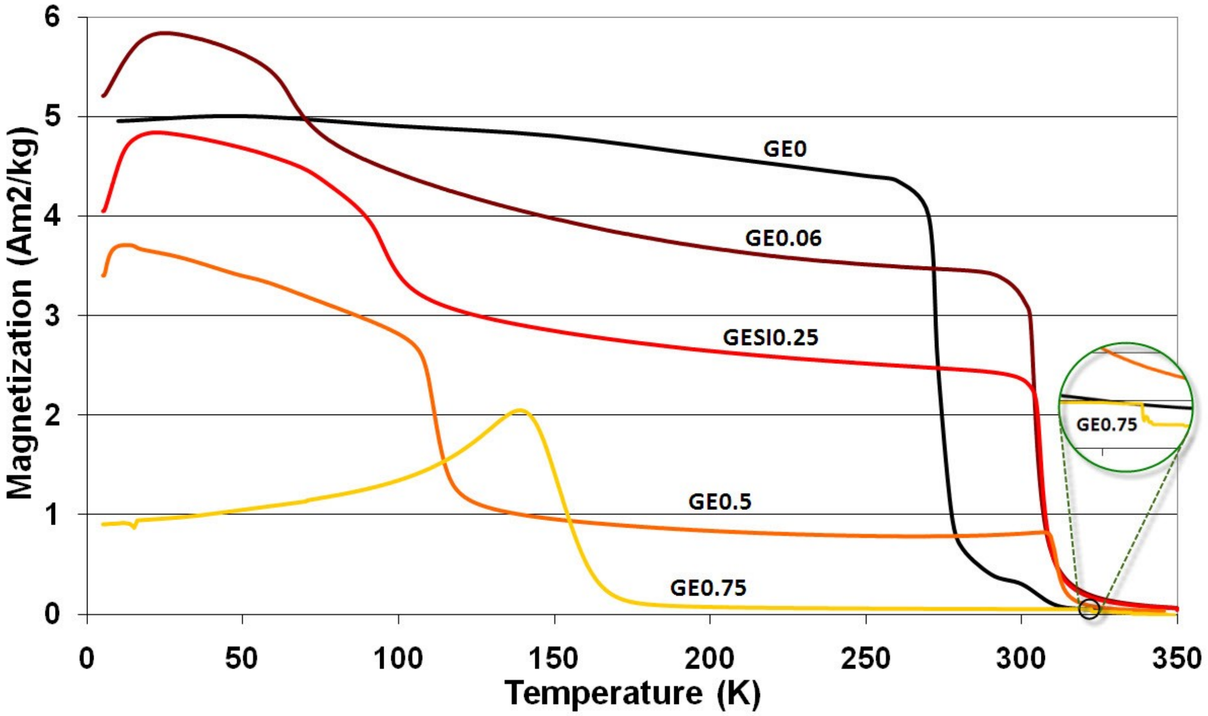

Figure 55: Thermomagnetic properties of the samples GE0.06, GE0.25, GE0.5 and GE0.75. The curve GE0 stands as a reference curve. The measurements were taken when heating up the sample.

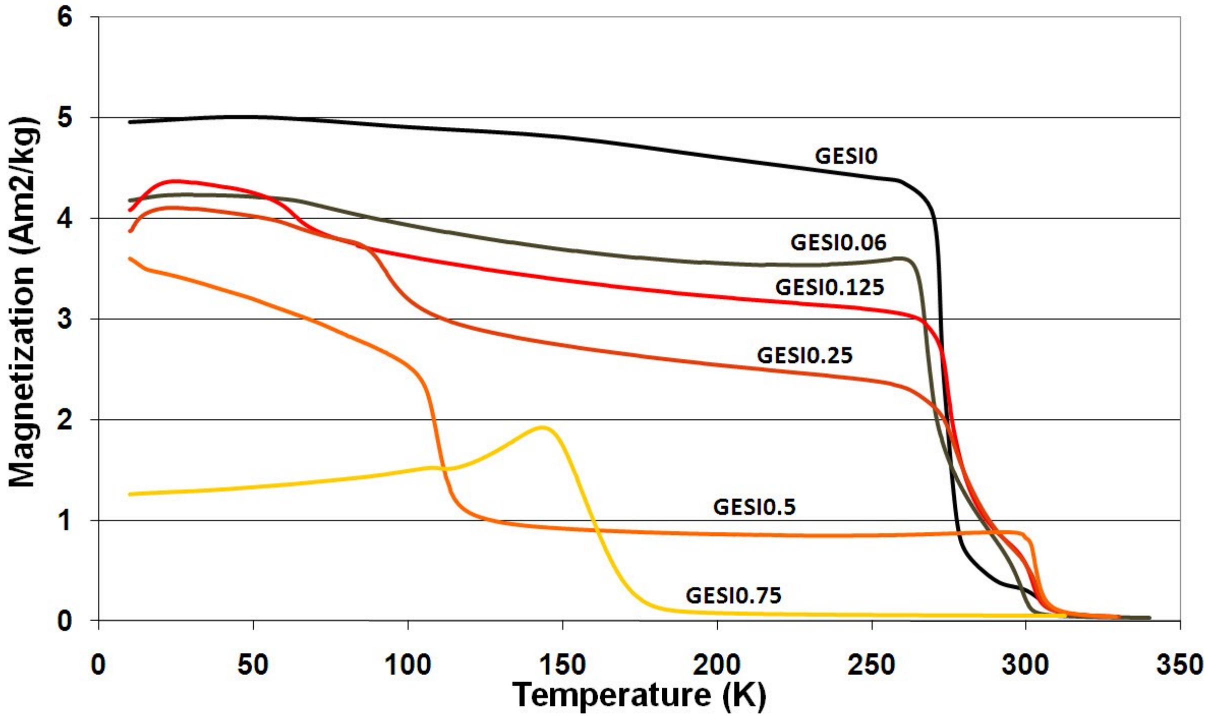

Figure 56: Thermomagnetic properties of the samples GESI0.06, GESI0.125, GESI0.25, GESI0.5 and GESI0.75. The curve SI0 stands as a reference curve. The measurements were taken when heating up the sample.

The changes in the thermomagnetic properties are quite obvious. We see that selecting which element we substitute and for how much changes the magnetic transition point significantly. By substituting Ge we increase the T_C while when substituting Si we decrease the T_C of the 5:4 phase. If we substitute both elements equally the T_C does not change at all. This is easily explained with the Si/Ge ratio in the main matrix phase. The ratio is changed by our substitution which reduces one element and also by iron itself, which has a desire for Si of the matrix phase. So by deciding which element we substitute we define the direction of temperature shift and more iron only increases this shift. With this we can easily control the magnetic transition temperature and create a material with the desired properties. One has to take into account that changing the transition temperature comes with a price of magnetization. This magnetization is lost because of the formation of a new phase which still has the magnetization, but at lower temperatures which is not useful for room-temperature applications. For this phase the same rule applies as for the 5:4 phase. Changing the Si/Ge ratio changes the magnetic transition temperature of the alloy. Si substitutions are shifting the transition temperature down and Ge substitutions are shifting the transition temperatures up.

Table 11: Magnetic transition temperatures for all phases in the samples SI, GE and GESI.

		Phase 5:4 (FOMT)	**Phase 5:4 (SOMT)**	**Phase 5:3 (antiferro.-param.)**
SI	0	272 K	306 K	–
	0.125	267 K	310 K	111 K
	0.25	255 K	307 K	110 K
	0.5	254 K	307 K	112 K
	0.75	–	–	100 K
GE	0	272 K	306 K	–
	0.06	–	304 K	65 K
	0.25	–	306 K	95 K
	0.5	–	311 K	112 K
	0.75	–	323 K	151 K
GESI	0	272 K	306 K	–
	0.06	268 K	299 K	–
	0.125	274 K	302 K	63 K
	0.25	276 K	303 K	91 K
	0.5	–	303 K	109 K
	0.75	–	–	158 K

4.2.5.2 Hysteresis loops

After defining the magnetic transition points of all the samples, we started measuring the hysteresis loops at different temperatures. The temperature span was set so that we measured the loops at several temperatures below and above the T_C. With this we could observe the changes in the magnetic hysteresis that occur when passing the magnetic transition temperature. The hysteresis loops were measured only in the first quadrant. We increased the external field to 1600 kA/m, equivalent to 2 Tesla, and then lowered it back to zero. Points were taken every 80 kA/m. Then we increased the temperature to the next setpoint and repeated the measurement.

The first set of images in Figure 57 shows the hysteresis loop measurements for the SI set of samples. The first images are the loop measurements of the reference sample SI0, which have been carried out at temperatures 260 K, 265 K, 270 K, 275 K, 280 K, 285 K, 290 K, 300 K and 310 K. All other SI sample have been measures at 5 K steps. For SI0 we have at 250 K a pure soft ferromagnetic response with no difference in magnetization as regards increasing or decreasing the magnetic field. At 265 K the loop starts to split between increasing and decreasing the magnetic field. At 270 K the splitting is the largest. We observe a two-step magnetization increase. The first step is due to domain-wall displacement and rotation of the magnetization of the domains in the fraction of the sample which is ferromagnetic at each temperature. The second step is due to a magnetic-field-induced PM/FM transformation of the fraction which is paramagnetic at a given temperature with a simultaneous magnetization of the formed ferromagnetic phase. When decreasing the magnetic field the magnetization sharply changes at lower fields then when increasing the field and returns almost to its original behavior. This results in a remanence-free hysteresis. At 275 K the split reduces again until 290 K where no splitting is observed anymore and we have only a paramagnetic response of the alloy. Inserting iron in the system reduces the broadness of the hysteresis loop significantly. The difference between SI0 and SI0.125 is quite obvious. We see that the hysteresis area of the loop has decreased by more than half and also the temperature where the maximum area is observed has shifted from 270 K for SI0 to 260K for SI0.125. Increasing iron only shifts the temperature with the highest loop area to lower temperatures and the width is also reduced even more. The hysteresis indicates that there is still a structural transformation taking place because there is still the 5:4

phase present in the sample. In the sample SI0.5 the area in the loops are already very small. The sample behaves ferromagnetically till 245 K, and then the transition starts and finishes at 270 K where no hysteresis can be observed and we have a purely paramagnetic sample. No measurements of the samples 0.75 have been conducted, because there was no magnetic transition temperature present in the range of room temperature. Comparing the magnetization of each sample at the same temperature we see a decrease of magnetization as was seen already in the thermomagnetic measurements.

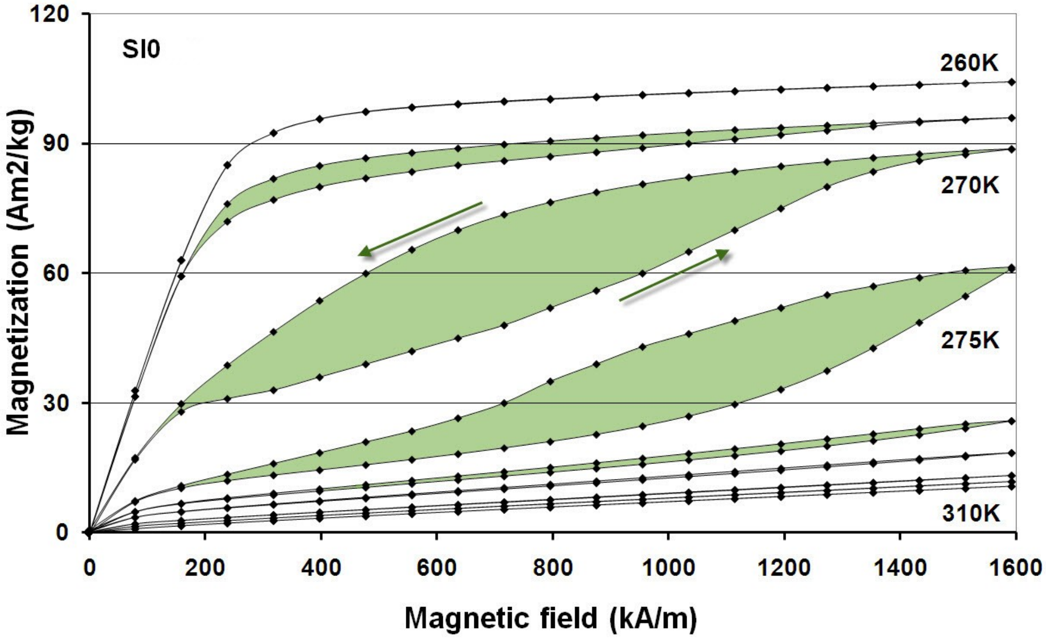

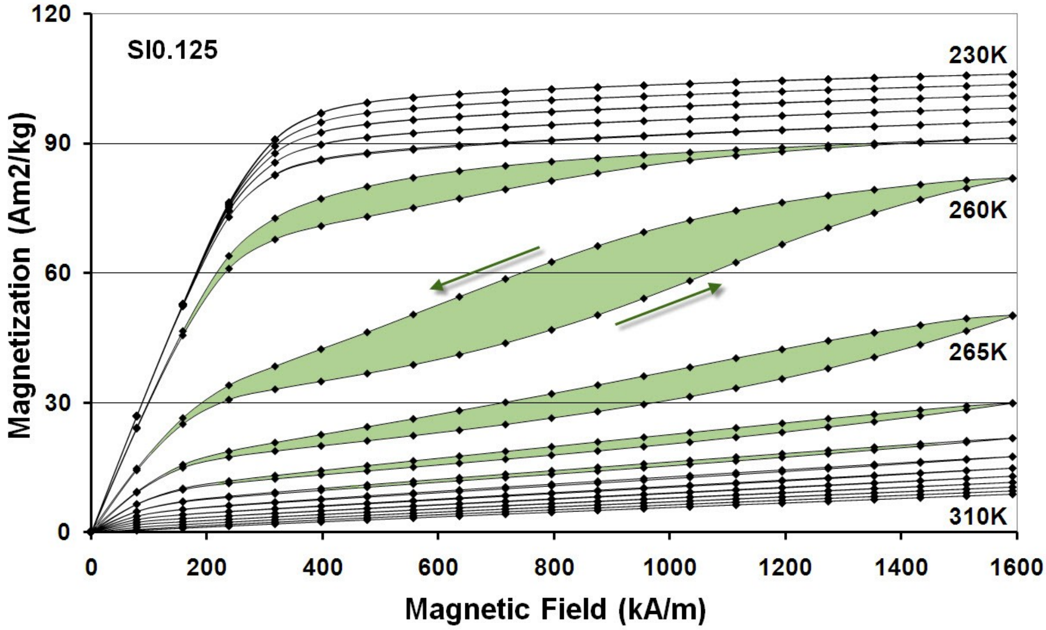

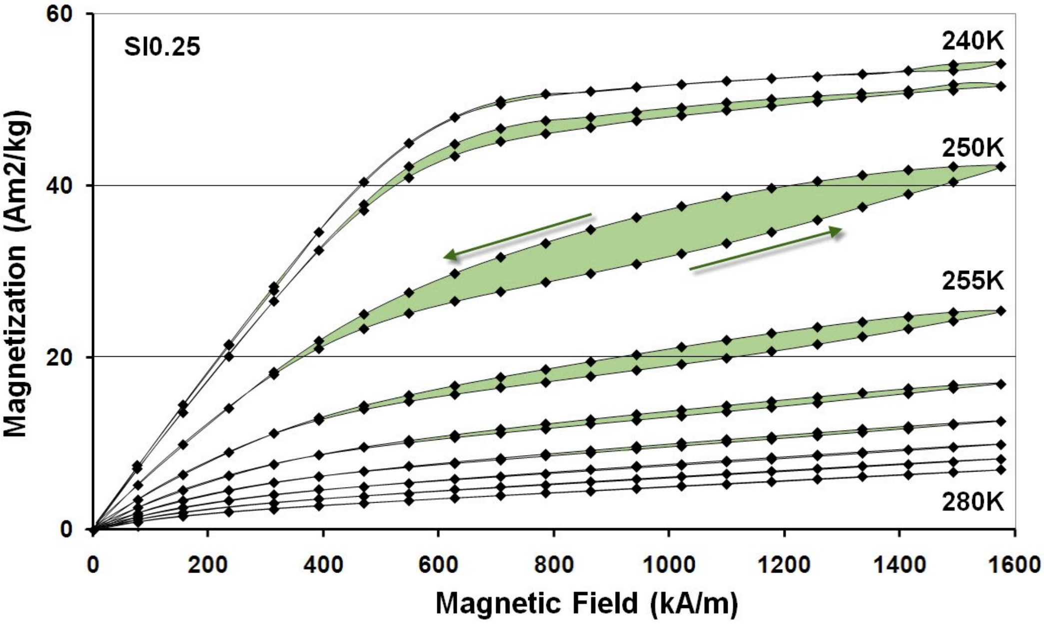

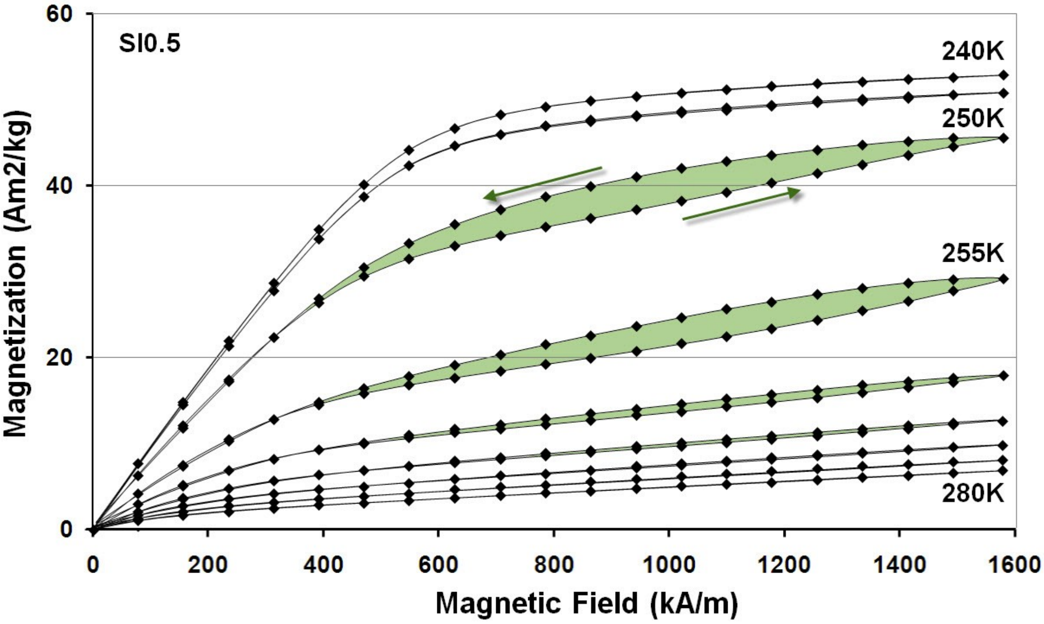

Figure 57: Magnetization versus field curves for the sample SI0, SI0.125, SI0.25 and SI0.5 measured at different temperatures. The arrows indicate the sequence of the measurement. The green area indicates the hysteresis losses that occur during the hysteresis loop.

The second set of images in Figure 58 belongs to the GE set of samples. The loops for the samples GE0.06, GE0.25 and GE0.5 where measured every 5 K. The hysteresis loops look quite different than for the SI samples. The hysteresis between the increase and decrease of the magnetic field reduces faster, with the same iron substitution. After the smallest addition of iron we see that the losses which are the green areas in the loop are already significantly reduced. The magnetic-field-induced PM/FM transformation of the fraction which is paramagnetic at a given temperature starts at 290 K, reaches its peak at 300 K and finishes at 310 K. After that only a paramagnetic response is observed. The samples GE0.25 and GE0.5 show that there is no hysteresis present anymore. The magnetic phase transition is a second-order phase transition with no structural transformation. Sample GE0.25 and GE0.5 clearly show that there are no hysteresis losses present. The structural transformation that we saw in the GE0.06 sample reflects the behavior only of this sample, where a simultaneous SOMT with the FOMT at the same temperature is plausible. After that no FOMT is present anymore and no hysteresis can be observed.

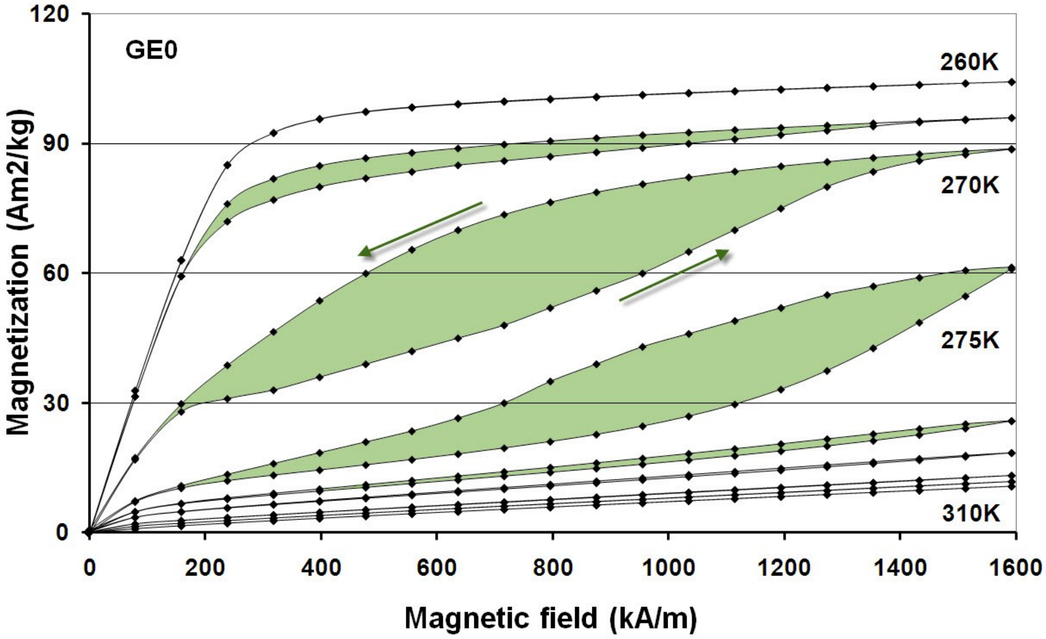
GE0
260K
270K
275K
310K
Magnetization (Am2/kg)
0
30
60
90
120
Magnetic field (kA/m)
0
200
400
600
800
1000
1200
1400
1600

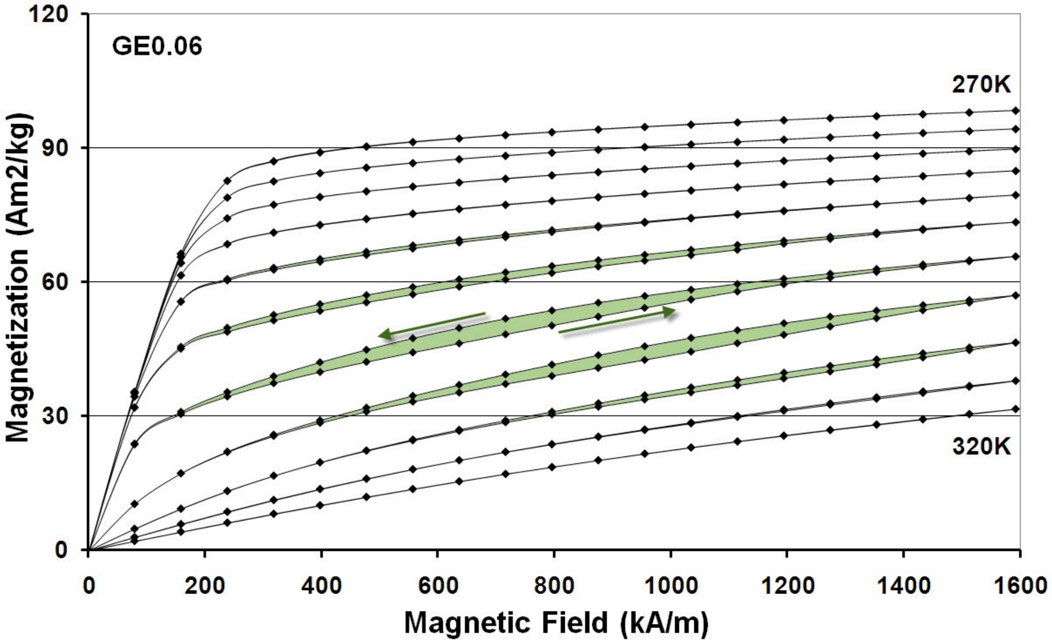
GE0.06
270K
320K
Magnetization (Am2/kg)
0
30
60
90
120
Magnetic Field (kA/m)
0
200
400
600
800
1000
1200
1400
1600

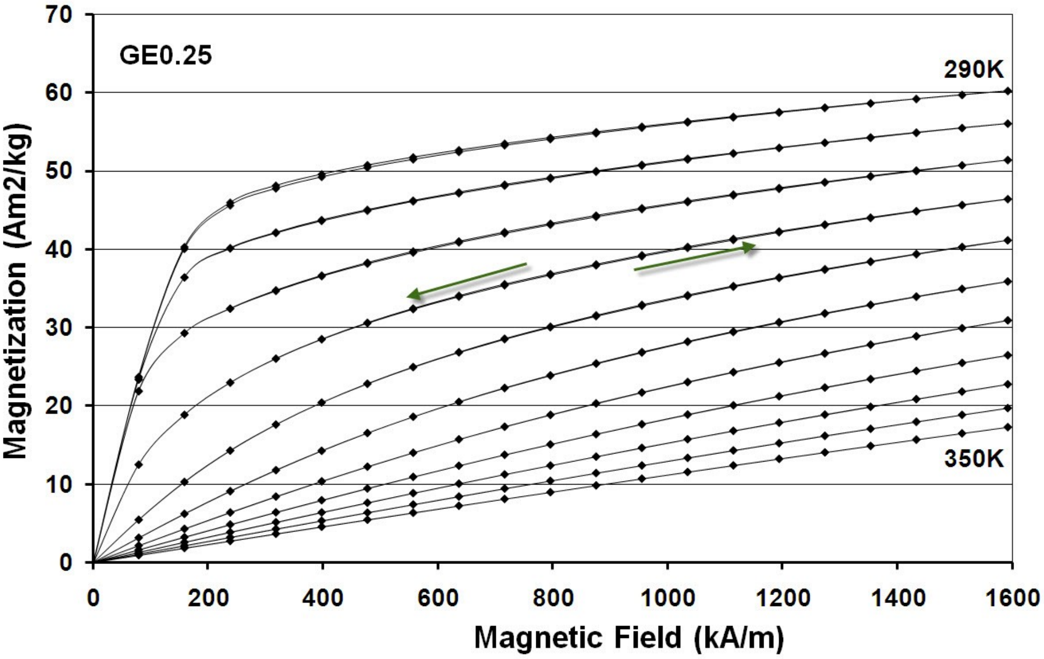

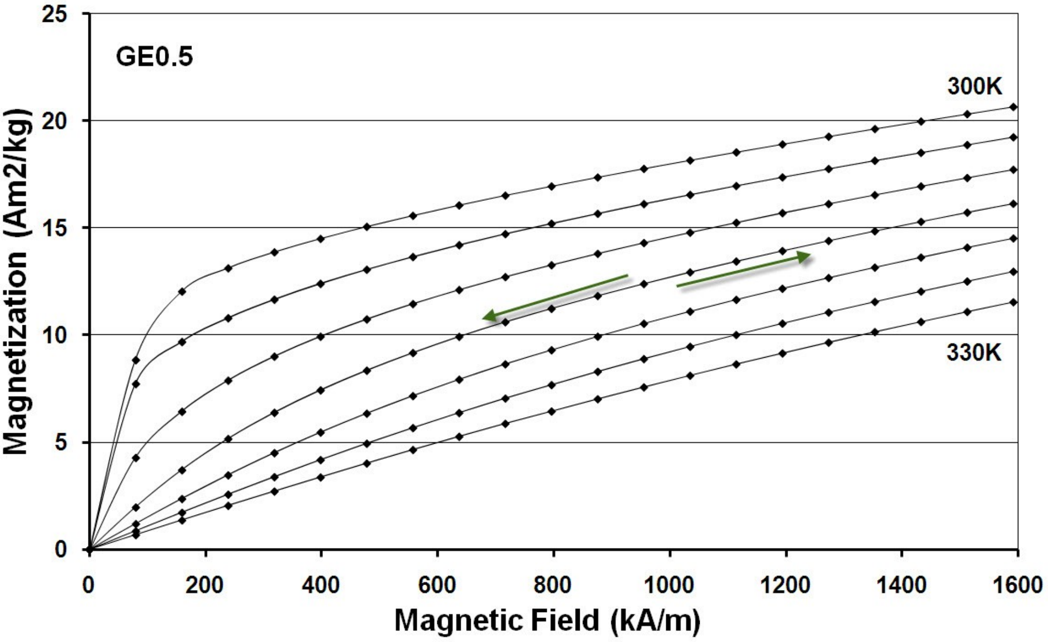

Figure 58: Magnetization versus field curves for the sample GE0, GE0.06, GE0.25 and GE0.5 measured at different temperatures. The arrows indicate the sequence of the measurement. The green area indicates the hysteresis losses that occur during the hysteresis loop.

Figure 59 shows the last hysteresis-loop measurements for the samples GESI0.06, GESI0.125 and GESI0.25. Compared to the reference sample GESI0 we see that the loops look similar to the SI set of samples. With the addition of iron we do not get such a fast reduction in the magnetic hysteresis as in the GE samples. The hysteresis occurs for all three samples with iron in the same range as in the GESI0 sample. For the GESI0.06 the hysteresis starts to occur at 260 K and disappears after 280 K. A good example of the two-step magnetization increase can be seen in the sample GESI0.125 at the temperature 275 K. The second step-like magnetization increase starts at a critical magnetic field of 800 kA/m and then reaches saturation at 1040 kA/m. These two points are shown with the numbers 1 and 2, respectively. During the magnetic-field reduction from its maximum to zero, the magnetization begins to decrease at 720 kA/m (point 3) and returns almost to its original behavior at 480 kA/m (point 4). In the sample GESI0.25 the hysteresis between increasing and decreasing of the magnetic field is even more reduced. The magnetization is reduced by almost 50 % compared to the first three samples, which is expected due to the reduction of the 5:4 phase. For the sample GESI0.5 we expect no hysteresis anymore.

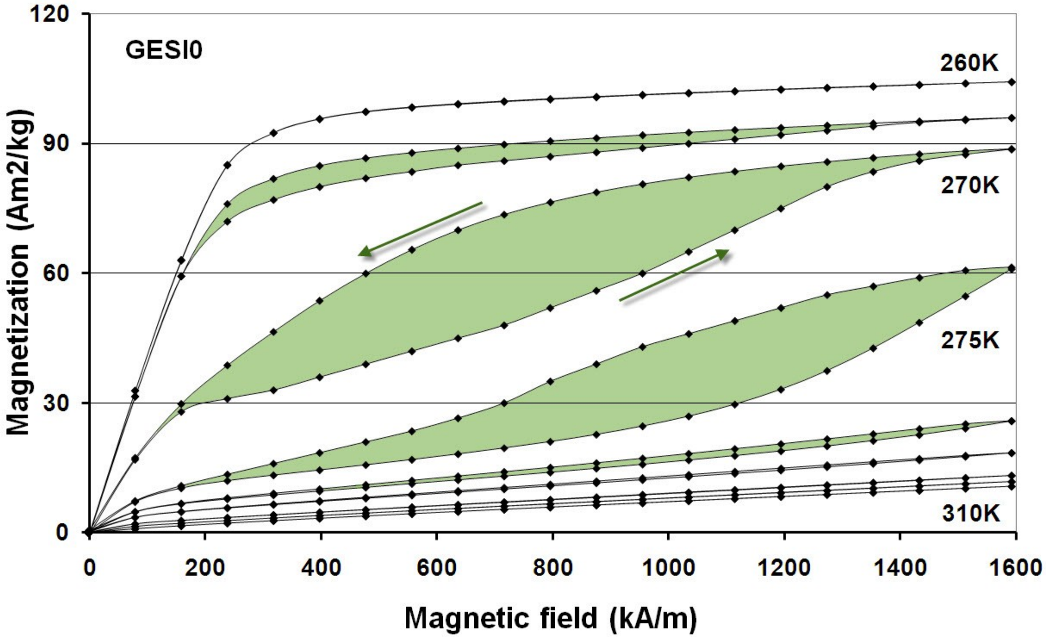
GESI0
260K
270K
275K
310K
Magnetization (Am2/kg)
0
30
60
90
120
Magnetic field (kA/m)
0
200
400
600
800
1000
1200
1400
1600

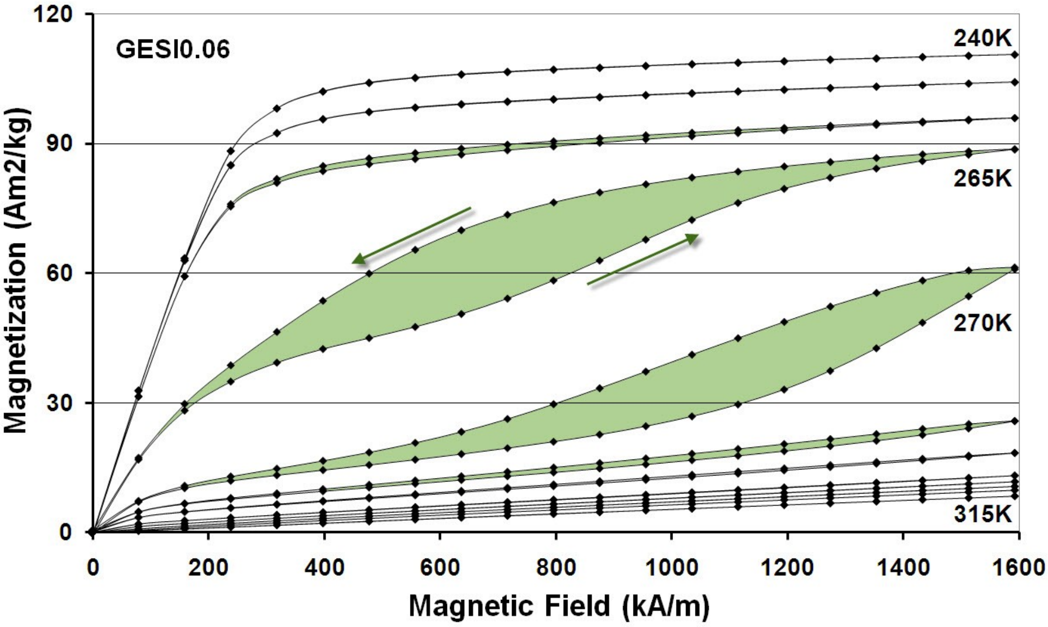
GESI0.06
240K
265K
270K
315K
Magnetization (Am2/kg)
0
30
60
90
120
Magnetic Field (kA/m)
0
200
400
600
800
1000
1200
1400
1600

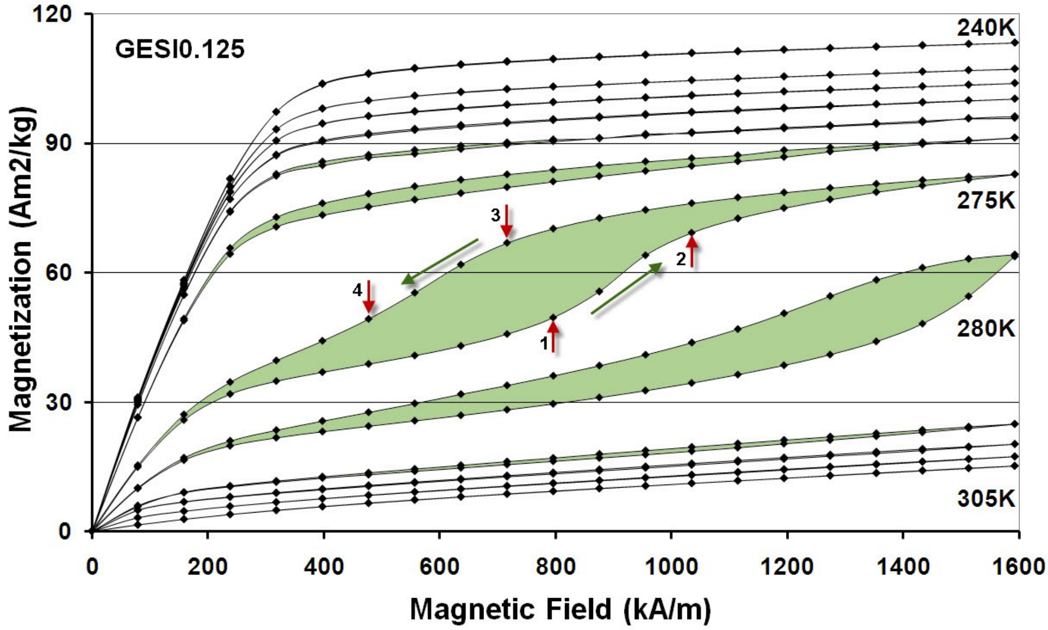
GESI0.125
240K
275K
280K
305K
1
2
3
4
Magnetization (Am2/kg)
0
30
60
90
120
Magnetic Field (kA/m)
0
200
400
600
800
1000
1200
1400
1600

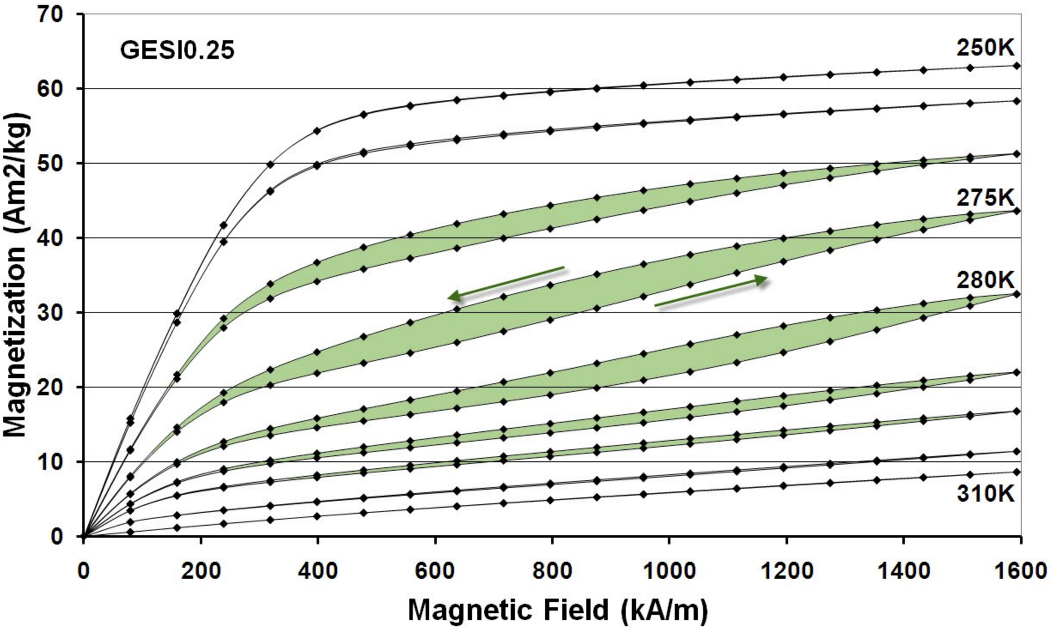

Figure 59: Magnetization versus field curves for the samples GESI0, GESI0.06, GESI0.125 and GESI0.25 measured at different temperatures. The arrows indicate the sequence of the measurement. The green area indicates the hysteresis losses that occur during the hysteresis loop.

4.2.5.3 Magnetic entropy and hysteresis losses calculations

The magnetic entropy changes were calculated from the magnetization loops of each sample. For this we used the modified Maxwell equation that was shown in equation (14). This equation is then numerically integrated by a set of magnetic isotherms taken at different temperatures. From the same set of data we also calculated the hysteresis losses that occur when cycling the sample through an external magnetic field. The hysteresis looses are defined as the area between the increasing field curve and decreasing field curve. We numerically integrate the area under both curves and then subtract them. This is done for every temperature. For our sample to have good properties we need high and wide peaks of the -ΔS_m curve and also small hysteresis losses, the area should be as small as possible between increasing field curve and decreasing field curve. To compare the peaks width we define it by measuring the temperature span between the half maximum -ΔS_m on both sides of the peak, the so-called full width at half-maximum.

Figure 60 shows the calculated magnetic entropy changes and the hysteresis losses for the SI0, SI0.125, SI0.25 and SI0.5. The magnetic entropy change of the reference sample SI0 increases with temperature from 240 K up to 273 K where it has a peak. After that -ΔS_m reduces very sharply back almost to zero. We can see a small hump before 300 K which indicates the SOMT of the sample. The maximum has a value of 15.1 J/kgK and the full width at half-maximum is 6.9 K. We see that the addition of iron decreases -ΔS_m and shifts the peaks to lower temperatures. For the sample SI0.125 -ΔS_m is reduced to 11.1 J/kgK which is reached at a temperature of 265 K, but the width at the half maximum is increased to 12.3 K. This trend is continued with more substituted iron. For the samples SI0.25 and SI0.5 the -ΔS_m peak is at 255 K with a value of 5.1 J/kgK and 4.0 J/kgK, respectively. The full widths at half-maximum are similar to the SI0.125 sample. The hysteresis losses represented in Figure 60 have a similar format. The hysteresis losses peaks are reduced and shifted to lower temperatures with more iron. The reduction and the shifts are higher than for the -ΔS_m peaks. The peaks occur at 260 K for SI0.125 and at 250 K for SI0.25 and SI0.5. Iron reduces the losses compared to the reference sample SI0 by 27 % for SI0.125, 78 % for SI0.25 and 87 % for SI0.5. All the values are presented in Table 11.

The most significant difference in the -ΔS_m and hysteresis losses curves can be seen in the GE samples, which we also saw in the magnetization versus magnetic field measurements. These curves are represented in Figure 61. The magnetic entropy change is reduced by up to 70 % already with the smallest amount of iron. For the sample GE0.5 -ΔS_m peak is reduced to even 96 % of the initial value. The widths of the peaks are also broadened. The peaks of the -ΔS_m mach quite well with the T_C of the samples. The reduction in the hysteresis area in the magnetization versus magnetic field measurements are nicely mirrored in the hysteresis losses curves. The scale in the hysteresis losses vs. temperature graph in Figure 61 has been reduced 3 times. This enables us to see the curves of the sample GE0.25 and GE0.5. The reductions of the losses are in the GE samples the highest with the equal amount of substituted iron. We can still see some hysteresis losses for the sample GE0.06, but for the two following samples these losses are almost zero.

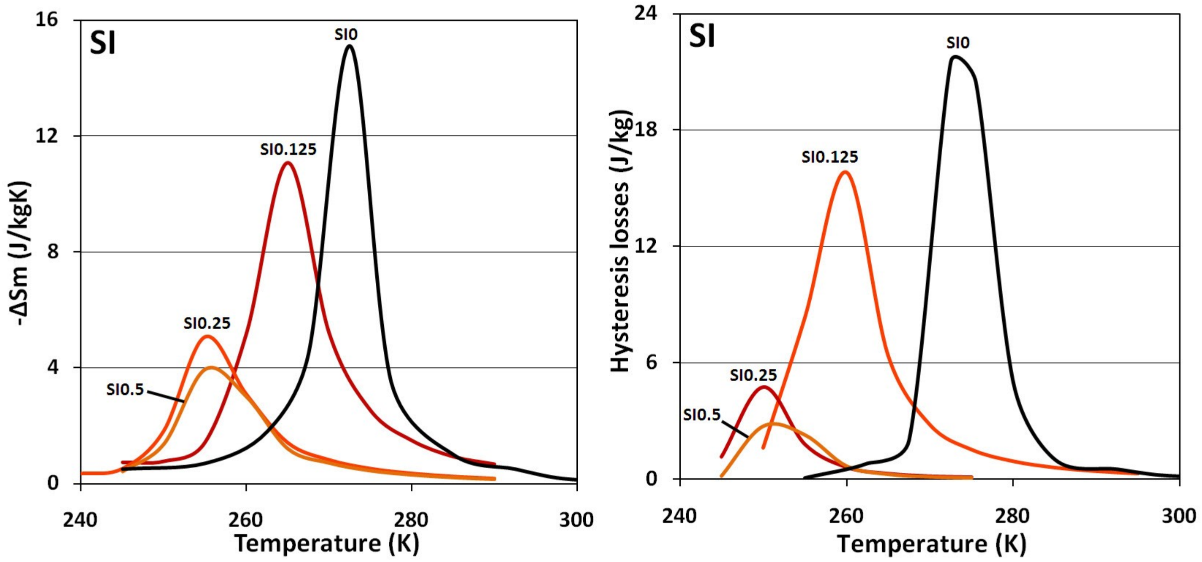

Figure 60: Computed ΔS_m and hysteresis losses for a field change of 1600 kA/m (2T), normalized with respect to the sample mass for the SI set of samples, plotted as a function of temperature.

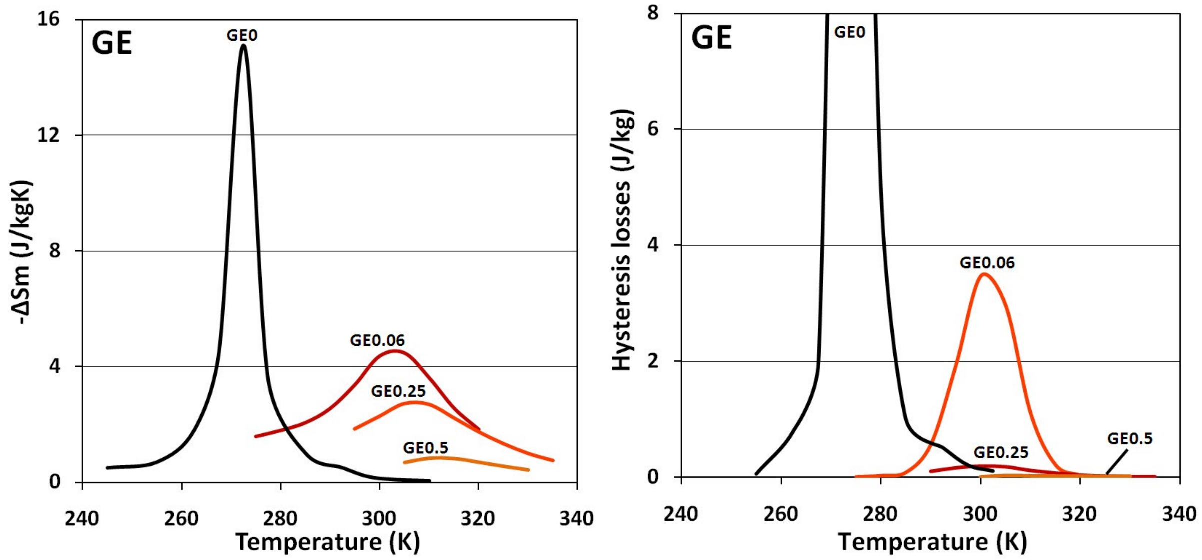

Figure 61: Computed ΔS_m and hysteresis losses for a field change of 1600 kA/m (2T), normalized with respect to the sample mass for the GE set of samples, plotted as a function of temperature.

The smallest reduction of the magnetic entropy change with the substitution of iron is in the GESI set of samples observed (Figure 62). - ΔS_m for the sample GESI0.06 is reduced only to the value 14.1 J/kgK and for GESI0.125 to 9.4 J/kgK. The still high magnetic entropy changes in GESI0.06 are a consequence of the small effect of iron on the reduction of the main phase, as was the case in the previous samples. The temperatures where the peaks occur, are only slightly different to the T_C's of the samples. The peak of GESI0.06 occurs at 268 K, for GESI0.125 at 278 K and for GESI0.25 at 277 K. The full width at half-maximum has changed significantly. From 6.9 K for the sample GESI0 we get an increase to the value of 9.1 K for GESI0.06 and the highest increase of 18.8 K for the sample GESI0.25. This has a positive effect on the refrigeration capacity of the material, which will be discussed in the next section. The high - ΔS_m also have high hysteresis losses, because of the FOMT which can be seen in the second image in Figure 62. Only with high concentrations of iron does the hysteresis losses reduce significantly, but not as in the GE samples.

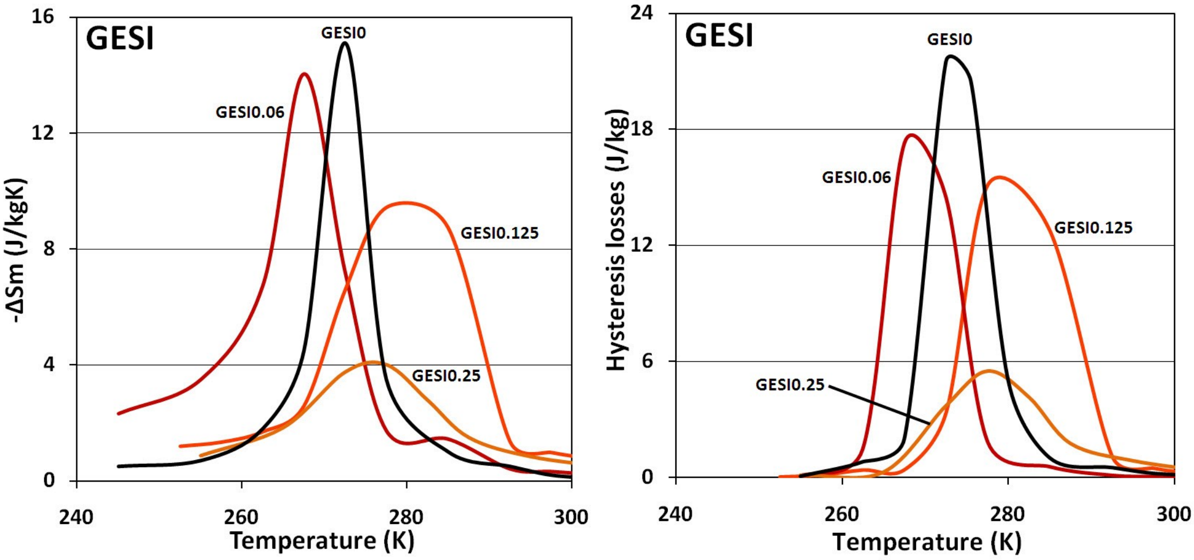

Figure 62: Computed ΔS_m and hysteresis losses for a field change of 1600 kA/m (2T), normalized with respect to the sample mass for the GESI set of samples, plotted as a function of temperature.

There is a difference in the temperatures of the magnetic phase transition which we got out of the thermomagnetic curve and the temperature where the $-\Delta S_m$ curve has a peak. The difference occurs because of two factors. The first is the measuring technique, because the hysteresis curves were measured every 5 K and not every Kelvin like in the thermomagnetic measurements. This can lead to a difference of approximately 2 K. The second reason is the magnetic field at which we measure the $-\Delta S_m$, because in theory these two temperatures are only equal when measured in zero magnetic field. But because there is an insufficient response at zero field to be exactly measured we measure in a magnetic field. The higher the measuring fields the higher the difference between those two temperatures. Usually these errors can be neglected, because the differences are only a few Kelvin. But one has to use caution, because there are examples where the peaks of the $-\Delta S_m$ can be as much as 60 K of the magnetic transition temperature. [175]

We can see that iron is consequently reducing the magnetic entropy change in the sample and the more iron we substitute for one of the semiconducting elements, the higher is the reduction of $-\Delta S_m$. The reduction of these values can be explained easily with the reduction of the main matrix phase and with it the magnetization of the sample. But this simple explanation can be only applicable for the SI and GESI set of samples. The reduction of $-\Delta S_m$ in the GE samples are too fast to be only explained with the phase reduction. Also the SEM images do not show a faster reduction of the 5:4 phase compared to the Si or GESI samples. An additional reduction of the $-\Delta S_m$ can be annotated to the faster reduction of Ge in the main 5:4 phase and thus changing the GE/Si ratio shifting the composition into the right section of magnetic phase diagram, shown in Figure 16. Here we get into the two-phase region where both monoclinic and orthorhombic (I) exits. This reduces $-\Delta S_m$ because only the monoclinic phase structurally transforms and the orthorhombic phase has a simple SOMT. If there is still a partial structural transformation occurring in the GE0.06 sample, there can be no evidence of structural change in the GE0.25 and GE0.5 sample. Here we sifted already so much right in the magnetic phase diagram that no monoclinic structure exits and we have a SOMT form a ferromagnetic phase to a paramagnetic phase as seen in Figure 16. This has a pronoun effect on the magnetic properties.

In all three series we see also that with the reduction of the maximum $-\Delta S_m$ there is a simultaneous broadening of the peaks. If the peaks in the samples with no or very small amounts of iron are very sharp so does the broadness of the peaks increase with the amount of iron. In the high iron concentration samples the shape of the $-\Delta S_m$ curves look similar to the pure Gd curve, which has a SOMT. This suggests that enough iron converts any FOMT into a simple SOMT, because of the shift in concentration. The broadness has a large effect on the calculated refrigeration capacity which is the criterion for a good magnetocaloric material; because the magnetic entropy change does not incorporate the hysteresis losses that are also critical and can reduce the effectiveness of the material up to 20 % [164].

Table 12: The table presents the data for the -ΔS_m and hysteresis losses. The maximum values the temperature where the maximum occurs and the width of the peak at half -$S_m$max (↔) for all three set of samples.

		T_C	-ΔS_m			Hysteresis losses	
		(K)	T_{max}(K)	max(J/kgK)	↔(K)	T_{max}(K)	max(J/kg)
SI	0	272	273	15.1	6.9	273	21.5
	0.125	267	265	11.1	12.3	260	15.8
	0.25	255	255	5.1	9.9	250	4.7
	0.5	254	255	4.0	11.4	250	2.7
GE	0	272	273	15.1	6.9	273	21.5
	0.06	304	304	4.6	28.8	300	3.5
	0.25	306	307	2.8	–	300	0.2
	0.5	311	312	0.9	–	305	0.03
GESI	0	272	273	15.1	6.9	273	21.5
	0.06	268	268	14.1	9.1	268	17.3
	0.125	274	278	9.4	18.8	279	15.1
	0.25	276	277	4.1	14.6	278	5.5

4.2.5.4 (Net) Refrigerant capacity

The method we used for determining the refrigeration capacity (RC), was taken from the article by Provenzano [164]. The RC values were obtained by numerically integrating the area under the -ΔS_m versus T curves, using the temperatures at half-maximum of the -ΔS_m peak as the integration limits.

Figure 63 shows the graph of refrigeration capacity versus the amount of substituted iron. The reference sample 0 has a refrigeration capacity of 114 J/kg for a field change of 2 T. We see that for the SI samples the RC decreases with increasing the amount of iron. Compared to the other two sets of samples it also decreases the fastest. The sample SI0.125 has only 80 J/kg of the refrigeration capacity left. Doubling the amount of iron even halves the previous value. Then in sample SI0.5 the reduction is not so sharp anymore and the curve levels out. For the GE set of samples the RC curve is almost a straight line. The samples GE0.06, GE0.25 and GE0.5 have a RC value of 105, 72, 21 J/kg, respectively. The values were obtained by simulating the course of the curve in GE0.25 and GE0.5, which were missing for a proper calculation. The RC reduces for 18 J/kg every 0.1 atom of iron that is substituted in $Gd_5Si_2Ge_2$. The GESI curve looks quite different from the first two. The RC value even increases with iron. For the sample GESI0.06 the RC is 115 J/kg. If we substitute more iron the value increases even more. We get a maximum of 120 J/kg for the sample GESI0.125. After that the RC decreases as in the SI and GE samples. Here the reduction of the main magnetocaloric phase is so high that it visibility reduces the RC.

The next figure represents the average hysteretic losses taken from the hysteresis losses versus temperature graph. This is an average of the hysteretic values at the same temperature interval in which the RC was calculated from the -ΔS_m. All three curves fall with the increasing amount of iron. Compared to the RC graph we see that the fastest falling curve is the GE curve, where the average hysteretic losses are already zero at GE0.25. The slowest reduction can be seen in the GESI samples. From the reference sample zero with a value of 19 J/kg the numbers reduce to 15.5, 13 and 4.5 for GESI0.06, GESI0.125 and GESI0.25, respectively. A similar reduction can be seen in the SI samples. Both reduce linearly till the samples 0.25. After that the average losses level out as for the GE samples. For the GE samples the average losses reduce 4 times faster than for the GESI and SI samples.

Figure 65 shows the net refrigeration capacity (NRC) of the samples. This represents the true comparison value for magnetocaloric materials, because it also incorporates the hysteresis losses the refrigeration capacity does not. To get the NRC values we have to subtract the average hysteretic losses from the refrigeration capacity. Here the samples with low hysteresis losses gain on the NRC compared to the samples with high hysteresis losses. The reference sample with the highest losses has a NRC of only 95 J/kg. We can clearly see that with the smallest iron substitution (0.06) the highest NRC is achieved from the Ge samples, because the RC almost does not change and stays high. But then the RC decrease is already too great that the small losses could compensate for it and it falls below the reference value. The good values of the GESI samples are reduced, but it loses less RC compared to the reference value, because of its smaller losses. We get a peak at GESI0.125 with a NRC value of 106.6 J/kg, which is the highest value achieved by our group. This increases the reference NRC by 12 %. After that the reduction of the main MC phase also decreases the NRC significantly and almost halves it. The already lower RC values of the SI samples and the quiet high hysteresis losses reduce the NRC values of these samples even more. Only for the sample SI0.5 are the values better than for the other 0.5 values.

We see that which element is substituted has a huge effect on the net refrigerant capacity. We see that just a high -ΔS_m(max) does not give a high RC. Also, a broad peak is important. This is nicely seen in the GESI0.125 sample. Even if the -ΔS_m is 30 % lower than the reference one it has a 3 times broader peak. This produces a 4 % higher RC and because the -ΔS_m(max) is lower than the reference it also has lower hysteresis losses, increasing the NRC to the earlier stated 12 %. We see that the highest effects of lowering the hysteresis losses are in the GE samples. The GE0.06 sample has a lower RC value, but with the average hysteretic losses of only 3 J/kg it has the highest NRC after the smallest substitution of iron, even higher than the reference sample. The two maxima for Ge and GESI are followed by a significant reduction following the trend of the SI samples where the NRC is reduced because of the small -ΔS_m values which are a result of the main matrix phase disappearance and the appearance of the secondary main matrix phase and the grain boundary phases with no visible MCE at room temperature.

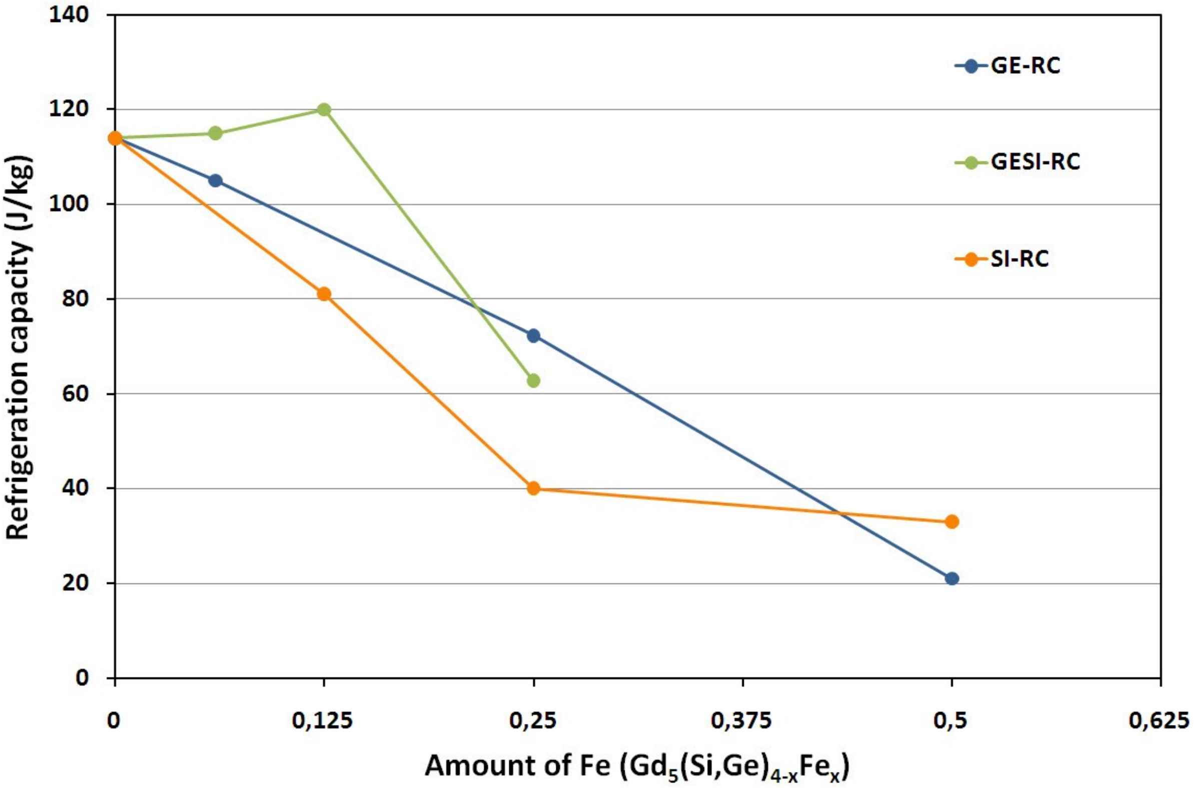

Figure 63: Refrigeration capacity (RC) as a function of the amount of substituted iron for different set of samples.

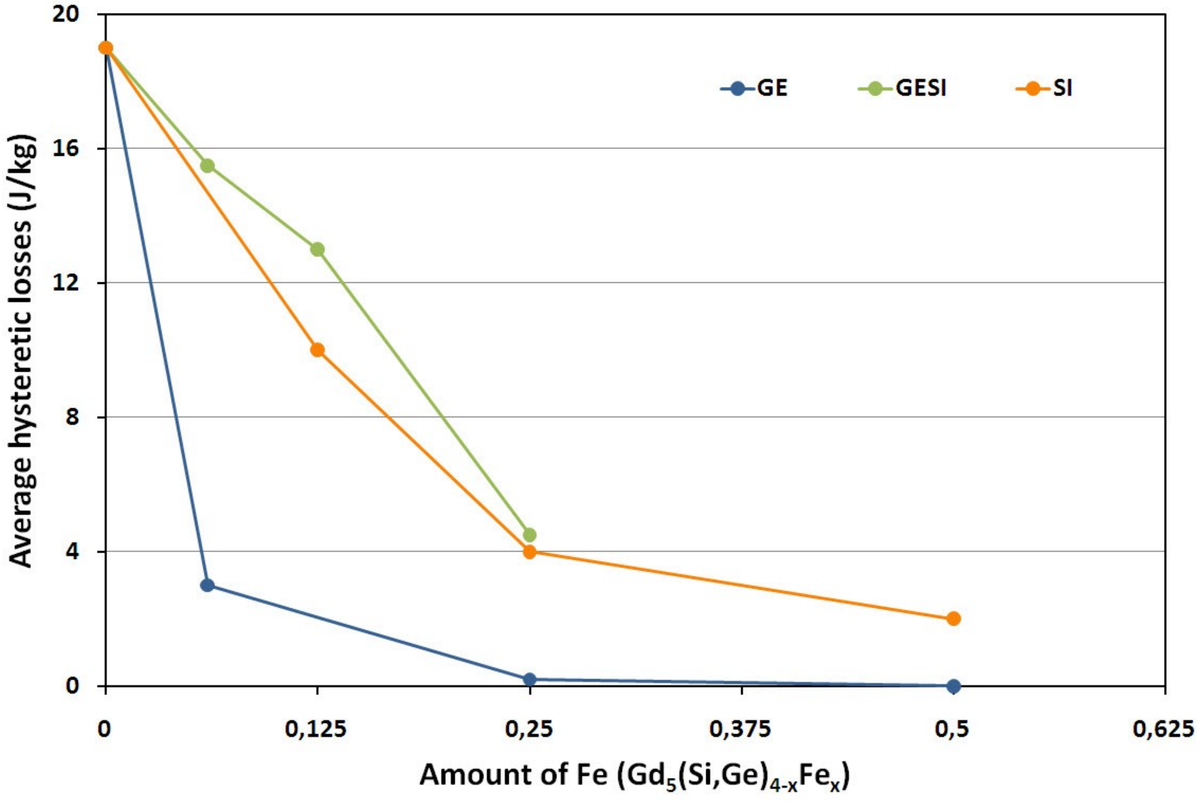

Figure 64: Average losses as a function of the amount of substituted iron for different set of samples.

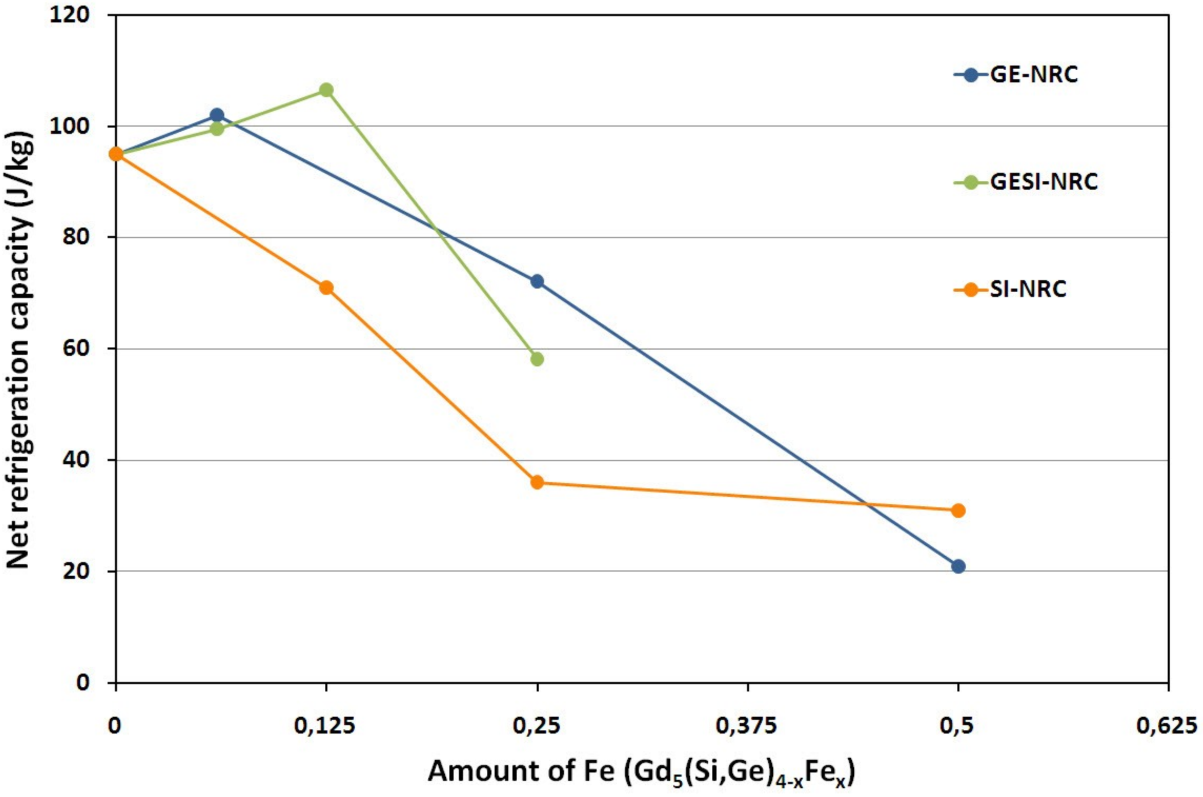

Figure 65: Net refrigeration capacity (NRC) as a function of the amount of substituted iron for different set of samples.

4.2.6 Direct measurement of the adiabatic temperature change (ΔT_{ad})

With these measurements a full characterization of the magnetocaloric properties is achieved. Usually they can be calculated from the heat capacity measurements, but these measurements are more trustworthy than the calculated ones. The reference sample could not be measured, so we will compare our results to the published ones. A direct comparison is difficult because of the different field that was used in our measurements, which were limited by our equipment.

The first graph, presented in Figure 66, shows the results of the sample GESI0.06. The measurements were conducted in such a way that the sample was heated or cooled to a specific temperature and then the magnetic field was fast increased and a temperature difference was measured. These maximum achieved temperatures where then combined into a graph in Figure 66. We can see that when measuring for the first time (green curve) we get, on heating, a maximum ΔT_{ad} at the temperature 266.5 K with the value of 3.1 K. On cooling the maximum is shifted to the temperature 261 K and the maximum increases to 4 K. After cycling through the transition temperature 10 times we see a change in the measured ΔT_{ad} (red curve). On heating the temperature where the maximum appears does not change but the maximum changes up to 3.9 K. On cooling also the temperature where the maximum appears changes to 263 K and the maximum changes to 5.1 K. After cycling for another 20 times though the transition point we see that the curve has stabilized and there are only minor increases in the maximum ΔT_{ad} (violet curve). The increase in ΔT_{ad} after cycling the sample is explained by tension in the sample, which is slowly released with cycling through the transition points. With the change of the crystal structure every time we pass the transition point the tension is more easily removed then in a sample without the structural transformation, because of the slit rearrangements of the atoms. There is an increase of the ΔT_{ad} maximum of 25 % on cooling. We see that there is no significant difference between 10 and 30 cycles, suggesting that there is almost no tension left in the sample. The difference between the temperature where the maximum peak occurs when cooling down or heating up is a result of the structural transformation taking place while passing the transition point. This difference is characteristic for first-order magnetic transformations. The difference is approximately 3.5 K. The maximum ΔT_{ad} also depends on the direction of changing the temperature while measuring. If we are cooling the sample while measuring the ΔT_{ad} is higher than the ΔT_{ad} when heating the sample. This is because of the latent heat that occurs on the structural transformation. When we heat the sample the heat is consumed by the transformation and thus ΔT_{ad} is lower. When we cool the sample heat is released and this increases the ΔT_{ad}. The value of 5.1 K we achieve with this alloy is, compared to the 7.4 K achieved at 2 T, [8] significantly lower. This cannot be explained by the reduction of the 5:4 phase, but must be explained with the discrepancy that is occurring when comparing calculated values with direct measurements. It is known that the calculations from the FOMT can exceed the real values. In Figure 67 we see the adiabatic temperature as a function of the magnetic field at different temperatures, while cooling and heating and as an initial measurement and after 30 cycles. Because our magnetic loop measurements have been conducted while heating up we achieve a similar peak of the ΔT_{ad} and -ΔS_m with 266.5 K and 268 K, respectively.

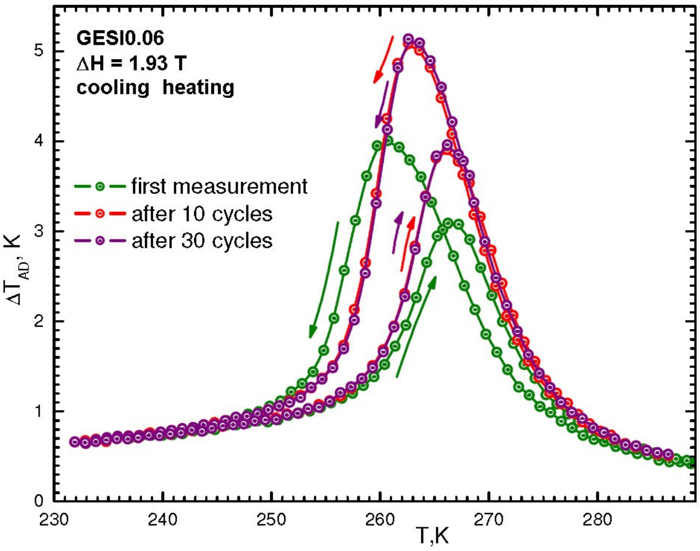

Figure 66: ΔT_{ad} vs. temperature measurements for the sample GESI0.06. The arrows show the direction of heating or cooling of the sample.

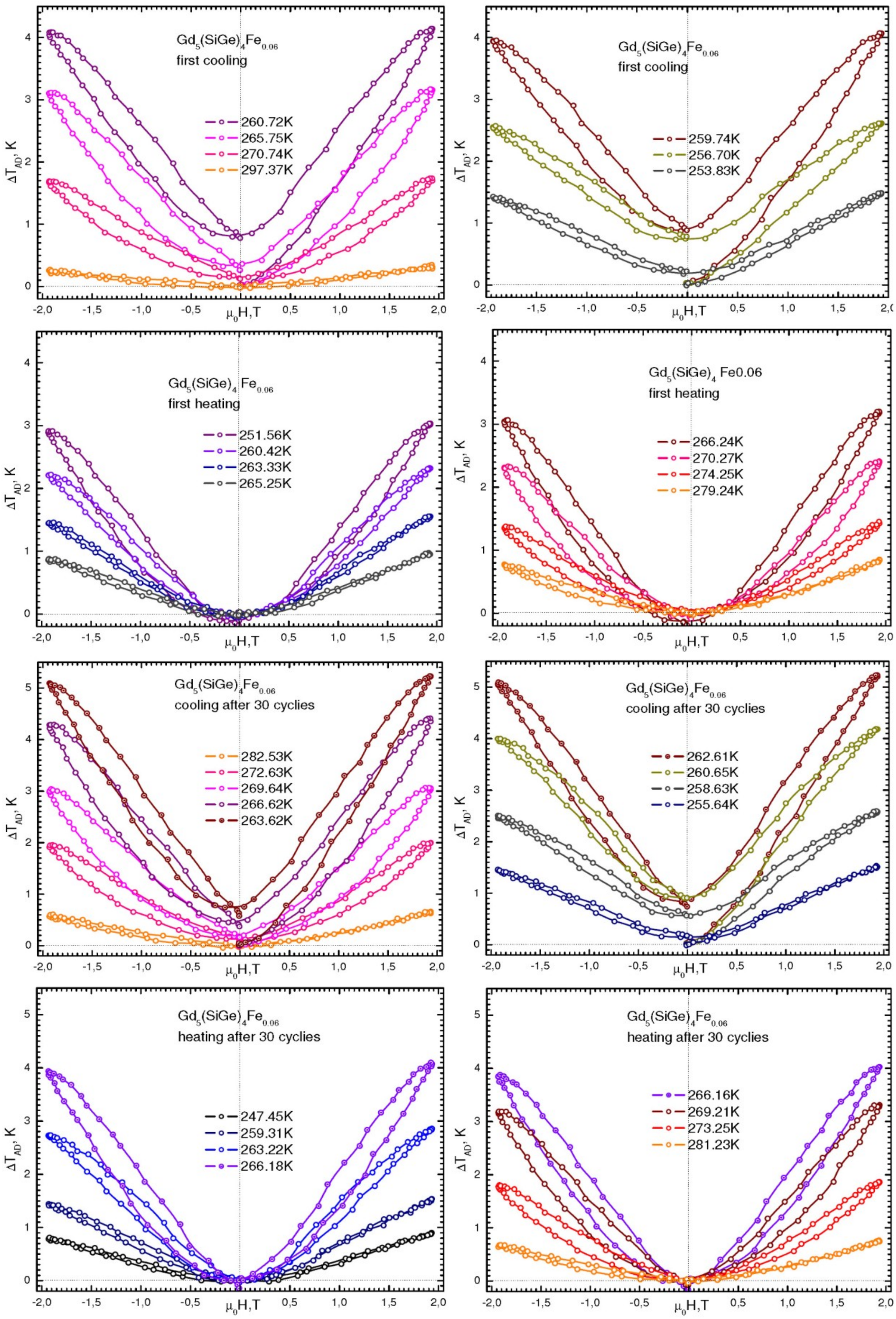

Figure 67: Adiabatic temperature change as a function of the magnetic field for the sample GESI0.06. The first two represents the first cooling of the sample and the third and fourth the first heating of the sample. Image five to eight show the measurements of the same sample after 30 cycles.

The next two images in Figure 68 belong to the adiabatic temperature change measurement for the samples GE0.125 and GE0.25. These two samples have been described as a SOMT in the magnetic measurements because of the absence of hysteresis losses. This can also be confirmed with these measurements. It is clear that there is no difference in the maximum adiabatic temperature change between cooling (blue curve) and heating (red curve) for both samples compared to the GESI0.06 sample. For the sample GE0.125 the peak occurs at 299 K with a value of 2.75 K. The peak of the sample GE0.25 is, as expected, lower with a value of 2.2 K at 302 K.

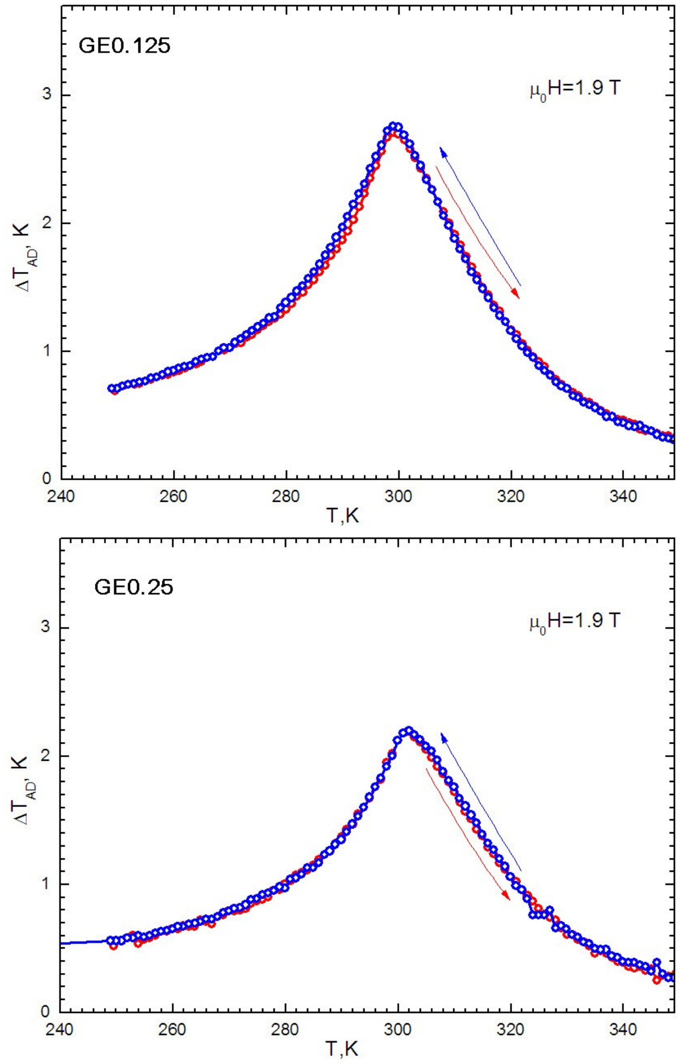

Figure 68: Adiabatic temperature change as a function of temperature for the samples GE0.125 and GE0.25.

From the SI samples we measured the sample SI0.125. The result can be seen in Figure 69. It is clear that we have two transition points. The first one is the FOMT at 277 K and the second is a SOMT at 297 K. Both temperatures are for heating the sample. The ΔT_{ad} peaks are at 2.3 K for the FOMT and at 1.85 K for the SOMT. As for the cooling the values are 3.35 K at 275 K (FOMT) and 1.35 K at 297 K (SOMT). The difference between the cooling and heating because of the FOMT can be nicely seen. The ΔT_{ad} peak is in between the GESI and the GE samples which is what we would expect comparing the ΔS_m peaks.

The ΔT_{ad} results show a reduction compared to the reference sample. This is in agreement to the ΔS_m results shown earlier. It also follows the same shape of the curve as the ΔS_m curves; the lower the value the broader the peak. This makes the material more useful because of the broader working temperature compared to $Gd_5Si_2Ge_2$. The distinction between the SOMT and FOMT can also be clearly seen. There is a hysteresis in the measurements of the GESI and SI samples and they show the two peaks belong to two phases. The first peak belongs to the FOMT and the second to the SOMT. There is no structural transformation observable in the GE samples and we see only the SOMT. To get reliable results we have to cycle the sample a few times through the transition point to remove any tension that is present in the sample because of the fast cooling after the heat treatment. The samples are all very brittle and all break after the measurement.

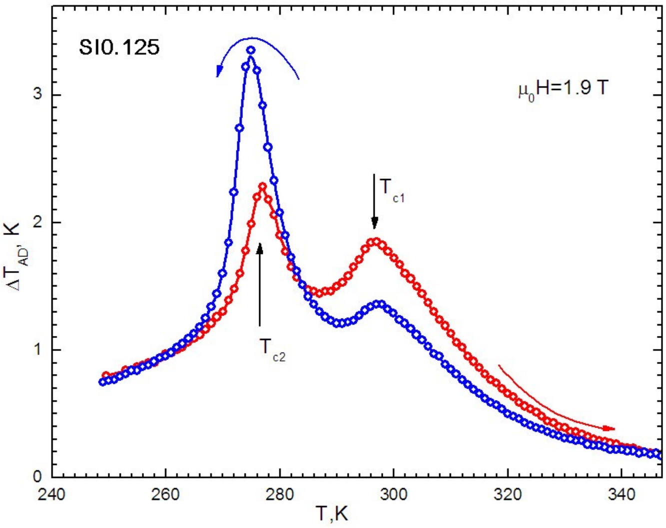

Figure 69: Adiabatic temperature change as a function of temperature for the samples SI0.125

4.2.7 TEM results

The transmission electron microscopy research was performed with the goal to observe the reported twin boundaries that occur in the $Gd_5Si_2Ge_2$ sample and also to investigate any other anomalies that cannot be observed with an SEM that could contribute to an explanation of the properties of the sample. Also, we wanted to verify Provenzano's statement that the addition of Fe creates a magnetic nanostructure, based on the superparamagnetic behaviour of the material at higher temperature. [164]

4.2.7.1 $Gd_5Si_2Ge_2$

TEM images were taken on a JOEL TEM 2010 F. Figure 70 shows a bright-field image of the $Gd_5Si_2Ge_2$ sample. We can observe planar defects all over the sample. The lines are twin boundaries. From the morphology of the defects it is very clear that a substantial number of dislocations are present (the curved lines with the non-uniform contrast, indicating the strain fields). The isolated "spots" with black-and-white contrast can be interpreted as dislocations that are perpendicular to the normal of the prepared disc sample. As well as these dislocations there are some parallel lines with a more uniform contrast, which can be attributed to planar defects, such as stacking faults or twin boundaries. However, for an exact determination of these types of defects a much more detailed examination is required.

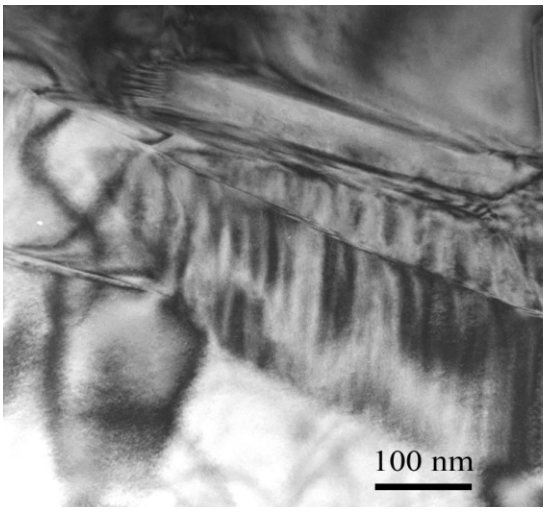

Figure 70: Bright field image of the Gd5Si2Ge2 sample.

Figure 71 shows the diffraction pattern of $Gd_5Si_2Ge_2$ and we can confirm the existence of twins in this material. The angle between the twins is 25°. In Figure 72 we have indexed the diffraction pattern and defined Z = [2 -4 7].

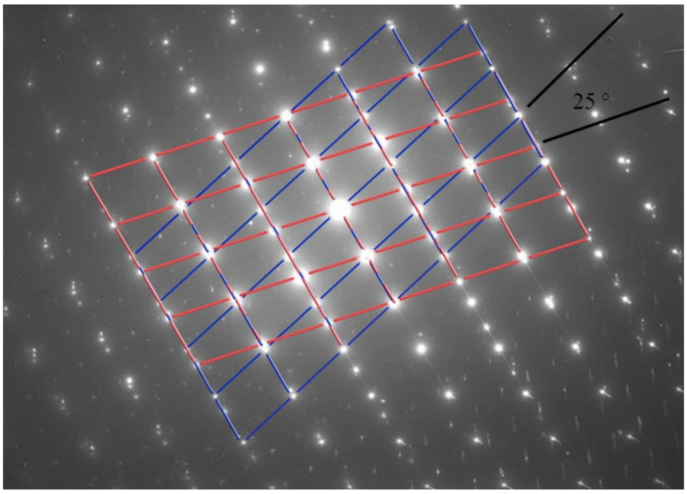

Figure 71: Diffraction pattern of a twin boundary.

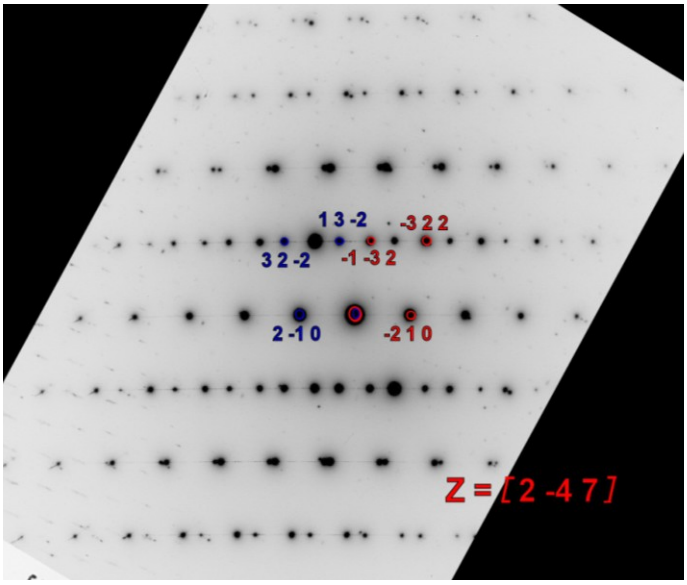

Figure 72: Indexation of the diffraction pattern.

4.2.7.2 $Gd_5(Si,Ge,Fe)_4$

Provenzano's earliest report on hysteresis losses remarked that the addition of Fe creates a magnetic nanostructure, based on the superparamagnetic behavior of the material at higher temperatures. The same authors also speculated that such samples might contain an inhomogeneous distribution of vacancies or defects in the Gd–Ge–Si matrix phase. For this reason we prepared samples for a TEM investigation. Figure 73 shows a high-resolution TEM micrograph of a powder sample of $Gd_5Si_2Ge_{1.75}Fe_{0.25}$ (GE0.25). The inset shows a fast Fourier transform (FFT) of the area indicated by the white square. Surprisingly, the micrograph exhibits the characteristics of an amorphous structure; there are no lattice fringes and no indication of any long-range order. The FFT, with its diffuse rings, confirms the amorphous nature of this area of the sample. A chemical analysis of this amorphous phase gave $Gd_{59}Si_{21}Ge_{20}$, with only trace amounts of Fe being detected.

The technique used to prepare this TEM specimen precludes any possibility of us knowing where exactly the amorphous regions are, relative to the other phases, or any assessment of the amount of amorphous material. Furthermore, an x-ray diffractogram did not indicate that there was any amorphous material in the sample. However, the x-ray penetration depth is limited and x-ray diffraction is not able to reliably confirm the presence of a few percent of any particular phase or structure. From this we can conclude that the regions of amorphous material must represent a very small fraction of the material.

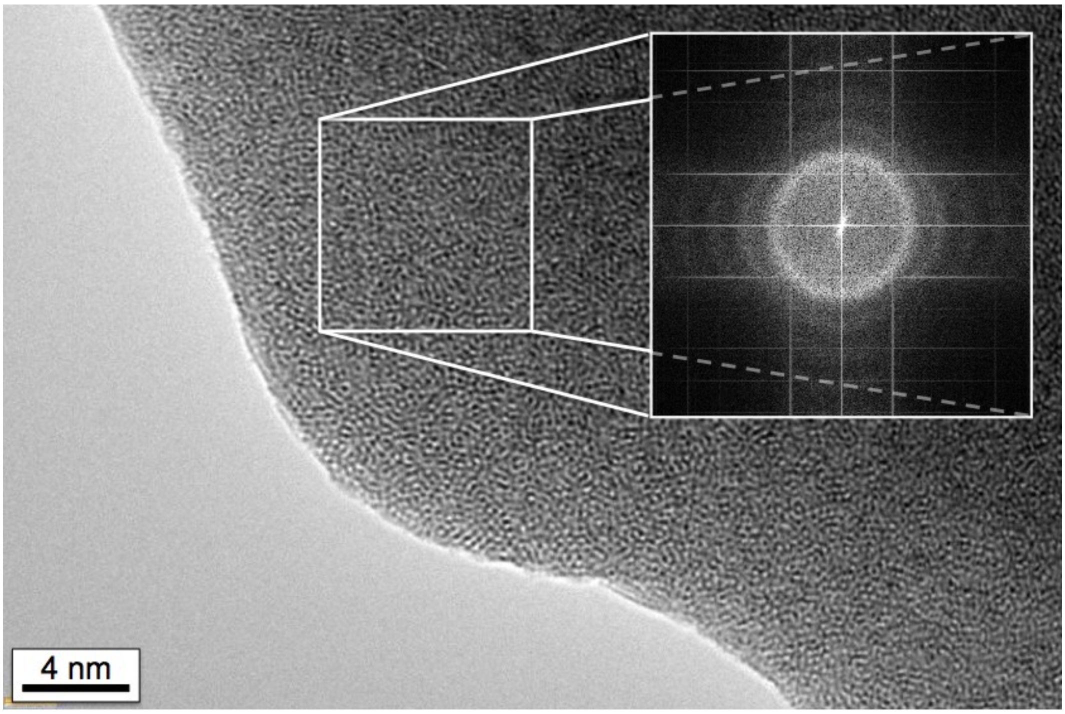

Figure 73: High-resolution TEM micrograph of a powder sample of $Gd_5Si_2Ge_{1.75}Fe_{0.25}$ (GE0.25) on a carbon-coated copper grid and the corresponding electron diffraction pattern.

Figure 74 shows a grain-boundary region from the sample $Gd_5Ge_2Si_{1.875}Fe_{0.125}$ (SI0.125) from a conventionally prepared sample. The insets are the respective selected-area electron-diffraction (SAED) patterns. The right-hand grain has the composition $Gd_{55}Ge_{25}Si_{20}$, while the left-hand grain is the Fe-containing $Gd_{35}Si_{25}Fe_{30}Ge_{10}$. The left grain is clearly the grain-boundary phase identified from the SEM. This figure shows clearly that there is no evidence of any nanoscale grain-boundary phases, no nanosized grains or unusual features. In the left-hand inset, where the SAED pattern of the iron-containing phase is displayed, narrow circles can be resolved. Such a detail is characteristic of randomly oriented nanocrystals.

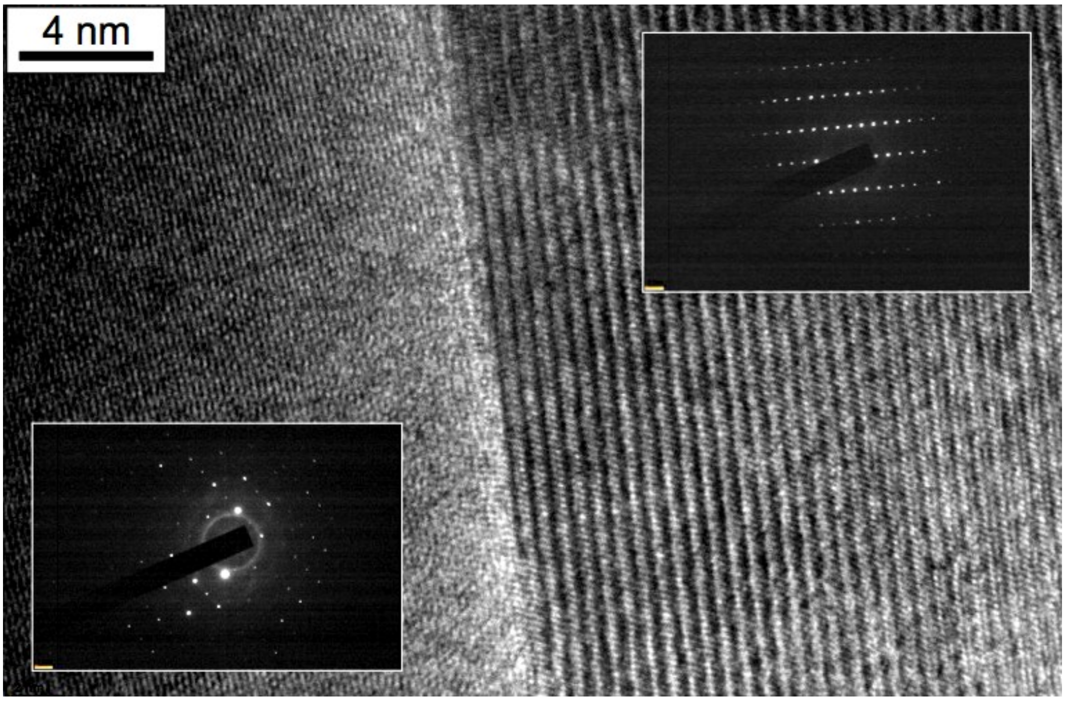

Figure 74: High-resolution TEM micrograph of a grain-boundary region from the sample $Gd_5Ge_2Si_{1.875}Fe_{0.125}$ (SI0.125) and the corresponding electron-diffraction patterns.

Closer inspection of the diffraction pattern suggests that the rings could be attributed to the presence of α-iron. In addition to the circles with their center at the central spot, an echo (a diffuse circle) can also be observed around the strong diffracting spots, characteristic of double-diffraction. From these observations we can conclude that α nanoparticles are present in the upper and lower sections of the TEM sample, but the method of sample preparation must always be considered here, since ion milling can be responsible for such artifacts. There is, however, clear evidence of a crystallographic relationship between the two grains; most probably we are dealing here with a low-angle grain boundary.

Figure 75 is a lower-resolution TEM micrograph of the same sample as Figure 74, this time showing the presence of some crystal defects. From the morphology of the defects it is very clear that a substantial number of dislocations are present (the curved lines with the non-uniform contrast, indicating the strain fields). The isolated "spots" with black-and-white contrast can be interpreted as dislocations that are perpendicular to the normal of the prepared disc sample. As well as these dislocations there are some parallel lines with a more uniform contrast, which can be attributed to planar defects, such as stacking faults or twin boundaries. This TEM investigation strongly suggests that the structure of Fe-substituted materials is a very complex one, and in need of intensive study.

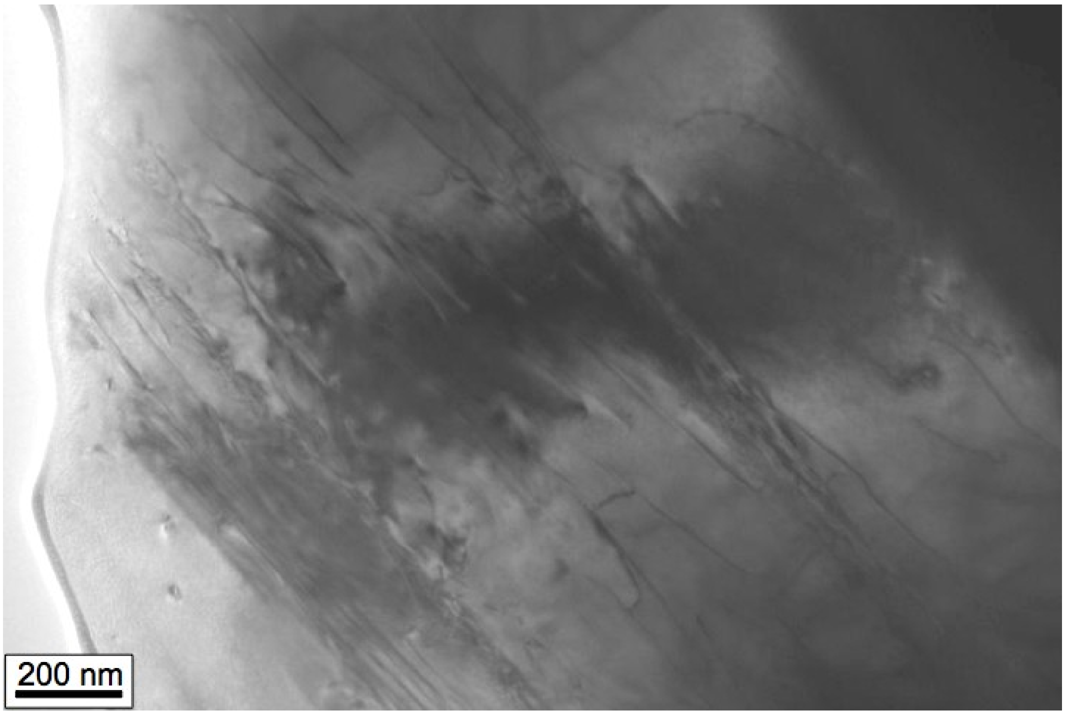

Figure 75: TEM micrograph of $Gd_5Ge_2Si_{1.875}Fe_{0.125}$ (SI0.125) showing the presence of some crystal defects.

5 Conclusions

In our investigations we wanted to compare different preparation techniques for the $Gd_5Si_2Ge_2$ alloy which would improve the properties of this material. Also we researched systematically how iron affects the system, by substituting Si or Ge or both with iron using different amounts. The results confirmed previous findings and also new interesting effects of iron on the system. The most important contribution of this thesis is an increase of the net refrigerant capacity compared to the reference $Gd_5Si_2Ge_2$ alloy which is essential to the magnetocaloric effect and increases the possibility of using these kinds of alloys as a working material in magnetic refrigeration.

Preparing the initial $Gd_5Si_2Ge_2$ alloy we found that the cooling rate has a profound effect on the macrostructure, with the formation of a "sinew" effect on the upper surface of the button for the faster cooled sample and a smoother surface consisting of fairly regular pentagons and hexagons for the slower cooled sample. The crystal structures of the main phases in the buttons were found to be largely independent of cooling rate, and a heat treatment at 1300°C for one hour was sufficient to produce the single-phase crystal structure.

Different techniques to produce this alloy failed to achieve the desired structure. The direct method of mechanical alloying $Gd_5Si_2Ge_2$ from pure elements was proven to be a very time consuming and not economical, because of the ductile nature of gadolinium. Even after 100 h no homogeneity in the sample could be observed. The same fate struck the melt spinning technique. Because of its inability to produce an amorphous phase and with it interesting properties we also abandoned this method. We did succeed to developing a melt spinning crucible that has the ability to heat the sample to over 1800 °C and not contaminate the sample with graphite.

When we add iron to the sample we see a pronounced effect on the macrostructure and microstructure of the sample. These effects are only affected by the amount of iron and not which element we substitute, Si, Ge or Si and Ge. The sample with no iron exhibits regular pentagons and hexagons reminiscent of a buckyball, which is characteristic for the solidification of so-called semi metals. If we substitute ¼ of the element the sample's surface shows a sinew effect which is because of the existence of two phases with different temperature expansion coefficients and if we substitute ½ of the element the sample has a smooth upper surface, much more characteristic of an intermetallic arc-melted button. The macrostructure shows that the addition of iron produces a new matrix phase with the composition $Gd_5(Si,Ge)_3$. This new matrix phase appears at the expanse of the $Gd_5(Si,Ge)_4$ which is slowly disappearing. With the appearance of the new phase also a grain boundary phase appears. No iron can be found in ether of the matrix phases. All the iron can be found in the grain boundary phases. Iron extracts mostly Si out of the main phase, forming a silicid and thus changing the Gd:(SI,Ge) ratio in the main matrix phase.

The XRD confirmed what we saw in the microstructure. A slow disappearing of the 5:4 phase with the increase of substituted iron, which is producing the new 5:3 matrix phase and the iron rich grain boundary phase with a unknown crystal structure. We also saw that the smallest amount of iron did not suppress the formation of monoclinic phase and a structural transformation was seen in all tree low iron concentration samples. Only higher concentrations of iron in the GE samples do suppress the orthorhombic monoclinic transformation as can be seen in the magnetic and adiabatic temperature measurements. This we explain with the shift of the Si/Ge ratio to the two phase region in the magnetic phase diagram. The Si/Ge ratio in the SI and GESI samples shifts in the opposite direction.

The substitution of different elements with iron has a very large effect on the magnetic properties. Substituting silicon changes the magnetic transition point of the sample to lower regions. The more iron we substitute the lower the T_C. If we substitute germanium with iron we get an increase of the T_C and if we substitute both elements (Si and Ge) the transition temperature almost does not change, even with larger amounts of iron. These changes can be explained by the change in the composition of the main phase with adding iron which shifts the T_C of the sample. With this we can tailor our T_C from 250 to 320 K and make the material suitable for different applications with different working temperatures. The magnetization versus magnetic field measurements and the calculations of $-\Delta S_m$ and hysteresis losses afterwards, showed that the magnetization of the sample is reduced in all three sets of samples by increasing the amount of iron, which is logical because the main phase is reduced and the new phase is already paramagnetic and does not contribute to the magnetization because of its magnetic transition point at around 100 K. The same effect can be seen in the -ΔS_m peaks, they all decrease, but become broader. The GE samples decrease faster because the shift in the composition changes the transition point of the alloy to a SOMT, while the SI and GESI still retain their FOMT. This reflects also on the hysteresis losses of the samples. Because of the SOMT they are the lowest in the GE samples and the highest in the GESI samples.

Comparing the net refrigeration capacity of the samples we see that in the GESI samples, although the losses are still high, we get an increase because of the broadening of the -ΔS_m peak. We achieve an increase of the NRC of 12 %, compared to the reference $Gd_5Si_2Ge_2$ sample, for the sample GESI0.125. After that the reduction because of the diminishing of the 5:4 phase is too fast to still have a good NRC.

The adiabatic temperature changes show a similar picture to the -ΔS_m. All the peaks decrease with more iron. The GE samples decrease faster than the GESI sample, but they become broader. The broadening of the peak increases the usability of the alloy over a wider temperature area than the reference alloy. We see also that the material needs training to achieve its maximum value, because of the tension that stayed in the sample after quenching the alloy.

TEM results confirmed the existence of twin boundaries in the $Gd_5Si_2Ge_2$ sample and also a substantial number of dislocations. The TEM investigations of the iron-substituted sample showed an amorphous structure which was not visible with XRD and presumably only a small amount is present in the sample. We also could not find any evidence of any nanoscale grain-boundary phases, no nanosized grains or unusual features. We found dislocations and some parallel lines with a more uniform contrast, which can be attributed to planar defects, such as stacking faults or twin boundaries.

6 Acknowledgements

My highest gratitude to Prof. Dr. Spomenka Kobe for giving me the opportunity to write this thesis, for taking me into her group and mentor me through this. Also I like to specially thank Assistant Professor Paul J. McGuiness which, as my working mentor, did an excellent job in showing me what is really important and encouraging me when it did not come as expected.

I would also like to thank the Institute Jožef Stefan, The Slovenian Ministry of Science and Higher Education and CMA for financially supporting my research.

What I could not do by myself, I ask my colleagues for help: Dr. Goran Dražič for my TEM results and Mrs. Medeja Gec for teaching me the TEM sample preparation, Dr. Norbert Mattern, Dr. Helmut Ehrenman and Mr. Edi Kranjec for the XRD results, Bjoern Schwartz for the PPMS results, Dr. Zoran Samardžija for SEM advices and Dr. Konstantin Skokov for the adiabatic temperature changes results. My dear thanks to our magnetic group who always questioned my work: Tina doing it the hard way, Matej doing it the quiet way, Andraž doing it the funny way and Tone doing it the "domače" way. Thanks goes to all the other colleagues that tried to put some sense in my head and making this journey easier.

A big thank you to my parents and brother and a very special thank you goes to my wife Lea, without whom I would not be where I am today and for giving me our two wonderful sons which gave me a new meaning in life. IOU big time.

7 References

[1] Poster, Magnetic Cycle Refrigeration, Cryofuel Systems Group, University of Victoria (1999)
[2] Warburg, E. *Ann. Phys. (Leipzig)* **13**, 141 (1881).
[3] Debye, P. *Ann. Phys.* **81,** 1154 (1926).
[4] Giauque, W. F. *J. Am. Chem. Soc.* **49,** 1864 (1927).
[5] Giauque, W. F.; MacDougall, D. P. *Phys. Rev.* **43,** 768 (1933).
[6] Brown, G. V. *J. Appl. Phys.* **47,** 3673 (1976).
[7] Zimm, C.; Jastrab, A.; Sternberg, A.; Pecharsky, V. K.; Gschneidner, K. Jr.; Osborne, M. and Anderson, I. *Adv. Cryog. Eng.* **43,** 1759 (1998).
[8] Pecharsky, V. K.; Gschneidner, K. A. Jr. *Phys. Rev. Lett.* **78,** 4494 (1997).
[9] Pecharsky, V. K.; Gschneidner, K. A. Jr. *J. Magn. Magn. Mater.* **200,** 44 (1999).
[10] Gschneidner, K. A. Jr.; Pecharsky, V. K. *Annu. Rev. Mater. Sci.* **30,** 387 (2000).
[11] Gschneidner, K. A. Jr.; Pecharsky, V. K. *Mater. Sci. Eng.* A **287,** 301 (2000).
[12] Tishin, A. M. and Spichkin, Y. I. *The Magnetocaloric Effect and its Applications* (Bristol: Institute of Physics Publishing, 2003).
[13] Gschneidner, K. A. Jr.; Pecharsky, V. K.; Tsokol, A. O. *Rep. Prog. Phys.* **68,** 1479 (2005).
[14] Tishin, A. M. *J. Magn. Magn. Mater.* **316,** 351 (2007).
[15] Gschneidner, K. A. Jr.; Pecharsky, V. K. *Inter. Jour. Refrige.* **31,** 945 (2008).
[16] Tishin, A. M. *Cryogenics* **30,** 127 (1990).
[17] Pecharsky, V. K.; Gschneidner, K. A. Jr.; Pecharsky, A. O.; Tishin, A. M. *Phys. Rev. B* **64,** 144406 (2001).
[18] Tishin, A. M. *J.Alloys Comp.* **250,** 635 (1997).
[19] Tishin, A. M.; Gschneidner, K. A. Jr.; Pecharsky, V. K. *Physical Review B - Condensed Matter and Materials Physics* **59 (1)**, 503 (1999).
[20] Cooke, A. H. *Proc. Roy. Soc.* A **62**, 269 (1949).
[21] Bleaney, B. *Proc. Roy Soc.* A **204**, 203 (1950).
[22] Cooke, A. H.; Duffus, H. J.;and Wolf, W. P. *Philos. Mag.* **44**, 623 (1953).
[23] Ishimoto, H.; Nishida, N.; Furubayashi, T.; Shinohara, M.; Takano, Y.; Miura, Y.; and Ono, K. *J. Low Temp Phys.* **55**, 17 (1984).
[24] Clark, A. E. and Alben, R. S. *J. Appl. Phys.* **41**, 1195 (1970).
[25] Levitin, R. Z.; Snegirev, V. V.; Kopylov, A. V.; Lagutin, A. S. and A. Gerber *J. Magn. Magn. Mat.***170**, 223 (1997).
[26] Shull, R. D.; McMichaek, R. D.; Ritter, J. J. *Nanostruct. Mater.* **2**, 205 (1993).
[27] Numazawa, T. and Sato, A., *Proc. ICEC 17* **1,** 287 (1999).
[28] Hashimoto, T.; Kuzuhara, T.; Sahashi, M.; Inomata, K.; Tomokiyo, A. and Yayama, H. *J. Appl. Phys.* **62**, 3873 (1987).
[29] Tishin, A. M.; Gschneidner, K. A. Jr.; Pecharsky, V. K. *Phys. Rev. B* **59**, 503 (1999).
[30] Takeya, H.; Pecharsky, V. K.; Gschneidner, K. A. Jr.; Moorman, J. O. *Appl. Phys. Lett.* **64**, 2739 (1994).
[31] Barclay J. A.; Overton, W. C.; Zimm, C. B. *in LT-17 Contributed Papers, (Elsevier Science, Amsterdam)* p. 157 (1984).
[32] Zimm, C. B.; Ludeman, E. M.; Serverson, M. C.; Henning, T. A. *Adv. Cryog. Eng.* **37B**, 883 (1992).
[33] Tomokiyo, A.; Yayama, H.; Wakabayashi, H.; Kuzuhara, T.; Hashimoto, T.; Sahashi, M.; Inomata, K. *Adv. Cryog. Eng.* **32**, 295 (1986).
[34] Dan`kov, S. Y.; Tishin, A. M.; Pecharsky, V. K.; Gschneidner, K. A. Jr. *Phys. Rev. B* **57**, 3478 (1998).
[35] http://www.goodfellow.com (accessed 14.03.2009).
[36] Pecharsky, V. K.; Gschneidner, K. A. Jr. *J. Alloys Compounds* **260,** 98 (1997).
[37] Choe, W.; Pecharsky, V.K.; Pecharsky, A. O.; Gschneidner, K. A. Jr.; Young, V. G. Jr.; Miller, G. J. *Phys. Rev. Lett.* **84,** 4617 (2000).
[38] Morellon, L.; Blasco, J.; Algarabel, P. A.; Ibarra, M. R. *Phys. Rev. B* **62,** 1022 (2000).
[39] Pecharsky, V. K.; Gschneidner, K. A. Jr. *Appl. Phys. Lett.* **70,** 3299 (1997).
[40] Thuy, N. P. *Solid State Sci. Technol. (Malaysia)* **10,** 1 (2002).
[41] Zhuo, Yi.; Chahine, R.; Bose, T. K. *IEEE Trans. Magn.* **39,** 3358 (2003).
[42] Giguère, A.; Foldeaki, M.; Gopal, B. R.; Chahine, R.; Bose, T. K.; Frydman, A.; Barclay, J. A. *Phys. Rev. Lett.* **83,** 2262 (1999).

[43] Gschneidner, K. A. Jr.; Pecharsky, V. K.; Brück, E.; Duijn, H. G. M.; Levin, E. M. *Phys. Rev. Lett.* **85,** 190 (2000).

[44] Pecharsky, V. K.; Gschneidner, K. A. Jr. *Adv. Mater.* **13** 683 (2001).

[45] Pecharsky, V. K.; Gschneidner, K. A. Jr. *Adv. Cryog. Eng.* **13,** 1729 (1998).

[46] M. Yue, J. Zhang, H. Zeng, and H. Chen, X. B. Liu, JOURNAL OF APPLIED PHYSICS **99**, 08Q104 (2006).

[47] Spichkin, Y. I.; Pecharsky, V. K.; Gschneidner, K. A. Jr. *J. Appl. Phys.* **89,** 1738 (2001).

[48] Deng J. Q.; Zhuang, Y. H.; Li, J. Q.; Zhu, Q. M. *Materials Letters* **61**, 2359 (2007).

[49] Carvalho et al. J. Appl. Phys. **97**, 10M320 (2005).

[50] Huang, H.; Pecharsky, A. O.; Pecharsky, V. K.; Gschneidner, K. A. Jr. *Adv. Cryog. Eng.* **48,** 11 (2002).

[51] Morellon, L.; Arnold, Z.; Magen, C.; Ritter, C.; Prokhnenko, O.; Skorokhod, Y.; Algarabe, P. A.; Ibarra, M. R.; *J. Kamarad Phys. Rev. Lett.* **93,** 137201 (2004).

[52] Ivtchenko, V. V.; Pecharsky, V. K.; Gschneidner, K. A. Jr. *Adv. Cryog. Eng.* **46,** 405 (2000).

[53] Gschneidner, K. A. Jr.; Pecharsky, V. K.; Pecharsky, A. O.; Ivtchenko, V. V.; Levin, E. M. *J. All. Comp.* **303-304**, 214 (2000).

[54] Thuy, N. P.; Tai, L. T.; Hien, N. T.; Nong, N. V.; Vinh, T. Q.; Thang, P. D.; Nguyen, T. P.; Molini´e, P. *Proc. 8th Asia-Pacific Physics Conf. (Taipei, Taiwan)* (Singapore: World Scientific) p 354 (2001).

[55] Pecharsky, A. O.; Gschneidner, K. A. Jr.; Pecharsky, V. K. *J. Appl. Phys.* **93,** 4722 (2003).

[56] Fu, H.; Chen, Y.; Tu, M.; Zhang, T. *Acta Materialia* **53**, 2377 (2005).

[57] Wu, W.; Tsokol, A. O.; Gschneidner, K. A. Jr.; Sampaio, J. A. *Journal of Alloys and Compounds* **403**, 118 (2005).

[58] Wada, H., Tanabe, Y. *Appl. Phys. Lett.* **79,** 3302 (2001).

[59] Wada, H.; Taniguchi, K.; Tanabe, Y. *Mater. Trans.* **43,** 73 (2002).

[60] Wada, H.; Morikawa, T.; Taniguchi, K.; Shibata, T.; Yamada, Y.; Akishige, Y. *Physica* B **328,** 114 (2003).

[61] Gama, S.; Coelho, A. A.; de Campos, A.; Carvalho, A. M. G.; Gandra, F. C. G.; von Ranke, P. J.; de Oliveira, N. A. *Phys. Rev. Lett.* **93,** 237202 (2004).

[62] de Campos, A.; Rocco, D. L.; Carvalho, A. M. G.; Caron, L.; Coelho, A. A.; Gama, S.; Da Silva, L. M.; Gandra, F. C. G.; Dos Santos, A. O.; Cardoso, L. P.; Von Ranke, P. J.; de Oliveira, N. A. *Nature Mater.* **5**, 802 (2006).

[63] Rocco, D. L.; de Campos, A.; Carvalho, A. M. G.; Caron, L.; Coelho, A. A.; Gama, S.; Gandra, F. C. G.; Dos Santos, A. O.; Cardoso, L. P.; Von Ranke, P. J.; de Oliveira, N. A. *Appl. Phys. Lett.* **90**, 242507 (2007).

[64] Sun, N. K.; Cui, W. B.;, Li, D.; Geng, D.Y.; Yang, F.; Zhang, Z. D. *Appl. Phys. Lett.* **92**, 072504 (2008).

[65] Liu, G. J.; Sun, J. R.; Shen, J.; Gao, B.; Zhang, H. W.; Hu, F. X.; Shen, B. G. *Appl. Phys. Lett.* **90**, 032507 (2007).

[66] Giguère, A.; Földeaki, M.; Ravi Gopal, B.; Chahine, R.; Bose, T. K.; Frydman, A.; Barclay, J. A.; *Phys. Rev. Lett.* **83**, 2262 (1999).

[67] Balli, M.; Fruchart, D.; Gignoux, D.; Zach, R. *Appl. Phys. Lett.* **95,** 072509 (2009).

[68] Tegus, O.; Brück, E.; Buschow, K. H. J.; De Boer, F. R. *Nature* **415**, 150 (2002).

[69] Brück, E.; Tegus, O.; Li, X. W.; de Boer, F. R.; Buschow, K. H. J. *Physica* B **327,** 431 (2003).

[70] Li, X. W.; Tegus, O.; Zhang, L.; Dagula, W.; Brück, E.; Buschow, K. H. J.; de Boer, F. R. *IEEE Trans. Magn.* **39,** 3148 (2003).

[71] Dagula, W.; Tegus, O.; Fuquan, B.; Zhang, L.; Si, P. Z.; Zhang, M.; Zhang, W. S.; Brück, E.; de Boer, F. R.; Buschow K. H. J. *IEEE Trans. Magn.* **41,** 2778 (2005).

[72] Cam Thanh D. T.; Brück, E.; Tegus, O.; Klaasse, J. C. P.; Gortenmulder, T. J.; Buschow, K. H. J. *J. Appl. Phys.* **99,** 08Q107 (2006).

[73] Cam Thanh D. T.; Brück, E.; Tegus, O.; Klaasse, J. C. P.; Buschow, K. H. J. *J. Magn. Magn. Mater.* **310,** e1012 (2007).

[74] Yabuta, H. ; Umeo, K.; Takabatake, T.; Chen, L.; Uwatoko, Y. *J. Magn. Magn. Mater.* **310**, 1826 (2007).

[75] Brück, E.; Kamarad, J.; Sechovsky, V.; Arnold, Z.; Tegus, O.; de Boer, F. R. *J. Magn. Magn. Mater.* **310** e1008 (2007).

[76] Hu, F.X.; Shen, B. G.; Sun, J. R.; Wu, G. H. *Phys. Rev. B* **64,** 132412 (2001).

[77] Zhou, X. Z.; Li, W.; Kunkel, H. P.; Williams, G. *J. Magn. Magn. Mater.* **293***,* 854 (2005).

[78] Yu, S. Y.; Cao, Z. X.; Ma, L.; Liu, G. D.; Chen, J. L.; Wu, G. H. *Appl. Phys. Lett.* **91**, 102507 (2007).

[79] Stadler, S.; Khan, M.; Mitchell, J.; Ali, N.; Gomes, A.M.; Dubenko, I.; Takeuchi, A.Y.; Guimarães, A.P. *Appl. Phys. Lett.* **88**, 192511 (2006).

[80] Krenke, T.; Duman, E.; Acet, M.; Wassermann, E. F.; Moya, X.; Manosa, L.; Planes, A. *Nat. Mater.* **4**, 450 (2005).

[81] Han, Z. D.; Wang, D. H.; Zhang, C. L.; Xuan, H. C.; Gu, B. X.; Du, Y. W. *Appl. Phys. Lett.* **90**, 042507 (2007).

[82] Oikawa, K.; Ito, W.; Imano, Y.; Sutou, Y.; Kainuma, R.; Ishida, K.; Okamoto, S.; Kitakami, O.; Kanomata, T. *Appl. Phys. Lett.* **88**, 122507 (2006).

[83] Sharma, V. K.; Chattopadhyay, M. K.; Kumar, R.; Ganguli, T.; Tiwari, P.; Roy, S. B. *J. Phys.: Condens. Matter* **19**, 496207 (2007).
[84] Kainuma, R.; Imano, Y.; Ito, W.; Sutou, Y.; Morito, H.; Okamoto, S.; Kitakami, O.; Oikawa, K.; Fujita, A.; Kanomota, T.; Ishida, K. *Nature London* **439**, 957 (2006).
[85] Moya, X.; Mañosa, L.; Planes, A.; Aksoy, S.; Acet, M.; Wassermann, E. F.; Krenke, T. *Phys. Rev. B* **75**, 184412 (2007).
[86] Krenke, T.; Duman, E.; Acet, M.; Moya, X.; Mañosa, L.; Planes, A. *J. Appl. Phys.* **102**, 033903 (2007).
[87]Xuan, H. C.; Xie, K. X.; Wang, D. H.; Han, Z.D.; Zhang, C.L.; Gu, B.X., Du, Y.W. *Appl. Phys. Lett.* **92**, 242506 (2008).
[88] Yasuda, T.; Kanomata, T.; Saito, T.; Yosida, H.; Nishihara, H.; Kainuma, R.; Oikawa, K.; Ishida, K.; Neumann, K. -U.; Ziebeck, K. R. A. *J. Magn. Magn. Mater.* **310,** 2770 (2007).
[89] Massalski, T. B. *Binary Alloy Phase Diagrams* vol 2, 2nd edn (Materials Park Ohio, USA: ASM International) p 1718 (1990).
[90] Kripyakevich, P. I.; Zarechnyuk, O. S.; Gladyshevsky, E. I.; Bodak, O. I. *Z. Anorg. Chem.* **358**, 90 (1968).
[91] Hu, F. X.; Shen, B. G.; Sun, J. R.; Cheng, Z. H.; Rao, G. H.; Zhang, X. X. *Appl. Phys. Lett.* **78** 3675 (2001).
[92] Fujita, A.; Fujieda, S.; Hasegawa, Y.; Fukamichi, K. *Phys. Rev.* B **67**, 104416 (2003).
[93] Hu, F. X.; Qian, X. L.; Sun, J. R.; Wang G. J.; Zhang, X. X.; Cheng, Z. H.; Shen, B. G. *J. Appl. Phys.* **92**, 3620 (2002).
[94] Wen, G. H.; Zheng, R. K.; Zhang, X. X.; Wang, W. H.; Chen, J. L.; Wu, G. H. *J. Appl. Phys.*91, 8537 (2002).
[95] Lyubina, J.; Gutfleisch, O.; Kuz'min, M. D.; Richter, M. *J. Magn. Magn. Mater.* **320**, 2252 (2008).
[96] Gutfleisch, O.; Yan, A.; Müller, K. -H. *J. Appl. Phys.* **97**, 10M305 (2005).
[97] Sun, Y.; Arnold, Z.; Kamarad, J.; Wang, G. -J.; Shen, B. -G.; Cheng, Z. -H. *Appl. Phys. Lett.* **89**, 172513 (2006).
[98] Hu, F.; Shen, B.; Sun, J.; Wang, G.; Cheng, Z. *Appl. Phys. Lett.* **80**, 826 (2002).
[99] Yan A.; Müller, K. -H.; Gutfleisch, O. *J. All. Comp.* **450,** 18 (2008).
[100] Fujieda, S.; Fujita, A.; Fukamichi, K. *J. Appl. Phys.* **102**, 023907 (2007).
[101] Fujieda, S.; Fujita, A.; Fukamichi, K. *J. Magn. Magn. Mater.* **310**, e1004 (2007).
[102] Fujieda, S.; Fujita, A.; Fukamichi, K. *Materials Science Forum* **561**, 1093-1096 (2007).
[103] Irisawa, K.; Fujita, A.; Fukamichi, K.; Yamazaki, Y.; Iijima, Y.; Matsubara, E. *J. All. Comp.* **316,** 70 (2001).
[104] Fujieda, S.; Fujita, A.; Fukamichi, K. *Appl. Phys. Lett.* **81**, 1276 (2002).
[105] Fujieda, S.; Fujita, A.; Fukamichi, *Mater. Trans.* **45**, 3228 (2004).
[106] Fujita, A.; Fujieda, S.; Hasegawa, Y.; Fukamichi, K. *Phys. Rev. B* **67,** 104416 (2003).
[107] Nikitin, S. A.; Tereshina, I. S.; Verbetsky, V. N.; Salamova, A. A.; Anosova, E. V. *J. All. Comp.* **367**, 266 (2004).
[108] Mandal, K.; Gutfleisch, O.; Yan, A.; Handstein, A.; Müller, K.-H. *J. Magn. Magn. Mater.* **290**, 673 (2005).
[109] Dan'kov, S. Y.; Tishin, A. M.; Pecharsky, V. K.; Gschneidner, K. A. Jr. *Rev. Sci. Instrum.* **68**, 2432 (1997).
[110] Gopal, B. R.; Chahine, R.; Bose, T. K.; *Rev. Sci. Instrum.* **68**, 1818 (1997).
[111] Chernyshov, A. S.; Filippov, D. A.; Ilyn, M. I.; Levitin, R. Z.; Pecharskaya, A. O.; Pecharsky, V. K.; Gschneidner, K. A. Jr.; Snegirev, V. V.; Tishin, A. M. *Physics of Metals and Metallography* **93**, S19 (2002).
[112] Hu, F. X.; Ilyn, M.; Tishin, A. M.; Sun, J. R.;Wang, G. J.; Chen, Y. F.; Wang, F.; Cheng, Z. H.; Shen, B. G. *Journal of Applied Physics* **93**, 5503 (2003).
[113] Hu, F. X.; Gao, J.; Qian, X. L.; Ilyn, M.; Tishin, A. M.; Sun, J. R.; Shen, B. G. *Journal of Applied Physics* **97**, 1 (2005).
[114] Brück, E.; Ilyn, M.; Tishin, A. M.; Tegus, O. *J. Magn. Magn. Mater.* **290**, 8 (2005).
[115] Ilyn, M.; Tishin, A. M., Hu, F. X.; Gao, J.; Sun, J. R.; Shen, B. G. *J. Magn. Magn. Mater.* **290**, 712 (2005).
[116] Wada, H.; Funaba, C.; Asano, T.; Ilyn, M.; Tishin, A. M. *Sci. Tech. Froid Comptes Rendus* **2005-4**, 37 (2005).
[117] Tishin, A. M. *Handbook of Magnetic Materials* **12**, 395 (1999).
[118] http://www.amtc.ru/en/catalog/Equipment/Magnetocaloric/ (accessed 26.11.2009).
[119] Gschneidner, K. A. Jr.; Pecharsky, V. K.; Brück, E.; Duijn, H. G. M.; Levin E. M. *Phys. Rev. Lett.* **85**, 4190 (2000).
[120] Khovaylo, V. V.; Skokov, K. P.; Koshkid'Ko, Yu. S.; Koledov, V. V.; Shavrov, V. G.; Buchelnikov, V. D.; Taskaev, S. V.; Miki, H.; Takagi, T.; Vasiliev, A. N. *Phys. Rev. B* **78**, 060403 (2008).
[121] McMichael, R. D.; Ritter, J. J.; Shull, R. D. *Journal of Applied Physics* **73,** 6946 (1993).
[122] Liu *et al.* Appl. Phys. Lett. **90**, 032507 (2007).
[123] Földeaki, M.; Chahine, R.; Bose, T. K. *J. Appl. Phys.* **77**, 3528 (1995).
[124] Pecharsky, V. K.; Gschneidner, K. A. Jr. *J. Appl. Phys.* **86**, 565 (1999).
[125] Levitin, R. Z.; Snegireva, V. V.; Kopylov, A. V.; Lagutin, A. S.; Gerber, A. *J. Magn. Magn. Mater.* **170 (1-2)**, 223 (1997).

[126] Zimm, C.; Jastrab, A.; Sternberg, A.; Pecharsky, V. K.; Gschneidner, K. A. Jr.; Osborne, M.; Anderson I.; *Adv. Cryog. Eng.* **43**, 1759 (1998).
[127] Bohigas, X.; Molins, E.; Roig, A.; Tejada, J., Zhang X. X., *IEEE Trans. Magn.* **36**, 538 (2000).
[128] Hirano, N.; Nagaya, S.; Takahashi, M.; Kuriyama, T.; Ito, K.; Nomura, S. *Adv. Cryog. Eng.* **47**, 1027 (2002).
[129] Rowe, A. M.; Barclay J. A. *Adv. Cryog. Eng.* **47**, 995 (2002).
[130] Zimm, C. *Paper No K7.003 Am. Phys. Soc. Meeting*, March 4, Austin, Texas (2003).
[131] Hirano, N. *Paper No. K7.002 Am. Phys. Soc. Meeting*, March 4, Austin, Texas (2003).
[132] Clot. P.; Viallet, D.; Allab, F.; Kedous-LeBouc, A.; Fournier, J. M.; Yonnet, J. P. *IEEE Trans. Magn.* **30**, 3349 (2003).
[133] Zimm, C; *Paper No. K7.003 Am. Phys. Soc. Meeting*, March 4, Austin, Texas (2003).
[134] Rowe, A. M.; Tura, A. *International Journal of Refrigeration* **29**, 1286 (2006).
[135] Zimm, C.; Auringer, J.; Boeder, A.; Chells, J.; Russek, S.; Sternberg, A. *Proceedings of the Second International Conference on Magnetic Refrigeration at Room Temperature*. International Institute of Refrigeration, Paris, pp. 341 (2007).
[136] Okamura, T.; Rachi, R.; Hirano, N.; Nagaya, S. *Proceedings of the Second International Conference on Magnetic Refrigeration at Room Temperature*. International Institute of Refrigeration, Paris, pp. 377 (2007).
[137] Smilh, G.S.; Tharp, A.G.; Johnson, Q.; *Acta Crystallogr.* **22**, 940 (1967).
[138] Holtzberg, F.; Gambino, R. J.; McGuire, T. R. *J. Phys. Chem. Solids* **28**, 2283 (1967).
[139] Smith, G. S.; Johnson, Q.; Tharp, A. G. *Acta Crystallogr.* **22**, 269 (1967).
[140] Gschneidner K A Jr, Pecharsky V K, Brück E, Duijn H G M and Levin E M 2000 *Phys. Rev. Lett.* **85** 4190.
[141] Morellon, L.; Algarabel, P. A.; Ibarra, M. R.; Blasco, J.; Garcia-Landa B. *Phys. Rev. B* **58,** R14721 (1998).
[142] Pecharsky, A. O.; Gschneidner, K. A. Jr.; Pecharsky, V. K.; Schindler, C. E. *J. Alloys Compounds* **338**, 126–35 (2002).
[143] Magen, C.; Arnold, Z.; Morellon, L.; Skorokhod, Y.; Algarabel, P. A.; Ibarra, M. R.; Kamarad, J. *Phys. Rev. Lett.* **91**, 207202 (2003).
[144] Morellon, L.; Arnold, Z.; Algarabel, P. A.; Magen, C.; Ibarra, M. R.; Skorokhod, Y. *J. Phys.: Condens. Matter* **16**, 1623 (2004).
[145] Pecharsky, V. K.; Samolyuk, G. D.; Antropov, V. P.; Pecharsky A. O.; Gschneidner, K. A. Jr. *J. Solid State Chem.* **171**, 57 (2003).
[146] Pecharsky, V. K.; Pecharsky A. O.; Gschneidner, K. A. Jr. *J. Alloys Comp.* **344**, 362 (2002).
[147] Smith, G. S.; Johnson, Q.; Tharp A. G. *Acta Crystallogr.* **22**, 940 (1967).
[148] Tegus, O.; Brück, E.; Zhang, L.; Dagula, Buschow, K. H. J.; de Boer, F. R. *Physica B* **319**, 174 (2002).
[149] Levin, E. M.; Gschneidner, K. A. Jr.; Lograsso, T. A.; Schlagel, D. L.; Pecharsky, V. K. *Phys. Rev. B* **69**, 144428 (2004).
[150] Magen, C.; Morellon, L.; Algarabel, P. A.; Ibarra, M. R.; Arnold, Z.; Kamarad, J.; Lograsso, T. A.; Schlagel, D. L.; Pecharsky, V. K.; Tsokol, A. O.; Gschneidner, K. A. Jr. *Phys. Rev. B* **72**, 024416 (2005).
[151] Tan, L.; Kreyssig, A.; Kim, J. W.; Goldman, A. I.; McQueeney, R. J.; Wermeille, D.; Sieve, B.; Lograsso, T. A.; Schlagel, D. L.; Budko, S. L.; Pecharsky, V. K.; Gschneidner, K. A. Jr. *Phys. Rev. B* **71**, 214408 (2005).
[152] Leib, J. S.; Lo, C. C. H.; Snyder, J. E.; Jiles, D. C.; Pecharsky, V. K.; Schlagel, D. S.; Lograsso, T. A. *IEEE Trans. Magn.* **38**, 2447 (2002).
[153] Samolyuk, G. D.; Antropov, V. P. *J. Appl. Phys.* **91**, 8540 (2002).
[154] Harmon, B. N.; Antonov, V. N. *J. Appl. Phys.* **91**, 9815 (2002).
[155] Tang, H.; Pecharsky, V. K.; Samolyuk, G. D.; Zou, M.; Gschneidner, K. A. Jr.; Antropov, V. P.; Schlagel, D. L.; Lograsso, T. A. *Phys. Rev. Lett.* **93**, 237203 (2004).
[156] Paudyal, D.; Pecharsky, V. K.; Gschneidner, K. A. Jr.; Harmon, B. N. *Phys. Rev. B* **73**, 144406 (2006).
[157] Levin, E. M.; Pecharsky, V. K.; Gschneidner, K. A. Jr. *Phys. Rev. B* **62**, R14625 (2000).
[158] Szade, J.; Skorek G.; Winiarski, A. *J. Cryst. Growth* **205,** 289 (1999).
[159] Meyers, J. S.; Chumbley, L. S.; Laabs F.; Pecharsky, A. O. *Scripta Mater.* **47,** 509 (2002).
[160] Gama, S.; Alves, C. S.; Coelho, A. A.; Ribeiro, C. A.; Persiano, A. I. C.; Silva, D. *J. Magn. Magn. Mater.* **272**, 848 (2004).
[161] Ugurlu, O.; Chumbley, L. S.; Schlagel D. L.; T.A. Lograsso *Acta Mater.* **53**, 3525 (2005).
[162] Moore, J. D.; Morrison, K.; Perkins, G. K.; Schlagel, D. L.; Lograsso, T. A.;Gschneidner, K. A. Jr.; Pecharsky, V. K.; Cohen L. F. *Advan. Mater.* **21**, 3780 (2009).
[163] Fu, H.; Chen, Y.; Tu, M.; Zhang, T. *Acta Mater.* **53**, 2377 (2005).
[164] Provenzano V.; Shapiro, A. J.; Shull, R. D. *Nature* **429**, 853 (2004).

[165] Pecharsky V. K.; Gschneidner K. A. Jr. *J. Magn. Magn. Mater.* **167**, L179 (1997).

[166] Shull, R.D.; Provenzano, V.; Shapiro, A. J.; Fu, A.; Lufaso, M. W.; Karapetrova, J.; Kletetschka, G.; Mikula V. *J. Appl. Phys.* **99**, 09K908 (2006).

[167] Zhuang Y. H.; Li, J. Q.; Huang, W. D.; Sun W. A.; Ao, W. Q. *Journal of Alloys and Compounds* **421**, 49 (2006).

[168] Zhang, T.; Chen, Y.; Tang, Y.; Du, H.; Ren, T.; Tu, M. *J. Alloys. Comps.* **433**, 18 (2007).

[169] Kumar, D. M. R.; Manivel Raja, M.; Gopalan, R.; Balamuralikrishnan, R.; Singh, A. K.; Chandrasekaran, V. *J. Alloys and Comps.* **461**, 14 (2008).

[170] Zhang, T.; Chen Y.; Tang, Y. *J. Phys. D: Appl. Phys.* **40**, 5778 (2007).

[171] Operating instructions for the Mini Arc Melting System MAM-1, Edmund Bühler GmbH, Germany (2007).

[172] Suryanarayana, C. *Progress in Materials Science* **46**, 1 (2001).

[173] http://www.riken.go.jp/lab-www/magmatlab/tour.html (08.03.2010)

[174] Magnetocaloric Measuring Setup Manual, Advanced Magnetic Technologies and Consulting, Ltd. (AMTC).

[175] Schwarz, B.; Podmiljšak, B.; Mattern, N.; Eckert, J. *J. Magn. Magn. Mater.* **322,** 2298 (2010).

Index of Figures

Index of Tables

Appendix: Publications related to this topic

Articles

1. PODMILJŠAK, Benjamin, MCGUINESS, Paul J., MATTERN, N., EHRENBERG, Helmut, KOBE, Spomenka. Magnetocaloric properties in the Gd[sub]5(Si[sub]2Ge[sub]2)[sub](1-z)Fe[sub]z(Z=0-0.75) system and magnetic properties of the newly formed Gd[sub]5(Si,Ge)[sub]3 phase. *IEEE trans. magn.*, 2009, vol. 45, no. 10, str. 4364-4367. [COBISS.SI-ID 23022887] tipologija 1.08 -> 1.01

2. PODMILJŠAK, Benjamin, MCGUINESS, Paul J., MIKLAVIČ, Blaž, ŽUŽEK ROŽMAN, Kristina, KOBE, Spomenka. Magnetocaloric properties and nanoscale structure of Fe-doped Gd[sub]5Ge[sub]2Si[sub]2 alloys. *J. appl. phys.*, 2009, vol. 105, no. 7, str. 07A941-1-07A941-3. [COBISS.SI-ID 22538023] tipologija 1.08 -> 1.01

3. PODMILJŠAK, Benjamin, ŠKULJ, Iztok, MARKOLI, Boštjan, ŽUŽEK ROŽMAN, Kristina, MCGUINESS, Paul J., KOBE, Spomenka. Microstructural changes in Fe-doped Gd[sub]5Si[sub]2G[sub]2. *J. magn. magn. mater.*. [Print ed.], 2008, vol. 321, no. 4, str. 300-304. [COBISS.SI-ID 22172199]

4. ŠKULJ, Irena, MCGUINESS, Paul J., PODMILJŠAK, Benjamin. Changes in the microstructure of Fe-doped Gd5Si2Ge2 = Spremembe v mikrostrukturi zlitine Gd5Si2Ge2, dopirane z Fe. *Mater. tehnol.*, 2008, vol. 42, no. 3, str. 117-120. [COBISS.SI-ID 678314]

5. PODMILJŠAK, Benjamin, ŠKULJ, Irena, MARKOLI, Boštjan, MCGUINESS, Paul J., ŽUŽEK ROŽMAN, Kristina, KOBE, Spomenka. Microstructural changes and hysteresis losses in Fe-doped Gd[sub]5Si[sub]2Ge[sub]2. *IEEE trans. magn.*, 2008, vol. 44, no. 11, str. 4529-4532. [COBISS.SI-ID 22330151]

Conferences

1. PODMILJŠAK, Benjamin, MCGUINESS, Paul J., ŠKULJ, Irena, MARKOLI, Boštjan, DRAŽIĆ, Goran, KOBE, Spomenka. A microstructural investigation of Gd[sub]5(SI[sub]xGe[sub](1-x))[sub]4 alloys produced. V: POREDOŠ, Alojz (ur.), ŠARLAH, Alen (ur.). *2nd International Conference on Magnetic Refrigeration at Room Temperature : proceedings, commissions B2, A1 with E2 : comptes rendus, commissions B2, A1 with E2, Portorož, Slovenia, 11-13,2007*, (Science et technique du froid, 2007-1). Paris: Institut International du Froid, 2007, str. 145-153. [COBISS.SI-ID 20702759]

2. PODMILJŠAK, Benjamin, ŠKULJ, Irena, MARKOLI, Boštjan, MCGUINESS, Paul J., KOBE, Spomenka. Phase formation and magnetic properties of Gd[sub]5Si[sub]2Ge[sub]2 with Fe substitutions. V: NIARCHOS, Dimitrios (ur.). *REPM'08 : proceedings of 20th International Workshop on Rare Earth Permanent Magnets & their Applications, September 8-10, Knossos, Crete*. [S. l.: s. n.], 2008, str. 95-99. [COBISS.SI-ID 21990951]

3. PODMILJŠAK, Benjamin, MCGUINESS, Paul J., KOBE, Spomenka. Preparation of magnetocaloric materials for a magnetic refrigerator. V: JENKO, Monika (ur.). 14. konferenca o materialih in tehnologijah = 14th Conference on Materials and Technology, 16-18 October, 2006,

Portorož, Slovenia. *Program in knjiga povzetkov*. Ljubljana: Inštitut za kovinske materiale in tehnologije, 2006, str. 127. [COBISS.SI-ID 20380967]

4. PODMILJŠAK, Benjamin, MCGUINESS, Paul J., KOBE, Spomenka. The effect of processing route and Fe substitutions on the microstructure of Gd[sub]5Si[sub]2Ge[sub]2. V: *MRS 2007 Fall meeting : 26-39 November 2007 : program and exhibit guide*. [S. l.: s. n.], 2007, str. 241. [COBISS.SI-ID 21434663]

5. PODMILJŠAK, Benjamin, MCGUINESS, Paul J., KOBE, Spomenka. Vpliv različnih proizvodnih procesov in substitucije Si z Fe na mikrostrukturo Gd5Si2Ge2 = The effect of processing route and Fe substitutions on the microstructure of Gd5Si2Ge2. V: JENKO, Monika (ur.). 15. konferenca o materialih in tehnologijah = 15th Conference on Materials and Technology, 8-10 October, 2007 Portorož, Slovenia. *Program in knjiga povzetkov*. Ljubljana: Inštitut za kovinske materiale in tehnologije], 2007, str. 43. [COBISS.SI-ID 21132071]

6. ŠKULJ, Irena, MCGUINESS, Paul J., PODMILJŠAK, Benjamin. Spremembe v mikrostrukturi zlitine Gd5Si2Ge2, dopirane z Fe = Changes in the microstructure of Fe-dopped Gd5Si2Ge2. V: JENKO, Monika (ur.). 15. konferenca o materialih in tehnologijah = 15th Conference on Materials and Technology, 8-10 October, 2007 Portorož, Slovenia. *Program in knjiga povzetkov*. Ljubljana: Inštitut za kovinske materiale in tehnologije], 2007, str. 118. [COBISS.SI-ID 654506]

7. MARKOLI, Boštjan, MCGUINESS, Paul J., PODMILJŠAK, Benjamin, ŠKULJ, Irena, KOBE, Spomenka. The synthesis of a magneto-caloric GD5 (GESI)4 alloy by arc melting = Sinteza magnetokalorične zlitine GD5 (GDSI)4 s taljenjem pod oblokom. V: *Zbornik referatov mednarodnega 47. livarskega posvetovanja, Portorož 2007*. Ljubljana: Društvo livarjev Slovenije, 2007, str. 48-49. [COBISS.SI-ID 735839]

8. PODMILJŠAK, Benjamin, ŠKULJ, Irena, MARKOLI, Boštjan, MCGUINESS, Paul J., KOBE, Spomenka. Microstructural changes and hysteresis losses in Fe-doped Gd[sub]5Si[sub]2Ge[sub]2. V: MIHAILOVIĆ, Dragan (ur.), KOBE, Spomenka (ur.), REMŠKAR, Maja (ur.), JAMNIK, Janko (ur.), ČOPIČ, Martin (ur.), DROBNE, Damjana (ur.). *Hot nano topics 2008 : incorporating SLONANO 2008, 3 overlapping workshops on current hot subjects in nanoscience, 23-30 May, Portorož, Slovenia : abstract book*. Ljubljana: [s. n.], 2008, str. 256. [COBISS.SI-ID 21757223]

9. PODMILJŠAK, Benjamin, ŠKULJ, Iztok, MARKOLI, Boštjan, MCGUINESS, Paul J., KOBE, Spomenka. Microstructural changes in Fe-doped Gd[sub]5Si[sub]2G[sub]2. V: IEEE International Magnetics Conference, Madrid, Spain, May 4-8, 2008. *INTERMAG Europe 2008 : digest CD*. [s.l.]: IEEE Magnetics Society, 2008, str. 1304-1305. [COBISS.SI-ID 22097959]

10. ŠKULJ, Irena, MCGUINESS, Paul J., PODMILJŠAK, Benjamin. Changes in the microstructure of Fe-doped Gd5Si2Ge2. *Metalurgija (Sisak)*, srpanj/rujan 2008, vol. 47, br. 3, str. 251. [COBISS.SI-ID 681898]

11. PODMILJŠAK, Benjamin, MCGUINESS, Paul J., KOBE, Spomenka, ŠKULJ, Irena. Magnetic changes in Fe-doped Gd[sub]5Si[sub]2Ge[sub]2. V: KOBE, Spomenka (ur.), ŽUŽEK ROŽMAN, Kristina (ur.), NOVAK, Saša (ur.), FIDLER, Sanja (ur.). *WomenInNano winter school : 7-9 February 2008, Kranjska Gora, Slovenia : abstract book*. [S.l.: s.n.], 2008, str. 95. [COBISS.SI-ID 21499943]

12. PODMILJŠAK, Benjamin, MCGUINESS, Paul J., MATTERN, N., EHRENBERG, Helmut, KOBE, Spomenka. Magnetne in strukturne spremembe v Gd[spodaj]5Si[spodaj]2Ge[spodaj2 zlitinah pri zamenjavi Si ali Gd z železom. V: KUŠČER, Danjela (ur.), PERC, Branka (ur.). 4. Dan Mladih Raziskovalcev KMBO, Ljubljana, Slovenija, 11.2.2010. *[Program in povzetki]*. Ljubljana: Institut "Jožef Stefan", 2010, str. 16. [COBISS.SI-ID 23419431]